Gas Turbine Vane Film Cooling for Engine-Realistic Combustor Flows



Jamie Jian Hui Saw

University College

University of Oxford

A thesis submitted for the degree of

Doctor of Philosophy

Hilary 2023

Acknowledgements

This project would not have been possible without Professor Budimir Rosic who introduced me to the exciting field of thermofluids and its application to the design of gas turbines. In particular, I would like to extend my deepest gratitude for his encouragement and valuable guidance during regular project meetings.

I would like also to express my appreciation to all those who have directly and indirectly guided me in carrying out this research project. I would like to thank Wesley Ramm for his support and guidance which were invaluable to overcoming the various challenges faced throughout this project, though his Americanisms have always left me guessing, e.g. like shootin' fish in a barrel. Thank you to all my friends at Osney, who have made the entire journey more enjoyable. Special thanks go to Simla Saglam, Oguzhan Murat, and Mark Baker for helping me run my experiments.

I would also like to express my gratitude to the maintenance staff, Bill Godfrey, Hal Surtell, and Jason McCluskey for their support in building the CO_2 facility. Much of the timeliness of the experimental work is due to their rapid response in maintaining the facility. Support from the Workshop technicians, in particular Duncan Blake, Harry Kachika, Leo Verling, and Dave O'Dell, in manufacturing my components have not only enabled my experimental campaigns, but also taught me much in my time here. I also want to thank Craig Parsons for providing IT support and Anna Erillo and Alex Weaving for handling the mountain of paperwork I sent their way.

WWF has been instrumental in retaining my sanity during the writeup of this thesis.

Finally, I owe much to my parents for their love, encouragement and support, without which, none of this would have been possible. Thank you for making my academic ambitions possible. This thesis is dedicated to both of you.

PS.[1]

[1]It was not my tuna

Abstract

While all lean-burn combustors follow the same design principles and intent, there exist a wide variety of combustor geometries in use, whose downstream aerothermal fields are unquantified. Conventional design processes for the nozzle guide vane (NGV) range from simple ones that use homogeneous isotropic turbulence intensity at the inlet to more advanced ones that use a turbulence intensity profile and/or swirl profile that is fixed in space and time.

This study shows that the inlet flow to the NGV is inherently unsteady and contains large scale turbulent structures when using a single large swirler. The swirl core changes the pressure field around the NGV, resulting in change in blade loading from hub to casing. Consequently, the migration of secondary flows is also altered in the presence of swirl and the size of vortices in the system can be weakened in some regions and strengthened in others. External film cooling flows are also affected by the change in pressure field, resulting in over or undercooling of certain regions.

While vanes can be designed to mitigate these effects in the steady state, the unsteadiness of the swirl core means these effects vary spatially and temporally. If not accounted for, this can result in localised instantaneous undercooling of a blade section. This thermal cycling occurs at frequencies in the range 1 - 100 Hz, which is much higher than typical fatigue studies performed on thermal barrier coatings, hence leading to more rapid degradation. Changes in blade loading and secondary flows in the NGV can also lead to varying inlet angles in the downstream rotor, hence affecting its performance.

Unique high speed and high resolution thin film gauge and infra-red instrumentation allow the visualisation and tracking of these large structures in space and time as they migrate across the vane surface. Large Eddy Simulation (LES) studies of single and multicore swirlers are also carried out to investigate the effects of the large unsteady coherent structures originating from the combustor on the NGV's aerodynamic

field and its corresponding secondary flow system.

Engine representative experiments simulating turbine operation at full load were carried out with six different inlet geometries. It is shown that the size and strength of these large scale structures are reduced by decreasing the size of the swirlers and increasing their number, thereby improving the inlet flow conditions to the NGV. As most conventional combustors today use a single large swirler, it is hoped that this study will be of interest in the design of future combustor geometries and demonstrates the need for an integrated design approach to the combustor-turbine region.

Contents

1 Introduction **1**

1.1 Gas Turbines in Decarbonising Power Generation and Aviation 1

1.2 Basics of a Gas Turbine 3

1.3 The Combustor-Turbine Interface in Land-Based Gas Turbines 7

1.4 Motivation for this Thesis 12

1.5 Scope and Aims of the Thesis 13

1.6 Limitations of the Thesis 15

1.7 Thesis Outline 15

2 Literature Review **18**

2.1 State of the Art in Combustor Geometries 18

2.2 The Aerothermal Field of Nozzle Guide Vanes 21

2.2.1 Secondary Flows 21

2.2.2 Loss Mechanisms 26

2.2.3 Heat Transfer 29

2.2.4 Film Cooling 33

2.2.4.1 Film Cooling Structures 35

2.2.4.2 Effect of Velocity Ratio, Blowing Ratio, and Momentum Flux Ratio 37

2.3 Interactions Between the Upstream Flow and the Nozzle Guide Vane 39

2.3.1 Characterisation of Upstream Flow 40

2.3.2 Effects of Turbulence 42

2.3.3 Effects of Temperature Gradients (Hot Streaks) 44

2.3.4 Effects of Swirl 46

2.3.5 Effects of Flow Unsteadiness 49

2.3.6 Effects of Combustion 50
2.3.7 Effects of Integration 52
2.3.7.1 On the Potential Field in the Combustor 53
2.3.7.2 On Acoustics in the Combustor 54
2.4 Conclusions 54

3 Methodology **57**
3.1 Experimental Facility 57
3.1.1 Geometric Parameters & Operating Conditions 59
3.1.2 Inlet Flow Conditions 60
3.2 Film Cooling System 62
3.2.1 Pressure Regulator 63
3.2.2 Relief System 65
3.2.3 Sonic Venturi Nozzle 65
3.2.4 Film-Cooled Nozzle Guide Vane 67
3.3 Infra-Red (IR) Thermography 69
3.3.1 Camera Calibration & Measurement Uncertainty 70
3.3.2 On the Use of the Semi-Infinite Assumption 73
3.3.3 Post-Processing Methodology 74
3.3.3.1 Determining the Driving Temperature 76
3.3.3.2 Determining Window Start Frame and Window Size 79
3.3.3.3 Decomposing Mean and Fluctuations 81
3.4 Thin Film Gauges 84
3.4.1 Operating Principle 85
3.4.2 Gauge Calibration & Measurement Uncertainty 87
3.4.3 Gauge Construction 88
3.4.4 Post-Processing Methodology 90
3.5 High-Speed Pressure Transducers 91
3.6 LES of Combustor-Turbine Interface 92

3.6.1 Mesh Sizing 93
3.6.2 TBLOCK Flow Solver 94

4 Numerical Evaluation of the Impulse Response for Solving the Heat Conduction Equation 100

4.1 Existing Methodologies for Obtaining Heat Flux 101
4.2 Green's Functions in Heat Conduction 103
4.3 Analytical Expressions of Green's Functions 106
4.4 Numerically Evaluating the Green's Function 108
4.4.1 Filter Deconvolution 111
4.4.2 Differentiation of Heavyside Step Input 111
4.5 Application of the Impulse Response Method to Multi-Layered Substrates 112
4.6 Application of the Impulse Response Method to Validating the Semi-Infinite Assumption 114
4.7 Extensions to Arbitrary 2D and 3D Geometries 119
4.7.1 General Procedure for Evaluating the Green's Functions in Discretised 2D & 3D Domains 122
4.7.2 Potential Applications 125
4.7.3 Methods for Accelerating the Green's Function Procedure . . 125
4.8 Summary 126

5 Flow Interactions at the Combustor-Turbine Interface for Single & Multicore Swirlers (LES) 128

5.1 Flow Field Downstream of the 8-Core Swirler 129
5.2 Time-Averaged Freestream Flow Deviation at the Inlet to the NGV . 135
5.3 Effects of Inlet Flow Conditions on the Aerodynamics of the NGV . . 139
5.3.1 At the Leading Edge 139
5.3.2 In the Vane Passages 141
5.3.3 At the Trailing Edge Exit Plane 143

5.4 Unsteadiness of the Freestream and Secondary Flows Around the NGV 146
5.4.1 Unsteadiness at the Inlet Plane to the NGV 146
5.4.2 Unsteadiness of Secondary Flows 148
5.4.2.1 Oscillations in the Position of the Horseshoe Vortex . 148
5.4.2.2 Oscillations in the Position of the Passage Vortex . . 154
5.4.3 Spectral Analysis of Unsteady Features 155
5.5 Summary 161

6 Time-Averaged Effects of Combustor Geometry on Uncooled and Film-Cooled NGVs 163
6.1 Heat Transfer on an Uncooled Vane 165
6.1.1 Clean Inflow and Uniform Turbulence 165
6.1.2 Single-Core Swirler and Reverse Single-Core Swirler 166
6.1.3 8-Core Swirler and 12-Core Swirler 168
6.2 Heat Transfer on a Film-Cooled Vane 172
6.3 Influence of Combustor Flows on Film Cooling Distribution 175
6.4 Summary 178

7 Unsteady Effects of Combustor Geometry on a Film-Cooled NGV 180
7.1 Spectra of Temperature and Pressure Fluctuations 180
7.2 Effect of Fluctuations on the Instantaneous Distribution of Cooling Effectiveness 182
7.3 Quantifying Levels of Fluctuations of Cooling Effectiveness 184
7.4 Effect of Fluctuations on Surface Temperature at Engine Conditions . 189
7.5 Identifying Sources of Fluctuations 193
7.6 Summary 201

8 Conclusions 203
8.1 Summary of Key Objectives 203
8.2 Summary of Main Findings 204

8.2.1 Generalisation and Application of the Impulse Response Method 204
8.2.2 Effect of Combustor Geometry on Downstream Flow 205
8.2.3 Effect of Swirl and a Total Pressure Gradient on the Potential Field 207
8.2.4 Effect of Unsteadiness on Secondary Flows 208
8.2.5 Effect of Combustor Flows on Heat Transfer and Film Cooling on the NGV 209
8.2.6 Integration of Numerical and Experimental Studies in the CTI 210
8.3 Future Work 211
8.4 Final Remarks 212

Bibliography **213**

List of Figures

1.1 Global power generation capacity showing additions and retirements from 2018 - 2040 [2] 1

1.2 General Electric 7FA heavy duty gas turbine for power generation . . 3

1.3 Process flow diagram and thermodynamic cycles of the Brayton and Rankine cycle 4

1.5 Real efficiency of Brayton cycle accounting for non-isentropic effects in the compressor and turbine for different maximum firing temperatures 7

1.6 Cross-section of gas turbine showing the combustor turbine interface and location of the combustor wall, shielded, and unshielded vanes . . 8

1.7 Internal and external cooling features of a nozzle guide vane [10] . . . 9

1.8 Damage of two JT9D NGVs with and without TBCs applied when subjected to thermal cycling engine tests 10

1.9 Simplified schematic of RQL and LPM combustors 10

1.10 Streamlines of weakly and highly swirling flow with subsequent vortex breakdown and formation of the recirculation zone 12

2.1 A conventional single-core combustor geometry 19

2.2 A multi-core General Electric DLN-2.6 combustor 19

2.3 A state-of-the-art dry low emission / dry low NO_x (DLE/DLM) hydrogen combustor geometry 20

2.4 Theory of secondary flow phenomenon as a result of a total pressure gradient in the boundary layer [28] 22

2.5 Model of secondary flows proposed by Langston [32] 23

2.6 Model of secondary flows proposed by Wang et al. [35] 24

2.7 Pressure loss and gain/decay in SKE through the NGV, and entropy generation rates on the endwall and NGV suction side 28

2.8 Heat transfer augmentation at the leading edge-endwall junction and endwall regions 31
2.9 Sherwood number distribution on vane suction side 32
2.10 Secondary flow structures of a perpendicular jet in crossflow [66] . . . 35
2.11 Regions of low and high heat transfer coefficient augmentation around a film cooling hole 36
2.12 Contours of temperature and adiabatic effectiveness of a coolant jet in crossflow for different blowing ratios 37
2.13 Profiles of turbulence intensity, temperature, and swirl angle measured at the inlet place to the NGV 41
2.14 RMS fluctuations of pressure along the axial length of the combustor for non-reacting and reacting cases 51

3.1 MHI high speed linear cascade facility 58
3.2 Experimentally measured combustor profiles for the single-core and 8-core swirlers in the MHI linear cascade facility 61
3.3 CO_2 film cooling supply system to the MHI linear cascade facility . . 63
3.4 $P - h$ diagram for CO_2 with various isotherms and an isenthalpic expansion process across the pressure regulator from 50 bar to 5 bar . . 64
3.5 Choked mass flow rate, $\dot{m}^*$, with line pressure, P, for 1, 4, and 8 cylinders and the relief system 65
3.6 Film-cooled F-type gas turbine NGV showing internal and external cooling features 67
3.7 Black body calibration curve for a single pixel of the FLIR X6900sc infra-red camera 71
3.8 Film-cooled vanes with matte black paint coat for IR thermography . 72
3.9 HTC post-processing methodology for a single pixel from an IR camera 75
3.10 Comparison of NRMSE for different HTC regression models in uncooled and film-cooled experiments 78

3.11 Effect of varying the post-processing window start frame and window size 79
3.12 Metrics for determining the post-processing window start frame and window size 80
3.13 Decomposition of fluctuations in heat flux into constituent fluctuations in the aerodynamic field and the thermal field 83
3.14 Circuit diagram of a Wheatstone bridge with one gauge connected in 1/4-bridge configuration 85
3.15 Cross-section of double-sided thin film gauge used in this study . . . 89
3.16 Film-cooled vane instrumented with double-sided thin film gauges . . 90
3.17 Cavity resonance of pressure transducer 92
3.18 LES flow domains for the single-core and 8-core swirler geometries . . 93
3.19 Resolved turbulent kinetic energy upstream and downstream of the non-conformal mesh interface 97
3.20 Power spectral density of axial velocity for both single-core and 8-core swirlers 98
3.21 Time trace of total pressure and its statistics showing convergence and stationarity of data 99

4.1 Impulse response of multi-layered substrate at $x = 0$ subject to temperature boundary conditions at $x' = 0$ and $x' = L$ 113
4.2 Comparison of the finite differencing and impulse response methods to post-process temperature to heat flux for double-sided thin film gauges 114
4.3 Sensitivity of penetration time to coolant-side HTC, h_c, and coolant total temperature, $T_{0,c}$, for Heaviside step boundary conditions 117
4.4 Sensitivity of penetration time to coolant-side HTC, h_c, and coolant total temperature, $T_{0,c}$, for real measured data 118
4.5 Physical representation of the 2D Green's function equation 121

4.6 Methodology to evaluate the Green's function for a single node of an arbitrary geometry 123
4.7 Comparison of temperature fields evaluated with the finite differencing and impulse response methodologies with time and spatially varying boundary conditions 124
4.8 Temperature field at four different timesteps from finite differencing and convolution with the Green's function 124

5.1 LES flow domain for the single and 8-core swirler cases 129
5.2 Cross-sectional views of the 8-core swirler showing time-averaged contours of axial velocity, total pressure, and RMS of total pressure . . . 130
5.3 Precession of the vortex cores for the main swirlers and pilot swirler for the 8-core swirler 131
5.4 PSD of total pressure just downstream of the pilot swirler of the 8-core swirler 132
5.5 Cross-section views of time-averaged axial vorticity in the transition duct and at the NGV inlet plane 133
5.6 Axial variation in mass-weighted plane average TKE and swirl number for both single and 8-core swirlers 135
5.7 Contours of total pressure, yaw angle, and pitch angle at the NGV inlet plane for the single-core swirler obtained from time-averaged LES and experiments 136
5.8 Contours of total pressure, yaw angle, and pitch angle at the NGV inlet plane for the 8-core swirler obtained from time-averaged LES and experiments 137
5.9 Interaction of the combustor wake with the vane's potential field leading to the formation of a new vortex pair 139
5.10 Static pressure distribution in the passage near the unshielded vane leading edge for the single-core and 8-core swirlers 140

5.11 Total pressure distribution in the passage near the unshielded vane trailing edge for the single-core and 8-core swirlers 141
5.12 Contours of normalised total pressure and streamwise vorticity at axial distance $x/C_{ax} = 0.739$ 142
5.13 Streamlines along the hub endwall boundary layer showing the migration of the passage vortex for the single-core and 8-core swirlers . . . 142
5.14 Contours of normalised total pressure at the exit plane obtained from time-averaged LES and experiments for the single-core swirler 144
5.15 Mass-weighted pitchwise average profiles of normalised total pressure and yaw angle at the exit plane for the single-core swirler 144
5.16 Contours of normalised total pressure at the exit plane obtained from time-averaged LES for the single-core and 8-core swirlers 145
5.17 Contours of RMS of total pressure at the NGV inlet plane obtained from time-averaged LES for the single-core and 8-core swirlers 146
5.18 Instantaneous snapshots of normalised total pressure at the NGV inlet plane, showing tracks of the swirl core migration 147
5.19 Instantaneous snapshots showing the migration of the horseshoe vortex (green) near the hub for the single-core swirler case 151
5.20 Migration of coherent structures along hub endwall for the single-core and 8-core swirlers 152
5.21 Pitchwise precession of the total pressure loss core and corresponding migration of the horseshoe vortex at two timesteps 153
5.22 Radial precession of the total pressure loss core and corresponding migration of the passage vortex at two timesteps 155
5.23 Time history of the position of the horseshoe vortex for both swirler geometries 156
5.24 Time history of the streamwise velocity measured at the centre of the mean horseshoe vortex location for both swirler cases 157

5.25 Comparison of power spectral densities of various quantities between the single-core and 8-core swirlers 158

6.1 Contours of HTC on the unshielded vane's suction side for clean inflow and turbulence grid 165
6.2 Spanwise distribution of HTC at axial distance, $x/C_{ax} = 0.739$, for clean inflow and turbulence grid 165
6.3 Contours of HTC on the unshielded vane's suction side for the single-core swirler and the reverse single-core swirler 168
6.4 Contours of HTC on the unshielded vane's suction side for the single-core swirler, 8-core swirler, 12-core swirler, and turbulence grid 170
6.5 Spanwise distribution of HTC at axial distance, $x/C_{ax} = 0.739$, for all inflow conditions 170
6.6 Contours of adiabatic cooling effectiveness on the unshielded vane's suction side for all inflow conditions 173
6.7 Spanwise distribution of adiabatic cooling effectiveness at axial distance, $x/C_{ax} = 0.739$, for the single-core swirler, 8-core swirler, 12-core swirler, and turbulence grid 174
6.8 Spanwise distribution of HTC and adiabatic cooling effectiveness at axial distance, $x/C_{ax} = 0.739$, for the single-core swirler, 8-core swirler, 12-core swirler, and turbulence grid 175
6.9 Adiabatic cooling effectiveness near cooling holes located around the hub, midspan, and casing 177

7.1 Normalised power spectral densities of experimentally measured temperature and pressure for the single-core swirler case 181
7.2 Contours of instantaneous adiabatic cooling effectiveness on the unshielded vane's suction side for all inflow conditions 183

7.3 Contours of normalised RMS of adiabatic cooling effectiveness on the unshielded vane's suction side for all inflow conditions 186
7.4 Contours of relative RMS of adiabatic cooling effectiveness on the unshielded vane's suction side for all inflow conditions 187
7.5 Laterally-averaged normalised RMS of adiabatic cooling effectiveness for all inflow conditions obtained from thin-film gauges 188
7.6 Peak-to-peak temperature fluctuations at engine conditions 192
7.7 Relevant length and volume scales of the facility and working section that may contribute resonance 195
7.8 Locations of pressure transducers on the unsteady pressure vane . . . 196
7.9 Power spectral densities of total pressure obtained from LES and experiments for the single-core swirler 196
7.10 Phase difference between sensors 3 and 5 for the single-core swirler (blue) and clean inflow (red) 198
7.11 Propagation of pressure wave from downstream of the vane to upstream for the clean inflow case 200

Nomenclature

Physical quantities

A	Area
c	Speed of sound
c_p	Specific heat capacity at constant pressure
h	Heat transfer coefficient
k	Thermal conductivity
L	Length
q	Heat flux
$T_{0,\infty}$	Freestream total temperature
$T_{0,\mathrm{r}}$	Recovery total temperature
$T_{0,c}$	Coolant total temperature
T_{ad}	Adiabatic wall temperature
V	Volume

Greek letters

α	Thermal diffusivity
ϵ	Emissivity
γ	Ratio of specific heat capacities
Λ	Integral length scale
λ	Turbulence microscale

ω Angular frequency

ρ Density

Non-dimensional quantities

Bi Biot number

M Mach number

Nu Nusselt number

Pr Prandtl number

Re Reynolds number

Sr Strouhal number

St Stanton number

S Swirl number

Tu Turbulence intensity

Acronyms

ADC Analogue-to-digital converter

CCGT Combined cycle gas turbine

CEESI Colorado Engineering Experiment Station Inc.

CTI Combustor-turbine interface

CTRZ Central toroidal recirculation zone

CVP Counter-rotating vortex pair

DAQ Data acquisition

DLE Dry low emissions

DLN Dry low-NOx

ENIG Electroless nickel immersion gold

GHG Greenhouse gas

HV Horseshoe vortex

IR Infra-red

LE Leading edge

LES Large eddy simulation

LPM Lean premixed

MHI Mitsubishi Heavy Industries

NGV Nozzle guide vane

NIST National Institute of Standards and Technology

PS Pressure side

PV Passage vortex

RQL Rich-burn, quick quench, lean-burn

SAF Sustainable aviation fuels

SAS Scale adaptive simulation

SGS Subgrid scale

SKE Secondary kinetic energy

SMT Surface mount technology

SNR Signal-to-noise ratio

SS Suction side

TE Trailing edge

Chapter 1
Introduction

1.1 Gas Turbines in Decarbonising Power Generation and Aviation

Over the years, an increasing population and rapid urbanization has boosted demand for power generation. At present, natural gas constitutes the second largest source of electricity generation globally [1], and will become the dominant source by 2040, followed by renewables [2], as shown in Fig. 1.1.

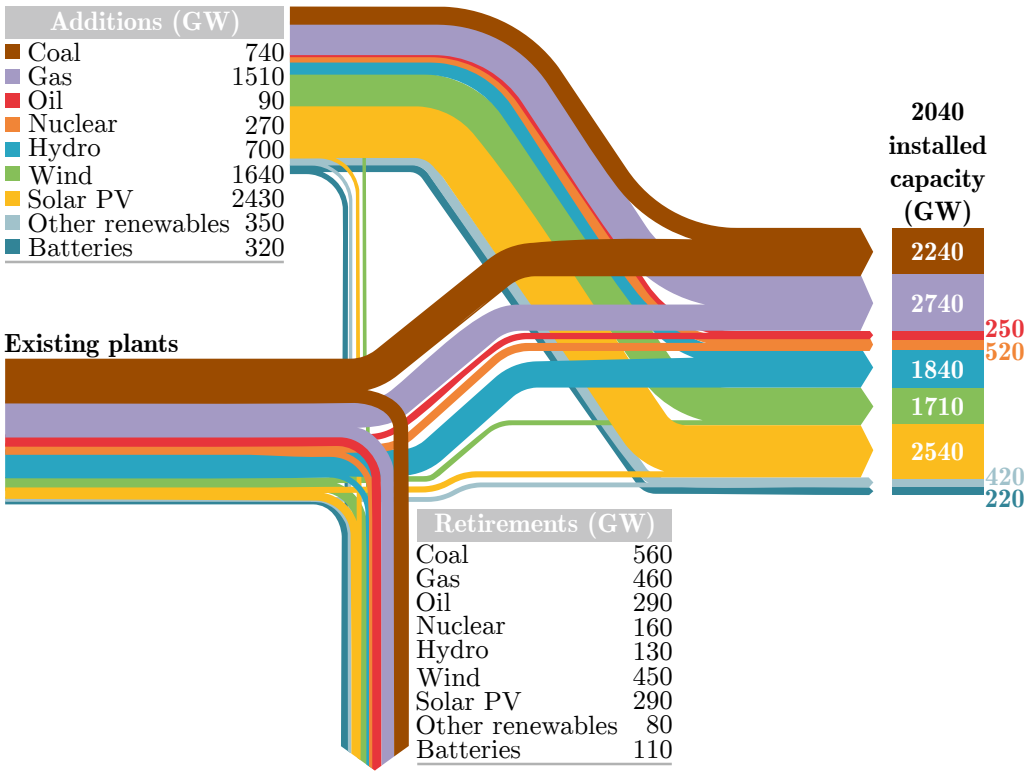


Figure 1.1: Global power generation capacity showing additions and retirements from 2018 - 2040 [2]

Despite the increase in renewables, the rising demand in total power will ensure that there is a net increase in fossil fuel-based power generation, suggesting that gas turbines will be the mainstay of power generation for the forseeable future. In

the aviation industry, open cycle gas turbines in their various configurations already dominate the market share by engine type compared to reciprocating engines. This is driven by a growing middle class and the introduction of low-cost airlines, with aviation traffic predicted to rise by 6% annually. The global market for gas turbines as a whole is predicted to grow by 37% by 2030 [3]. Therefore, gas turbines will play a critical role in the decarbonisation of these industries in its efforts to achieve a net-zero economy.

Following the recent COP26, COP27 and IPCC report, there is global consensus to keep the Paris and Glasgow targets alive by limiting greenhouse gas (GHG) emissions. Furthermore, increasingly ambitious emissions targets and favourable government policies have accelerated the electrification of industries - such as transport - and increased demand for renewable energy and low-carbon fuels [4]. These efforts introduce challenges such as the intermittency of renewables and the requirement for fuel flexibility.

In the short to medium term, gas turbines enable the transition from coal and oil-fired power plants towards using low-carbon fuels. Modern large scale power plants operate a combined cycle gas turbine (CCGT) which are some of the lowest GHG emitting and most efficient thermal power plants. For example, Mitsubishi Heavy Industries' (MHI) heavy-duty M701J gas turbine claims a combined cycle efficiency of 64% [5] and plant output of 650 - 840 MW. There is also increasing interest in aero-derivative type engines for distributed power systems as the energy mix becomes more varied when renewable energy plants are brought online. Aero-derivative gas turbines offer higher efficiencies, modularity and easier maintainability allowing deployment in remote locations, and more rapid start-up and response times compared to large frame gas turbines.

Gas turbines are also able to run on a variety of fuels aside from natural gas, including biofuels, blends containing hydrogen, and in the future even running on pure hydrogen. This presents a route for incorporating low-carbon fuels into energy mix, as

exemplified by the UK government's Jet Zero plan as part its Net Zero strategy, which aims to deliver 10% sustainable aviation fuels (SAF) by 2030 through the investment of £180 million to support the development of SAF plants [6]. Forecasts of global demands for natural gas, sustainable fuels, and hydrogen predict a rise by 10%, 300%, and 500% respectively, with global energy consumption predicted to rise by 14% by 2050 [4]. As recently as November 2022, Rolls Royce, in partnership with easyJet, conducted a ground test on a modified demonstrator turboprop engine running on green hydrogen.

In the long term, the scalability of gas turbines from these smaller aero-derivative engines to large-scale heavy-duty engines provides flexibility when conforming to the needs of an evolving energy landscape - allowing for peaking operation as well as base load operation. In the future, new technologies such as 3D printed parts, composite materials, novel combustor designs, etc. will enable further improvements in efficiencies and flexibility.

1.2 Basics of a Gas Turbine

A gas turbine is a type of internal combustion engine that operates with a continuous flow of air and fuel through the system, as opposed to reciprocating engines which operates on a fixed mass of air and fuel. Fig. 1.2 shows a cross-section of a land-based power generation gas turbine in open cycle configuration.

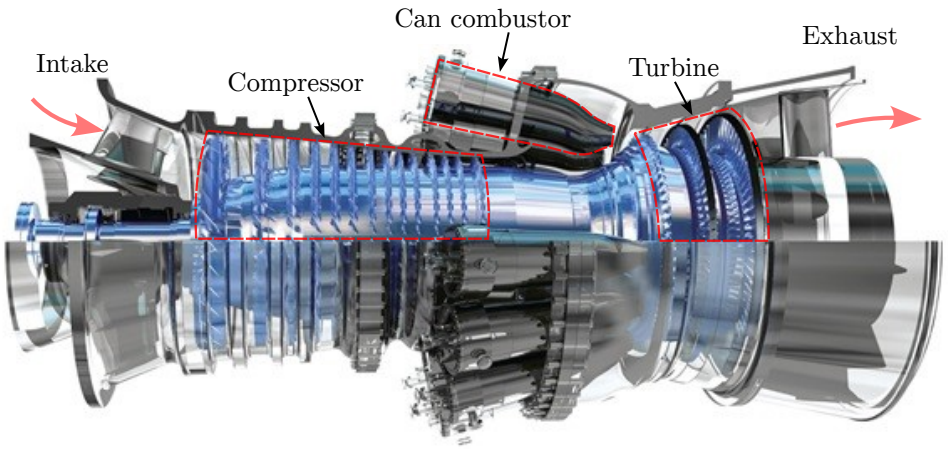


Figure 1.2: General Electric 7FA heavy duty gas turbine for power generation

Air enters the intake at atmospheric conditions and is compressed by the compressor stage to typically 21 bara. This high pressure air flows into the can combustors and is premixed with fuel before being combusted. This raises the temperature of the fluid to approx. 1600 °C. High pressure and high temperature fluid now passes through the turbine stage, where it is expanded to turn the rotor and drive the shaft where work is extracted. Various configurations of gas turbines exist, depending on its end-use, e.g. power generation or aviation, shaft work or thrust, etc. The process described above is idealised by the Brayton cycle shown in Fig. 1.3.

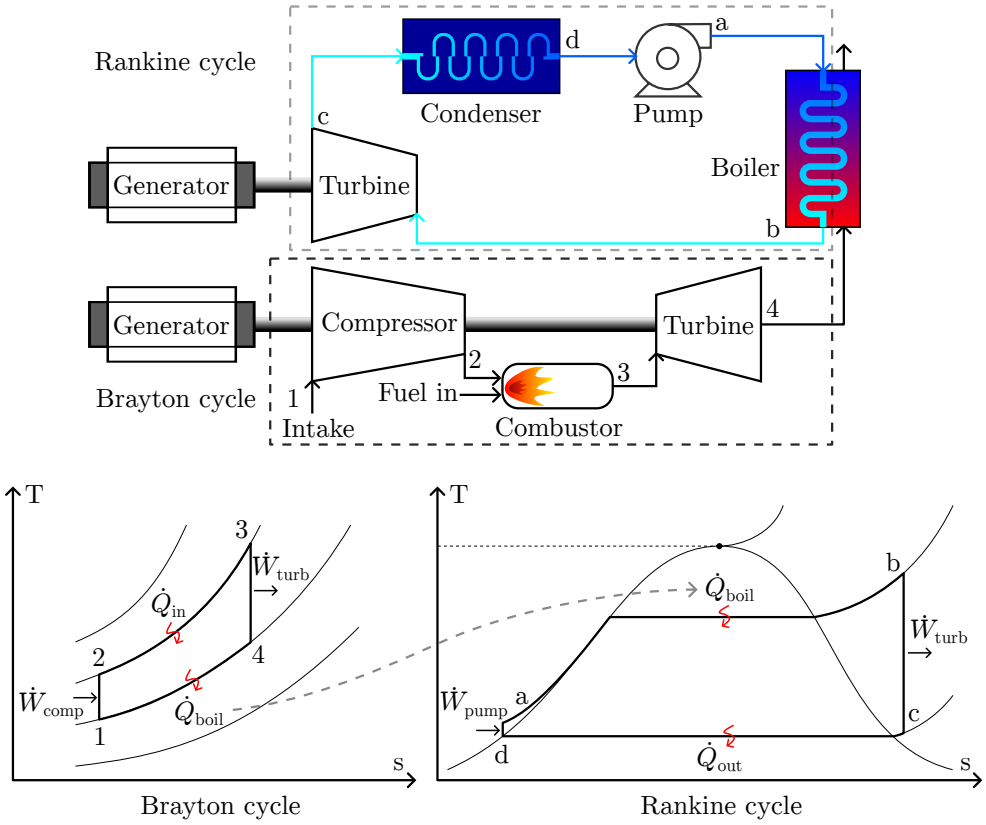


Figure 1.3: Top: Process flow diagram of the Brayton cycle combined with a Rankine cycle. Bottom: Thermodynamic cycles plotted on temperature-entropy graphs for the Brayton cycle (left) and Rankine cycle (right)

The four processes from intake to exhaust are: (1) isentropic compression, (2) isobaric heat addition, (3) isentropic expansion, and (4) isobaric heat rejection. In an isobaric process, for the same heat input, the temperature change along any isobar is always the same, $\mathrm{d}q = \mathrm{d}h$. If the process is reversible, then $\mathrm{d}q = T\,\mathrm{d}s$, showing that heat input/rejection at higher temperatures results in a smaller change in entropy.

Thus, by relating heat input/rejection to temperature change, it can be seen that isobars on a temperature-entropy diagram diverge, ${}^{\mathrm{d}T}/_{\mathrm{d}s} = {}^{T}/_{c_p}$. So gains in work extracted over the work input to compress the fluid from one isobar to another is due to the divergence of isobars. Therefore, the thermal efficiency of the Brayton cycle, η_{B}, is only governed by the compression ratio,

$$\eta_{\mathrm{B}} = 1 - \frac{1}{\left({}^{P_2}/_{P_1}{}^{(\gamma-1)/\gamma}\right)} \tag{1.1}$$

with higher compression ratios giving higher efficiencies.

However, practical limits in turbine technology constrain the maximum operating temperature in the combustor-turbine interface. This is the temperature of the freestream as it enters the turbine and is seen by the nozzle guide vanes, also called the turbine entry temperature (TET). This can be specified this as ratio of maximum to minimum temperature, $\theta = {}^{T_3}/_{T_1}$. Referring back to Fig. 1.3, it can be seen that varying the pressure ratio will alter the net work that can be extracted from the cycle. In the limit of the compressor doing no work, $T_2 \to T_1$, then the net work extracted is zero since $T_4 \to T_3$. In the limit of the compressor exit temperature approaching the maximum temperature, $T_2 \to T_3$, then the net work is also zero since $T_2 - T_1 = T_3 - T_4$. It can be shown that the optimum pressure ratio where net work extracted is maximised is determined by θ,

$$\frac{P_2}{P_1} = \theta^{\left(\frac{\gamma}{2(\gamma-1)}\right)}$$

with higher TETs requiring higher compression ratios for maximum work extraction leading to higher efficiencies. This trend can be seen over the years in Fig. 1.4.

Since the exhaust gases exit at elevated temperatures around 600 °C, there is still capacity to extract further work from it by using it as a heat source in a closed loop steam Rankine cycle. This is shown in Fig. 1.3 by the additional cycle, a-b-c-d, also known as a 'bottoming' cycle. Waste heat from the exhaust of the gas turbine is recovered in a boiler that heats water from a liquid state to produce supercritical

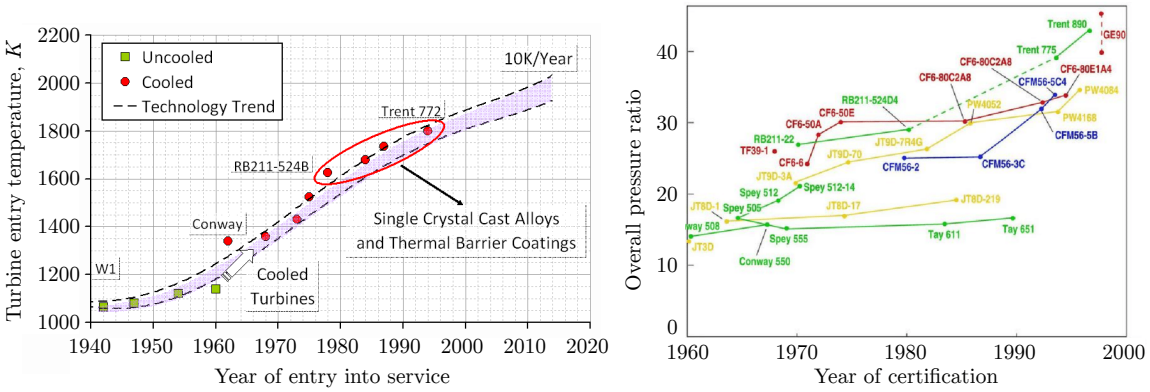


Figure 1.4: Historical turbine entry temperature (left) [7] and pressure ratio (right) [8] of various aviation gas turbines over the years

steam (process a-b). This is expanded across a steam turbine to extract additional work (process b-c). Saturated steam exits the turbine and is condensed back into a liquid state and pumped back into the boiler (process c-d and d-a).

Denoting the thermal efficiency of the Rankine cycle as η_{R}, it can be shown that the combined cycle efficiency, η_{CC}, is given by:

$$\eta_{\mathrm{CC}} = \eta_{\mathrm{B}} + \eta_{\mathrm{R}} - \eta_{\mathrm{B}}\eta_{\mathrm{R}}$$

and using the following typical values, $\eta_{\mathrm{B}} = 41\%$ [5] and $\eta_{\mathrm{R}} = 40\%$ [9], this gives a combined cycle efficiency of 65%. This makes combined cycle power plants very attractive, especially towards larger scales where they benefit from economies of scale.

So far, it has been assumed that the compression and expansion processes above are isentropic, which requires that they are adiabatic and reversible. In reality, heat transfer to surroundings, losses due to turbulence, friction in bearings, degradation of components etc. result in irreversibilities that can be accounted for by specifying the compressor and turbine isentropic efficiencies, η_c and η_t, respectively. The real efficiency of the Brayton cycle is then:

$$\eta_{\mathrm{B,real}} = \frac{\left(r^{(\gamma-1)/\gamma} - 1\right)\left(\eta_t\eta_c\theta - r^{(\gamma-1)/\gamma}\right)}{r^{(\gamma-1)/\gamma}\left(\eta_c\left(\theta - 1\right) - \left(r^{(\gamma-1)/\gamma} - 1\right)\right)} \tag{1.2}$$

where r denotes the pressure ratio. Fig. 1.5 and Eqn. 1.2 show that when the compressor and turbine operate isentropically ($\eta_c = 1, \eta_t = 1$), then the result of Eqn.

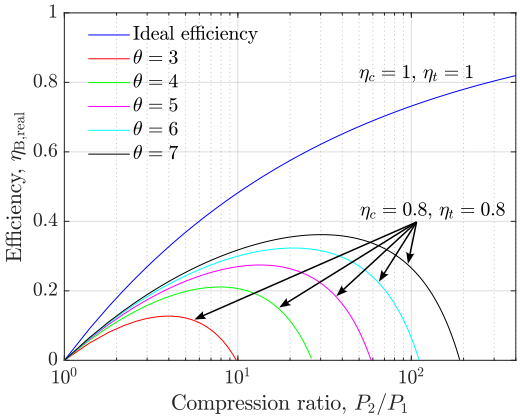


Figure 1.5: Real efficiency of Brayton cycle accounting for non-isentropic effects in the compressor and turbine for different maximum firing temperatures. Compressor and turbine isentropic efficiencies are $\eta_c = 0.8$, $\eta_t = 0.8$

1.1 is recovered, and small changes in the isentropic efficiencies of the compressor and turbine can significantly affect the real cycle efficiency. It can also be seen that the maximum firing temperature now influences the cycle efficiency. Thus, increasing the pressure ratio, turbine entry temperature, and isentropic efficiencies of the compressor and turbine will increase the cycle efficiency. There remains much room for improvement in both cycle optimisation as well as engine and component innovation. This thesis will address the latter - component innovation - with regards to the combustor-turbine interface geometry, to permit higher firing temperatures and improve turbine performance.

1.3 The Combustor-Turbine Interface in Land-Based Gas Turbines

This thesis is primarily concerned with land-based gas turbines for power generation, and specifically focusses on the combustor-turbine interface. This differs from aero-engines due to design considerations. Combustion in land-based gas turbines takes place in individual can combustors arranged annularly around turbine. A salient feature in these interfaces that differ with aero-engines are the presence of combustor walls that extend radially from hub to casing, as seen in Fig. 1.6.

The engine configuration studied here has 20 can combustors and 40 nozzle guide

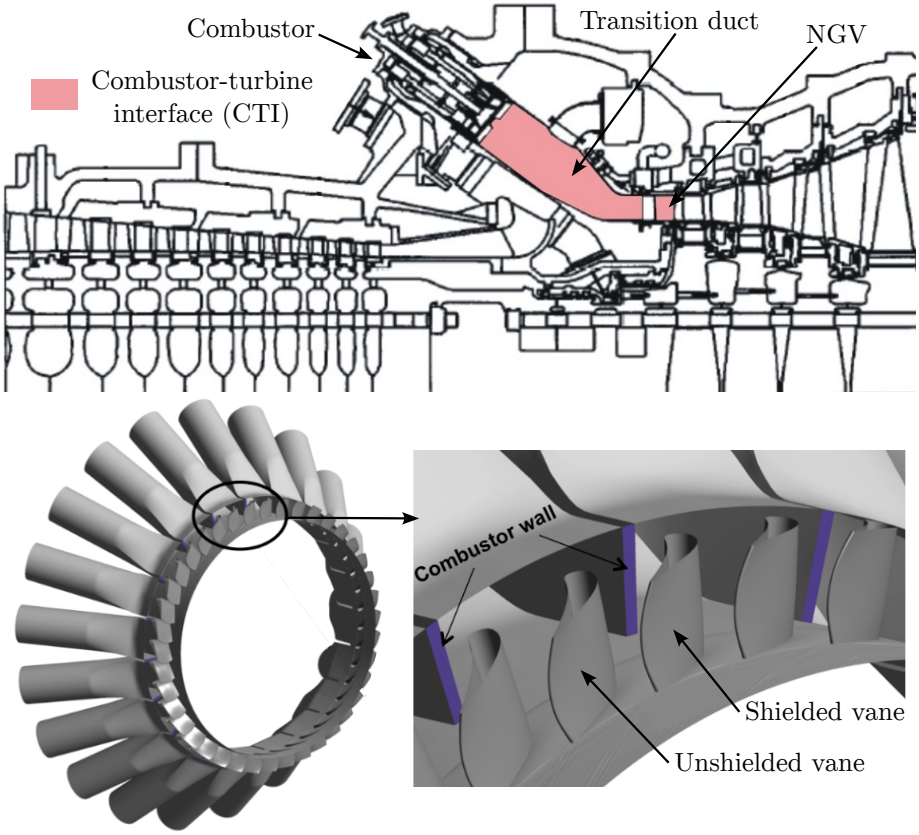


Figure 1.6: Top: Cross-section of gas turbine with combustor-turbine interface highlighted. Bottom left: Annular can combustors and nozzle guide vane row. Bottom right: Division of combustor-turbine interfaces by combustor walls upstream of the NGV. Shielded vanes are directly behind a combustor wall. Unshielded vanes are in centreline of the transition duct axis.

vanes (NGV). This gives one vane placed at the centreline of each can combustor, effectively exposing it to the incoming hot freestream. Hence it is referred to as the 'unshielded' vane. Adjacent to each unshielded vane is a vane placed directly behind a combustor wall, shielding it from the incoming hot freestream. It is referred to as the 'shielded' vane.

The NGV blade row experiences the highest thermal load in the engine since the freestream at this point is the turbine entry temperature. A typical TET of a modern gas turbine is 1600 °C, with the next generation targeting 1700 °C. A key limiting factor on the firing temperature is the thermal and structural properties of materials used in the manufacture of NGVs and the thermal barrier coatings (TBC) applied to them. The blades are typically cast from a nickel superalloy and can be polycrystalline or monocrystalline for improved corrosion, creep, and fatigue resistance. However, even these metals have a melting temperature of approx. 1300 °C - far below modern

day TETs.

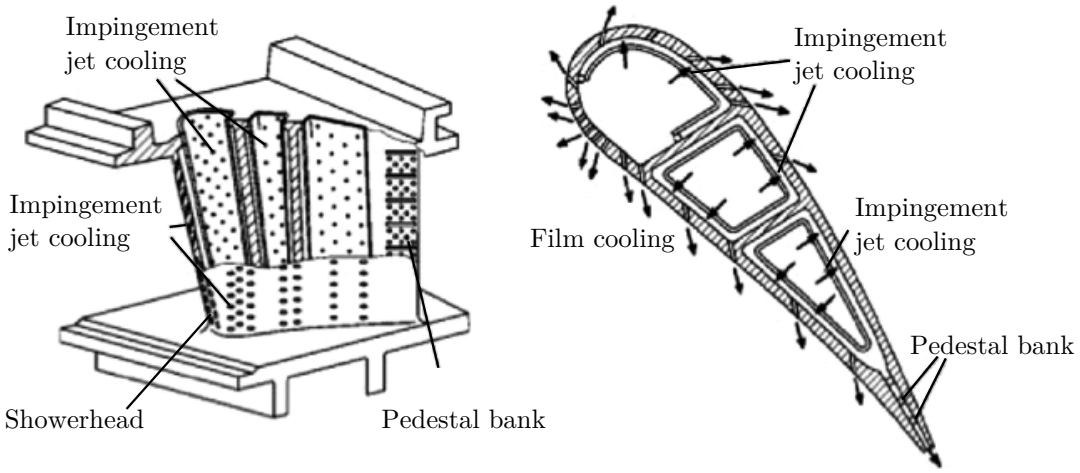


Figure 1.7: Internal and external cooling features of a nozzle guide vane [10]

To overcome this, the combustor and NGV are actively cooled using air that is bled from the compressor stage. Internal cooling channels within the blade feature turbulators, pins, and a serpentine flow path to increase heat transfer from the metal walls into the coolant. The coolant then exits back into the freestream through slots and cooling holes in the combustor liner and NGV; see Fig. 1.7. This flows over the walls of the combustor and vane surface, forming a protective film that maintains the surface temperature below its melting point. In heavy-frame gas turbines, 5 - 20% of the compressor air is used in the cooling of the turbine alone [11]. In aviation gas turbines, this can be as much as 20 - 30% of compressed air. This leads to a reduction in overall efficiency of the engine for the sake of maintaining the thermo-mechanical integrity of components. Hence engine efficiency can be increased by reducing the amount of cooling air bled from the compressor.

This can be achieved with the application of a thermal barrier coating (TBC), typically formed from yttria-stabilised zirconia. These coatings are able to tolerate higher temperatures than nickel-superalloys and have low thermal conductivities, thus limiting the surface temperature of the metal blade itself. This reduces the amount of film cooling required to protect the NGV, or for the same amount of cooling, can extend the life of the blade, as seen in Fig. 1.8. Consequently, a significant amount of materials research has gone into the field of TBCs, to understand and address its

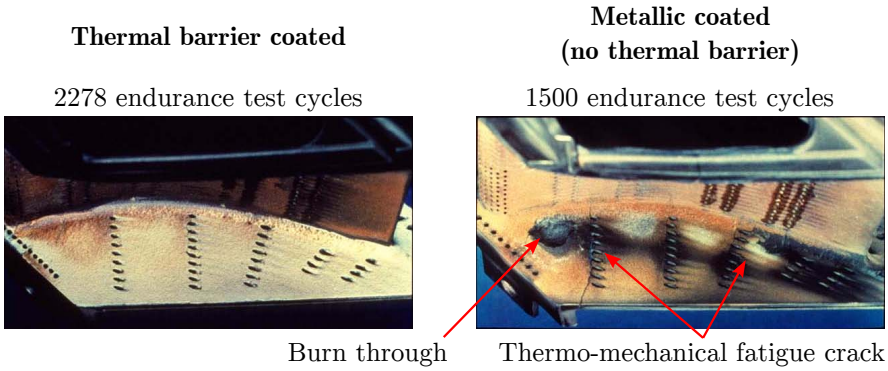


Figure 1.8: Comparisons in life and damage of two JT9D nozzle guide vanes with (left) and without (right) a thermal barrier coat applied, subjected to thermal cycling in engine tests [12]

different failure mechanisms.

Another limiting factor on TET is the formation rate of nitrous oxides, NOx, which increases exponentially with increasing combustion temperature. This peaks near stoichiometric condition, where flame undergoes complete combustion and maximum heat is released. Efforts to reduce NOx emissions have exploited this fact by operating far away from stoichiometric conditions, in either the rich-burn or lean-burn regime. This has led to the development of Rich-burn Quick-quench Lean-burn (RQL) combustors and Lean-Premixed (LPM) combustors.

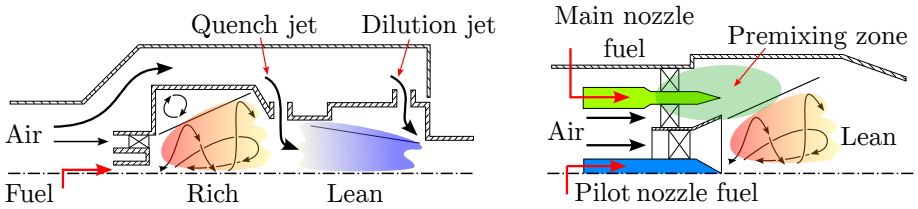


Figure 1.9: Simplfied schematic of two different dry, low-NOx (DLN) combustor technologies: the rich-burn, quick quench, lean burn (RQL) combustor (left) and the lean-premixed (LPM) combustor (right). Adapted from [13]

RQL combustors operate on a rich burn mixture in the primary combustion zone, which is then rapidly quenched to a lean mixture However, this relies on the efficacy and speed of mixing process between the primary zone effluent and the quenching air to rapidly create a homogeneous lean mixture. Hence the design of the quench section is critical in minimising the time spent near stoichiometric conditions - when NOx formation rate is highest - and in producing a homogeneous lean mixture to avoid the formation of locally stoichiometric conditions which can lead to hotspots and increased NOx formation.

In this regard, LPM combustors avoid this altogether by premixing the air and fuel and operating solely in the lean regime, near the lean blowout limit, thus making flame stability difficult to control at all operating loads. The combustion process can be staged by varying air and/or fuel across the pilot and main nozzles at different loads. However, low-load operation and transients such as start-up and ramping may require the addition of more pilot fuel which can produce a diffusion flame [13]. Other efforts to reduce NOx emissions include, water/steam injection, exhaust gas recirculation, and selective catalytic reduction. Lefebvre and Ballal [14] gives a review of combustion thermodynamics, combustor technologies in gas turbines, and the complexities that arise in the move towards LPM combustors such as thermoacoustic resonance.

Both combustors shown in Fig. 1.9 use swirlers to stabilize the flame. In the case of the LPM combustor, the swirlers also aid in premixing the the air and fuel mixture. Fig. 1.10 shows a schematic of weakly and strongly swirling flows as it expands into a diffuser section. A reduced form of the radial momentum equation is given as:

$$\frac{\partial P}{r} = \frac{\rho w^2}{r}$$

where r is the radius from the vortex centreline, and w is the tangential or swirl velocity. The inward radial pressure gradient provides centripetal acceleration to maintain circular motion. Integrating the equation above gives the local static pressure. Since the swirl velocity decays in the axial direction, there is an axial adverse pressure gradient.

In strongly swirling flows, these pressure gradients are sufficient to result in a breakdown of the vortex structure and the formation of a recirculation zone, called the central toroidal recirculation zone (CTRZ). This low pressure recirculating zone is necessary to mix and stabilise the flame and prevent flashback or backfiring. Gupta et al. [15] reviews the theoretical basis of swirling flows and their applications in combustion.

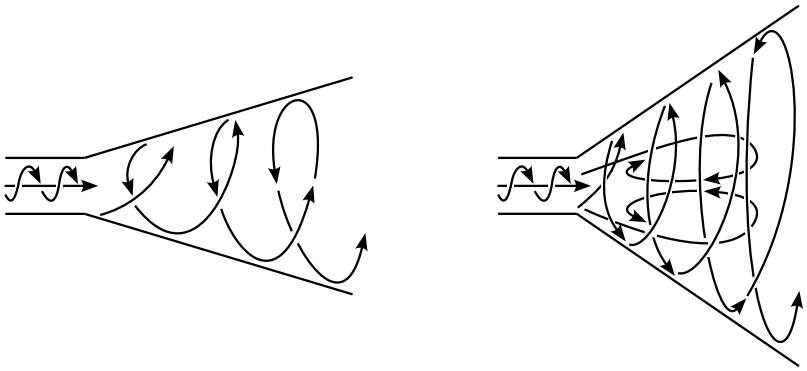


Figure 1.10: Sketch of streamlines in weakly swirling flow (left) and highly swirling flow (right) and subsequent vortex breakdown and formation of the recirculation zone. Adapted from Gupta et al. [15]

1.4 Motivation for this Thesis

Mitsubishi Heavy Industries (MHI), as part of a Japanese national project, have identified six key technologies to enable the development of a 1700 °C gas turbine. These are: exhaust gas recirculation to the combustor, turbine cooling technologies, higher temperature materials, improved thermal barrier coatings, high efficiency, high loading turbine, and a high efficiency, high pressure compressor. To that end, this thesis addresses the development of high efficiency turbines by investigating the impact of combustor geometries on the aerothermal field around the NGV. Improvements in thermal management on the blade can reduce the amount of film cooling required, thus increasing overall efficiency and the lifespan of components.

There is also growing interest in simulating the full combuster-turbine interface. Aslanidou et al. [16] have shown that there are improvements in thermal load and potentially cooling requirements by integrating their designs. At present, many studies on the upstream effects on the NGV do not simulate the full CTI. Combustion chambers are typically designed and tested in isolation, with little reference to the downstream turbine except through targeted bulk flow properties. The design of the NGV then relies on simple models for the inlet profile such as isotropic turbulence intensity, a turbulence intensity profile, or a swirl profile that is static in space and time. The underlying assumption is that the flow field around the NGV is essentially

steady.

However as stated previously, most modern industrial gas turbines are tending towards lean premixed, swirl stabilised combustion which lowers the flame temperature, thus reducing the formation of NOx. A recirculation zone that is created downstream of the swirler results in a lower total pressure swirl core that persists far downstream of the swirler and even convects downstream of the NGV. This central low pressure core is not simply the 'wake' of the swirler centre body, but rather is created by so-called vortex breakdown of the swirl in the expanding transition duct.

As a result, the flow downstream of a combustor is inherently unsteady and is characterised by large scale coherent structures. These structures have been shown to significantly affect the aerodynamics and heat transfer on an NGV. At steady state, these structures can result in a change in incidence angle of the NGV, spanwise variation in blade loading, and overturning or underturning of flow as it leaves the NGV blade row. This will have consequences on the downstream rotor which needs to be accounted for. Few studies consider the unsteady state, and of those that do, the full CTI is rarely modelled. Identifying and understanding these unsteady effects is necessary to determine if they are likely to damage components.

As combustor geometries continually evolve to accomodate new fuels and increased flexibility, this study will help identify general design trends and features that can either negatively or positively impact the NGV and form design rules for combustor-turbine interfaces of the future. The results presented in this thesis will highlight the importance of having an integrated design methodology of the combustor and turbine.

1.5 Scope and Aims of the Thesis

This thesis investigated the steady and unsteady effects of different combustor swirler geometries on the aerodynamics and heat transfer on two different NGVs. One was uncooled and another is fully cooled with engine-representative internal and external

film cooling. Four different swirler geometries, a turbulence grid, and a clean inflow were used to simulate six different inlet flow conditions. §3.1.2 details the choice of each geometry. The experimental and numerical studies were carried out with non-reacting flows at scaled engine conditions of a combustor and turbine operating at full load.

Experiments were carried out on an existing high speed blowdown linear cascade facility. As part of the study, a mass flow controlled foreign gas supply system was designed, built, and commissioned to provide film cooling to the existing facility. §3.2 details the operating conditions and range of this foreign gas supply system. While this study used it exclusively for film cooling in the NGV, this new extension to the facility enables future studies of foreign gas cooling to be carried out in other locations such as the upstream slot cooling and the midpassage purge flow.

As this study is concerned with unsteady flow phenomena, the experimental methodologies must have sufficiently high sampling rates to capture most of the power in the signal and prevent aliasing, since real signals are not bandlimited. Double-sided thin film gauges were used to directly measure heat flux through the substrate and high-speed pressure transducers were used to measure unsteady acoustic phenomena over vane surface. Both instruments were sampled at 20 kHz. It would also be helpful in the design of blades to fully resolve the temperature field across the vane surface, to identify regions of high/low heat load and regions of over or under-cooling, and obtain local heat transfer coefficients and adiabatic film cooling effectiveness. A state-of-the-art high-speed high-resolution IR camera was used in this study to obtain time-varying, full surface maps of temperature across the vane suction side (SS).

LES simulations of the full combustor-turbine interface were also carried out for two swirler geometries. This fully resolved the flow field in the regions of interest, namely the transition duct and around the NGV. The large scale coherent structures arising from the swirler were also resolved and can be seen impinging on the NGV downstream. These simulations were used to study the effect of these structures on the

aerodynamic field and secondary flow migration around the NGV. Modelling the CTI as a single domain instead of two loosely coupled domains also inherently accounts for the two-way coupling of the turbine to the combustor, allowing the presence of the NGV to influence the potential field in the combustor and allowing the propagation of acoustic waves into the turbine domain and reflecting back.

1.6 Limitations of the Thesis

This thesis is aimed at identifying and quantifying the effects of large turbulent structures impinging on the NGV and how these changed with different swirler geometries. The scope of the experimental work was limited by cost and instrumentation availability. As such, it was necessary to constrain the scope of work so that results could be delivered in a timely and cost effective manner. This meant that it was not possible to carry out hot-wire traverses at the inlet and outlet planes. The hot-wire system was not available during the experimental campaign of the study, as such it is not possible to confirm the inlet and outlet profiles obtained from LES simulations with experimental results for the 8-core swirler.

The LES simulations do not included film cooling as this would have been prohibitively time consuming to mesh and solve. The simulations only model two of the 4 swirler geometries used in this study. Due to the size of the two meshes (185 million and 340 million), it was not possible to carry out mesh independence studies within the available time frame. Only one subgrid scale (SGS) model was used for both simulations.

1.7 Thesis Outline

The following chapters present a review of literature followed by the theoretical, experimental and numerical work carried out previously, and the findings are discussed. Chapter 2 provides a background on secondary flows and reviews relevant literature on trends in combustor technologies and fundamental studies on interactions of up-

stream non-uniformities with the NGV. The focus of these interactions is on the aerodynamic and thermal performance of the vane with and without film cooling present.

Chapter 3 provides an overview of the experimental facility and a detailed description of the operating conditions and range of the foreign gas supply system. A review of the experimental techniques and numerical methodology is also presented, along with some developments of the in-house solver, TBLOCK.

Chapter 4 presents the development of the impulse response method for solving the conduction/diffusion equation by generalising it to multi-layered substrates and arbitrary 2D and 3D geometries. Its potential applications are discussed and applied to the current experimental methodology.

Chapter 5 discusses results from the numerical investigation of two different swirler geometries. These are broken down into time-averaged and unsteady effects on the NGV. Snapshots at fixed intervals are presented to demonstrate the inherent unsteadiness of the swirl core and its influence on secondary flow migration. Low frequency oscillations in static pressure have also been observed throughout the flow domain that is consistent with experimentally measured fluctuations.

Chapter 6 presents steady state results of the thermal field on the vane surface for both uncooled and cooled vanes. Comparisons with LES results are made to highlight the key finding that thermal loads and film cooling flow distribution are strongly influenced by vortical motion. Numerical results of the migration of these structures appear to correlate well with experiments.

Chapter 7 highlights the scale of the low frequency fluctuations on the thermal load on the vane surface. These fluctuations are scaled back to engine conditions to estimate the peak-to-peak temperature band that would occur should the vane be subjected to similar fluctuations. Possible sources of these fluctuations are investigated and it is found that facility-related resonance lies in the same frequency band of interest as the swirl core precession. This is clearly seen for the case of clean in-

flow but not for the cases with a swirler geometry. This suggests that the effect of swirler-related fluctuations must be quantified relative to a baseline without a swirler.

Finally, Chapter 8 provides a brief summary of each section of work and concludes its findings. Some potential applications are listed and prospective future studies are highlighted.

Chapter 2
Literature Review

This chapter reviews the fundamentals of flow and heat transfer around the nozzle guide vane and the governing mechanisms. Relevant literature pertaining to combustor flows and combustor-turbine interactions is then reviewed and the physics of these interactions is noted. Each flow characteristic reviewed here, turbulence, temperature gradient, swirl, unsteadiness, combustion, and integration, will influence many aspects of the NGV, such as aerodynamic loss, heat transfer, blade life, etc. Evidently there are many metrics to quantify "performance" of the NGV, depending on the end use. Hence the literature reviewed and their findings will be framed in the context of the aerodynamic loss, external heat transfer, and film cooling performance only.

§2.1 presents some state-of-the-art combustor geometries that are in use today as well as those in development for the next generation of gas turbines operating with very high concentrations of H_2. §2.2 establishes fundamental flow physics around the NGV with ideal 2D inlet flows to provide background and guide interpretations of results in later chapters. §2.3 characterises features of the flow exiting the combustor and entering the turbine and discusses the effect of each of these features on the nozzle guide vane. Finally, §2.4 concludes on the state of current research into combustor-turbine interactions, identifies areas for further research, and highlights the areas that will be addressed in this thesis.

2.1 State of the Art in Combustor Geometries

In the case of land-based gas turbines, a conventional can combustor typically features a single large axisymmetric swirler, with the cans arranged around the annulus of the turbine. This is referred to as a can-annular arrangement. Fig. 2.1 shows a conventional single-core combustor with the pilot burner in the center and the main annular burner surrounding the pilot. Air into the pilot burner enters axially and is

swirled by an axial swirler. Air into the main burner enters radially and is swirled by the radial swirler before exiting axially, forming an annulus around the pilot flow.

Goldstein et al. [17] and Goebel et al. [18] provide typical velocity and turbulence profiles of such swirlers. More recently Schroll et al. [19] used PIV to fully resolve the three dimensional velocity field of a single core lean burn combustor. These combustors make use of rapidly expanding highly swirling flows and the subsequent vortex breakdown to produce a central toroidal recirculation zone (CTRZ) to stabilise flame. Flow in this region is therefore characterised by high shear, high turbulence, and the formation and shedding of large scale coherent structures.

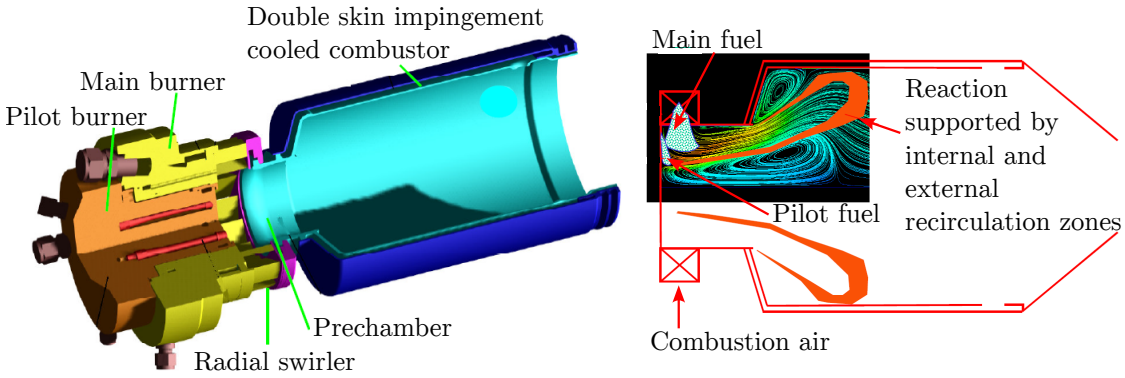


Figure 2.1: Conventional single-core combustor geometry reproduced from Turrell et al. [20]

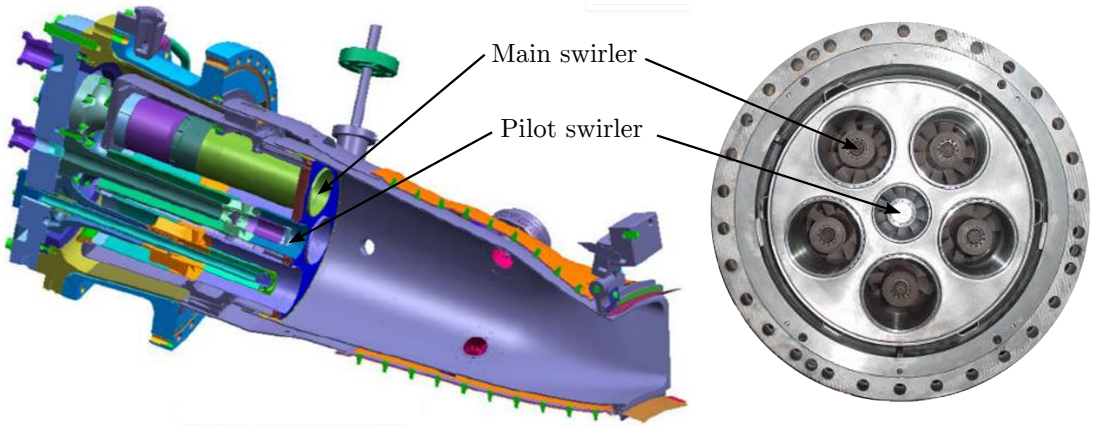


Figure 2.2: Multi-core General Electric DLN-2.6 combustor reproduced from Vandervort et al. [21] and Goldmeer [22]

There is a trend towards lean premixed (LPM) combustors for its low NO_x emissions, with many of these modern combustors featuring smaller pilot burners with multiple main burners arranged concentrically around it. An example of this is shown in Fig. 2.2 which is a General Electric (GE) DLN-2.6 combustor. This improves the

operating range (also called the turndown ratio) of the combustor while still maintaining a stable flame by fuel staging across different combinations of burners at different loads/RPM [23].

Increasing pressures to reduce CO_2 emissions and rising prices of fossil fuels are some of the factors pushing the industry to invest into the development of low NO_x combustors that can operate with high concentrations of H_2. Noble et al. [24] points out that diffusion burners operating on 100% H_2 already exist. However most dry low emission / dry low NO_x (DLE/DLN) combustors are currently limited to 60% H_2. They review the technical challenges associated with high H_2 combustion and present a number of geometries under investigation by OEMs around the world.

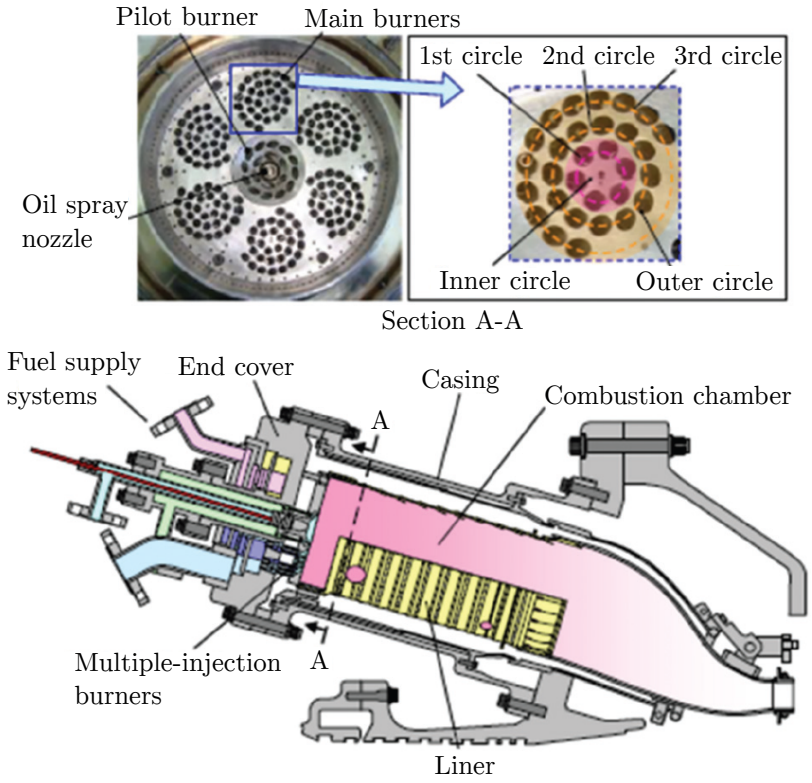


Figure 2.3: State-of-the-art dry low emission / dry low NO_x (DLE/DLM) hydrogen combustor geometry, reproduced from Noble et al. [24]

These new state-of-the-art combustor geometries for hydrogen are a paradigm shift away from the conventional single-core swirler geometries. Compare for example Fig. 2.1, which is a conventional single-core can combustor, with Fig. 2.3, which is a state-of-the-art hydrogen combustor being developed by Mitsubishi Heavy Indus-

tries (MHI). Asai et al. [25] provides a report on its developments with the hydrogen combustor pictured in Fig. 2.3. A single combustor consists of a multi-cluster arrangement of small injectors arranged with an inward draft angle causing each individual jet to converge and then rapidly diverge to induce vortex breakdown. This produces a lifted flame off the surface of the combustor and is key to achieving low NO_x. There do not appear to be conventional swirlers, e.g. central blunt body with vanes, in this hydrogen combustor, instead relying on an inward draft angle and a compound angle (in the circumferential direction) to produce discrete swirling jets. Another radically different combustor design is that of Lee and Kim [26], which contains a circular arrangement of sixty mesoscale swirlers in a single combustor. The trend seen with each of these new combustors is the reduction in size of the swirlers. As will be shown later in this study, the reduction in size of the swirl core reduces the size of coherent structures formed, which leads to lower turbulence and a more uniform flow field at the inlet to the NGV blade row.

2.2 The Aerothermal Field of Nozzle Guide Vanes

2.2.1 Secondary Flows

The ideal freestream flow path through a cascade blade row can described by potential field theory on a 2D blade profile. However, real flows in turbine blades exhibit cross-stream migration and flow structures which deviate from the freestream or primary flow streamlines. These are termed secondary flows and contribute to aerodynamic losses and increased heat transfer on surfaces. The formation of secondary flows itself is an inviscid phenomena due to the presence of non-zero vorticity in the flow, which represents a total pressure gradient [27]. This can be understood intuitively by considering the two streamlines shown in Fig. 2.4.

As flow along the streamline A-A-A is turned by the blade, the pressure gradient

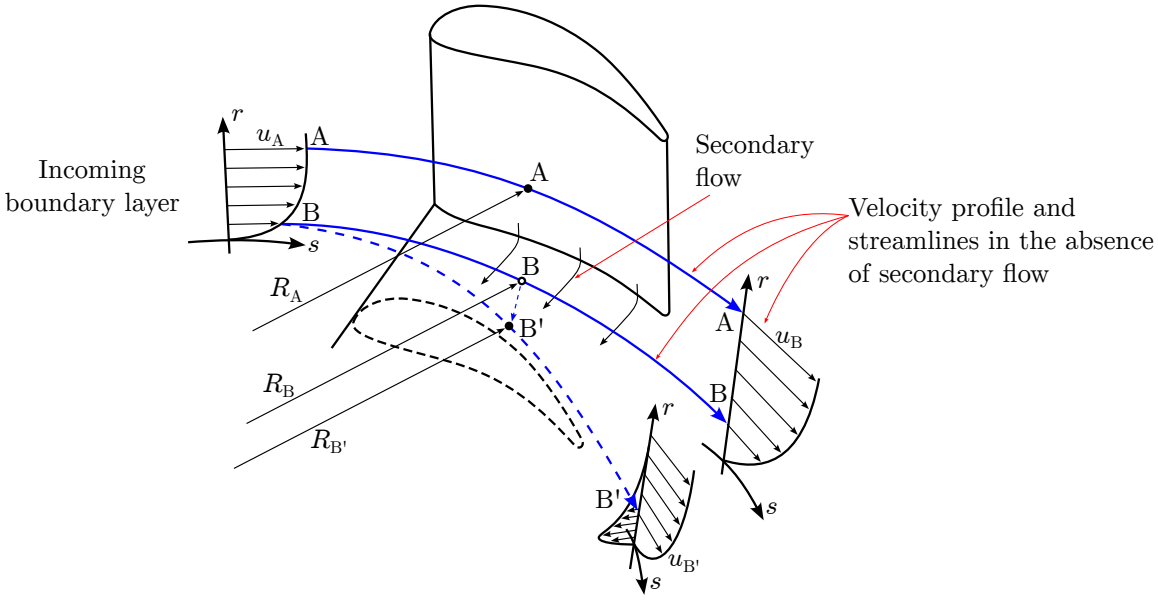


Figure 2.4: Theory of secondary flow phenomenon as a result of a total pressure gradient in the boundary layer [28]

from the pressure side to suction side balances the centripetal acceleration of the fluid:

$$\left(\frac{\partial P}{\partial n}\right)_{\mathrm{A}} = \frac{\rho u_{\mathrm{A}}}{R_{\mathrm{A}}}$$

where u_{A} and R_{A} are the streamwise velocity and radius respectively. This can be derived from the normal component of the inviscid Euler equations in curvilinear coordinates.

A total pressure gradient in the r-direction is represented by constant static pressure and a velocity gradient. Since there is no static pressure gradient:

$$\left(\frac{\partial P}{\partial n}\right)_{\mathrm{A}} = \left(\frac{\partial P}{\partial n}\right)_{\mathrm{B}}$$

$$\frac{\rho u_{\mathrm{A}}}{R_{\mathrm{A}}} = \frac{\rho u_{\mathrm{B}}}{R_{\mathrm{B}}}$$

$$u_{\mathrm{A}} > u_{\mathrm{B}} \quad \Rightarrow \quad R_{\mathrm{A}} > R_{\mathrm{B}}$$

which shows that lower velocity fluid will deflect more, forming a cross-passage migration of boundary layer fluid from the pressure side to the suction side, following the streamline B-B'-B'. The streamline B-B-B shows the path the fluid would take in the absence of secondary flows, i.e. no total pressure gradient.

The example of a boundary layer is used here to demonstrate the effect of a total

pressure non-uniformity, which manifests as a result of viscous shear forces acting on the fluid. However, this can also occur in inviscid flows, such as temperature gradients causing a change in density and therefore dynamic head. This would be typical of combustor flows, in which the hot freestream in the core of the flow is surrounded by relatively colder film cooling flows along the walls. This gives a temperature ratio between the freestream and wall of approximately 2. Hermanson and Thole [29] numerically simulated an NGV cascade with different temperature and velocity gradients. Their results showed that a large temperature gradient can result in a large total pressure gradient that drives secondary flows and that a zero total pressure gradient did not give rise to secondary flows, thus confirming the theoretical analysis of Hawthorne [27].

Over the years, extensive research has been conducted on the drivers, impacts, and mitigation of secondary flows. Due to its impact on losses - as much as 30 - 50% of total aerodynamic loss in a stator row [30] - there is potential for significant gains in efficiency from the control of secondary flows. Langston et al. [31] presented one of the first detailed descriptions of the major features of the secondary flow system in a cascade blade row. These are the horseshoe vortex, the endwall crossflow, and the passage vortex, as shown in Fig. 2.5

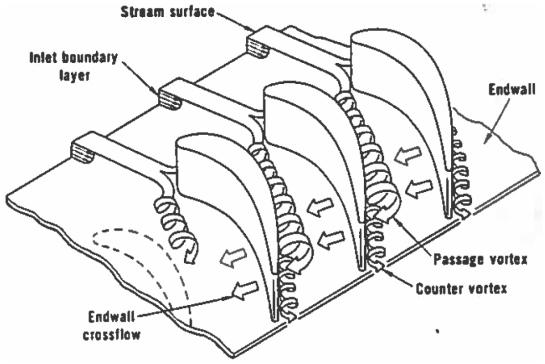


Figure 2.5: Model of secondary flows proposed by Langston [32]

During this time, many workers proposed different flow models describing the secondary flow system [30, 33, 34]. Each model contained the main features (horseshoe vortex, passage vortex, and endwall crossflow), but each grew in complexity and they disputed the position of the suction side leg of the horseshoe vortex. To resolve these

discrepancies, Wang et al. [35] carried out extensive flow visualisation experiments with multiple smoke wires and a laser light sheet to illuminate cross-sections of the flow. Using these results, they proposed a new model of the secondary flow system, as shown in Fig. 2.6. Their model is more detailed and suggests a more complex system of vortices, particularly near the leading edge - endwall junction. This model will be used in this thesis and its main components are described below.

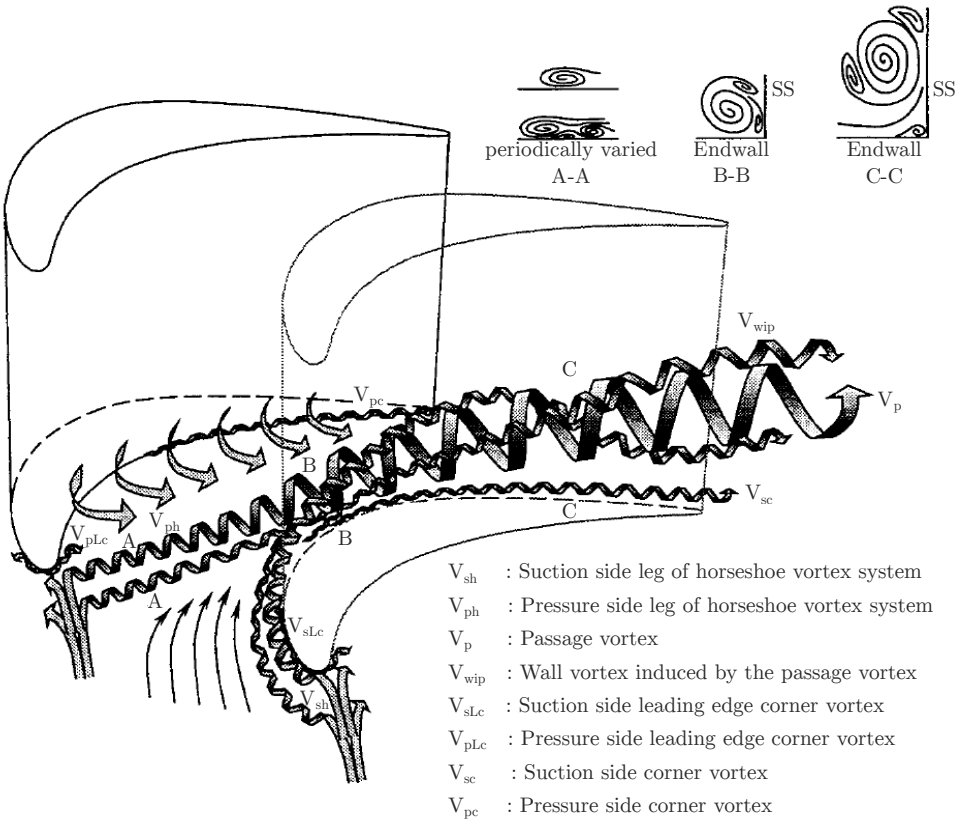


Figure 2.6: Model of secondary flows proposed by Wang et al. [35]

Incoming fluid to the blade has a radial total pressure gradient near the hub and casing as a result of viscous shear acting on the fluid. The fluid stagnates on the blade's leading edge, creating an axial adverse pressure gradient that causes the incoming boundary layer at some distance upstream of the blade to separate. This separated boundary layer rolls up to form a recirculation zone. The pressure on the stagnation line is higher in the mainstream than inside the boundary layer. This creates a downwash effect that entrains fluid near the wall into the recirculating region, hence setting up the sense of rotation of the vortex. The vortex wraps around the

blade and is convected downstream on both sides of the vane. This is the horseshoe vortex and the two legs are referred to as the suction side leg and the pressure side leg. This can also be visualised as the boundary layer having a line of vorticity in the circumferential direction that impinges on the leading edge of the vane. The vortex line wraps around the vane to form the two legs of the horseshoe vortex and their sense of rotation is described by that line.

The cross-passage pressure gradient sweeps the pressure side leg towards the suction side of the adjacent blade. This can be traced by the migration of the separation line, where the incoming boundary layer stagnates, separates, and feeds into the vortex. A new boundary layer forms downstream of the separation line and also migrates towards the suction side of the adjacent blade. This boundary layer is much thinner than the incoming boundary layer and is termed endwall crossflow. Cross-passage flows such as these are turned more than the freestream due to its lower fluid momentum, as explained in Fig. 2.4 above.

As the pressure side leg migrates, it entrains fluid from the separated incoming boundary layer, the freestream, and endwall crossflow, thus increasing in size and is termed the passage vortex. It then merges with the suction side leg of the adjacent blade, with the latter remaining a distinct vortex and precessing around the axis of the passage vortex. Near this point of merging, a small and very intense vortex is produced that is then swept by the passage vortex onto the blade's suction surface, where it remains attached very close to the surface. This wall vortex is shown to remain above the passage vortex and counter-rotate against it. This counter-rotating pair structure is thought to be responsible for the peak and valley in mass transfer on the blade surface, observed in experiments by Goldstein et al. [36]. Jabbari et al. [37] compared their own results from flow visualisations experiments with the mass transfer results of Chen and Goldstein [38] and Goldstein and Spores [34] which suggest the presence of smaller corner vortices at the leading edge and along the blade-endwall junctions on the pressure and suction sides. These are responsible for

significant local variations in heat transfer.

These endwall vortices are the result of boundary layer separation and roll-up, which has prompted many studies into endwall junction flows and the mitigation of secondary flows, e.g. [39, 40]. Baker [41] and Lin et al. [42] note that the horseshoe vortex itself is a system of vortices that can be steady, oscillate with a distinct frequency, or oscillate chaotically, depending on Reynolds number. Dimensional analysis by Baker [41] showed that the location of the saddle point is a function of Reynolds number and the boundary layer displacement thickness. Eckerle and Awad proposed the non-dimensional parameter, E, to predict the existence of a saddle point at the leading edge [32]. Radomsky and Thole [43] found that a high inlet turbulence intensity resulted in thinner displacement and momentum thicknesses and the horseshoe vortex migrating towards the leading edge.

2.2.2 Loss Mechanisms

To improve the efficiency of the turbine, a detailed understanding of the sources of loss is required. Losses in a turbine result in a reduction in the available work that can be extracted from the expansion process. In cascade tests of nozzle guide vanes, this is typically quantified as the reduction in total pressure. The basis for this is described as follows. The state of an ideal gas is fully described by any two of its thermodynamic states, in this case, T_0 and P_0, because they are the easiest to measure. Since the NGV does no work and assuming it is adiabatic, then $T_{0,1} = T_{0,2}$, where states 1 and 2 are upstream and downstream of the NGV respectively. If the process is reversible, then $P_{0,1} = P_{0,2}$. However viscous shear acting on the fluid introduces an irreversibility and extracts work, w, from the system, thus reducing the stagnation pressure, $P_{0,2}$:

$$w = \frac{1}{\rho_{0,1}} \left(P_{0,1} - P_{0,2} \right) \tag{2.1}$$

Denton [44] argues that in the rotating frame, relative stagnation quantities can vary with radius without any loss of work. He proposes the use of entropy change, Δs, as

a measure of loss which generalises Eqn. 2.1 by removing the adiabatic assumption:

$$\Delta s = c_p \cdot \ln\left({}^{T_{0,2}}/_{T_{0,1}}\right) - R \cdot \ln\left({}^{P_{0,2}}/_{P_{0,1}}\right) \tag{2.2}$$

The total loss across a turbine stage can be broken into three components: profile loss, endwall loss, and leakage loss, although these are not necessarily independent. Each component contributes roughly 1/3 of the total loss in turbines [44]. Since this thesis in only concerned with the NGV, leakage losses are not reviewed here. Entropy is generated (and therefore losses are incurred) during viscous shearing of boundary layers, wakes, jets, and vortices, in mixing processes, across rapid expansions or shocks, and heat transfer across finite temperature differences.

Profile loss refers to the loss generated by the blade's boundary layer flow, that is sufficiently far from the endwall and secondary flow structures such that flow is 2D. Within the viscous sublayer, viscous stresses dissipate energy cascaded from the freestream and generate entropy. This is dependent on the velocity gradient in the wall normal direction, with larger gradients leading to higher rates of entropy generation. Consequently, profile loss is dependent on the state of the boundary layer, e.g. laminar, transition, or turbulent, and therefore Reynolds number. The suction side also sees the highest loss as it scales with the cube of surface velocity. Mixing processes between two streams, such as between a coolant jet and the freestream or the mixing out of the trailing edge wake also generates entropy. In the uncovered turning region, the boundary layer and passage vortex grow rapidly due to an adverse pressure gradient, leading to separation and a blockage effect in the freestream [31, 44]. These effects result in a loss in lift and therefore turbine work.

Endwall loss is comprised of two components: a 'background loss' and a 'secondary-flow-induced loss'. The former is due to viscous dissipation from boundary layer flow over the the endwall and is independent of secondary flows. The latter is due to three loss generating mechanisms: interactions between secondary flows and the blade's boundary layer, viscous dissipation of secondary kinetic energy (SKE), and

the mixing-out process of different fluid streams. Denton [44] states that boundary layer drag loss on the endwalls accounts for roughly ⅔ of the total endwall loss. Sharma and Butler [30] found that the inlet boundary layer loss is convected through the blade row and is not mixed out to contribute to endwall profile loss or endwall secondary-flow-induced loss. If the latter two are independent of the inlet boundary layer thickness, this suggests that there is little mixing loss of the inlet boundary layer from secondary flows. Coull et al. [45] numerically investigated the sensitivity of endwall loss to inlet boundary layer thickness for a large number of turbine cascade designs. This was found to be design-dependent, with low-turning blades being largely insensitive and high-turning blades being highly sensitive to the inlet conditions.

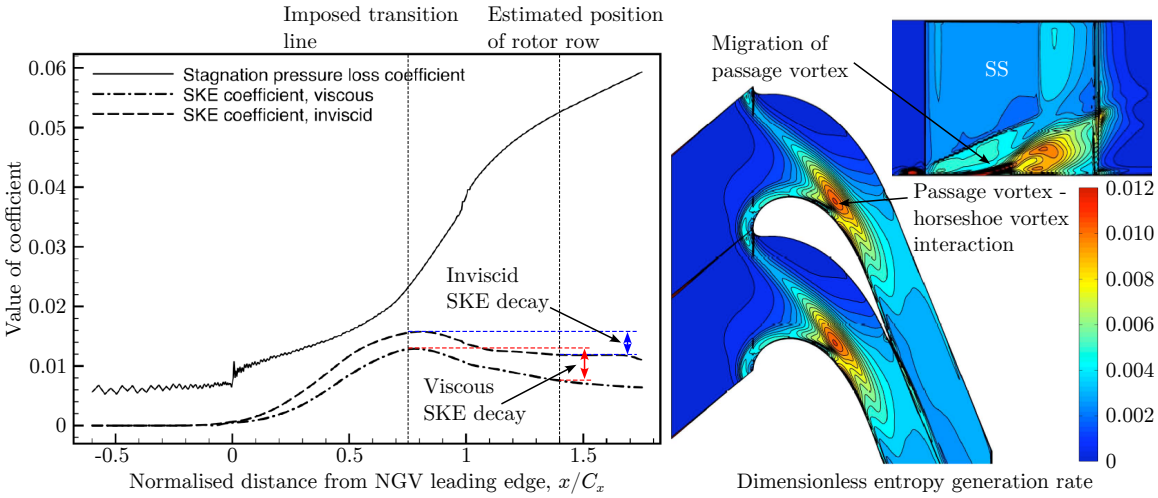


Figure 2.7: Left: Pressure loss and gain/decay in secondary kinetic energy (SKE) through the NGV. Only a fraction of the decay in SKE can be attributed to viscous dissipation since vortex compression also reduces SKE and is an inviscid process. Right: Entropy generation rates on the endwall and NGV suction side. Adapted from Denton and Pullan [46]

While cascade tests typically assume all of this is dissipated and therefore counts as a loss, this is not necessarily the case in real turbines. Not all of the secondary kinetic energy will have decayed before entering the rotor blade row and could therefore still contribute towards work. However it is not clear how much of this could be recovered and how much would have dissipated and should count as a loss. Numerical simulations by Denton and Pullan [46] on a cascade tested by Harrison [47] showed that only 15% of the decay of SKE contributed towards loss, with significant amount

of SKE entering the next blade row, as shown in Fig. 2.7. The remaining decay of SKE is due to vortex compression in decelerating flow, which is an inviscid effect and does not contribute towards loss. Their study highlighted locations of highest entropy generation where the passage vortex interacts with the suction side leg of the horseshoe vortex and where the passage vortex migrates spanwise up the suction surface. However they found no single dominant source of loss, as entropy generation was split roughly similarly between the endwalls, blade surface, and freestream.

While the rotor blade row is not considered in this thesis, it is worth noting that the wake from the trailing edge, endwall boundary layers, and passage vortices from NGV are seen by rotor. Overturning boundary layer fluid on the endwalls and underturning of freestream fluid further along the blade span due to the passage vortices changes the incidence angle at the rotor blade. This can either strengthen secondary flows or weaken it, and consequently increase SKE and loss or decrease them [44, 48].

2.2.3 Heat Transfer

Efforts to increase the efficiency of gas turbines has led to a trend of increasing turbine entry temperatures far above the melting point of the metal blade. Heat load management of the NGV is therefore crucial in ensuring the thermo-mechanical integrity of not just the blade but also the protective thermal barrier coating over their lifetimes. Over the years, many studies of heat transfer within the blade passages have been carried out to identify locations of high or low heat load and their driving mechanisms. The fundamentals of the thermal field on the endwall and blade surfaces of an uncooled NGV with uniform inlet is reviewed here, with respect to convective heat transfer. The influence of factors such as turbulence intensity, temperature distortions, etc. are reviewed later in §2.3.

Ideally, the figure of merit when evaluating heat load on the surface is the wall temperature at engine conditions. However, the practicalities of measuring this in real engines or operating experiments at real engine conditions make this very difficult;

very few studies do this and the resolution of the data is sparse - see for example Gladden and Livingood [49], Hylton et al. [50], and Greiner et al. [51]. Instead it is calculated indirectly from Newton's Law of Cooling, which gives the heat transfer rate per unit area as, $q = h\,(T_{\text{ref}} - T_w)$, where T_w is the wall temperature, T_{ref} is some reference driving temperature, and h is the heat transfer coefficient (HTC). This provides the boundary condition of a solid domain whereby, for a given h and T_{ref}, Fourier's equation is solved to give T_w. Hence research has focussed on measuring heat transfer coefficients across the vane surface.

The HTC can be shown to be a function of the aerodynamic field under some simplifying assumptions and can be thought of as a measure of conductive heat transfer for a unit temperature difference between the wall and the fluid, and the driving temperature difference is then a proportionality constant. Considering the dimensions of h, it can be written as $h = {}^{k}/_{\Delta}$, where k is the thermal conductivity of the fluid and Δ is some unknown conduction length that is related to the boundary layer of the fluid. Evidently for a thicker conduction length, the HTC is lower, and conversely a thinner conduction length gives higher HTC. Hence, the HTC is dependent on the state of the boundary layer and is influenced by similar factors such as Reynolds number, surface roughness, fluid properties, freestream turbulence, pressure gradients, etc. The similarity between the momentum boundary layer and thermal boundary layer is the basis for the Reynolds analogy, which relates skin friction to the heat transfer coefficient [52, 53].

Early studies at the University of Minnesota used a naphthalene sublimation technique and a heat and mass transfer analogy to identify regions of high and low heat transfer on the endwall and blade surfaces of an uncooled NGV [34, 36, 38]. Comparisons between these results and flow visualisation experiments by Jabbari et al. [37] show that these regions are attributed to different secondary flow structures. More recently, high resolution infra-red thermography is being used to capture surface temperatures at very high resolution [54].

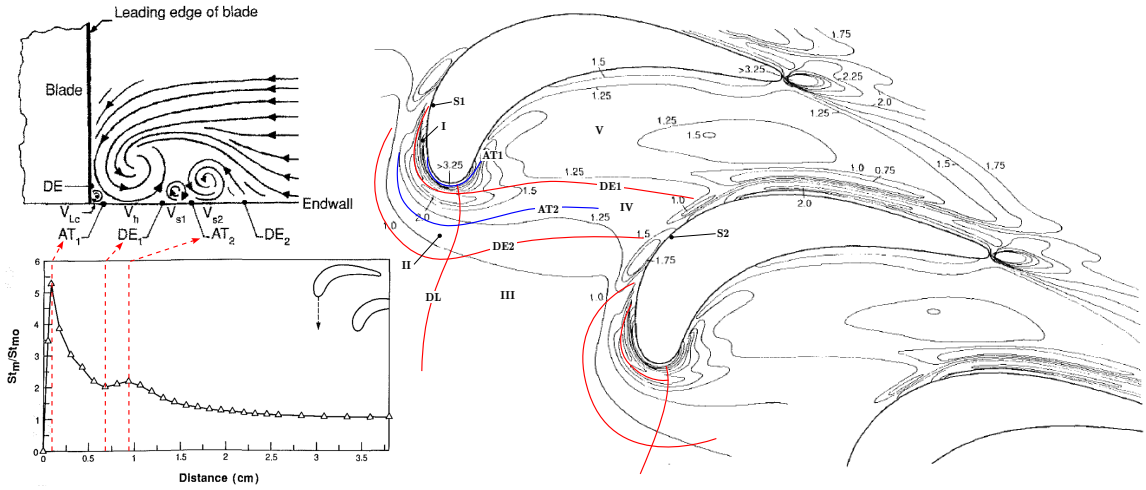


Figure 2.8: Left: Heat transfer augmentation at leading edge-endwall junction due to horseshoe vortex system comprising of the leading edge corner vortex, V_{Lc}, the main horseshoe vortex, V_h, and two leading edge stagnation point vortices, V_{s1} and V_{s2}. Right: Heat transfer augmentation on endwall with superimposed detachment (DE) and attachment (AT) lines. Adapted from Goldstein and Spores [34] and Jabbari et al. [37]

The salient features are briefly described here and make use of the secondary flow diagram of Wang et al. [35] shown in Fig. 2.6 and the heat transfer contour plots in Fig. 2.8. The set of papers from the University of Minnesota referenced above provide a more thorough treatment. The detachment and attachment lines in Fig. 2.8 show multiple vortices in the horseshoe vortex system, with the leading edge corner vortex, V_{Lc}, contributing to the local band of high Stanton number on the leading edge-endwall junction (region I). This is due to a 'downwash' effect of hot freestream fluid onto the endwall. The suction side leg of the horseshoe vortex, V_{sh}, separates and lifts-off the endwall at point S1 and migrates spanwise along the vane. Region II underneath V_{sh} still has a local trough and peak in heat transfer corresponding to the detachment (DE) and attachment (AT) lines, DE1 and AT2, respectively, however this peak is much lower than region I underneath V_{Lc}.

The pressure side leg of the horseshoe vortex, V_{ph}, migrates across the endwall, impinges on the suction side of the adjacent vane and separates from the endwall at point S2. Region IV underneath V_{ph} spans a much larger area of the endwall and heat transfer is slightly elevated. The boundary layer in region V is very thin as it is reformed from fluid swept from the pressure side of one vane and migrates up the suction side of the adjacent vane. Most of this region only has slightly elevated

heat transfer, but at the pressure and suction side-endwall junctions this is enhanced locally by corner vortices, V_{pc} and V_{sc}. The effect of these corner vortices on the vane suction side can be seen in Fig. 2.9. The spanwise migration of the passage vortex and the wall vortex it induces, V_{wip} can also be seen as a trough and peak in Sherwood number (mass transfer) although this is much less than the peak due to the corner vortex.

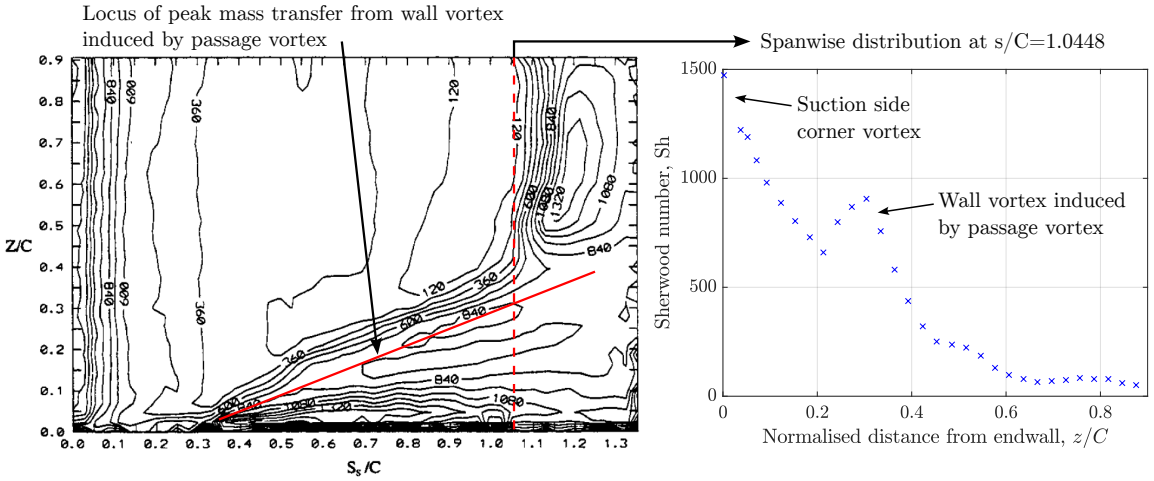


Figure 2.9: Sherwood number distribution on the vane suction side. A mass-heat transfer analogy relates high mass transfer to high heat transfer and vice versa. Only the lower region near the endwall is shown. Spanwise distance from the endwall is z, curvilinear streamwise distance from the leading edge is s, dimensions are normalised by chord length, C, and the midspan is at $z/C = 1.77$. Left: Contour of Sherwood number on the suction side. Right: Spanwise distribution of Sherwood number at $s/C = 1.0448$ showing the trough and peak caused by the wall induced vortex. Adapted from Goldstein et al. [36]

We therefore see that heat transfer around the NGV is dominated by the vortical motion of secondary flows. The exact values of HTC and the size of these regions will differ depending on operating conditions, blade geometry, and whether secondary flow control strategies are used, e.g. fillets, endwall fences, etc. However, the qualitative distribution of HTC remains the same as secondary flows are determined by the aerodynamic field. See for example Harvey et al. [55], who experimentally and numerically measured Nusselt number distribution on the endwall at three different operating conditions (one design condition, two off-design conditions). They note that differences between their numerical and experimental results are due to underestimation of secondary flows effects. Some of the earlier studies of heat transfer on the NGV has been reviewed by Harvey and Jones [56] and more recently by Dunn

[57], Simon and Piggush [58], and Han et al. [59].

2.2.4 Film Cooling

Such is the scope of current research into film cooling that a full review is not possible in this thesis. Indeed, it is estimated that there are more than 2700 published works pertaining to film cooling alone [60]. This is partly driven by the complexity in predicting film cooling performance, as shown in Table 2.2. Furthermore, recent works have shown that combustor flows will also have an effect [61], which introduces the additional factor of swirl. Ornano and Povey [62] also derived 11 independent non-dimensional groups which must be matched for complete similarity between the experimental and engine adiabatic film effectiveness, five of which are in addition to the Table 2.2. This thesis is concerned with the interactions between combustor flows and the external aerothermal field of an NGV based on a linearised Mitsubishi R1V vane. This fixes the geometrical and operating parameters and therefore will not be explored further here. Instead the reader is directed to reviews by Goldstein [63], Bogard and Thole [64], Han et al. [59] which address the factors above as well as studies of internal cooling. This section will review the general distributions of a coolant jet from an axially aligned cylindrical hole and the flow structures involved. The influence of mainstream factors that arise as a result of combustor flows will be reviewed in §2.3.

Table 2.1: Factors affecting film cooling performance [64]

Coolant/Mainstream Conditions	Hole Geometry/Configuration	Airfoil Geometry
Blowing ratio, M[a]	Hole shape[a]	Hole location
Momentum flux ratio, I[a]	Injection/compound angle[a]	Surface curvature[a]
Density ratio	Hole spacing, P/D	Surface roughness
Freestream turbulence[a]	Hole length, L/D	
Freestream Mach number	Row spacing	
Freestream unsteadiness	Number of rows	
Approach boundary layer		
Rotation		

[a]Factors that have a significant effect on predictability of film cooling performance

To maintain the blade temperature within safe operating limits, relatively cooler

air is bled from the compressor and passed into the NGV. Convective heat transfer occurs between the metal walls and coolant flow, and is promoted with the use of various geometrical features such as pedestals, impingement jets, and ribs. This increases the HTC and therefore the heat removed from the external blade surface, thus reducing the external wall temperature and the temperature gradient inside the metal wall. Some of this coolant is ejected out onto the external surface through discrete film cooling holes to form a protective layer between the freestream and the wall.

The necessity for film cooling incurs a penalty on overall efficiency of the engine since there is a loss of work and the mixing of the coolant with the freestream will lower the total temperature entering the rotor blade row. Current in-service industrial gas turbines use 5 - 20% of the compressor discharge air for cooling of the turbine [11, 13]. Increasing the turbine entry temperature will then require more cooling flow to maintain the same surface temperature, all else being constant, e.g. same cooling technology. Horlock et al. [65] predicts that this places a limit on the maximum achievable thermal efficiency for increasing TET - any further increase in TET decreases the efficiency. This drives the need for further advances in materials and heat transfer technologies to allow higher blade temperatures and reduce the amount cooling required.

The NGV used in this study can be seen in §3.3.1 and features impingement jet arrays and a pedestal bank at the trailing edge to increase internal HTC. Staggered rows of film cooling holes are located on both the suction and pressure sides, with the more dense array of holes on the leading edge since flow stagnates there and therefore sees the highest thermal load; this array is referred to as the showerhead. The design of a blade's cooling system is a trade-off between thermal, aerodynamics, and structural requirements, hence no single cooling technology is optimal for all cases. For example, a serpentine channel would not be used in the NGV of the high pressure turbine stage due to the low pressure margin available.

2.2.4.1 Film Cooling Structures

Film cooling on turbine blades is provided by coolant injection through discrete holes as opposed to 2D continuous slots which may initially be the more intuitive choice since, intuitively, slots provide a more uniform coverage and higher film cooling effectiveness for the same flow rate. However, the large thermo-mechanical loads experienced by turbine blades make slotted geometries unsuitable. They are only used in interfacial leakage gaps such as the gap between the combustor liner and the hub wall. Discrete holes on the other hand introduce edge effects resulting in highly three dimensional flow.

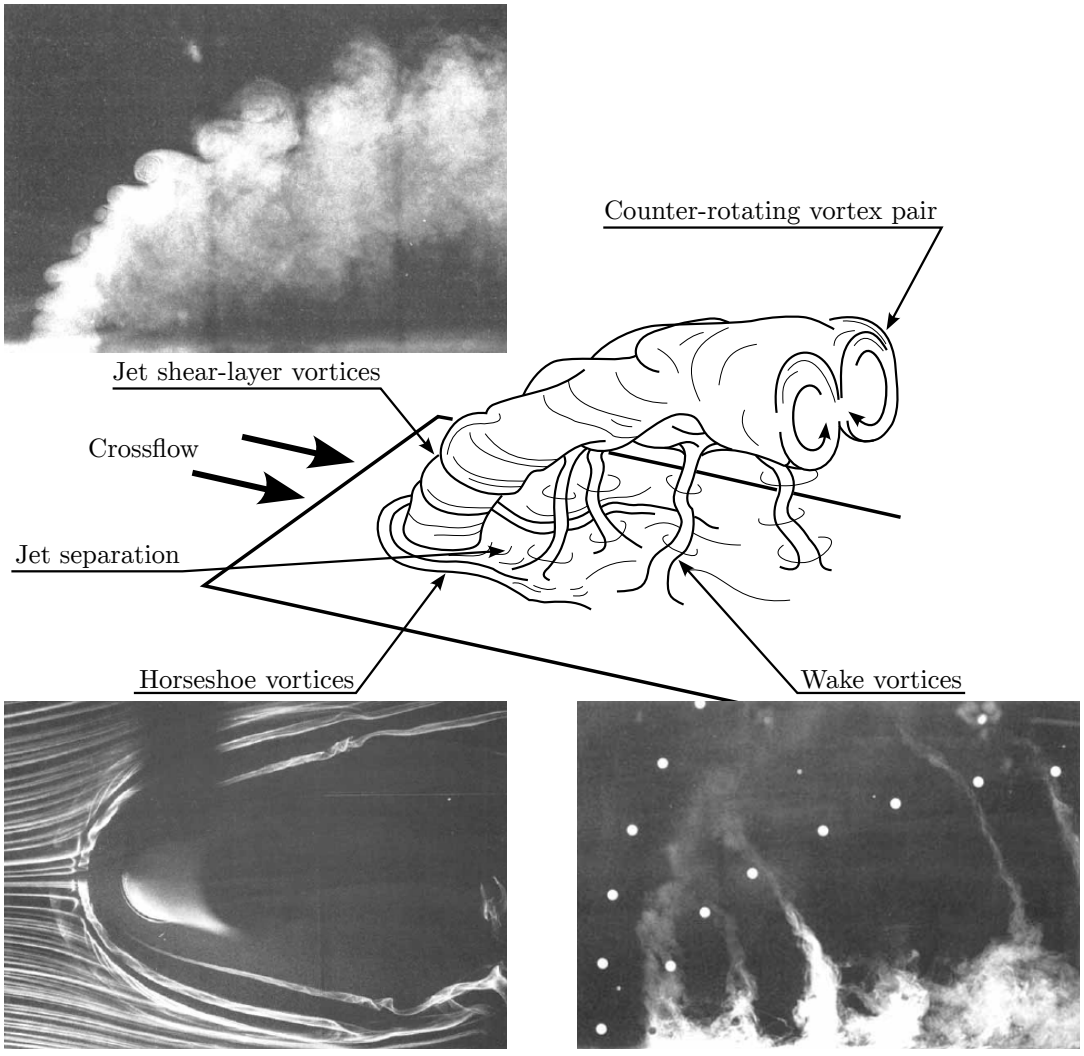


Figure 2.10: Secondary flow structures of a perpendicular jet in crossflow [66]

A prominent feature of this flow is the formation of a counter-rotating vortex pair (CVP) at the hole exit that persists far downstream of the hole. The presence of the

CVP is detrimental for film cooling as it entrains fluid from the hot freestream onto the surface and enhances mixing resulting in more rapid dissipation of the coolant. The CVP in close proximity also induces lift between them, which lifts coolant off the surface that opposes lateral diffusion, thus reducing film cooling effectiveness.

Fig. 2.11 shows the effect of this structure on HTC. The downwash caused by the CVP on either side of the cooling hole enhances heat transfer giving the characteristic double-streak of high HTC. Region C is a small stagnation region immediately downstream the cooling hole with low HTC. The size of this region increases with increasing blowing ratio, M [59]. Region E is directly below the CVP and also experiences an increase in HTC. For attached jets, this increase is very small, however when the jet detaches, the mainstream penetrates underneath the jet to form large eddies and increase HTC further.

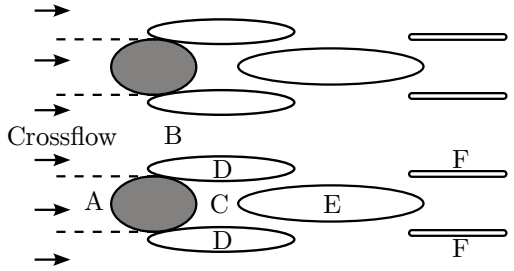


Figure 2.11: Regions of low and high heat transfer coefficient augmentation around a film cooling hole. Regions A, B, and C have relatively low heat transfer coefficient augmentation from a baseline case with no film cooling. Regions D, E, and F have high heat transfer coefficient augmentation due to vortical motion of counter-rotating vortex pair. Adapted from [67]

It should be noted that Fig. 2.10 is a fundamental study of a perpendicular jet in crossflow that investigated a wide range of velocity ratios, V_r, including values far above those seen in film cooling. As such, some structures shown above may not be present. Film cooling holes have an inclination angle of typically 30°, which weakens the stagnation of boundary layer fluid, so the horseshoe vortices may not form. They also operate at $V_r < 2$ which reduces the separation of the jet from the surface (or may be completely attached). The wake vortices are either not present or cannot be detected with smoke visualisation. Walters and Leylek [68] reason that the dominant mechanism affecting film cooling performance is the CVP and most studies also attribute their findings to it.

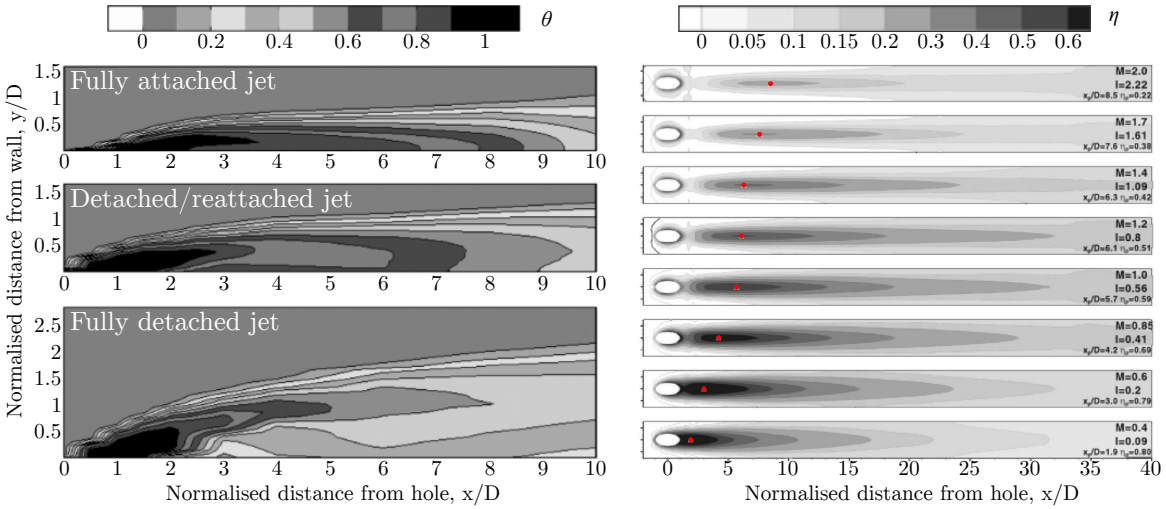


Figure 2.12: Contours of temperature (left) and adiabatic effectiveness (right) of a coolant jet in crossflow for different blowing ratios. Left: Non-dimensional temperature showing three general states of jetting. Right: Adiabatic cooling effectiveness showing lateral spreading of coolant and variation in the locations of peak values (red dot) [64]

The jet can also lift-off and separate from the wall upon exiting the hole, before reattaching further downstream, as shown in Fig. 2.12. This is found to scale with the momentum flux ratio, I. This makes sense since the freestream impinges on the exiting jet and is deflected upwards, thus exerting a force on the jet causing it to turn downwards onto the wall. The degree of turning is therefore a ratio between the coolant momentum and the freestream momentum. Increasing I shifts the reattachment point further downstream from the hole. This introduces two more detrimental effects: the low pressure separation zone entrains freestream fluid underneath the coolant jet, and the CVP persists for much longer since it is further from the the wall - which is responsible for viscous dissipation of vorticity.

2.2.4.2 Effect of Velocity Ratio, Blowing Ratio, and Momentum Flux Ratio

So far, the velocity ratio, V_r, blowing ratio, M, and momentum flux ratio, I, have been used here but not defined. While this thesis does not vary these quantities to study their effects, a brief explanation of their physical significance is provided nonetheless. These are also summarised in Table 2.3 below.

For fixed coolant and freestream densities, these three quantities are not independent as fixing any one of them will determine the other two, making sensitivity

studies of adiabatic effectiveness, η, to each parameter difficult. The blowing ratio, M, is the mass flux ratio of coolant to freestream. The use of M as a scaling parameter was first proposed for slot cooling, which can be assumed to be 2D. While this was found to work well, discrete hole film cooling is inherently 3D, for which the slot cooling correlations do not describe accurately. Nevertheless, M remains the most commonly reported scaling parameter due to historic usage and practical convenience - experimentally, it is easy to control mass flow rates of the freestream and coolant but not their velocities or momentum.

The momentum flux ratio, I, has been shown to scale η well in the near-hole region since the jet structure and the resulting turbulent mixing is strongest here [69, 70, 71, 72, 73]. Further downstream, the jet structure will have mixed out and more closely resembles a wake-like structure [68]. Mixing in this region is then dominated by freestream turbulence. Ornano and Povey [62] argue that this region scales with a new dimensionless parameter, the specific heat capacity flux ratio, E, which is related to the blowing ratio by $E = M^{c_{p,c}}/_{c_{p,\infty}}$, where subscript c refers to the coolant and subscript ∞ refers to the freestream. This governs the relative heat storage capacity of the coolant and freestream, i.e. the degree to which the coolant resists temperature change.

The velocity ratio, V_r, is the ratio of the coolant jet velocity to the freestream velocity and is a measure of the velocity difference and shearing at the freestream-coolant jet interface. When two fluids of different densities or viscosities experience shear flow, an instability can arise at the interface - this is the viscous analogue of the Kelvin-Helmholtz instability which only requires a velocity difference across the fluid interface. This shearing motion destabilizes the jet and affects the rate of mixing of the two streams. Ornano and Povey [62] show that for fixed I, E, and temperature ratio, V_r is inversely proportional to M, which allows the physical significance of the blowing ratio in scaling to be explained in terms of the velocity ratio. They find that M - and by extension V_r - scales η well in the intermediate region between the binary

region and fully mixed out region.

Parameter	Symbol	Expression	Regions of η Scaling Applicability
Velocity Ratio	V_r	U_c/U_∞	Between the binary and fully mixed out regions
Blowing Ratio	M	$\rho_c U_c/\rho_\infty U_\infty$	Between the binary and fully mixed out regions
Momentum Flux Ratio	I	$\rho_c U_c^2/\rho_\infty U_\infty^2$	Binary region near the hole
Heat Capacity Flux Ratio	E	$M c_{p,c}/c_{p,\infty}$	Fully mixed out region

Table 2.3: Summary of film-cooling scaling parameters, their expressions, and corresponding regions of η scaling applicability

2.3 Interactions Between the Upstream Flow and the Nozzle Guide Vane

Historically, the combustor and turbine sections have typically been designed in isolation. Many studies of combustors do not include the cascade, instead exhausting to either to atmosphere or a choked nozzle. On the other hand, many earlier studies of the NGV do not include the combustor geometries and instead only simulate the turbulence at the inlet plane as being high isotropic grid turbulence [74] or turbulence resembling that from combustor liners [75]. Later studies then included either 1D or 2D profiles of mean turbulence intensity or total pressure or temperature to study the steady state effects on the vane [29, 76, 77].

By studying each factor - turbulence, temperature gradients (hot streaks), swirl, and flow unsteadiness - in isolation, their effects on the aerodynamic field, heat transfer, and film cooling can be decoupled and a physical explanation can be deduced for each observed phenomena. They also provide an important database for validating future work. However, these factors are not necessarily independent, since swirl generation and subsequent vortex breakdown generates turbulence and unsteadiness. Swirl can also influence hot streak migration through the turbine, while high turbulence intensity can cause it to to dissipate more rapidly. Hence, the complexity of real combustor flows arises not just from the characteristics above, but also from their coupled interactions and their time-varying nature. More recently, there is a

trend towards integrating the combustor and turbine domains to achieve more realistic combustor flows at the inlet, and therefore more representative distributions of loss and cooling effectiveness around the NGV.

At the Technische Universität Darmstadt, Germany, the Large Scale Turbine Rig studies 1.5 stages of the turbine and features upstream swirlers and hub-side film cooling [78]. The Turbine Research Facility (TRF), located at the Wright Patterson Air Force Base, is a short duration (5 s) blowdown facility with a full turbine stage, featuring a combustor simulator with opposed dilution holes and hub and casing-side film cooling [79]. The Trisector Rig [80] at the University of Florence, Italy, which features liner effusion cooling and is able to achieve high temperature ratios, allows studies of combined hot streaks and high combustor swirl to be carried out. At the University of Oxford, three such facilities exist to study combustor-turbine interactions. These are the Oxford Turbine Research Facility (OTRF) [81], the Engine Component AeroThermal (ECAT) facility [82], and the MHI Linear Cascade facility [83].

This section reviews relevant studies of the effects of different combustor flow characteristics on the NGV. It also highlights the coupled nature of the combustor and turbine sections and therefore the need for integrating them into a single domain when carrying out numerical simulations or experiments.

2.3.1 Characterisation of Upstream Flow

Regardless of the combustor architecture in use today, most feature a swirler immediately followed by a sudden expansion to produce a central toroidal recirculation zone (CTRZ) for flame holding. The strong shearing at the interface of the CTRZ and the center of the swirl core contribute to high levels of turbulence intensity. The turbulent length scale is typically the diameter of the swirler itself since it will not have dissipated significantly by the combustor exhaust. At this point, there also remains significant radial and circumferential velocity imparted by the swirler and a low total pressure core is seen at the NGV inlet. This low pressure core is not always

exactly central, but precesses with a particular frequency, known as the precessing vortex core (PVC) [15, 84]. The frequency of this precession was observed to increase with increasing flow rate and swirl intensity [85]. Corner vortices are also established where the flow exits the swirler into the main chamber and separates from the walls, thus resulting in high shear.

Distinct combustion zones also create temperature gradients outward from the hot core towards the cooler walls. This is exacerbated in the radial direction by the combustor liner cooling. The temperature profile therefore exhibits a distinct hot zone in the center, called a hot streak. In RQL architectures, cooling is supplied by dilution jets, while LPM architectures feature effusion and film cooling, which do not penetrate as far into the freestream to break down the structure, as it is only intended to protect the combustor walls. LPM combustors therefore feature more severe radial temperature gradients. Fig. 2.13 shows example profiles of turbulence intensity, temperature, and swirl angle.

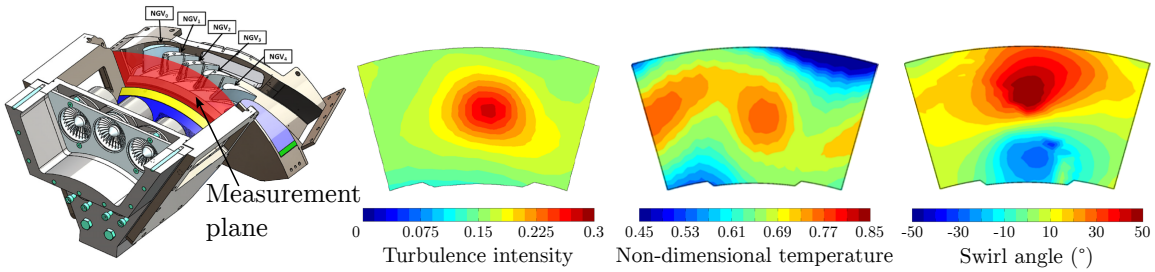


Figure 2.13: Profiles of turbulence intensity, temperature, and swirl angle measured at the inlet place to the NGV. Experiments carried out in the Trisector facility by Bacci et al. [86, 87]

Cha et al. [88] shows that the classical picture of vortical flows in Wang is not accurate when considering combustor flows. Classical secondary flows considers a 2D upstream flow where vorticity is only generated in the boundary layer and is predominantly in the circumferential direction. However, LES results show that significant vorticity generated outside the boundary layer due to combustor liner cooling flows and the rear inner discharge nozzle (RIDN) and rear outer discharge nozzle (RODN) flows, which are directionally opposed dilution jets. This jetting from the wall into the freestream breaks up the boundary layer and therefore little vorticity is generated there. Additionally, coherent structures being shed from the swirler will travel in the

freestream and eventually have their vorticity realigned in the axial direction.

Fluctuations in heat release during the combustion process results in an oscillating pressure field. These acoustic waves travel downstream into the NGV row and are reflected back towards the combustor and can establish standing waves. Some of these modes will be damped, while others can couple with the heat release process, providing a positive feedback mechanism that amplifies these modes. This can lead to excessive noise, vibration, and ultimately severe damage to the combustor. Fluctuations due to acoustic modes are differentiated from those due to a precessing vortex core (PVC) or vortex shedding, which are hydrodynamic modes. Candel [89], Ducruix et al. [90], and Huang and Yang [91] review the relevant flow dynamics and instabilities in modern lean premixed combustors.

2.3.2 Effects of Turbulence

Turbulence intensity of combustor flows entering the turbine section can be as high as 25 - 30% [59]. Ames and Plesniak [75] showed that increasing turbulence intensity correlated with increasing losses in the 'core' part of the flow and also resulted in broader wakes with lower velocity deficits due to improved mixing. This is consistent with the findings of Barringer et al. [92], where realistic pressure and temperature inlet profiles were used. The formation and migration of the horseshoe vortex is also significantly affected by turbulence intensity, Tu, and length scale, Λ. Higher turbulence intensity flattens out the approaching boundary layer and increases the near wall velocity, causing the horseshoe vortex to form closer to the leading edge. The separation lines of the suction side and pressure side legs of the vortex also move further downstream and closer to the vane surfaces [43, 93]. Experiments on a flat plate by [94] showed that increasing Λ at low Tu advances transition, and for high Tu, increasing Λ delays transition, suggesting that there exists an optimal ratio between Λ and the boundary layer thickness at the onset of transition. Studies at the University of Texas at Austin [95, 96] investigated the effect of turbulence on hot streak dispersion, and found that high Tu attenuated hot streaks more than low Tu.

In general, increased freestream turbulence has been shown to lead to increased skin friction, and heat transfer [75, 97, 98, 99] and many correlations exist to predict this [100, 101]. Thole and Bogard [97] showed that heat transfer enhancement with increasing turbulence intensity is greater than skin friction enhancement. They found that for Tu $>$ 10%, freestream turbulence penetrates the boundary layer and inactive motions replace shear-stress producing motions. Inactive motions do not contribute to shear stress but are active in heat transfer. Thole et al. [102] found that simple correlations based on cylinders in cross flow and flat plates perform poorly in predicting heat transfer in a turbine vane at high turbulence intensities. Even with uniform inlet turbulence, velocity fluctuations were found to be highly anisotropic on approach to the vane leading edge.

The effect of increasing turbulence intensity and length scale is has two competing effects in heat transfer. Increasing turbulence intensity thins the boundary layer leading to increased heat transfer [93, 101, 103] at locations where flow is 2D. However, it also reduces the strength of secondary flows, which are responsible for localised regions of very high HTC around the vane. Consequently, in regions dominated by secondary flows, such as near the leading edge and near the passage vortex migration path, little to no augmentation was observed [43, 102]. Ames et al. [104] found that the effect of high turbulence is to weaken the impact of the secondary flows on the heat transfer coefficient patterns, though they report that regions of high heat transfer in the wake and around the leading edge due to the horseshoe vortex are still present. A numerical study by [93] found that increasing freestream turbulence led to weaker secondary flows, which resulted in reduced heat transfer near the leading edge and in the passage near the passage vortex region, but was increased in the upstream region. The studies do however at least agree that heat transfer in regions dominated by secondary flows is due to vortical motion and not freestream turbulence. A higher freestream turbulence intensity also results in a more uniform thermal load distribution due to increased diffusion of secondary flows.

Similar findings are reported for film cooling jets - turbulence increases the mixing between the coolant jet and freestream which results in a more uniform coolant distribution but reduced effectiveness over a shorter downstream distance since the coolant dissipates more rapidly. Schmidt & Bogard [105] studied film cooling over a flat plate and found that freestream turbulence decreased cooling effectiveness at low momentum flux ratios but increased it at high momentum flux ratios. This was attributed to high momentum flux jets detaching from the surface at low turbulence conditions but then reattaching more rapidly under high turbulence conditions due to increased dispersion of the coolant jet. A similar argument was proposed by Cruse et al. [106]. Ames [107] and Ames [108] studied film cooling on a linear cascade and found that increasing turbulence intensity substantially reduced film cooling effectiveness levels on the pressure side and showerhead. The effect was less pronounced on the suction side due to higher velocities.

Werschnik et al. [78] carried out tests in the Large Scale Turbine Rig (LSTR), which simulates the full combustor-turbine interface. In this case, turbulence is generated by the swirling inflow $\left(\mathrm{Tu} \approx 30\%\right)$ and therefore cannot be decoupled from swirl intensity. They found that while there was an overall decrease in effectiveness, the increased turbulence resulted in more mixing of the coolant streaks, resulting in improved lateral surface coverage. They also observed local variations in the blowing ratio of some holes due to local variations in the mainstream dynamic pressure. These changes were found to depend on the swirler clocking position.

2.3.3 Effects of Temperature Gradients (Hot Streaks)

Interest in the effects of hot streaks and their migration through the turbine has resulted in a number of recent facility developments related to HS generation. Povey and Qureshi [77], Dorney et al. [109], and Koupper [110] review early facilities and more recent ones related to hot streak studies. In total, there are no less than 10 facilities worldwide related to HS studies that have been commissioned since the 80's.

One of the first studies on HS migration was performed by Butler et al. [111] on a

low-speed single stage turbine. Air was seeded with heated CO_2 to generate the HS and its migration tracked by measuring CO_2 concentration. Theoretical analysis by Munk and Prim [112] showed that for a fixed Mach number profile or stagnation and static pressure profile, a change in stagnation temperature does not alter streamline patterns. Since the inlet total pressure profile to the stator row was uniform, no additional secondary flow effects were observed. The hot streak splits into two legs that travel on either side of the vane and merges back downstream little spanwise or pitchwise migration. It only deforms slightly under the effects of the NGV's profile, boundary layer, passage vortex, and trailing edge wake [113].

However, the aerodynamic field around the rotor is significantly affected by the hot streak. The temperature gradient creates a density gradient and therefore a change in absolute velocity. In the relative reference frame there are now gradients in rotor relative inlet angle and relative velocity that depend on the profile of the hot streak. The hot zone will have higher absolute velocity compared to the cooler outer zone, and so in the rotor's reference frame, the hot streak has a relative velocity that is oriented towards the blade's pressure side, while colder fluid is oriented towards the blade's suction side. This preferential migration of hot streaks towards the rotor's pressure side is called the segregation effect. A second mechanism that contributes to the distortion of the rotor's aerodynamic field is the secondary flow effect. Since the relative velocity profile is altered, the relative stagnation pressure profile is altered accordingly, thus giving rise to additional secondary flows in the rotor blade row.

A consequence of the segregation effect is that rotor pressure side temperatures tend to be higher than the suction side. Dorney et al. [114] also finds that the rotor hub and tip experience the highest temperatures. Ong and Miller [115] numerically studied the effects of hot streaks on the first stage with film cooling and slot cooling on the hub. They found that the bulk of the coolant migrates towards the suction side, with little reaching the pressure side. This is partially due to endwall secondary flows entrain boundary layer fluid along the separation streamlines, as well as the

segregation effect whereby colder fluid preferentially migrates towards the suction side and hotter fluid migrates towards the pressure side. The hot streak also deforms under the action of the horseshoe vortex, passage vortex, and the vortex shed from the wake of the NGV.

While hot streaks do not significantly alter the aerodynamic field around the NGV, it can still result in regions of high heat transfer [116]. This is due to local changes in driving temperature while the HTC remains relatively unchanged since the aerodynamic field is not affected. As highlighted above, understanding the effects and migration of hot streaks is crucial in the identification and thermal management of hot spots, improving thermo-mechanical integrity, and optimising coolant flow distribution.

2.3.4 Effects of Swirl

A key characteristic of combustor flows is the high swirl intensity present due to the use of swirlers to generate a recirculation zone. This zone is also responsible for high turbulence generation and the formation of hot streaks. Swirl is typically quantified with the swirl number, S, defined by Gupta et al. [15] as the ratio between the axial flux of angular momentum to the axial flux of axial momentum:

$$S = \frac{\int_0^R u_x u_\theta r^2 \, \mathrm{d}r}{R \int_0^R u_x^2 r \, \mathrm{d}r}$$

where R is the radius of the nozzle. Above a certain critical value, swirl intensity is said to be high when vortex breakdown occurs and forms the central toroidal recirculation zone (CTRZ). Gupta et al. [15] gives a critical value of $S > 0.6$.

The literature reviewed so far has only considered cases of high turbulence or the presence of hot streaks without swirl. More recent studies have included real combustor geometries upstream to generate more realistic turbulence levels and swirl at the inlet to the NGV cascade. The effect of swirl was found to result in positive incidence on either the hub or casing and vice versa, depending on the sense of rotation of the swirler. This was found to shift the stagnation line, thus changing blade loading

across its span [61, 81, 117]. Giller and Schiffer [61] also found swirl to persist far into the passage and even downstream of the vane and multiple loss cores were present rather than just the loss core due to the passage vortex. Classical secondary flow structures that are typically present in fully axial flow are no longer dominant.

Pyliouras et al. [118] applied a 2D swirling inlet boundary condition to the first stage and report a decrease in stage efficiency by 1.5%-pts. They also found that secondary flow structures such as the horseshoe vortex and passage vortex are partially suppressed. Schmid et al. [119] also numerically estimated a reduction in stage efficiency of between 1 - 2% depending on swirl direction. They attribute most of this loss in efficiency to increased turbulence from the recirculation zone and only a small fraction as being due to the mismatch of incidence angles at the NGV inlet. Jacobi et al. [120] showed numerically and experimentally, that swirl led to flow redistribution and a radial static pressure gradient. The study also showed the formation of midspan vortex cores that migrate to either the hub or casing depending on the incoming swirl direction. These midspan vortex cores merge with the passage vortex resulting in a larger loss core. These vortex cores are also resolved here experimentally in space and time, showing their migration across the vane surface. A similar structure is noted by Mansouri and Belamadi [121].

The formation of the midspan vortex itself is an inviscid consequence of the low total pressure core, and is similar to how secondary flows develop due to a boundary layer with a total pressure gradient [27]. Fig. 2.4 in §2.2.1 above showed that a total pressure gradient resulted in lower velocity fluid being deflected more than higher velocity fluid, thus giving rise to secondary flows. Hermanson and Thole [29] showed numerically that secondary flow formation is influenced by the presence of a total pressure gradient in the boundary layer - the lack of a total pressure gradient was achieved with a constant Mach number inlet profile and resulted in no horseshoe vortex forming.

Duchaine et al. [122] carried out an LES study of the full CTI and compared it to

another case with only the turbine stage modelled. It showed that the aerodynamic field is similar in both studies. Differences arise in the injection of eddies which cannot be replicated with just the turbine stage. The temperature field of the full CTI also appears more diffuse whereas the turbine stage model shows more distinct patterns. Cubeda et al. [123] compared SAS and RANS models of the turbine stage alone and the full CTI. They made similar observations regarding similarities in the aerodynamic field, and large discrepancies in the temperature field, highlighting the need for a fully integrated approach to heat transfer modelling of the NGV.

Turrell et al. [20] modelled the full combustor-turbine interface of an ALSTOM 13.4 MW power generation gas turbine. They found that the NGV closest to the combustor centreline had the highest surface temperature compared its adjacent vanes. This was caused by the highly rotating swirl core being convected across its suction side and remaining in that passage. They observed little variation in the position of the vortex core over a single time step of the transient solution. Khanal et al. [124] and Mansouri and Belamadi [121] studied the combined effects of swirl and hot streaks for a full first stage. The hot streak was observed to split to either side of the vane and would migrate radially towards the hub or casing, depending on the direction of swirl.

Giller and Schiffer [61] found that the shift in the stagnation line due to swirl resulted in some showerhead jets turning over to the other side, thus leaving some parts of the vane completely uncooled. However the increased turbulence and swirl counters the lift-off and separation of discrete jets when it exits the hole. Cha et al. [88] suggests that upstream cooling holes in the combustor are responsible for generating small structures that can disrupt the incoming boundary layer to the vane, leading to weaker secondary flow structures. Werschnik et al. [78] found that swirl increased endwall HTC, decreased adiabatic cooling effectiveness, but improved lateral coverage compared to axial inflow. This is because swirl thins the endwall boundary layer, leading to higher heat transfer and better mixing out of cooling flows.

2.3.5 Effects of Flow Unsteadiness

Some examples of sources of unsteadiness are those originating from vortex shedding off the combustor wall, the precessing vortex core, and acoustic resonance. Simulations without the full CTI, such as those by Pyliouras et al. [118], cannot replicate the latter two effects because the 2D boundary condition is fixed and the lack of the NGV row prevents reflection of acoustic waves. Studies of the former effect are relatively easier to carry out as the computational domain is smaller. Mazzoni et al. [125] and Mazzoni et al. [126] carried out LES studies on the unsteady response of film cooling flows to vortex shedding off combustor walls based on the experimental setup of Cruse et al. [106]. They showed that these vortices would impinge on the leading edge, periodically sweeping the coolant off the surface, exposing it to the freestream. Mass flow through each hole was also found to oscillate periodically depending on the direction of rotation of the closest shed vortex.

A series of papers from the University of Utah [127, 128, 129, 130, 131] investigated the effects of bulk flow pulsations on film cooling. These pulsations can arise as a result of potential field changes (acoustic resonance and swirl core precession), a passing shock wave, and passing wakes (vortex shedding, swirl core impingement, and relative motion of stator and rotor blades). This causes a change in static pressure at the hole exit, which either increases or decreases the pressure ratio across an individual cooling hole. Since the subsonic mass flow across a constriction or orifice is proportional to the square root of differential pressure, $\dot{m} \propto \sqrt{\Delta P}$, these pulsations result in pulsating coolant mass flow exiting the holes. The experiments created pulsations in static pressure while keeping total pressure constant. They found that effectiveness decreases as the frequency of the pulsations increase. The pulsation frequency appears to have a greater effect on effectiveness compared to blowing ratio or length to diameter ratio.

Shaikh [132] experimentally and numerically studied the full CTI and found that the residual swirl core impinges on the unshielded vane and precesses across either

passage. This instantaneously alters the potential field around the NGV, which gives rise to fluctuations in vane loading, secondary flows, and heat transfer. They observed that the position and size of the horseshoe vortex oscillates from being large and forming further away from the leading edge to being small and forming closer to the leading edge. This correlates with the precession of the swirl core as downwash thins the boundary layer and increases the velocity close to the wall, while upwash thickens the boundary layer and reduces the near wall velocity. Unsteadiness was measured as the root-mean-square (RMS) of HTC, with the leading edge-endwall junction and trailing edge-endwall junction having the highest fluctuations.

2.3.6 Effects of Combustion

As this thesis is only concerned with non-reactive isothermal flows, we must ask how applicable or scalable the literature reviewed here and the findings of this thesis are to engine conditions with reactive flows. We therefore wish to compare salient features of combustor flows for cases with and without reaction. An obvious difference is the lack of temperature gradients and a uniform temperature profile in isothermal flows by definition. This has been addressed in §2.3.3; current methods replicate these temperature profiles with hot gas injection into the isothermal freestream. Studies of non-reactive flows have shown that turbulence levels at the combustor exhaust are in the range 20 - 30% due to the swirl core [59, 87, 133]. Cha et al. [88] reports a maximum of 35% however this is due to the unstable collision of opposed dilution jets of an RQL combustor. The presence of a precessing vortex core (PVC) is also noted in non-reacting swirl flows in simple geometries with sudden expansions [134, 135] and in realistic combustor geometries [136].

Cameron et al. [137] experimentally studied flows through an RQL combustor both with and without reaction and found significant differences between the two cases. The CTRZ - a result of vortex breakdown and used for flame holding - that was present in isothermal tests upstream of the primary jets, was no longer observed in reacting tests. Although the swirl number was not reported and the flow split to the

swirler was less than that to the primary and dilution jets, they note that increasing the split to the swirler beyond 45% recreated the CTRZ. Roux et al. [138] used two codes to solve the same computational domain; one is an LES code to resolve the full flow field, and the other is an acoustic solver that solves the Helmholtz equation to identify acoustic modes. The influence of reaction is integrated into the solver through the speed of sound, c, that is obtained by averaging LES results, but does not consider the role of combustion as an active acoustic generator. Hence it cannot determine whether acoustic modes will be amplified or damped. The combination of these tools allows the separation of fluctuations due to acoustic modes from the fluctuations due to the hydrodynamic modes such as the PVC.

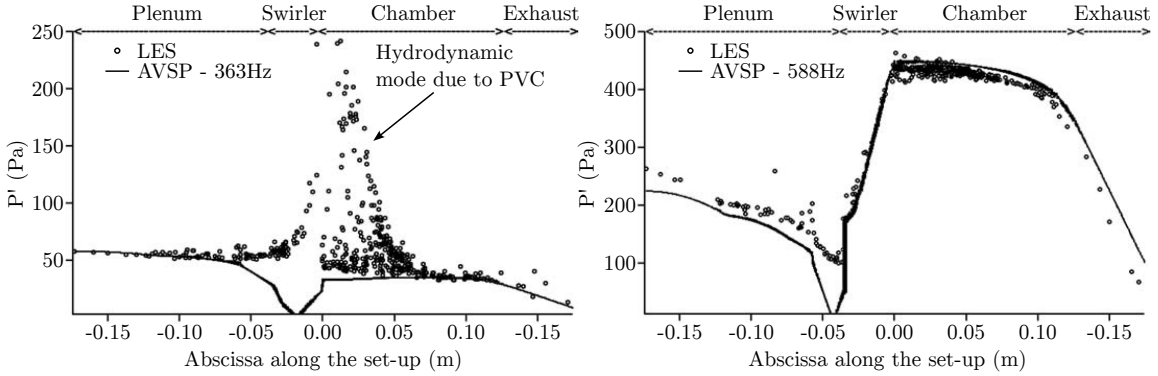


Figure 2.14: RMS fluctuations of pressure along the axial length of the combustor for non-reacting (left) and reacting (right) cases. Two solvers used to obtain fluctuations: LES solver resolves whole spectra; Acoustic solver (AVSP) resolves fluctuations for a given acoustic mode. Adapted from Roux et al. [138]

They observed the presence CTRZ in both non-reacting and reacting cases, but the precession of the vortex core was significantly damped. Fig. 2.14 shows the RMS of static pressure for both cases, plotted along the axial length. The LES results resolve fluctuations across the whole spectra up to the Nyquist frequency. The acoustic solver only shows fluctuations for a given acoustic mode (non-reacting - 363 Hz, reacting - 588 Hz). In the non-reacting case, the fluctuations match everywhere else except in the swirler and chamber. This shows that fluctuations in this region is dominated by the hydrodynamic mode of the PVC. In the reacting case, the fluctuations match everywhere and their magnitudes is greater, indicating that the whole flow is oscillating due to an acoustic mode, which has been amplified, while the hydrodynamic

mode of the PVC has been damped. They attribute this damping to flow dilation due to heat release and an increase in viscosity in burnt gases. The RMS fluctuations of velocity components (and therefore turbulence intensity) were also slightly lower in the non-reacting case compared to the reacting case. The frequency of the same acoustic mode has also shifted from 363 Hz (non-reacting) to 588 Hz (reacting). This makes sense since a resonant frequency is proportional to the speed of sound, which increases with increasing temperature. Selle [139] makes a similar observation of the suppression of the PVC in reacting flows.

2.3.7 Effects of Integration

The literature presented so far has focussed on the effects of different aspects of combustor flows on the NGV. Some profiles can be achieved without integration with combustors, through the use of turbulence grids, heated gas injection, imposing 2D inlet boundary conditions, etc. Others are harder to replicate due to its time-varying or stochastic nature and require full integration of the turbine section with the combustor. While studies abound which consider one-way coupling of the effect of combustor flows on the NGV, there are very few studies which consider two-way coupling, i.e. the effect of the NGV on the combustor exit boundary condition. Combustor studies typically assume choked conditions in the NGV row and the exhaust is fitted with a nozzle to simulate the reflection of acoustic waves at the sonic throat. Of the studies which integrate the combustor and turbine, this two-way coupling is usually not discussed.

The presence of vanes, whether choked or unchoked, exerts a static pressure field on the exit of the combustor At steady state, we might therefore impose a 1D or 2D static pressure boundary condition. However, the presence of the swirl core has been shown to alter the potential field around the vane, and also precess across different passages. Acoustic waves generated in the combustor can also travel downstream, reflect off the NGV, and travel back towards the combustion chamber. We might therefore expect the presence of the NGV row to affect the static pressure boundary

condition and the acoustic boundary condition at the combustor exhaust.

2.3.7.1 On the Potential Field in the Combustor

Salvadori et al. [140] and Insinna et al. [141] simulated the CTI as two separate flow domains but couple the RANS solvers by exchanging information at the boundaries. Combustion is assumed to occur only in the first domain. This method offers improved stability and accelerated solution times compared to modelling the entire interface as a single domain with combustion. They also simulated the decoupled approach, whereby the combustor exit profiles were applied as the inlet boundary conditions to the NGV domain with no feedback from the turbine to combustor. The effect of coupling between the domains resulted in a significant variation in Nusselt number distribution on the vane surfaces, by as much as -34% to +22%, depending on radial position.

Roux et al. [142] carries out LES simulations of an RQL combustor with reacting flows. Two different domains are investigated. One with the combustor and the NGV row explicitly computed and the other replaces the NGV row with a constant static pressure outlet boundary condition. Comparisons of the mean flow field at different cross-sections along the central axis of the combustor show that there is little effect of the presence of the NGV row on the rich zone prior to the dilution jets. Consequently, the flame structures from both simulations are also very similar.

At the combustor exit plate, the difference in the axial, radial, and tangential velocity profiles between both simulations are more apparent. The temperature profile also has a circular hot streak; without the NGV row, the profile is more uniform. This finding is of practical importance since the outlet temperature profile is one of the main results used in the design of combustors. These findings highlight the importance of including the NGV row in combustor studies.

Escudier et al. [143] finds that for highly swirling flows, the outlet geometry can have a significant effect throughout the flow field, including the upstream combustion zone. There is a trend towards increasing swirl numbers in LPM combustors, which

may mean that the finding of Roux et al. [142] - of the limited influence of the NGV row on the aerodynamic field in the rich zone - does not hold in LPM combustors.

2.3.7.2 On Acoustics in the Combustor

In reacting flows, a driving process such as heat release fluctuations generates perturbations in the flow, which functions as a pressure source term in the wave equation. This generates acoustic waves that provide a feedback mechanism to couple the perturbation to the combustion process. These acoustic waves will propagate downstream and reflect off the NGV row. The combustion chamber itself functions as a closed acoustic environment and therefore functions like a Helmholtz resonator with different resonant modes. In non-reacting flows, there is much less energy to drive pressure fluctuations however resonance in the chamber still occurs. These acoustic waves constitute pulsations in the freestream static pressure which has been shown to reduce film cooling effectiveness. Replicating such conditions without the combustor whether numerically or experimentally in turbine cascade studies would require a separate study to identify the acoustic modes of the combustion chamber first.

Roux et al. [142] observes much higher RMS fluctuations of pressure, temperature and axial, radial, tangential velocities in the case where the NGV row is included, compared to the case with a constant static pressure outlet. This is likely due to the imposed non-reflecting pressure outlet boundary condition, which prevents reflection of acoustic waves at the outlet. Frequency analysis of pressure in the combustion chamber also reveals very different spectra between both domains. The study concludes that the inclusion of the NGV row is vital to the accurate prediction of unsteady phenomena at the inlet to the turbine stage.

2.4 Conclusions

The aerothermal field around the NGV is dominated by secondary flows that arise from total pressure gradients in the incoming fluid. An example is the gradient at the wall due to the boundary layer. The vortical motion from secondary flows is the

main contributor to aerodynamic loss and localised regions of very high heat transfer. Film cooling flows also exhibit highly 3D flow structures that result in increased heat transfer near the jet, before mixing out and forming a protective film. The effectiveness of this film was found to scale well with the momentum flux ratio, I, in the binary region near the hole. In the fully mixed out region far downstream of the hole, it scales well with the specific heat capacity flux ratio, E. In between these two regions, it scales well with the blowing ratio, M.

In non-reacting isothermal flows in a combustor, strong swirl results in vortex breakdown and the formation of the central toroidal recirculation zone. High shear rates at the interface of this separation zone generate significant turbulence. Coherent structures also detach from this recirculation zone and convect downstream. The vortex core originating from this zone also precesses about the central axis and has a turbulent length scale comparable to the diameter of the swirler. This precessing vortex core and the shed coherent structures persist far downstream and are seen at the inlet to the NGV. This is not simply an increase in turbulence levels but also significantly modifies the aerodynamic field around the NGV, resulting in steady state freestream and coolant flow redistribution, as well as unsteady effects such as bulk fluid pressure oscillations that pulse the coolant flow.

In reacting flows, radial temperature gradients are present across the hot combustion gases in the center to the cold film coolant along the walls. These hot streaks persist across the whole first stage and have a tendency to accumulate on the pressure side of the rotor blade. Heat release fluctuations during combustion also result in acoustic waves that provide a positive feedback mechanism that can amplify certain modes. These acoustic waves travel into the NGV row and are seen as pulsations in static pressure, which can affect film cooling effectiveness. The two-way coupling of the NGV row and the combustor has also been shown to significantly affect the pressure and temperature profiles at the interface, which precludes the use of a static pressure outlet boundary condition on the combustor alone.

Evidently, these combustor flow characteristics are not independent and will interact with each other to determine the overall aerothermal field around the NGV. Simple profiles which inadequately represent these main flow features run the risk of inaccurate prediction of NGV performance and the loss of thermo-mechanical integrity. If scalable aerodynamic, heat transfer, and film cooling results are desired, then these characteristics cannot be fully decoupled from each other and must be replicated as accurately as possible. This highlights the need for fully integrated combustor-turbine studies, as opposed to conventional isolated studies or loosely coupled numerical approaches where information is exchanged at the interface to set boundary conditions. In this respect, there are relatively few studies of the full domain. Furthermore, none of these studies investigate the effects of different swirler geometries on the NGV; to the author's knowledge, these studies still use a conventional single-core combustor. There is a need to explore more advaced geometries, given the current trends in combustor architecture towards multiple small main swirlers, and ultimately multicluster type burners - see §2.1. Finally, of the few studies here which investigate the effects of flow unsteadiness, two use very simple geometries (cylinder and flat plate), while the third does not include film cooling.

This thesis therefore aims to investigate the effects of four different swirler geometries on a fully cooled NGV, in a fully coupled combustor-turbine interface. High-speed, high resolution measurements on the vane surface and in transition duct allow the effects of unsteadiness on film cooling to be studied and correlated with certain flow structures. An LES study will be carried out on two of these swirlers to fully resolve the flow field and aid physical interpretation of experimentally measured quantities.

Chapter 3
Methodology

§2 has emphasised the complexity of combustor flows and, which necessitates a high degree of flow similarity to accurately recreate the main flow features at scaled engine conditions. This thesis models the combustor and turbine sections in a single domain, which fully couples them, and a joint numerical and experimental approach has been taken to investigate the steady and unsteady interactions of combustor swirl flows on an uncooled and film-cooled nozzle guide vane.

High-speed infra-red (IR) thermography, double-sided thin film gauges, and high-speed pressure transducers were used to measure fluctuations in temperature and pressure on the vane surface and in the transition duct. High-fidelity large eddy simulations (LES) were also carried out of the whole combustor-turbine interface to resolve 90% of the turbulent fluctuations and coherent structures in the whole flow field. This aids identifying dominant structures responsible for the effects observed in experiments. Theoretical models of conductive and convective heat transfer were also developed for post-processing and data reduction into quantities of interest and to highlight unsteady features on the vane surface.

3.1 Experimental Facility

Experiments were carried out in the Mitsubishi Heavy Industries High Speed Linear Cascade, which is a blowdown facility; see Figure 3.1. Ambient air is pressurised to $400\,\psi$ by 4 compressors and dehumidified, before being stored in supply tanks that serve the whole laboratory. The facility is connected to the supply tanks and isolated by two ball valves. A controlled flow rate is fed to this facility by means of a pressure regulator that sets the upstream pressure of a choked nozzle. Flow passes through a circular-to-rectangular transition section with 5 splitters to reduce the diffusion angle and prevent flow separation. This is then conditioned by a series of perforated plates

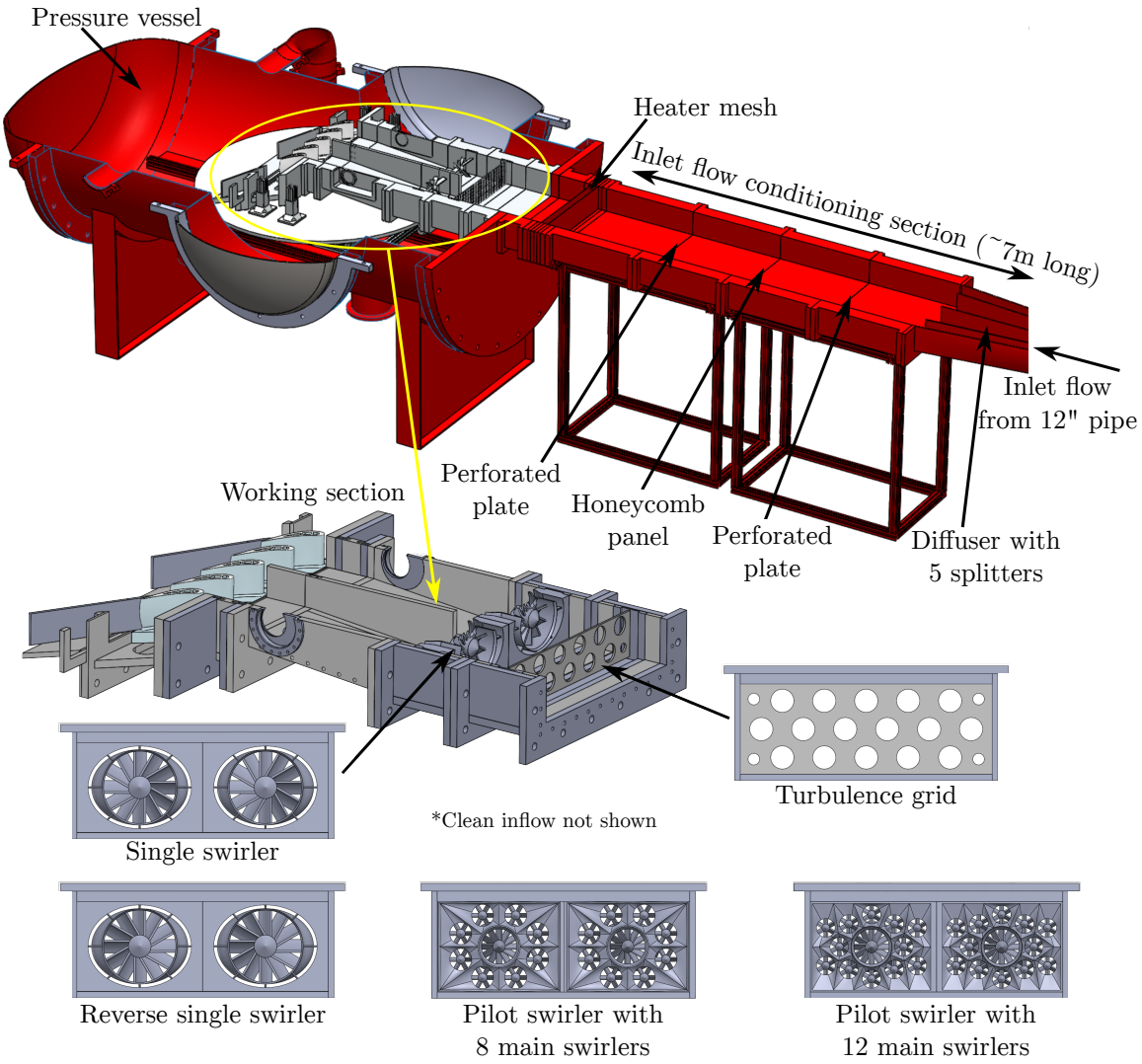


Figure 3.1: The MHI high speed linear cascade facility provides a flexible platform for performing tests on NGV geometries with different combustor inflow conditions. A turbulence grid and four different swirlers are shown. The clean inflow removes these geometries from the flow path

and a honeycomb panel.

If desired, the air can then be preheated prior to entering the pressure vessel using a series of fast response heater meshes. The maximum voltage delivered is 115 V, which gives a current flow of around 1300 A. Losses across the transmission lines result in only approx. 86 V across the heater mesh. For a flow rate of 5 kg/s (and $c_p = 1005$ J/kgK for air), this gives a temperature rise of approx. 22 °C. At this mass flow, the facility can achieve a run time of 2 minutes before the supply tank pressure falls sufficiently low that the pressure regulator can no longer maintain the set pressure.

The working section models two can combustors with two NGVs and two passages per can. The vane positioned behind the combustor wall is termed the 'shielded' vane. The vane positioned directly in the path of the swirler is termed the 'unshielded' vane. This study is only concerned with flow around the unshielded vane. Inlet flow conditions are modified by means of replaceable upstream cassettes, which hold various turbulence grids and/or swirlers. All flows in this study are non-reacting and isothermal. Luque et al. [83] and Aslanidou and Rosic [144] describe the design of the facility in greater detail.

3.1.1 Geometric Parameters & Operating Conditions

For dynamic similarity of viscous compressible flow over a body with a ideal uniform inlet, the Reynolds number, Re, Mach number, M, and Prandtl number, Pr, must be matched. The Reynolds number is the ratio of inertial forces to viscous forces, and determines whether inertial effects dominate in producing large scale fluctuations or viscous effects dominate in damping out these fluctuations. The Mach number accounts for compressibility effects of the gas, i.e. changes in density as a result of high speed flows. The Prandtl number is the ratio of momentum diffusivity to kinematic diffusivity and governs the relative thickness of the momentum and thermal boundary layers, i.e. how fast momentum dissipates compared to heat in a given fluid. The value of Pr remains roughly constant over a large range of pressures and temperatures.

In terms of the measured quantities of interest, these non-dimensional quantities govern boundary layer transition, aerodynamic loading, loss, and heat transfer. Geometric and dynamic similarity can be achieved very simply by using the full scale NGVs and operating the facility at the same engine mass flow rate. However, this would require an enormous amount of compressed air and would severely limit run time. At scaled engine conditions, without independent control over density or viscosity, it is often not possible to match both Reynolds and Mach numbers. A compromise is required between the requirements of the experimental methodology, instrument accessibility, repeatability, resolution, operational flexibility, and the achievable non-

dimensional quantities. Aslanidou [145] performed this trade-off analysis and scaled the NGV used in this study to 62% of its original size where the exit Mach number is matched and the Reynolds number is 49% of the real engine. Table 3.1 summarises the geometric parameters and operating conditions of the facility.

Parameter	Unit	Experiment	Engine
Vane true chord	mm	150	242
Vane axial chord	mm	89	143
Vane pitch	mm	120	193
Vane span	mm	104	168
Combustor wall thickness	mm	15.3	25
Inlet total pressure	Pa	1.55E5	16E5
Exit static pressure	Pa	1.19E5	-
Freestream mass flow rate (per passage)	kg/s	1.2	13
Exit Mach number	-	0.625	0.625
Exit Reynolds number (based on true chord)	-	2.51E6	5.1E6
Prandtl number	-	0.69	0.72
Inlet turbulent intensity	-	2 - 13%	13%
Run time	s	120	-

Table 3.1: Geometric parameters and operating conditions of the MHI high speed linear cascade with the MHI R1V NGV cascade installed. Adapted from Aslanidou [145]

3.1.2 Inlet Flow Conditions

Six different inlet conditions were used in this study. These are a clean inflow, a turbulence grid, and four different combustor geometries, shown in Figure 3.1. The clean inflow and turbulence grid cases function as baseline cases for comparison with swirling inflow cases, to aid identification of the effects of swirl. The turbulence grid case is similar to numerical simulations of the NGV alone with an imposed turbulence intensity and length scale. The turbulence grid was designed following the empirical correlation of Roach [146] in order to give an isotropic freestream turbulence intensity, Tu = 12%, at the NGV inlet plane. It is fabricated from a 5 mm aluminium plate with circular apertures 45 mm in diameter. This gives a streamwise integral length scale, $\Lambda_x = 31.1$ mm, and streamwise turbulence microscale, $\lambda_x = 1.9$ mm, at the NGV inlet plane.

The single swirler was studied as it is representative of combustors in use today; see for example Qureshi and Povey [81], Bacci et al. [87], and Cameron et al. [137]. Its mirror image was also included to study the effects of swirl orientation. The MHI 8-core swirler was included as it is representative of an advanced LPM combustor in use by MHI. It features 8 main burners arranged concentrically around the pilot burner. This was designed by Jacobi and Rosic [147], and provided a mean swirl angle of 8° at the vane inlet. The 12-core swirler builds on this design by increasing the number of main burners and decreasing their diameter while the diameter (or in this case hydraulic diameter) of the whole combustor is remains the same. Fuel injection in the nozzles (the centrebody of an individual burner) is not modelled so all the flow passes axially through the swirler.

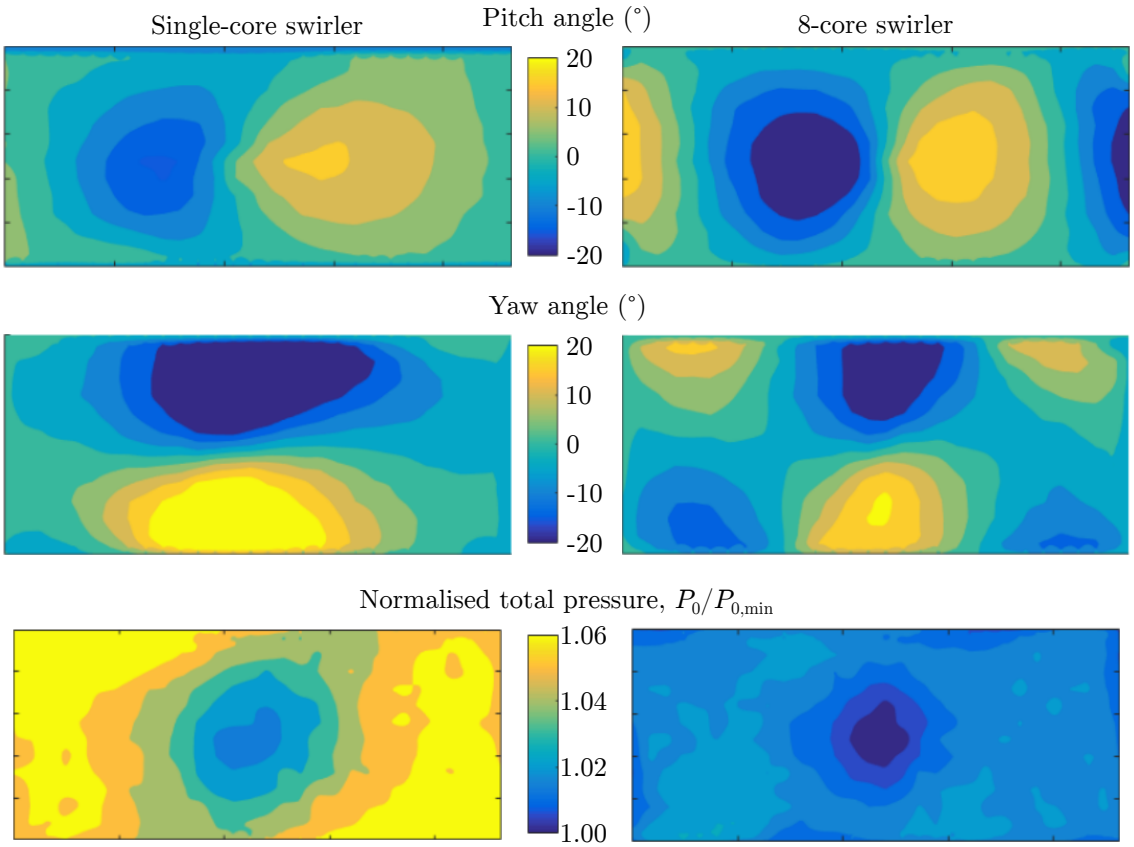


Figure 3.2: Experimentally measured pitch angle, yaw angle, and normalised total pressure contours for the single-core and 8-core swirlers in the MHI linear cascade facility. Measured by and adapted from Shaikh [132]

Fig. 3.2 shows the experimentally measured pitch angle, yaw angle, and normalised

total pressure for the single-core and 8-core swirlers. This was measured by Shaikh [132] with a five-hole probe mounted on an automated two-axis traverse to scan across the transition duct outlet (which is the inlet plane to the NGV cascade). The local total pressure was normalised by the global minimum across the plane.

Past studies on this facility by Aslanidou [145] have investigated the influence of these inflow conditions (except the 12-core swirler) on the aerothermal performance of the NGV using infra-red thermography and traverse measurements with a five-hole probe. Shaikh [132] extended this to include the 12-core swirler and also studied the unsteadiness of the thermal field using single-sided thin film gauges. So far, only uncooled NGVs have been examined. This thesis studies the effects of combustor flows on a film-cooled NGV and extends the study of unsteadiness to identify the sources of fluctuations in the thermal field.

3.2 Film Cooling System

A new coolant supply system was designed by the author to provide foreign gas to the test section to be used for film cooling. The gas of choice is currently CO_2, which was chosen for its relative density (1.67 times that of air at STP), availability, stability, and it has been shown to require the least correction [148] in the measured adiabatic effectiveness. The purpose of using a foreign gas in film cooling is to match - as closely as possible - the density ratio, DR, as an analogue to matching the temperature ratio seen in real engines, ${}^{T_\infty}/_{T_c=2}$.

CO_2 from the cylinders is supplied at 50 barg and ambient temperature. This is then regulated down twice, which sets the inlet pressure to the sonic Venturi nozzle. Since flow in the nozzle is choked, coolant mass flow, $\dot{m}_c$, only depends on this upstream pressure. Thus, $\dot{m}_c$ is controlled using the pressure regulator. There are two relief systems installed - before and after the Venturi nozzle. The former is to protect the system in the event of complete failure of the pressure regulator. The latter is to protect the working section. All equipment is rated to more than 40 barg except the

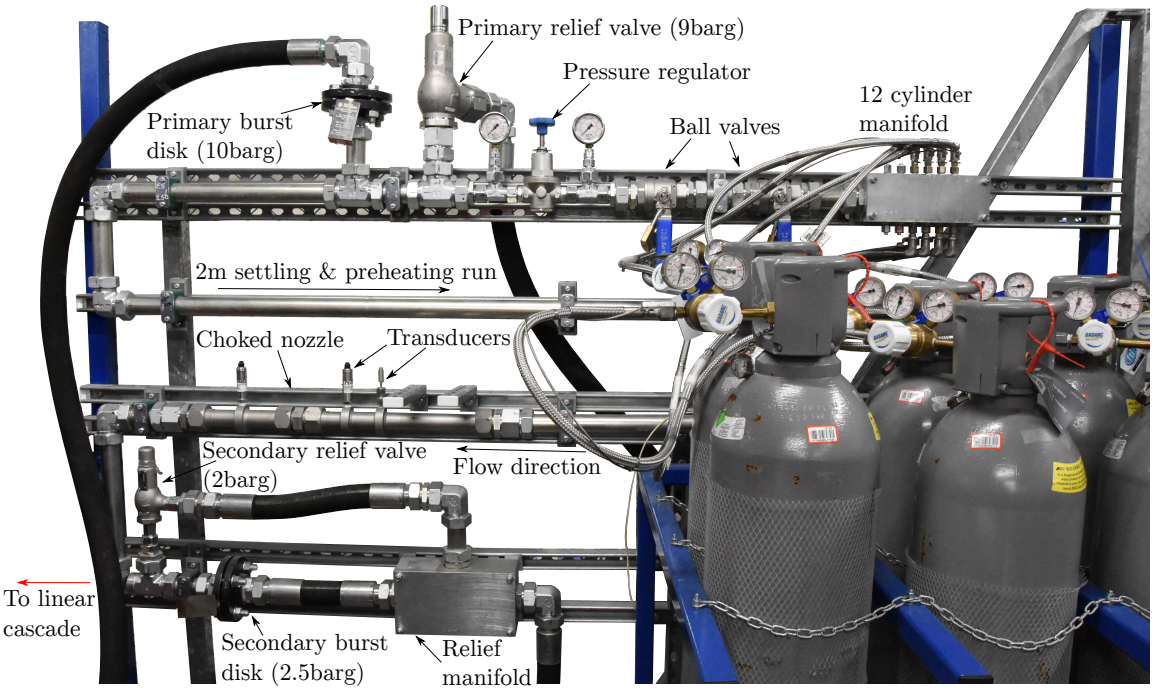


Figure 3.3: CO_2 film cooling supply system to the MHI linear cascade facility

sonic Venturi nozzle and the relief, which is rated to approx. 30 barg. In the event of total failure of the regulator, it is expected that the system will choke at the smallest orifice - which is at the cylinder valve outlet - and the rest of the line will be at a pressure lower than 30 barg; see §3.2.2. Flow out of the sonic Venturi nozzle enters the MHI Linear Cascade Rig where the working section is located. The system was designed to be scaled up to allow full film cooling across three NGVs to be achieved, including endwall cooling. This requires $\dot{m}_c$ at approx. 5% of $\dot{m}_\infty$, which in this case is $\dot{m}_c = 0.25\,\mathrm{kg/s}$.

3.2.1 Pressure Regulator

A single stage diaphragm regulator is used to set the upstream pressure to the sonic Venturi nozzle, and therefore control $\dot{m}_c$. The regulator has $K_v = 2.4\,\mathrm{m^3\,h^{-1}}$, which can support a mass flow of $\dot{m}_c \approx 0.063\,\mathrm{kg\,s^{-1}}$ for $\Delta P = 1\,\mathrm{bar}$, $P_2 = 5\,\mathrm{bara}$, and $T_1 = 288\,\mathrm{K}$. Thus, the regulator at full travel is capable of supplying the full mass flow range the sonic Venturi nozzle is rated for.

For a coolant run time of $\sim 30\,\mathrm{s}$, this is a loss in 7.5 kg per cylinder per run. Evidently each run requires a significant proportion of a single cylinder, which is

initially filled with 25 kg of CO_2. To reduce the supply pressure effect (SPE) due to the variation in cylinder pressure 4 cylinders are used, with each cylinder fitted with a two stage diaphragm regulator. This was also a safety measure as the maximum inlet pressure to the regulator is 50 bar, which is the nominal fill pressure of the cylinders. Daily variations in room temperature caused this to rise to 58 bar. Furthermore, regulating across a large drop in pressure for large mass flow rates is not advised.

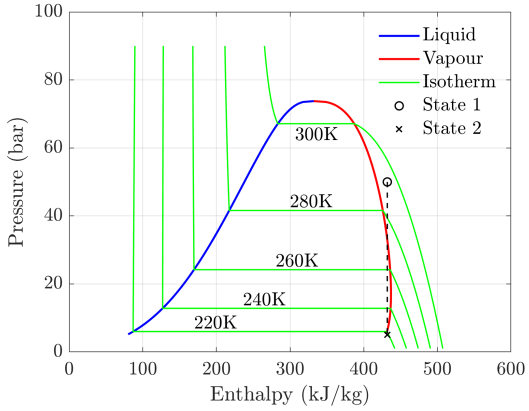


Figure 3.4: $P-h$ diagram for CO_2 with various isotherms and an isenthalpic expansion process across the pressure regulator from 50 bar to 5 bar. Properties of state from data published by the National Institute of Standards and Technology (NIST)

Fig. 3.4 shows the behaviour of CO_2 across an isenthalpic expansion from a cylinder pressure of 50 bar to 5 bar. It is not advisable to regulate a large pressure drop at high mass flow rates across a single cylinder due to isenthalpic expansion (or Joule-Thomson expansion in the case of real gases). Depending on the exit pressure - and therefore desired $\dot{m}_c$ - the fluid can enter the saturation curve and the temperature of coolant can fall by as much as 70 K. This can potentially violate temperature ratings of the equipment used. If $\dot{m}_c$ is small, this is not usually an issue since the heat lost to the surroundings prevents the regulator from reaching such low temperatures. However, icing was noticeable on the outside of the regulator during runs. So it was decided to regulate in two stages, first across each cylinder, before finally regulating with the main regulator.

3.2.2 Relief System

The assumption that flow chokes at the cylinder valve is only true if the relief system is capable of supporting the mass flow rate at failure, $\dot{m}_f$, at the rated relieving/burst pressure without choking. That is, the following must be satisfied: $\dot{m}^*_{\text{relief}} > \dot{m}^*_{\text{cylinder}}$, where $\dot{m}^*$ is the choked mass flow rate calculated using Eqn. 3.1. Otherwise the line pressure will increase until this condition is satisfied. Fig. 3.5 shows that the system is safe up to 8 cylinders. The figure shows that $\dot{m}^*_{\text{relief}} > \dot{m}^*_{\text{cylinder}}$ for a single cylinder

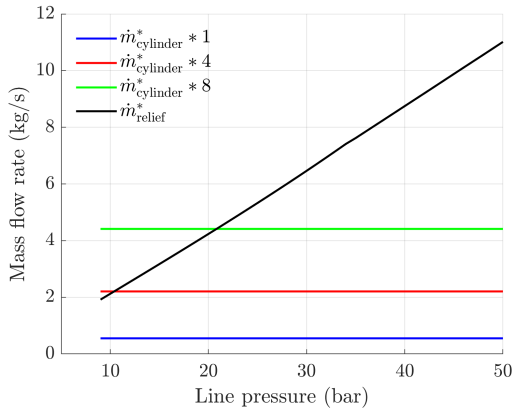


Figure 3.5: Choked mass flow rate, $\dot{m}^*$, with line pressure, P, for 1, 4, and 8 cylinders and the relief system

at all line pressures above the relieving pressure (9 barg) and burst pressure (10 barg). Hence the relief system is able to safely support a single cylinder in the event of the total failure of the regulator. The intercept of the two lines gives the pressure at which the line pressure will rise to before flow starts choking at the cylinder. Hence if the upper limit on the line pressure was set at $P = 25$ barg, then 8 cylinders can be supported. This is a conservative estimate as it assumes the outlet has been blanked off, that flow chokes at a throat with diameter, $D_t = 1/4$", and the discharge coefficient of the cylinder is $C_d = 1$.

3.2.3 Sonic Venturi Nozzle

The system is intended to supply a constant $\dot{m}_c$ to the test section with the ability to vary it so that $\frac{\dot{m}_c}{\dot{m}_\infty}$ can be varied. This is achieved using the sonic Venturi nozzle which chokes flow through it as long as the pressure ratio, P_2/P_1, across it remains

below 0.9. It is therefore invariant with downstream pressure and is dependent only on upstream pressure and temperature. The upstream pressure is then varied using the pressure regulator. Mass flow rate is calculated using the following equation:

$$\dot{m}^* = \frac{P_{0,1}}{\sqrt{RT_{0,1}}} A_t C_d C^* \qquad \text{where} \qquad C^* = \sqrt{\gamma \left(\frac{2}{\gamma+1}\right)^{\left(\frac{\gamma+1}{\gamma-1}\right)}} \tag{3.1}$$

where the subscript 0,1 refers to stagnation quantities upstream of the nozzle. Since it is more convenient to measure static quantities, the pipe diameter was chosen to be excessively large (1.5") so that coolant flow in the pipe was slow. Stagnation quantities were then approximated with static quantities. Note however, that if calibration was performed, then this discrepancy is accounted for in C_d, essentially removing the approximation. The nozzle was calibrated by Colorado Engineering Experiment Station Inc. (CEESI) using standards traceable to the National Institute of Standards and Technology (NIST). This gives C_d as a function of Re.

The lower limit on the upstream static pressure to the nozzle, P_1 - and therefore $\dot{m}_c$ - is set by the requirement that $P_2/P_1 < 0.9$ for flow to be choked. The upper limit on P_1 is set by requirement that the fluid remains as a superheated vapour, i.e. it does not enter the saturation region, which may occur in the throat as flow accelerates through it causing a drop in P and T. The operating range of the nozzle is given in Table 3.2 below:

$\mathbf{D_t = 0.2438''}$	Max. Flow	Min. Flow
P_1 [bara]	7.58	3.79
T_1 [K]	283.2	283.2
$\dot{m}^*$ [kg/s]	0.0670	0.0331

Table 3.2: Operating range of sonic Venturi nozzle with throat diameter, $D_t = 0.2438''$.

3.2.4 Film-Cooled Nozzle Guide Vane

The NGV used in this study was rescaled and linearised from an MHI F-type gas turbine NGV. It features impingement jet arrays generated by the inserts shown in Fig. 3.6 and a pedestal bank at the trailing edge. The latter promotes conductive and internal convective heat transfer as well as provides structural support to a very thin trailing edge. The jets impinge on the internal surface, resulting in regions of very high heat transfer coefficient, then exiting through the cooling holes to form the external film cooling layer. For geometric similarity, the hole shape, inclination/compound angles, hole/row spacing, length-to-diameter ratio, and number of rows of the coolant holes were also preserved. The showerhead features 5 rows of staggered compound angled holes. Other film cooling rows on the pressure and suction side are aligned axially. The total coolant mass flow for all blade surfaces and the endwalls is 0.057 kg/s, which constitutes 4.7% of the incoming freestream flow.

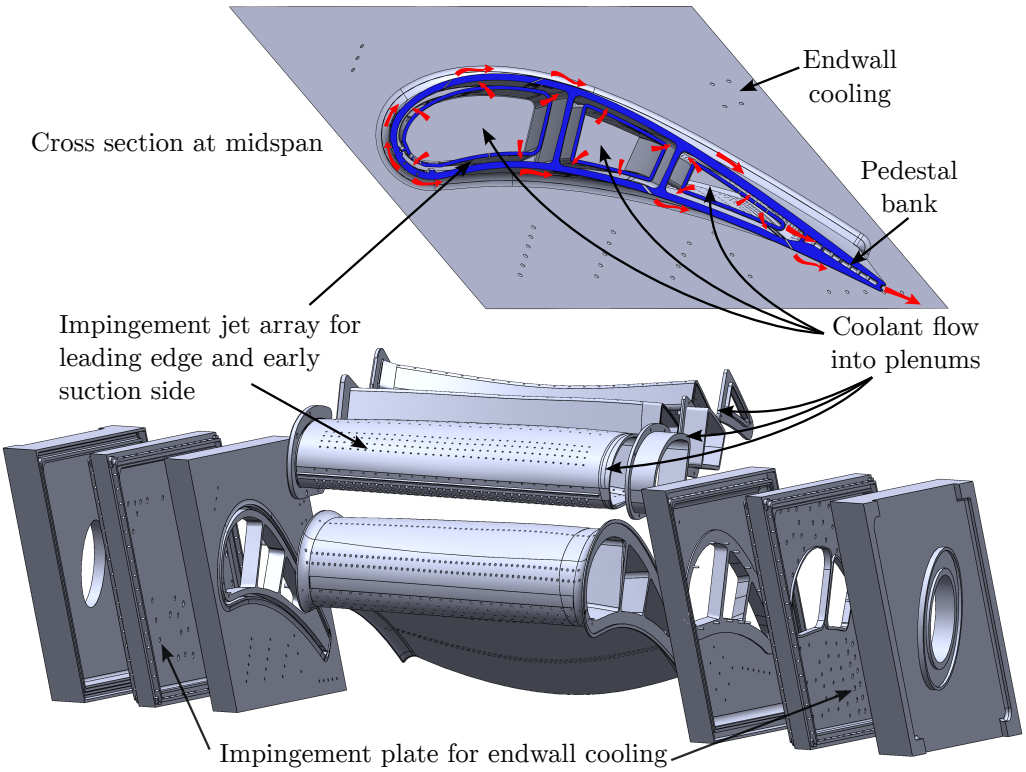


Figure 3.6: Film-cooled F-type gas turbine NGV showing internal and external cooling features

The vane was 3D printed with a UV-curable material (3D Systems VisiJet M2R-TN) using a MultiJet Printer (3D Systems MJP 2500) with a print resolution of

32 µm. The parts were then sanded until the surfaces felt smooth, however the surface roughness was not measured. This material was chosen for its thermal and structural rigidity to withstand to the significant thermal and mechanical cycling that the NGV will experience during each run and over the course of this study. The printed component also needs to withstand temperatures up to 70 °C because this printing technology uses a wax support which requires additional post-processing to remove. This can be done either in an oven heated up to 70 °C or an ultrasonic bath filled with water or D-Limonene. Such (relatively) high temperatures are necessary due to the fine features in the NGV such as cooling holes, which can trap pockets of wax.

This printing technology was chosen out of the other available technologies such as stereolithography (SLA), fused deposition modelling (FDM), digital light process (DLP), direct metal laser sintering (DMLS), etc. due to the following factors: print resolution, surface finish, ease of assembly, post-processing required, warping, and cost. The smallest features in this component are the cooling holes, with a diameter of approx. 0.6 mm. Test prints on coupons with holes of the same size and wall thickness using SLA and FDM yielded partially formed holes for the former while no holes were formed for the latter. Furthermore, SLA prints require a lattice support structure on overhanging walls, which in this case is the entire internal wall of the vane. The lattice can be broken off easily, however this will leave indents on the surface, which require further sanding and polishing to remove. Since these are internal surfaces, they are very difficult to access, especially in the trailing edge cavity.

DLP technology is relatively new and offers a similar print resolution to MJP technology, however this capability was not available in-house and was therefore much more expensive to print. DMLS technology was considered for the structural integrity of its printed parts, especially with such thin walls present in the NGV. However, the print resolution is lower and has a much rougher surface finish that would require grinding to smooth out - a much more laborious task than sanding. Internal surfaces

would be impossible to smooth out, thus introducing the additional factor of surface roughness into heat transfer measurements. There is also a high likelihood of incomplete hole formation, which would require drilling at very steep angles; some regions on the vane are not accessible to the drill spindle due to interference.

3.3 Infra-Red (IR) Thermography

Infra-red thermography involves the use of a microbolometer to detect the amount of incident radiative power per unit area on the sensor. After calibration, the radiative power detected can be converted to temperature, which is then used to calculate HTC using a transient method of Oldfield [149]. This provides a non-intrusive method for full surface resolution of temperature. Past studies on this facility [132] have used the FLIR A655sc for measuring time-averaged h. This has a resolution of 640 x 480 pixels and a sampling rate of 50 Hz at full frame. The experimental setup allows for views of the vane leading edge (through a zinc-selenide window) and suction side for both the shielded and unshielded vane. The zinc-selenide window has been sized for the low-wavelength IR (LWIR) range and has an anti-reflective coating applied to both sides to further increase its transmisivity.

Experiments on an uncooled vane with thin film gauges and high-speed surface mount pressure transducers suggest that there is significant unsteady content in the flow field that is seen by the vane surface. To resolve this high frequency phenomena across the whole vane surface, the FLIR X6900sc camera was used. This features a cryocooled indium-antimonide sensor, allowing even shorter integration times and higher frame rates. For working temperatures up to 55 °C, the maximum frame rate at full frame is 1004 Hz. This gives a Nyquist frequency of 502 Hz. §7.4 will show that there is little frequency content beyond this due to the material attenuating high frequency fluctuations in temperature, effectively acting like a lowpass filter, thereby preventing aliasing.

The resolution of this camera is 640 x 512, allowing high quality imaging of the

whole vane surface. The cooling holes, which are 0.6 mm in diameter, could also be identified but at high zoom and much lower resolution - with the hole outline corresponding approximately to a 3 x 3 grid of pixels. An alternative model (FLIR X8580) is capable of a much higher resolution (1280 x 1024 HD), however this only allowed a maximum frame rate of 181 Hz. This compromise was made since the intent was to study the unsteady effects of combustor flows on the whole vane surface, not just locally at the hole exit, with an emphasis on high frame rates. The cooled sensor has much lower noise levels, allowing it to differentiate smaller fluctuations in temperature due to unsteady flow structures from the mean temperature. This offers a form of flow visualisation, by tracking the passage of flow structures as it migrates across the vane surface.

3.3.1 Camera Calibration & Measurement Uncertainty

Incoming radiation to the focal plane array (FPA) is digitised by a 16-bit ADC into a raw count value $R(x,t)$ between 0 and 65356. This raw count data is approximately linear with the incident radiation. The equation for each pixel can be written as:

$$q_{\text{cam}}(x,t) = a \cdot R(x,t) + b$$

where q_{cam} is the incident radiative heat flux on the pixel, and the constants a and b are the calibration factors to be determined by performing a black body calibration. Factory calibration provides default values for a and b and quote an accuracy of $\pm 1\,^{\circ}\text{C}$ or $\pm 1\%$ over the range $-20\,^{\circ}\text{C}$ to $350\,^{\circ}\text{C}$ [150].

To improve on this, the camera was recalibrated in-situ prior to running the experiments. A black body calibrator was placed in front of the camera such that the whole field of view of the camera was occupied by the calibrator. The calibrator stepped through a range of surface temperatures (10-40 °C) and the count values for the entire FPA was recorded. At each set temperature, 100 frames were collected and averaged to obtain the mean count value. This is then used to build the quartic curve above for each pixel, relating the black body temperature to the raw count value.

The calibration curve for a single pixel is shown in Fig. 3.7.

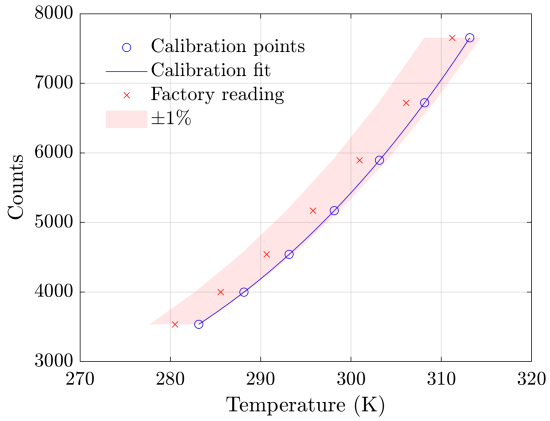


Figure 3.7: Black body calibration curve for a single pixel (blue) of the FLIR X6900sc infra-red camera, with factory default calibration shown (red) and quoted 1% accuracy band from its datasheet

The total incident radiation on the camera from a grey body can be written as:

$$q_{\text{cam}} = q_{\text{body}} + q_{\text{reflected}} + q_{\text{atm}}$$

$$T_{\text{cam}}^4 = \tau\varepsilon T_{\text{body}}^4 + \tau\left(1-\varepsilon\right) T_{\text{reflected}}^4 + \left(1-\tau\right) T_{\text{atm}}^4$$

where ε is the emissivity of the target grey body and τ is the transmittance of the optics or surrounding medium. The test article was sprayed matte black, as shown in Fig. 3.8, to increase its emissivity and this was assumed to be $\varepsilon = 0.95$ [151]. Furthermore, it was assumed that the reflected radiation from the target body and the emitted radiation from the surrounding fluid medium are negligible compared to that from the target grey body.

In Kirollos and Povey [151], the reflected and ambient radiation terms are grouped into a single term for surrounding radiance, q^*. They provide a methodology for calibrating $\tau\varepsilon$ and q^*, however this requires in-situ monitoring during each run by instrumenting another vane with thermocouples and placing it adjacent to the target body so that it is also within camera's field of view. This was not possible due to time constraints and the methodology does not allow for retrospective calculation. However, it is postulated that a relation may be drawn between the freestream temperature and the surrounding radiance term, q^*, assuming experimental setup remains the same, i.e. view angle and all reflective surfaces remain the same. Given this

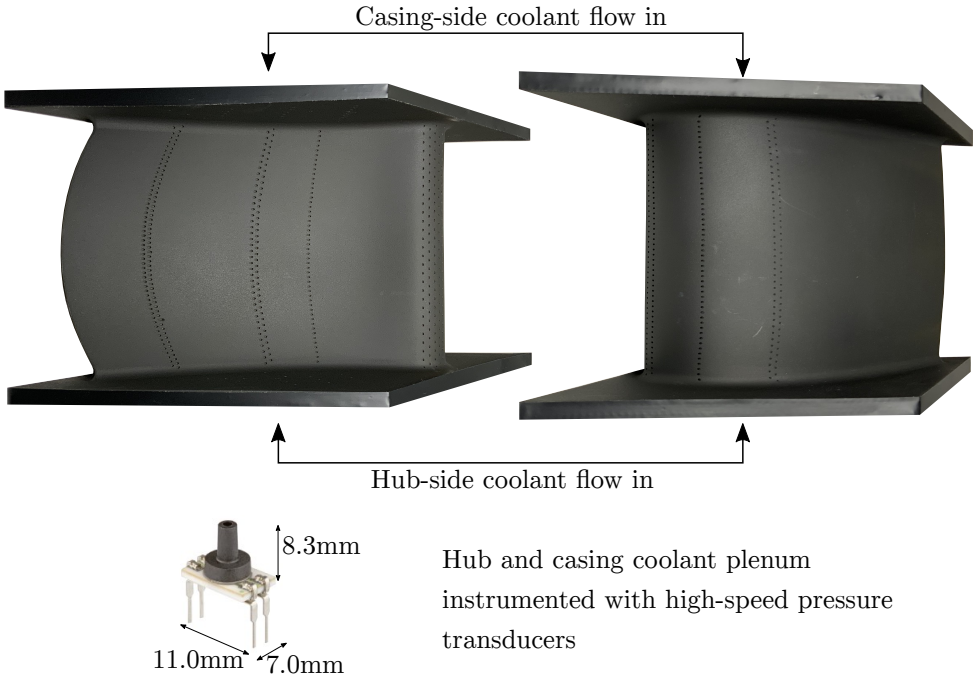


Figure 3.8: Film-cooled vanes with matte black paint coat for IR thermography. High-speed pressure transducers were placed in the coolant supply plenums in the hub and casing to measure pressure fluctuations

relation, and past recordings of freestream temperature, it would then be possible to retrospectively calculate the contribution of q^* for a previous run.

The black body calibration was performed in-situ and at roughly the same view angle and distance-to-target as the test article would be to account for some of this surrounding radiance, and any spatial variations in emissivity due to steep view angles. As shown in Fig. 3.7, the difference in absolute temperature can be as much as 2 K, although it is not known how much of this is due to the q^* term, and how much is due to a drift in calibration from when the camera was last factory calibrated. Kirollos and Povey [151] quote, for their setup, that the q^* term can account for up to 13-15% of the total incoming radiance, which gave them an absolute temperature difference of ± 1 K. O'Dowd [152] argues that the variation in viewing angle result in a maximum temperature difference of ± 1 K. Depending on the driving temperature model chosen (see §3.3.3.1), it may also be necessary to use information from K-type thermocouples placed in the freestream and coolant plenums, which have a quoted accuracy of ± 2.5 K (for Class 2 and 3). These uncertainties in temperature measurement will propagate through the post-processing methodology to feed into the

accuracy of derived quantities such as HTC, h, and adiabatic cooling effectiveness, η. Luque et al. [83] showed that the main contribution to the uncertainty in Nusselt number is the uncertainty in determining the thermal product of the material, $\sqrt{\rho ck}$. They estimated that a $\pm 3.54\%$ uncertainty in $\sqrt{\rho ck}$ gives $\pm 4.87\%$ uncertainty in Nu.

3.3.2 On the Use of the Semi-Infinite Assumption

Post-processing of IR data to obtain the surface heat flux, $q(0,t)$, follows the impulse response methodology of Oldfield[149]. In the case of an uncooled vane, a sufficiently thick substrate allows the use of semi-infinite assumption. The method involves the convolution of the body's impulse response, g_0, with the surface temperature:

$$q(0,t) = g_0(0,t) * T(0,t) \tag{3.2}$$

In the case of a film-cooled vane, the wall thickness is 3 mm, which calls the use of this assumption into question. For a 1D slab, Eqn. 3.2 is replaced with:

$$q(0,t) = g_0(0,t) * T(0,t) + g_L(0,t) * T(L,t) \tag{3.3}$$

where $g_0(0,t)$ and $g_L(0,t)$ are the body's impulse responses at $x = 0$ subject to boundary conditions at the top and bottom surfaces, $T(0,t)$ and $T(L,t)$ respectively. §4.6 performs a sensitivity analysis using Eqn. 3.3 and demonstrates that for this experimental setup, the semi-infinite assumption is valid.

To summarise §4.6, the influence of the internal boundary condition on the external wall heat flux was found to be negligible due to two factors. (1) The extremely low diffusivity of the wall reduces the rate at which heat from the internal wall propagates to the external wall. (2) The temperature of the coolant as it enters the coolant plenum is nearly equal to the initial isothermal temperature of the body and remains roughly constant across the duration of the run.

The converse of factor (1) is also true, i.e. heat propagates very slowly from the external wall to the internal wall, such that there was no detectable change in the coolant temperature. Since the temperature difference between the coolant tempera-

ture and the internal wall is small, the heat flux from the internal wall is also small. Heat flux on the external wall is therefore primarily a function of the external boundary condition.

A consequence of the impulse response method is the amplification of high frequencies: The impulse response $G''(x, j\omega)$ relating heat flux at a point, x, to a Dirichlet (temperature) boundary condition is given as (in the frequency domain):

$$G''(x, j\omega) = \sqrt{\rho c_p k} \cdot \sqrt{\omega} \cdot e^{-x\sqrt{\frac{\omega}{2\alpha}}} \cdot e^{-j\left(-x\sqrt{\frac{\omega}{2\alpha}} - \frac{\pi}{4}\right)}$$

where it can be seen that the magnitude, $\left|G''(x, j\omega)\right|$, scales with frequency, $\sqrt{\omega}$. Consequently, white noise which is characterised by having a flat power spectrum across all frequencies, will be amplified much more for higher frequencies. To avoid this, the signal is low-pass filtered to the frequency range of interest, 0 - 100 Hz.

3.3.3 Post-Processing Methodology

Given the wall heat flux, $q(t)$, and surface temperature, $T_w(t)$, the heat transfer coefficient, h, and adiabatic wall temperature, T_{ad}, can be calculated from the gradient and intercept respectively of the q-T_w graph, as shown in Fig. 3.9. Although the trace is shown for the entire duration of the run, only the data when the flow field is established and has reached a steady state, can be used for curve-fitting. This post-processing window is demarcated by the black dashed lines. The line of best-fit is calculated for the data in this window and the gradient and intercept can be extracted.

Determining when this steady state occurs (start of window) and the post-processing duration (window size) is not straightforward. Technically, this method only applies to periods of flow where the driving temperature is constant. This can be seen by

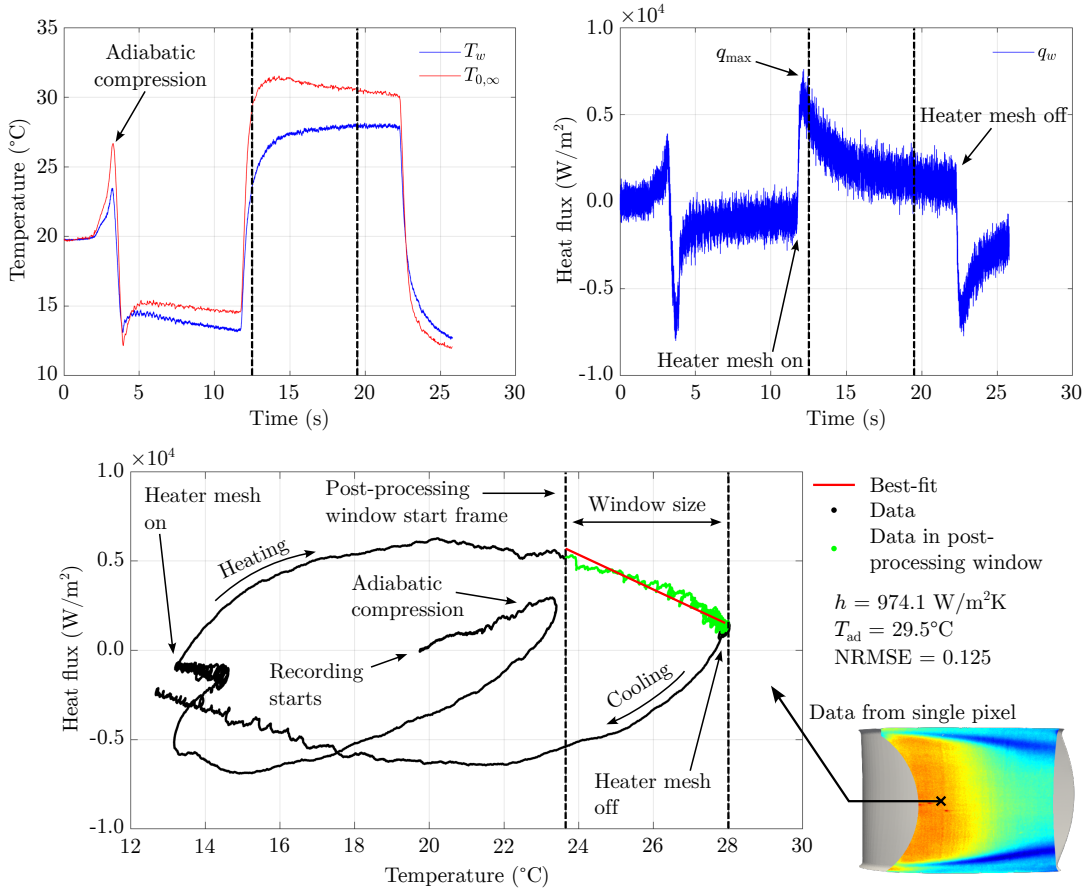


Figure 3.9: HTC post-processing methodology for a single pixel from an IR camera. Top left: Wall and freestream temperature traces over run duration. Top right: Wall heat flux over run duration. Maximum heat flux, $q_{\max}$, occurs shortly after heater mesh comes on. Bottom: Plot of q-T_w with salient features labelled. Data points within the post-processing window is coloured green. Best-fit line from linear regression of data points in post-processing window is shown in red. Start and end frames of post-processing window demarcated with black dashed lines

taking the partial derivative of Newton's Law of Cooling:

$$q = h\left(T_{\text{ad}} - T_w\right) \tag{3.4}$$

$$\left.\frac{\partial q}{\partial T_w}\right|_{T_{\text{ad}}} = -h \tag{3.5}$$

Ideally, a perfect step rise in freestream temperature permits the use of this method. However, expansion of air in the supply tanks causes adiabatic cooling which results in a falling temperature over the duration of the run. The amount of cooling and subsequent heat pickup as it flows through the pipes depend on the tank pressure and ambient temperature when the run is carried out. This presents three considerations for the user when post-processing an IR dataset:

1. Deciding how to model the driving temperature

2. Deciding the starting frame of the post-processing window

3. Deciding the duration of the post-processing window

3.3.3.1 Determining the Driving Temperature

The driving temperature, T_{ad}, will differ at each point on the vane surface and will depend on whether the vane is film-cooled or not. If the vane is uncooled, then the driving temperature is the recovery temperature, T_r, which is related to the freeestream total temperature by a Mach number-dependent factor:

$$T_r = T_{0,\infty} \frac{1 + r\frac{\gamma-1}{2}\mathrm{M}^2}{1 + \frac{\gamma-1}{2}\mathrm{M}^2} \tag{3.6}$$

where r is the recovery factor with values $r = \mathrm{Pr}^{1/2}$ and $r = \mathrm{Pr}^{1/3}$ for laminar and turbulent boundary layers respectively [53]. If the vane is film-cooled, then the driving temperature will be somewhere between the coolant and freestream temperatures.

We therefore seek a way of evaluating h which allows for variations in T_{ad} over time. The following models were derived for uncooled and cooled cases and are presented here as linear functions in the form, $q(t) = mT_w(t) + c$, with the coefficients to be calculated by linear regression:

1. Model 1 is the most basic and requires that T_{ad} remains constant since it forms the y-intercept.

$$q(t) = -hT_w(t) + hT_{\text{ad}} \tag{3.7}$$

2. Model 2 assumes that the driving temperature is the recovery temperature which is related to the freestream temperature by a constant factor, a; see Eqn. 3.6.

$$\begin{aligned} T_{\text{ad}}(t) &= aT_{0,\infty}(t) \\ \frac{q(t)}{T_{0,\infty}(t)} &= -h\frac{T_w(t)}{T_{0,\infty}(t)} + ha \end{aligned} \tag{3.8}$$

3. Model 3 assumes that the driving temperature is related to the freestream and coolant temperatures by a mixing fraction, a.

$$\begin{aligned} T_{\text{ad}}(t) &= aT_{0,\infty}(t) + (1-a)T_{0,c}(t) \\ \frac{q(t)}{T_{0,\infty}(t) - T_{0,c}(t)} &= -h\frac{T_w(t) - T_{0,c}(t)}{T_{0,\infty}(t) - T_{0,c}(t)} + ha \end{aligned} \tag{3.9}$$

4. Model 4 extends Model 3 by accounting for the different specific heat capacities of air and CO_2, denoted as $c_{p,\infty}$ and $c_{p,c}$ respectively. This can be thought of as the conservation of enthalpy between two mixing streams. This model has to be solved iteratively since the specific heat capacity of the mixture, $c_{p,\text{mix}}$, depends on the mixing fraction, a.

$$\begin{aligned} c_{p,\text{mix}}T_{\text{ad}}(t) &= ac_{p,\infty}T_{0,\infty}(t) + (1-a)c_{p,c}T_{0,c}(t) \\ c_{p,\text{mix}} &= ac_{p,\infty} + (1-a)c_{p,c} \\ \frac{q(t)}{\frac{c_{p,\infty}}{c_{p,\text{mix}}}T_{0,\infty}(t) - \frac{c_{p,c}}{c_{p,\text{mix}}}T_{0,c}(t)} &= -h\frac{T_w(t) - \frac{c_{p,c}}{c_{p,\text{mix}}}T_{0,c}(t)}{\frac{c_{p,\infty}}{c_{p,\text{mix}}}T_{0,\infty}(t) - \frac{c_{p,c}}{c_{p,\text{mix}}}T_{0,c}(t)} + ha \end{aligned} \tag{3.10}$$

Model 2 is used for experiments without film-cooling. Tests with Models 3 and 4 return numerically similar results but the latter is computationally more intensive and prone to instability. Consequently Model 3 is used to post-process experiments with film-cooling.

We might argue that if the chosen model is correct, then the predicted value of h by said model must be invariant to the choice of window start frame and window size. That is to say, the quantities $\partial h/\partial t_{\text{start}}$ and $\partial h/\partial \Delta t$ must be zero, where t_{start} and Δt are the window start frame and window size respectively. This does not appear to be the case for any of the models - all models show some non-zero variation of h with t_{start} and Δt. Instead, the relative performance of each model in predicting a constant value of h is evaluated by comparing the normalised root mean square error (NRMSE) of the linear regression.

Fig. 3.10 shows the consequence of assuming a constant driving temperature (Model 1). The same window size and start frame was used between comparisons

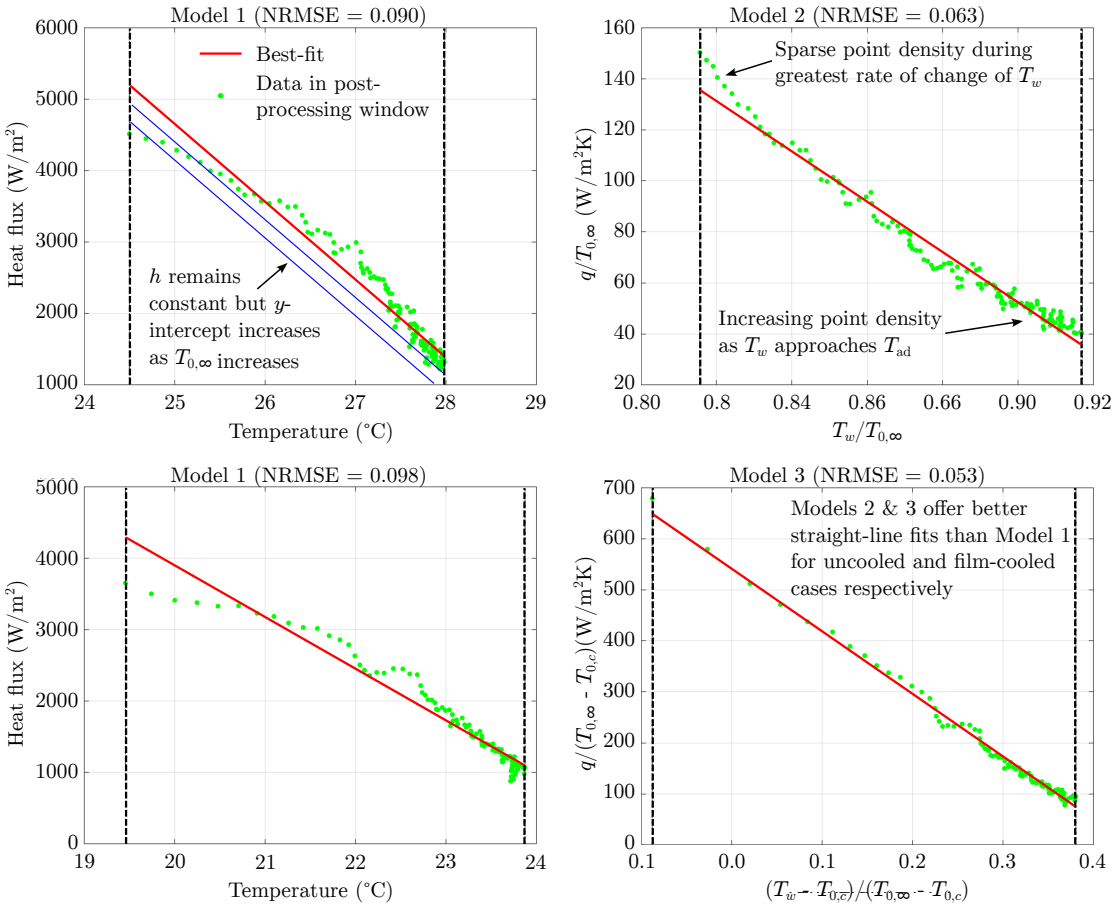


Figure 3.10: Comparison of NRMSE for different HTC regression models in uncooled (top) and film-cooled (bottom) experiments. Models 1 and 2 used for an experiment with no film cooling. Models 1 and 3 for an experiment with film cooling. Moving average smoothing applied to emphasise curvature of data points and deviation from best-fit line. The same window start frame and size was used. Model 1 shows greater deviation from best-fit line due to a rising freestream temperature. Models 2 and 3 allow for this and therefore result in less deviation as $T_{0,\infty}$ increases

of models. Note that the scales of each model are different, which is why their root mean square errors are *normalised* by their respective means. If the aerodynamic field is steady, then h must be constant. As the freestream temperature increases, so does the driving temperature. These two statements mean that the gradient of the fit, h, remains constant, but the y-intercept is increasing as $T_{0,\infty}$ increases. This effect is more drastic in Model 1 than in Models 2 and 3. The latter two reduce this effect by allowing the driving temperature to vary with time, so they have lower NRMSE values than Model 1.

3.3.3.2 Determining Window Start Frame and Window Size

Fig. 3.9 showed that heat flux peaks at $q_{\max}$ when the heater mesh is switched on, since at this point the temperature difference between the freestream and wall is the greatest. Over time, this difference decreases as wall temperature increases and the freestream temperature decreases. When the temperature difference tends towards zero, i.e. the wall temperature approaches the adiabatic wall temperature, then q tends to zero. Thus the plot of q-T_w shows the greatest rate of change in q and T_w when the heater mesh is switched on and the lowest rate of range as $T_w \to T_{\text{ad}}$.

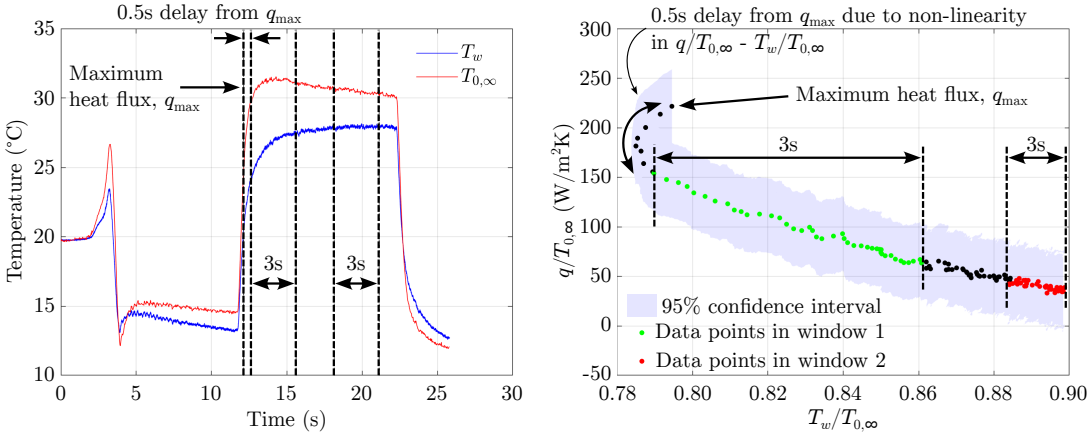


Figure 3.11: Effect of varying the post-processing window start frame and window size. Left: Wall and freestream temperature traces over run duration, showing locations of peak heat flux and two post-processing windows of 3 s duration. Right: Plot of $q/T_{0,\infty}$-$T_w/T_{0,\infty}$ (Model 2 used) when the heater mesh is on. Corresponding window sizes shown with black dashed lines

This is reflected in the distribution of data points in Fig. 3.11, where it can be seen that the number of data points in region near $q_{\max}$ is sparse, with increasing data point density over time. Therefore, for the same window size, the linear regression spans a greater range of T_w (or $T_w/T_{0,\infty}$ in the case of Model 2) near to $q_{\max}$ and a smaller range closer to T_{ad} since there is nearly no variation in q and T_w in that region. Both window sizes in Fig. 3.11 are 3 s, with one starting near $q_{\max}$ and another starting after a 2.5 s delay from $q_{\max}$. This might suggest that the point $q_{\max}$ can be used as the start of the post-processing window and that delaying the window will result in higher uncertainty on h and T_{ad} as the data points becomes more uncorrelated. Fig. 3.12 shows the consequence of delaying the post-processing window from $q_{\max}$.

Consider first the plot for a 3 s window (blue line). Delaying this window decreases

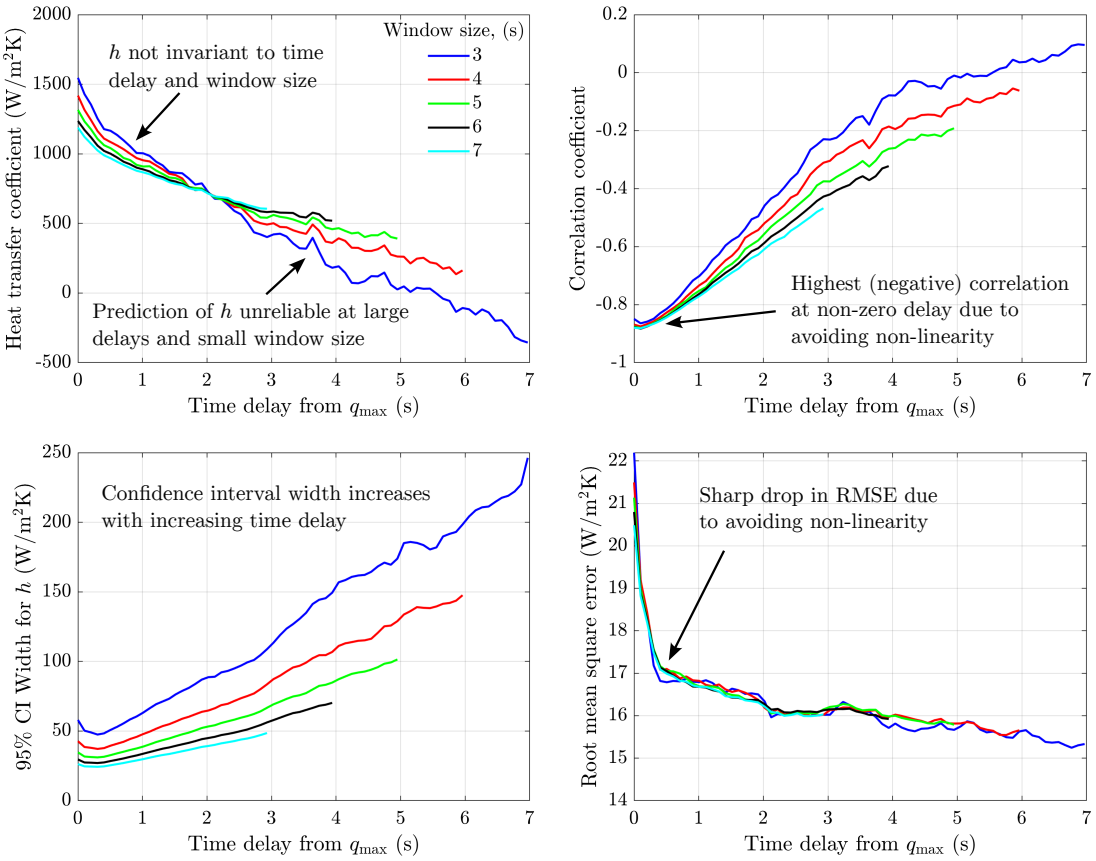


Figure 3.12: Metrics for determining the post-processing window start frame and window size. Plots of h (top left), correlation coefficient (top right), 95% confidence interval of the linear regression (bottom left), and its RSME (bottom right) as a function of time delay from $q_{\max}$ for different window sizes. Data was obtained from a single run without film cooling and Model 2 was used during post-processing

the (absolute) correlation coefficient until it is zero, which means that q is not correlated to any change in T_w, so the gradient is meaningless since a straight line can be drawn at any gradient and still have the same RMSE value. The width of the confidence interval also increases with increasing delay since it is inversely proportional to the width of the regressor ($^{T_w}/_{T_{0,\infty}}$ for Model 2).

However, this does not mean that using $q_{\max}$ as the start frame is suitable, since this is the greatest rate of change of T_{ad}. Fig. 3.11 shows some non-linearity that is greatest near $q_{\max}$, which necessitates a time delay to avoid this. This is why the RMSE is highest at zero delay, while the correlation coefficient and 95% confidence intervals show a minima at some non-zero delay from $q_{\max}$. The plot of RMSE (bottom right graph of Fig. 3.12) displays a sharp initial drop up to 0.5 s and then a more

shallow linear decrease. The time delay at this sharp change in gradient coincides roughly with the minima of the correlation coefficient and confidence interval. So any of these salient features can be used to set the window start frame, hence the delay shown in Fig. 3.11.

It can also be seen that increasing the window size increases the (absolute) correlation and reduces the confidence interval width. A longer post-processing window is preferred, but this is more computationally intensive, especially so when using the FLIR X6900sc which has a very high frame rate and resolution. A window size of 5 s was used throughout the entire campaign when post-processing all IR data sets.

3.3.3.3 Decomposing Mean and Fluctuations

The curve fitting method of q-T described above gives mean values for $\overline{h}$ and $\overline{T}_{\mathrm{ad}}$. Instantaneous heat transfer into the vane surface is governed by this mean and instantaneous changes to the boundary layer and fluid temperature. The former results in fluctuations in HTC, denoted as h', and the latter results in fluctuations in the adiabatic wall temperature, denoted as T'_{ad}. The instantaneous heat flux can then be decomposed as:

$$\begin{aligned} q\left(t\right) &= \left(\overline{h} + h'\left(t\right)\right)\left(\overline{T}_{\mathrm{ad}} + T'_{\mathrm{ad}}\left(t\right) - T_w\left(t\right)\right) \\ &= \overline{h}\left(\overline{T}_{\mathrm{ad}} - T_w\left(t\right)\right) + h'\left(t\right)\left(\overline{T}_{\mathrm{ad}} - T_w\left(t\right)\right) + \left(\overline{h} + h'\left(t\right)\right) T'_{\mathrm{ad}}\left(t\right) \\ \Rightarrow q'\left(t\right) &= \left(\overline{T}_{\mathrm{ad}} - T_w\left(t\right)\right) h'\left(t\right) + \overline{h} T'_{\mathrm{ad}}\left(t\right) + h'\left(t\right) T'_{\mathrm{ad}}\left(t\right) \end{aligned} \tag{3.11}$$

which shows that fluctuations in heat flux comprise of an unsteady component that scales with pseudo-steady temperature difference, an unsteady component that is independent of the temperature difference, and a cross term.

Further decomposition is not possible without some kind of model for h' or T'_{ad}. The simplest model is to assume that either one of them is zero, which gives:

$$T'_{\mathrm{ad}}\left(t\right) = 0 \Rightarrow h'\left(t\right) = \frac{q'\left(t\right)}{\overline{T}_{\mathrm{ad}} - T_w\left(t\right)} \qquad , \qquad h'\left(t\right) = 0 \Rightarrow T'_{\mathrm{ad}}\left(t\right) = \frac{q'\left(t\right)}{\overline{h}}$$

An example of a source of h' is the impingement and precession of the swirl core, which

alters the potential field around the vane and results in the formation of additional vortical structures. In a completely isothermal flow field, $T'_{\text{ad}} = 0$. An example of a source of T'_{ad} is the impingement of hot streaks onto the NGV and then its migration off the surface and into the rotor stage. Literature reviewed in §2.3.3 has shown that the presence of hot streaks cause significant spanwise temperature gradients, but do not alter the aerodynamic field, so $h' = 0$. Results of fluctuations in adiabatic cooling effectiveness, η', presented later in §7.3 have been calculated in this manner by assuming $h' = 0$.

While $q'(t)$ cannot decomposed further to get $h'(t)$ and $T'_{\text{ad}}(t)$, their relative contributions to $q'(t)$ can be estimated by studying their statistics. It is assumed that the fluctuating quantities are independent random variables, normally distributed about zero mean with their respective standard deviations, σ_q, σ_h, and $\sigma_{T_{\text{ad}}}$. Writing Eqn. 3.11 in terms of its variances,

$$\begin{aligned}
\sigma_q^2 &= \text{var}\left(h'\Delta T + \overline{h}T'_{\text{ad}} + h'T'_{\text{ad}}\right) \\
&= (\Delta T)^2 \sigma_h^2 + \overline{h}^2 \sigma_{T_{\text{ad}}}^2 + \text{var}\left(h'T'_{\text{ad}}\right) + \ldots \\
&\qquad 2\overline{h}\Delta T \cdot \text{cov}\left(h'T'_{\text{ad}}\right) + 2\Delta T \cdot \text{cov}\left(h'^2 T'_{\text{ad}}\right) + 2\overline{h} \cdot \text{cov}\left(h'T'^2_{\text{ad}}\right)
\end{aligned}$$

where var () and cov () denote the variance and covariance respectively. The covariance of two independent random variables is zero, so the fourth term is zero. Now expanding all variance and covariance terms:

$$\begin{aligned}
\sigma_q^2 = (\Delta T)^2 \sigma_h^2 + \overline{h}^2 \sigma_{T_{\text{ad}}}^2 + \left(\sigma_h^2 + \mu_h^2\right)\left(\sigma_{T_{\text{ad}}}^2 + \mu_{T_{\text{ad}}}^2\right) - \mu_h^2 \mu_{T_{\text{ad}}}^2 + \ldots \\
2\Delta T \cdot \left(\text{E}\left[h'^2 T'_{\text{ad}}\right] - \text{E}[h']\text{E}[h'T_{\text{ad}}]\right) + \ldots \\
2\overline{h} \cdot \left(\text{E}\left[h'T'^2_{\text{ad}}\right] - \text{E}[T_{\text{ad}}]\text{E}[h'T_{\text{ad}}]\right)
\end{aligned}$$

where $\text{E}[X]$ is the expectation of a random variable, X. Now applying Isserlis' theorem

to the expectations of odd-numbered moments, which gives zero for these terms:

$$\sigma_q^2 = (\Delta T)^2 \sigma_h^2 + \overline{h}^2 \sigma_{T_{\text{ad}}}^2 + \left(\sigma_h^2 + \mu_h^2\right)\left(\sigma_{T_{\text{ad}}}^2 + \mu_{T_{\text{ad}}}^2\right) - \mu_h^2 \mu_{T_{\text{ad}}}^2 + \ldots$$
$$2\Delta T \cdot \left(0 - \mu_h^2 \mu_{T_{\text{ad}}}\right) + 2\overline{h} \cdot \left(0 - \mu_h \mu_{T_{\text{ad}}}^2\right)$$

and recalling that the random variables have zero mean, this simplifies to:

$$\underbrace{\sigma_q^2}_{\text{y}} = \underbrace{(\Delta T)^2}_{\text{x}} \underbrace{\sigma_h^2}_{\text{m}} + \underbrace{\overline{h}^2 \sigma_{T_{\text{ad}}}^2 + \sigma_h^2 \sigma_{T_{\text{ad}}}^2}_{\text{c}} \tag{3.12}$$

which gives a straight line plot, as shown in Fig. 3.13. Eqn. 3.12 is similar to Eqn. 3.11 but written in terms of its variances, and is a statement of the relative contribution of the fluctuating h' and T'_{ad} fields. The former scales with the mean driving temperature difference, while the latter scales with the mean HTC. The equation also suggests that the contribution of the h' field varies over time, i.e. it is greatest when ΔT is highest when the heater mesh is just switched on and decreases over time as the wall temperature approaches the adiabatic wall temperature. The contribution of the T'_{ad} field remains constant throughout the experiment.

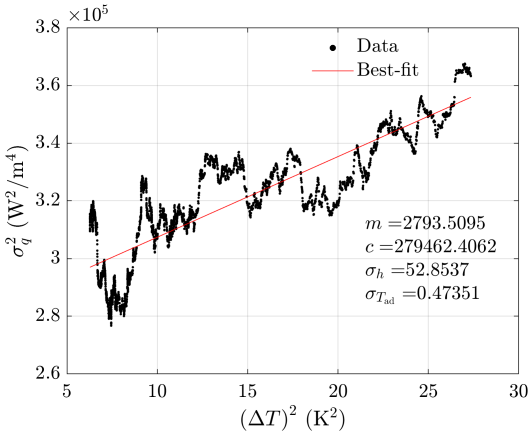


Figure 3.13: Linear regression to decompose statistics of fluctuations in heat flux into statistics of constituent components - fluctuations in aerodynamic field and fluctuations in thermal field

Data from a single pixel of from an IR run is post-processed to calculate σ_q^2 and $(\Delta T)^2$ and is plotted in Fig. 3.13. The best fit line gives an estimate for $\sigma_h = 52.9\,\text{W/m}^2\text{K}$ and $\sigma_{T_{\text{ad}}} = 0.47\,\text{K}$. The 95% confidence intervals of h' and T'_{ad} are calculated as $1.96\sigma_h = \pm 104\,\text{W/m}^2\text{K}$ and $1.96\sigma_{T_{\text{ad}}} = \pm 0.93\,\text{K}$ respectively (assuming

a normal distribution). Substituting these range of values into Eqn. 3.12 and assuming typical values of $\Delta T = 4\,\mathrm{K}$ and $\overline{h} = 1000\,\mathrm{W/m^2K}$, it can be seen that all three terms contribute to q', with the T'_{ad} term having the largest fluctuations $\left(470\,\mathrm{W/m^2}\right)$, followed by the h' term $\left(212\,\mathrm{W/m^2}\right)$, then the $h'T'_{\mathrm{ad}}$ term $\left(25\,\mathrm{W/m^2}\right)$.

As stated previously, decomposition of q' into time-resolved fluctuations of the h' and T'_{ad} fields is not possible without a model for either of them - the simplest being to set one of them to zero. This is not entirely accurate, since the calculation above has shown that these terms are non-zero. Setting one of them to zero will misattribute an observed fluctuation in q' to the other non-zero variable, which overestimates its magnitude of fluctuations. However, over time the wall temperature approaches the adiabatic wall temperature, resulting in a decreasing ΔT, and therefore decreasing contribution of the h' term to overall fluctuations in q. Thus the observed fluctuations will tend to be dominated by the T'_{ad} term, which lends confidence to use of the above assumption of $h' = 0$ in calculating η'.

3.4 Thin Film Gauges

The use of thin film gauges (TFGs) for measurements of heat transfer has a long history in the Oxford Thermofluids Institute, as a result of transient facilities like the Oxford Turbine Research Facility (OTRF) and many of its researchers. Reviews of their use are provided by [153, 154].

The initial manufacturing process of the gauges follows that of flexible PCB circuits. First, a mask is created to apply photoresist onto a polyimide copper-clad flexible laminate. The laminate can be clad on either one or both sides depending on the desired construction of the gauge circuitry. The copper is then etched off in a bath, leaving only the copper tracks and landing pads. Another layer of photoresist is applied, this time masking the entire circuit, leaving only the shape of the gauge uncovered. Platinum is sputtered over these locations and the excess is etched off, leaving only the previously uncovered regions now bonded to a layer of platinum in

the shape of the gauge.

The PCB manufacturing process is well established and the technologies are sufficiently mature such that quality checks by a commercial manufacturer guarantee the integrity of the copper tracks. This allows for copper track widths down to 100 µm and profiles with tolerances of ±50 µm are achievable. However such designs may be unreliable in practice due to the harsh environments these gauges are placed in. Damage to either the tracks or gauge may occur during installation or run time and will result in either excessively large resistances or a loss of connectivity, i.e. an open circuit. For example, bending of the circuit around very small bend radii may damage the tracks and small debris such as dust particles, metal dust, etc. may impinge on the platinum gauge element, damaging it.

3.4.1 Operating Principle

A thin film gauge functions in the same way as a positive temperature coefficient thermistor, whereby its resistance is highly dependent on its temperature. The gauge comprises of a very thin layer of platinum (250 nm) sputtered in an M-shape. Its thinness is necessary for the whole body to be able to respond rapidly to changes in temperature and to ensure that it heats up uniformly.

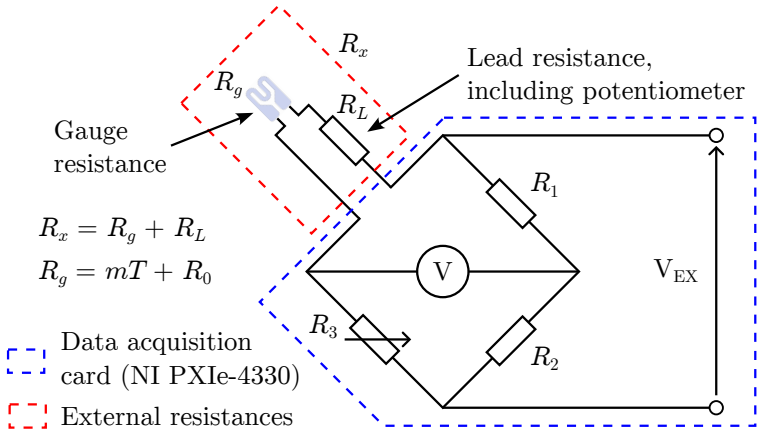


Figure 3.14: Circuit diagram of a Wheatstone bridge with one gauge connected in 1/4-bridge configuration

The change in resistance of the gauge is measured via a Wheatstone bridge as shown in Fig. 3.14. The state-of-the-art NI PXIe-4330 8-channel bridge input mod-

ule was used, which introduces minimal noise into the readings and allows for sampling rates up to 25 kHz. The gauge is connected in 1/4-bridge type 1 configuration, whereby only one leg of the Wheatstone bridge has a sensing element. The remaining resistors on the other three legs have fixed resistances - R_3 is only shown as a variable resistor to denote that it is a 1/4-bridge completion resistor, chosen to match the sensing element when the bridge is balanced; it is fixed for this experimental setup.

The gauge, with resistance R_g, is connected in series to a potentiometer, whose resistance is captured by R_L, which also includes the lead resistance, contact resistances, etc. The potentiometer allows the bridge to be balanced to avoid saturation as some gauges have very high or very low nominal resistances; a consequence of manufacturing variance and assembly and handling damage. Note that the balance does not need to be exactly zero. Indeed, changes to the ambient temperature will contribute to imbalance in the bridge output so the gauge is technically in a constant state of strain.

The bridge output is given by r, the ratio of the voltage across the bridge to the excitation voltage. This can be written as:

$$r = \frac{V}{V_{\text{EX}}} = \frac{R_3}{R_3 + R_x} - \frac{R_2}{R_1 + R_2} \qquad \text{where} \quad R_x = R_L + mT + R_0 \tag{3.13}$$

In this case, the 1/2-bridge completion resistors are equal and R_3 is set through the data acquisition software to be 120 Ω. The constant, m, is the gain of resistance with temperature and R_0 is the nominal resistance of the gauge. These are obtained from the calibration curves for each gauge. Rearranging the equation above for temperature gives:

$$T = \frac{1}{m}\left(\frac{1-2r}{1+2r}R_3 - R_L - R_0\right) \tag{3.14}$$

Prior to each run, the test article is allowed to cool to isothermal conditions so that its surface temperature stabilises to a constant value. This is assumed to be the temperature of the surrounding fluid as measured by a thermocouple placed in the

freestream, and denoted as T_{init}. Substituting this into the equation above gives:

$$R_L = \left.\frac{1-2r}{1+2r}\right|_{\text{init}} \cdot R_3 - mT_{\text{init}} - R_0 \tag{3.15}$$

The first 1 s of r and T_{init} values are averaged to calculate R_L. This procedure must be carried out using exactly the same setup as the experimental campaign and must not be varied between runs, i.e. same cables, connectors, and potentiometer settings.

3.4.2 Gauge Calibration & Measurement Uncertainty

The gauges are calibrated after assembly onto the vane by thermally soaking the whole test article in a temperature controlled environment at set temperatures. It is left at a fixed temperature for an hour to become isothermal; this is checked with thermocouples placed around the test article. Once it has become isothermal, the resistances of all gauges are recorded. This gives a linear temperature-resistance graph for each gauge.

A typical gradient is $0.15\,\Omega\,^{\circ}\text{C}^{-1}$. This corresponds to a rise in $1.5\,\Omega$ for every $10\,^{\circ}\text{C}$ rise in temperature, making the temperature predictions very sensitive to absolute values of resistance. Each gauge has a nominal resistance of $80\,\Omega$ at room temperature, which is governed by its material and geometric properties. The resistance of an ideal resistor can be written as:

$$\begin{aligned} R &= \frac{\rho l}{A} \\ &= \frac{l}{A} \cdot \rho_0 \left(1 + \alpha \left(T - T_0\right)\right) \\ &= \frac{\rho_0 \alpha l}{A} \cdot T + \left(\frac{\rho_0 l}{A} - \frac{\rho_0 \alpha l}{A} \cdot T_0\right) \end{aligned}$$

where ρ is the resistivity of the material, α is the coefficient of resistivity, and l and A are the length and cross-sectional area respectively. Thus it can be seen that to improve the response of gauge, the aspect ratio, l/A, of the gauge can be increased, or a different material with higher resistivity and coefficient of resistivity can be used. The former method was attempted by Shaikh [132] who designed a gauge with a very

narrow profile and multiple twists. The overall footprint of the gauge was kept the same. Some success was achieved with the gauge but it was found to be too unreliable for multiple tests due to the narrow profile being extremely susceptible to damage. In this study, the typical M-profile gauge is used for its robustness.

The high sensitivity of the sensor's reported temperature to changes in resistance requires a data acquisition system (DAQ) of sufficiently high resolution to digitise voltage changes in the sub-millivolt range. Eqn. 3.14 shows that a change in temperature of 0.5 °C results in a change in voltage on the order of 0.1 mV, assuming an excitation voltage of 1 V and a measured voltage ratio of 1 mV. The DAQ card has a 24-bit analogue-to-digital converter (ADC), allowing for resolutions down to 59 nV. The noise introduced during ADC conversion must also be lower than the signal being measured. The quoted accuracy of the DAQ card is ±24 µV, assuming a 1 mV reading with 1 V excitation voltage, sampling rate of 20 kHz, and no smoothing applied. This translates to an accuracy in temperature determination of ±0.08 °C. Another source of uncertainty is in determining R_L, which requires the use of a K-type thermocouple, which has an accuracy of ±2.5 °C (Class 2 and 3). Additionally, the impulse response of the gauge depends on the material properties of the polyimide strip. Piccini et al. [155] reported an uncertainty of 4.2% in the measured thermal product of polyimide. These known uncertainties can be propagated to calculate the overall uncertainty in h and η.

3.4.3 Gauge Construction

A number of possible designs were considered to increase the reliability and robustness of the thin film gauge circuit. For example, to protect exposed copper tracks and gauges from damage caused by foreign object impact, a layer of coverlay can be applied over the whole circuit. However, this decreases the frequency response of the gauge, which prevents its use for measurements of high frequency unsteady phenomena. Assuming a semi-infinite coverlay body with thermal diffusivity, α, subject to a time-varying temperature boundary condition with oscillating frequency, ω, the

temperature response, $G'(x, j\omega)$, at some depth, x, is given by:

$$G'(x, j\omega) = e^{-x\sqrt{\frac{\omega}{2\alpha}}} \cdot e^{-jx\sqrt{\frac{\omega}{2\alpha}}}$$

which shows attenuation and phase lag for non-zero x. Typical material properties for coverlay are: $\alpha = 8.17\text{E}{-8}\,\mathrm{m^2\,s^{-1}}$ and $k = 0.12\,\mathrm{W\,m^{-1}\,K}$. At a depth of 26 µm (one of the thinnest coverlays available), a 100 Hz fluctuation is attenuated by a factor of approx. 5, which corresponds to −14 dB. This is unacceptable for this study which is concerned with unsteadiness so coverlay was not used.

PCB manufacturing technologies also allow for a circuit to be built up in layers, offering additional complexity to the gauge design and protection of copper tracks by burying them between layers. Fig. 3.15 shows the cross section of the double-sided gauge configuration used in this study.

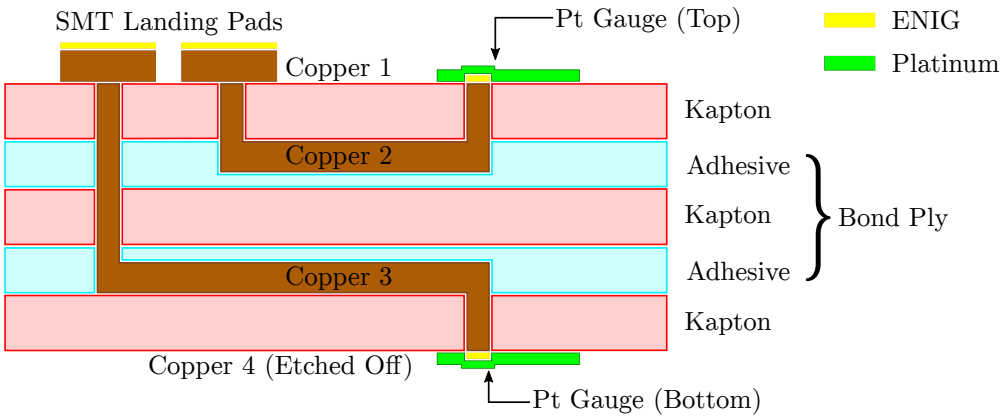


Figure 3.15: Cross-section of double-sided thin film gauge used in this study

The use of double-sided gauges avoids the need for the semi-infinite 1D assumption that is used in single-sided gauges [149] at the cost of halving the channel count. For the vane shown in Fig. 3.16, a total of 160 gauges are present in double-sided configuration, effectively giving 80 pairs of gauges, with 10 pairs per circuit strip. Each circuit strip is placed just downstream of a row of cooling holes. A depression in the surface was added into the CAD model of the NGV, which was then 3D printed at very high resolution. This surface depression houses the circuit strips and prevent them from protruding into the flow since this may cause jet impingement onto the

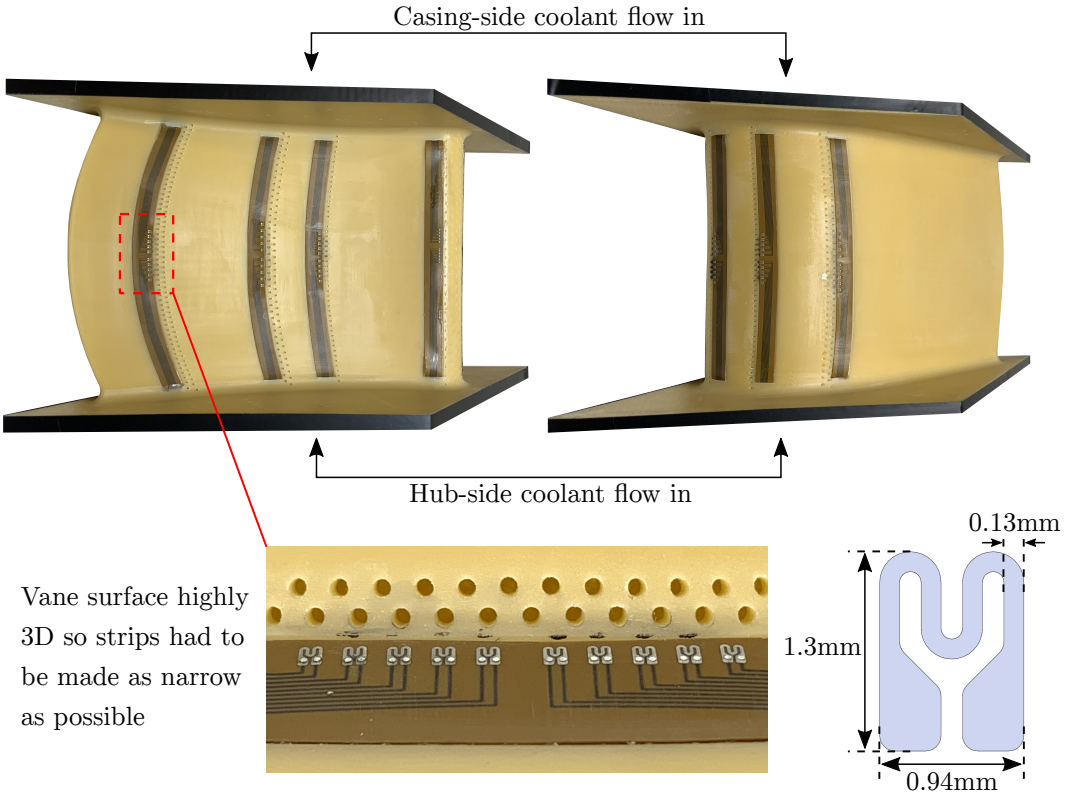


Figure 3.16: Film-cooled vane instrumented with double-sided thin film gauges

edge of the strip and local recirculation and high HTC. The thickness of the circuit can be estimated during construction and the depression is then sized accordingly. The data acquisition equipment available allows for simultaneous recording of 96 channels in quarter-bridge configuration.

3.4.4 Post-Processing Methodology

Heat flux can be calculated from the gauge readings by solving the 1D heat equation numerically with the temperatures applied as boundary conditions. The Crank-Nicolson method is one such solver that is unconditionally stable and relatively fast due to solution of a tridiagonal problem. However, to accurately calculate heat flux, gradients must be well captured, which necessitates a fine computational mesh. The entire length of data must also be simulated to achieve the correct temperature distribution within the body. The duration of each run was 40 s and the sampling rate was 20 kHz, thus requiring 800000 timesteps to be simulated. This must then be carried out for all 80 pairs of gauges, for all 38 runs. Consequently numerical schemes were

not used due to the excessive computational time required.

Oldfield describes an impulse response method for post-processing temperature measured using double-sided gauges to surface heat flux [149]. The substrate is treated as a 1D slab comprising only of a single material (polyimide) and the impulse response is calculated from its analytical solutions. The method used in this study extends this impulse response method to multi-layered substrates such as that shown in Fig. 3.15 above. Two approaches are proposed for obtaining the impulse response. The first is the numerical deconvolution of known analytical solutions to N-layered substrates. The second is the numerical differentiation of the numerical solution to an imposed Heavyside step boundary condition. These approaches are described in more detail in §4.4.1 and §4.4.2 respectively.

Once the impulse responses have been obtained, heat flux is calculated with Eqn. 3.3 using a fast convolution operation. Unlike numerical schemes, this method is many orders of magnitude faster since it does not involve solving a system of equations. The remaining post-processing steps are similar to those used for IR datasets as detailed in §3.3.3, whereby the relevant driving temperature model is chosen, the window start time is determined and linear regression carried out to calculate h, h', T_{ad}, and T'_{ad}.

3.5 High-Speed Pressure Transducers

A vane instrumented with high-speed pressure transducers was fabricated by Shaikh [132] and was used in this study to measure unsteady pressure fluctuations on the vane surface. A total of 48 Honeywell NBP pressure transducers were placed evenly around the vane to obtain good resolution. The sensors were chosen for their low cost while still offering a flat spectral response over a large bandwidth and reasonable signal-to-noise ratio (SNR). Other alternatives such as Kulite sensors offer much higher bandwidths but are much more expensive by comparison.

The vane was fabricated in two parts via SLA and contains depressions on the internal surfaces where the transducers can be secured. Small narrow taps were

printed into the centres of each depression to expose the sensing element to the flow. The piezoresistive sensing element itself sits inside a housing that functions like a Helmholtz resonator, which determines the maximum frequency that can be sensed. However since it is not fully flush with the vane surface, the neck is longer due to the wall thickness, which reduces the actual maximum frequency. The resonant frequency of the cavity, f, is calculated as:

$$f = \frac{c}{2\pi}\sqrt{\frac{A}{VL}}$$

where c is the speed of sound, A is the area of the neck, V is the volume of the cavity, and L is the length of the neck.

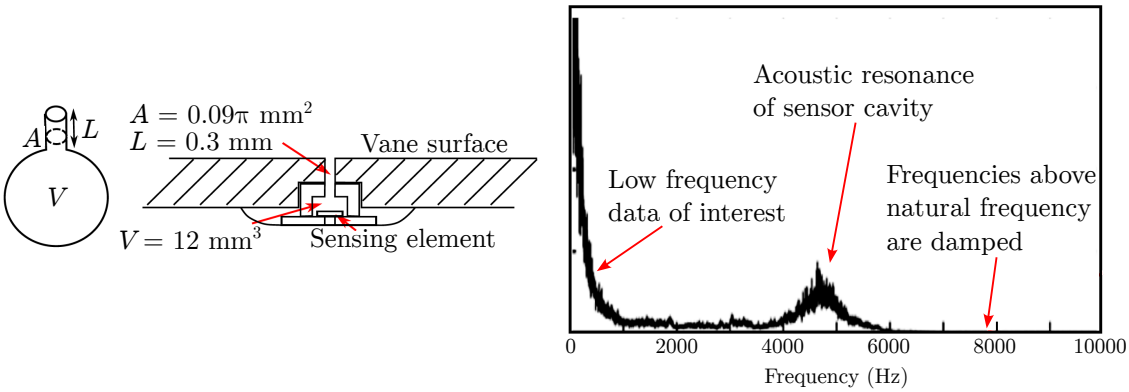


Figure 3.17: Cavity resonance of pressure transducer. Left: Schematic of sensor with internal volume, V, mounted in vane surface with neck area, A, and length, L. Right: Power spectral density of sensor reading showing the resonance peak. Adapted from Shaikh [132]

Fig. 3.17 provides values for the geometric quantities, A, V, and L for the chosen design. These give a natural frequency of 4800 Hz, which is sufficient bandwidth to look at unsteady phenomena due to upstream swirl. Fig. 3.17 also shows this resonant peak for a single sensor.

3.6 LES of Combustor-Turbine Interface

Large eddy simulations of the full combustor-turbine interface were carried out for the single-core swirler and 8-core swirler. Both the upstream combustor domain and the downstream NGV cascade domain must be included in the simulations to ensure that unsteady interactions between the coherent structures from the swirler and the

NGV are resolved and that information is allowed to propagate upstream due to any coupling mechanism that may exist. Fig. 3.18 shows the computational domain for both cases. The mesh for the single-core swirler was produced by Jacobi and Rosic [147]. The mesh for the 8-core swirler was produced by the author.

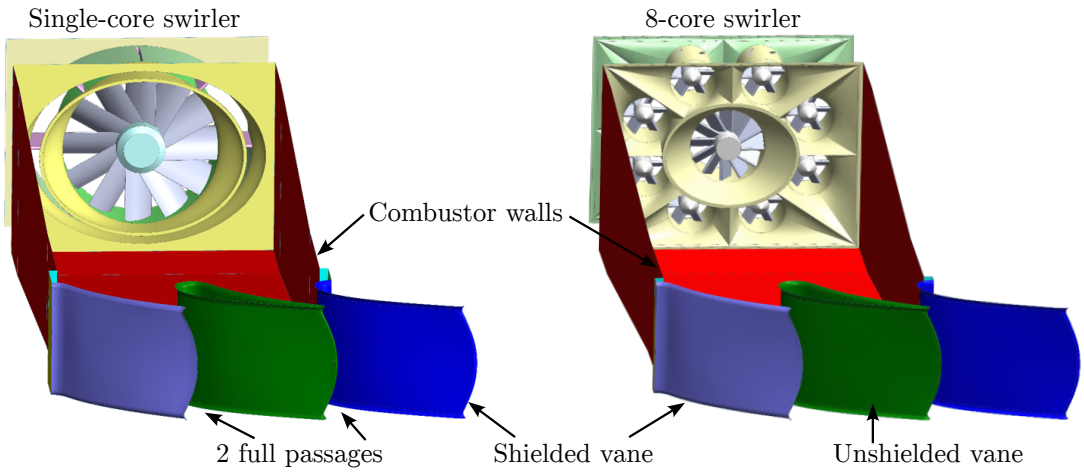


Figure 3.18: LES flow domains for the single-core and 8-core swirler geometries

3.6.1 Mesh Sizing

Initially Ansys Fluent, which is an unstructured solver, was used to obtain a precursor RANS simulation on a coarser mesh. Estimates of the necessary mesh size were made from this precursor RANS. Pope [156] recommends that a cell size of $x^+ = y^+ = z^+ = 1$ to fully resolve the boundary layer, however this metric does not say anything about the region of interest, which is the freestream. The purpose of this study is to study the interactions of large coherent structures with the vane. These structures arise as a result of the precessing swirl core, shedding from the recirculating zone(s), etc. Hence their length scales are larger than the boundary layer thickness. Furthermore, sizing the mesh to fully resolve the boundary layer will be prohibitive, especially for a structured mesh. Wall shear stress and heat flux can be calculated with wall functions, so accurate resolution of gradients near the wall is of secondary importance to fully resolving the freestream.

To determine an appropriate length scale for cells in the freestream, the Taylor microscale was used as it characterises the length scales at the end of the inertial

range and the start of the dissipation range. This gave a length scale of approximately 5E−4 m. The volume of the flow domain is approximately 3.45E−2 m^3, which gives a mesh size of approximately 276 million cells. If this is limited to the region of interest, i.e. the swirler, transition duct, and passages, then the volume is 2.43E−2 m^3, which gives a mesh size of approximately 195 million cells. This is somewhat close to the mesh sizes of the single-core and 8-core swirler domains. The former has 117 million cells and the latter has 150 million cells. An unstructured mesh of that size is difficult to generate and handle due to long read/write times. An attempt was made using Boxer, however the maximum size that could be generated on a workstation with 64 GB of RAM was 70 million before it failed. Solution times for an unstructured solver would also be excessively long. Consequently, the in-house structured solver, TBLOCK, was used instead.

3.6.2 TBLOCK Flow Solver

TBLOCK was initially written by John Denton as a finite volume 3D flow solver designed specifically for turbomachines. Many years of development have introduced new capabilities such as parallelisation across multiple cores, the addition of the one-equation Spalart-Allmaras model, LES, and DES. Thermal wall functions for calculating heat flux were also implemented by Mazzoni et al. [157]. The benefits of TBLOCK over other solvers are its robustness to cell quality and its speed, making it highly suited to a wide range of flows and geometries. Klostermeier [158] describes its implementation and capabilities in more detail.

Additional modifications were made by the author to build on its capabilities as a very fast solver, increase its run time on the cluster, and decrease the downtime spent on the cluster queue. These include remote real-time handling of the solver while it is running on the cluster, autosaves, etc. This allows the simulation to be restarted or interpolated onto a different mesh during run time without having to stop it. Simulation parameters such as LES models, thermal wall function models, timestepping, exporting, etc. can now be changed on-the-fly. Previously, any changes

to the solver settings required a resubmission of the job to the cluster. Now with the introduction of the 'long' partition in Oxford's HPC ARC-C clusters, nodes can now be reserved indefinitely, effectively allowing this simulation to run with infinite uptime.

As TBLOCK is a structured solver, a structured mesh was generated in ICEM. However, this poses additional complexities not faced with an unstructured mesher/solver. Unstructured solvers have automated partitioning of cells, such as ParMETIS, which try to achieve a balanced load distribution across all processors. In the case of TBLOCK, blocks are user-assigned to a processor, which forms part of the load balancing procedure. This would be feasible for a few blocks by manually calculating the the number of nodes in each block and heuristically assigning them to minimise imbalance. However the single-core swirler has 857 blocks and the 8-core swirler has 4276 blocks. Thus all blocks must have roughly similar dimensions to each other in the I, J, and K directions so that they can be assigned somewhat arbitrarily without overloading a single processor. This requirement is also partly due to the fact that TBLOCK, which was written in Fortran 77, uses static arrays not dynamic arrays, i.e. where array sizes are fixed at compile time. Conservative variables form the largest arrays, and are predefined by the largest I, J, K dimensions of all blocks present on a single processor. Thus, if a single block is much larger than the rest in the entire flow domain, then the size of arrays must scale with this block. This increases the amount of memory required and makes very inefficient use of it as most of the arrays will be sparse. It also slows down the rate of data transfer via the message passing interface (MPI) as a much larger array has to be sent and received.

The meshing process in an unstructured mesher is mostly automated, driven by algorithms such as the Octree algorithm to satisfy user-imposed constraints. A structured mesh is more labour intensive since every block has to be individually placed, associated to the geometry, and then sized. Furthermore, a structured mesh imposes constraints on the blocking topology since mesh lines must be conformal across blocks,

which can lead to over-refinement in some areas. Multiple blocks are required to wrap around a single body, such as a swirler vane. The 8-core swirler has many of these small bodies compared to the single-core swirler, hence requiring many more blocks. A conformal mesh requires this topology to be extruded across the whole domain and wrapped around the NGV. This is extremely difficult due to the number of blocks present.

To alleviate this requirement, a non-conformal mesh interface was added to TBLOCK and is parallelised with MPI. It should be noted that while a non-conformal interface patch type did previously exist, it was only implemented for a one-to-one patch association, i.e. where one block face is non-conformal with another block face. This was intended for mesh coarsening or refinement across blocks. The newly added interface removes this restriction and allows a many-to-many patch association, where any block face can share an interface with any number of other block faces.

Information transfer across the interface takes place as follows. Blocks with a non-conformal interface will first identify all blocks on the opposite side of the interface and broadcast its node coordinates to them, while also receiving node coordinates from them. These broadcasts, send, and receive commands take place via MPI. Every node now has access to all nodes on the opposing side of the interface. The distance between the current node and all nodes on the opposing side is calculated. The n-nearest neighbours are identified, where n is a user-specified value up to 6. Since this is a static mesh, the neighbours of each node is fixed. Once they have been identified, their indices are stored so that they do not need to be searched for again. This searching algorithm takes place prior to the main solver running and speeds up the transfer of data across the non-conformal interface. The weights associated with each neighbour, w_i, is based on their radial distance, d_i, and must satisfy the following conditions:

$$\sum_i w_i = 1 \qquad d_i \to 0 \Rightarrow w_i \to 1 \qquad d_i \to \infty \Rightarrow w_i \to 0$$

and the appropriate weights can be derived by considering the average value of some scalar field, ϕ:

$$\overline{\phi} = \frac{\sum_i \frac{1}{d_i} \cdot \phi_i}{\sum_i \frac{1}{d_i}}$$
$$\Rightarrow w_i = \frac{1}{d_i \sum_j \frac{1}{d_j}}$$

During run time, conservative variables at the interface are transferred across via MPI send and receive commands and then weighted and summed. The node value is then the average of this transferred value and the original node value.

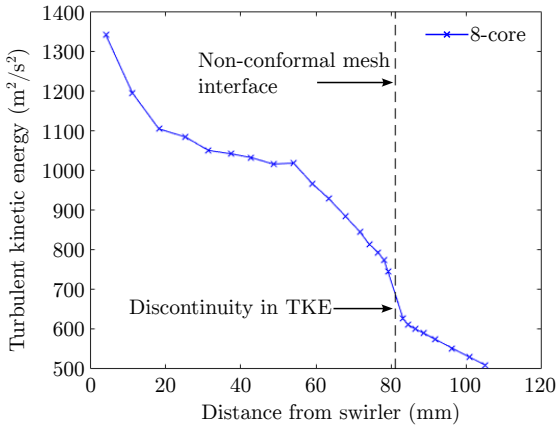


Figure 3.19: Resolved turbulent kinetic energy upstream and downstream of the non-conformal mesh interface. Interface location marked with black dashed line

The averaging procedure results in smoothing out of fluctuations, and the degree of smoothing depends on the number of neighbours chosen and is highly grid dependent. Obviously a perfect one-to-one correspondence means no averaging takes place and the interface behaves exactly like a normal periodic interface. Since the goal is to capture these turbulent fluctuations, this smoothing effect must be minimised. So only 2 nearest neighbours were chosen for averaging and the mesh density of the existing mesh was doubled from 150 million cells to 340 million cells. The effect of this averaging on resolved turbulent kinetic energy can be seen in Fig. 3.19.

Simulations were run with a 4 µs timestep (250kHz) to capture turbulent scales. Fig. 3.20 shows that the timestep is sufficient to resolve the inertial subrange of the energy cascade. The power spectral density (PSD) is calculated from fluctuations in

axial velocity taken at the transition duct (Point 1), the NGV inlet plane (Point 2), and in the vane passage (Point 3).

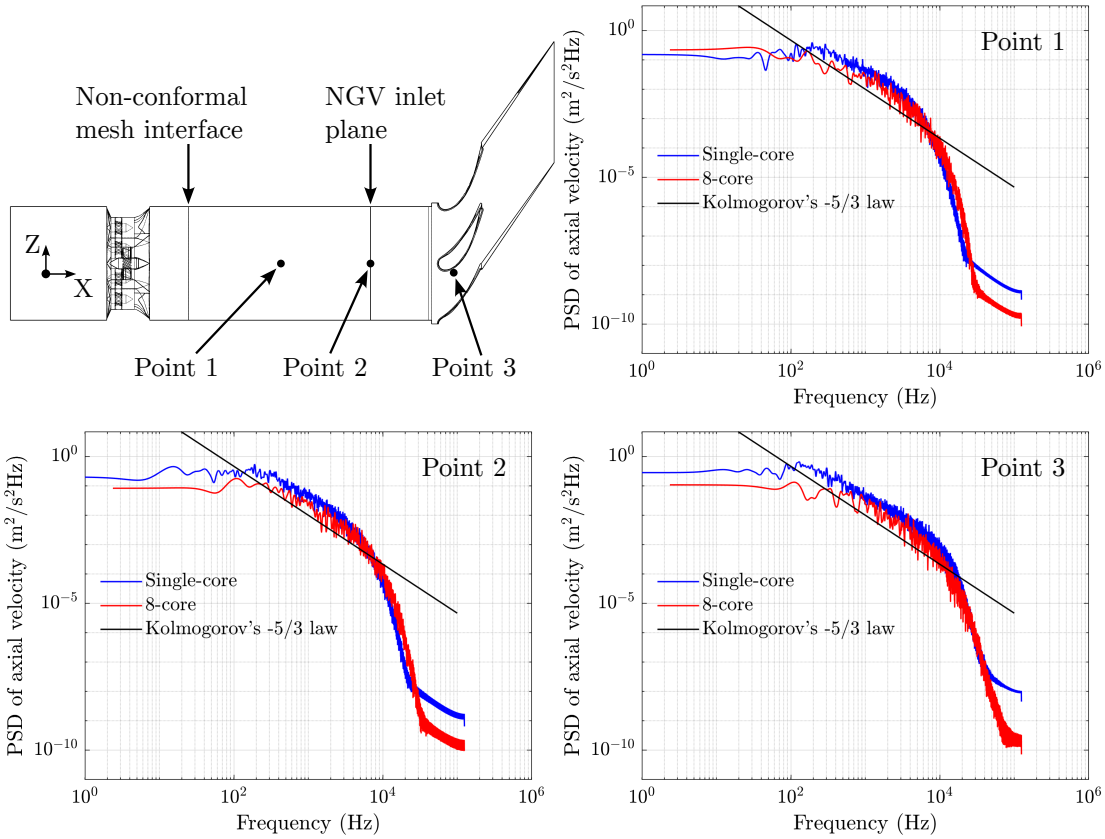


Figure 3.20: Power spectral density of axial velocity for both single-core and 8-core swirlers. Data sampled at the centre of the inlet plane to the NGV

The simulations were run for at least 12 convection passes for the single-core case and at least 5 convection passes for the 8-core case before sampling occurred, to establish quasi-steady flow in the domains. Both cases were run for 0.45 s and statistics were collected for every timestep, but the fluid domain was sampled at 10 kHz for 0.05 s. The fluid domain export duration was chosen to give at least two convection passes. Fig. 3.21 shows the total pressure trace sampled at Point 2 over the entire duration (0.45 s) for both cases and the statistics of the traces calculated over a 0.05 s sliding window. The window duration corresponds to the fluid domain export duration.

The traces appear converged and are stationary over the entire duration of the simulation, as the statistics do not vary or show periodicity. That is to say, the sliding window mean only varies by less than 1% relative to the mean of the whole duration,

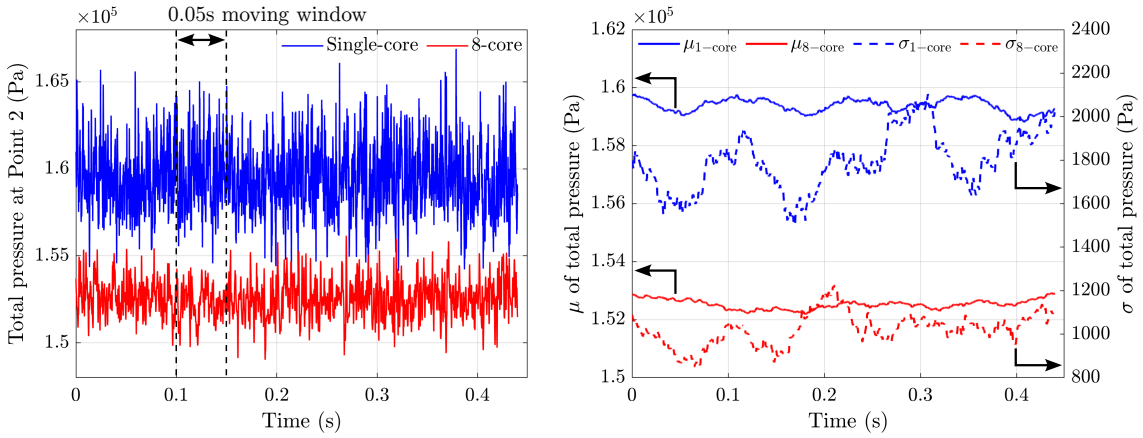


Figure 3.21: Left: Time trace of total pressure sampled at Point 2 over the full simulation duration of 0.45 s. Right: Statistics calculated over a 0.05 s sliding window. Simulations are converged and data is stationary over the full duration, but non-stationary over a single 0.05 s window

while the sliding window standard deviation appears periodic. This shows that the simulations have converged and that the flow can be considered stationary over the full duration of 0.45 s. However, a single 0.05 s window is insufficient to capture the periodic behaviour of the standard deviation, implying that the fluid domain exported is non-stationary. This is an acceptable compromise due to file size, since the mean is still constant over this window.

Exports of the fluid domain only sample every 4^{th} point due to immense size of data files. This is a reduction of 64 times of full size if all points were exported. While it would be more accurate to calculate gradients internally prior to exporting, this would require more memory. Instead gradients were calculated externally in the post-processor. While less accurate, this is still sufficient to resolve salient features such as turbulent structures and secondary flows. It should also be noted that TBLOCK stores data at nodes but performs some operations using cell-centred values. This mix of node and cell values can result in visually sharp gradients at block interfaces. For example, the mixing length is a cell-centred value, meaning that nodes at block boundaries are set to zero. This does not affect the simulation in any way since these values are never accessed, however during visualisation with the post-processor and when calculating gradients externally, these zero node values can result in sharp outlines at block boundaries. This is simply a visual aberration, not a physical one.

Chapter 4
Numerical Evaluation of the Impulse Response for Solving the Heat Conduction Equation

Post-processing of temperature measurements from infra-red thermography and thin film gauge experiments involve solving the heat conduction equation to obtain surface heat flux. Two methodologies that have been used in the past are the impulse response method and a numerical scheme such as a Crank-Nicolson solver. Difficulties in their application arise as the former requires the use of some assumptions and the latter is impractical for these datasets.

This chapter formalises the impulse response methodology of Oldfield [149] in terms of a Green's function solution and presents a procedure for numerically evaluating the impulse response. §4.1 highlights the difficulties in applying these existing methods to the experimental setup in this thesis. §4.2 discusses the theory of the impulse response method in terms of a Green's function solution. §4.3 presents the analytical forms of some Green's functions and their derivatives, which are effectively the impulse response. The impracticality of these analytical forms for the purposes of numerical integration is highlighted. To overcome this, §4.4 presents a procedure for numerically evaluating the impulse response of a 1D slab for different types of boundary conditions. §4.5 and §4.6 then present two applications of this methodology in this thesis to overcome the difficulties discussed in §4.1. Finally, §4.7 generalises this methodology to modelling heat conduction in arbitrary 2D and 3D geometries.

4.1 Existing Methodologies for Obtaining Heat Flux

Obtaining the wall temperature, $T_w(t)$, in experiments is relatively straightforward through the use of IR thermography and thin film gauges. However, concurrent measurement of both surface temperature and heat flux is more difficult. While analytical solutions exist for $q(t)$ in a 1D case, these are only tabulated for a limited number of functional forms of $T_w(t)$, thus limiting their use to cases where $T_w(t)$ can be controlled or approximated as such. This is not true in this facility, where start-up transients are on the order of 10-20 seconds and can significantly affect the surface temperature.

A widely used methodology for obtaining surface heat flux, $q\,(0,t)$, from a temperature trace is the impulse response method [149]. This involves finding the impulse response, $g_0(t)$, of a semi-infinite body from known basis functions. The convolution of the impulse response with the temperature trace then gives the surface heat flux:

$$q(0,t) = g_0(0,t) * T(0,t) \tag{4.1}$$

This method makes it suited for non-homogeneous time-varying boundary conditions (BCs), as is the case with experimental results which form these boundary conditions. However, it requires that the test article remains semi-infinite for the duration of the test; a penetration depth of $x = 4\sqrt{\alpha t}$ is recommended [153]. This rule-of-thumb is based on a 1% change in the temperature and heat flux of a body at some depth, x, when subject to a step change in heat flux, i.e. ${}^{q(x,t)}/_{q_0} < 0.01$. It is assumed that the back surface is kept at the same temperature as the body's initial temperature.

However, this rule-of-thumb cannot be applied to the geometry under consideration in this thesis due to the presence of internal cooling, which changes the back surface temperature, $T\,(L,t)$. The depth, x, at which ${}^{q(x,t)}/_{q_0} < 0.01$ depends on the heat flux at the back surface, $x = L$; it is not just half the thickness of the material. This quantity is unknown and is difficult to determine experimentally. Fig. 3.6 shows the internal cooling geometry which includes ribs and impingement walls. This

results in a spatially varying heat flux boundary condition, with localised regions of very high HTC where coolant jets exit the inner wall and impinge onto the outer wall. Furthermore, the test article is subjected to a time-varying heat flux boundary condition, not a step change. The penetration depth is expected to depend on the actual boundary condition applied and should ideally be evaluated for every experiment.

It is not possible to thicken the walls of the vane to meet the semi-infinite assumption as this will also change the internal and external cooling geometry, such as the length-to-diameter ratio of the cooling holes, thereby changing the overall cooling distribution inside and outside the vane. As the purpose of this study is to investigate the effect of different swirlers on an F-type MHI gas turbine NGV, any change to its design and cooling parameters are not allowed. We are now faced with the following questions:

1. Is the semi-infinite assumption still valid for the vane geometry used in this study?

2. What is the effect of the boundary condition at $x = L$ on the surface heat flux?

3. What is the maximum run time when subjected to a time-varying boundary condition, such as that in Fig. 4.4?

Oldfield [149] extends the impulse response methodology for use with double-sided gauges, which eliminates the need for the semi-infinite assumption. Now the heat conduction problem is restricted to the polyimide layer, which is treated as a 1D slab. The assumption here is that the circuit only comprises of a polyimide layer. This is not true in more complex gauge circuits that are constructed from multiple polyimide layers bonded together with adhesive, such as the gauges used in this study; see Fig. 3.15 in §3.4.3. At pseudo-steady state, it is possible to group individual thermal properties of the polyimide and adhesive layers into a single bulk property. However, this cannot be done if accurate high-speed unsteady heat flux is desired.

A possible solution is to discretise the 1D domain and numerically solve the conduction equation with a Crank-Nicolson solver. However, §3.4.4 has pointed out the impracticality of such a method due to the fine computational mesh required and the number of timesteps to be simulated for a single gauge. §4.5 compares the execution time of this solver with the impulse response method used in this study and shows that the latter is many orders of magnitude faster than the former.

4.2 Green's Functions in Heat Conduction

The Green's function is widely used as a fundamental solution to a variety of partial differential equations such as the wave equation, Poisson equation, diffusion (heat) equation, etc. In the context of 1D heat conduction, the Green's function, $g\left(x,t|x',\tau\right)$, is the solution to:

$$\frac{\partial g}{\partial t} - \alpha\frac{\partial^2 g}{\partial x^2} = \delta\left(x-x'\right)\delta\left(t-\tau\right) \tag{4.2}$$

and can be thought of as the response of the system at any point x in the domain and at some time t when subjected to an instantaneous point source at x' and τ. Noting then that any source is just the sum of scaled and shifted delta functions, the solution to the 1D heat equation is then also the sum of scaled and shifted Green's functions, by superposition.

The 1D heat conduction equation with internal heat generation, $H\left(x,t\right)$, in a body with initial condition, $f\left(x\right)$, and subject to a time-varying boundary condition, $\phi\left(t\right)$, is written as:

$$\begin{aligned} \frac{\partial T}{\partial t} &= \alpha\frac{\partial^2 T}{\partial x^2} + \frac{\alpha}{k}H\left(x,t\right) \\ k\frac{\partial T}{\partial x} + hT &= \phi(t) \\ T\left(x,0\right) &= f(x) \end{aligned} \tag{4.3}$$

or more compactly: $D\left(T\right) = H$, where D is the linear differential operator. The solution is then $T = D^{-1}\left(H\right)$. The inverse of a differential operator is an integral, so

this has the form: $T(x,t) = \int_0^t g\left(x,t|x',\tau\right) H\left(x',\tau\right) \mathrm{d}\tau$. The kernel of the integral, $g\left(x,t|x',\tau\right)$, is the Green's function and is also the impulse response of the system. This is easily shown by substituting H with the impulse function, δ, which returns the kernel itself. The general solution written in terms of its Green's function is:

$$\begin{aligned} T(x,t) = &\int_L g\left(x,t|x',\tau\right)\Big|_{\tau=0} f(x') x'^p \,\mathrm{d}x' \\ &+ \frac{\alpha}{k}\int_{\tau=0}^{t}\int_L g\left(x,t|x',\tau\right) H(x,t)\, x'^p \,\mathrm{d}x'\,\mathrm{d}\tau \\ &+ \frac{\alpha}{k}\sum_{i=1}^{N}\left(\int_{\tau=0}^{t}\left[x'^p g\left(x,t|x',\tau\right)\right]\Big|_{x'=x_i}\phi(\tau)\,\mathrm{d}\tau\right) \\ q(x,t) = &-k\int_L \frac{\partial g}{\partial x}\Big|_{\tau=0} f(x')\,\mathrm{d}x' - \alpha\int_{\tau=0}^{t}\int_L \frac{\partial g}{\partial x} H(x,t)\, x'^p \,\mathrm{d}x'\,\mathrm{d}\tau \\ &- \alpha\sum_{i=1}^{N}\left(\int_{\tau=0}^{t}\frac{\partial g}{\partial x}\Big|_{x'=x_i}\phi(\tau)\,\mathrm{d}\tau\right) \end{aligned} \tag{4.4}$$

where first term accounts for the initial condition, $f(x)$, and is the integral over the whole domain. The second term accounts for the contribution of internal heat sources within the body. Throughout this thesis, there is no internal heat generation so this term is zero. The third term is just the convolution integral of the Green's function with the boundary condition, $\phi(t)$. The summation is performed over all boundaries, i, that fully define the domain. The term, x'^p, is the Sturm-Liouville weight function with exponent:

$$p = \begin{cases} 0 & , \quad \text{for a slab} \\ 1 & , \quad \text{for a cylinder} \\ 2 & , \quad \text{for a sphere} \end{cases}$$

so the equation is equally applicable to cylindrical and spherical coordinates. Eqn. 4.4 expresses the impulse response method in terms of Green's functions and is referred to as the *Green's function solution*. As shown above, the Green's function or its derivative is the impulse response of a linear system. Eqn. 4.4 is used here without proof as its derivation is well documented in various texts [159, 160, 161]. The

following observations can be made regarding Eqn. 4.4:

1. g is independent of the initial condition, $f(x)$
2. g is independent of the value of the boundary condition(s), but depends on the type of boundary condition, e.g. Dirichlet (temperature), Neumann (heat flux), or Robin (convection)
3. The initial condition term can be a function of time, even if the body is initially isothermal at T_i. This can be alleviated by defining a new temperature $\vartheta = T(x,t) - T_i$ and solving for ϑ
4. The effect of each boundary condition is decoupled and contributes to the solution via superposition. Each boundary condition can be further decomposed such that their sum remains the same via linearity of the convolution operator
5. Any point x is solved independently of every other point and only depends on the boundary conditions

The solution above was derived with a Robin boundary condition for generality as a weighted combination of Neumann and Dirichlet types, with the weights being the thermal conductivity, k, and the heat transfer coefficient, h, respectively. A Robin boundary condition is also known as a convection boundary condition. Conceptually, this is equivalent to specifying $q = h\left(T_{\text{ad}} - T_w\right)$ on a boundary and rearranging this into the form shown in Eqn. 4.3, it can be seen that the the inhomogeneous term is given by, hT_{ad}.

In the case of a Neumann type BC, Eqn. 4.4 can still be used. In the case of a Dirichlet BC, the substitution:

$$\frac{1}{k}g = \pm\frac{1}{h}\frac{\partial g}{\partial x'}$$

is made. The analytical expression of g will depend on the type of boundary condition (BC). In the context of the experiments carried out here, the Dirichlet BC is the most appropriate. However, the Robin BC is also useful as will be shown later.

4.3 Analytical Expressions of Green's Functions

The analytical approaches to finding the Green's functions are similar to those used to solving PDEs. Many of the these can be derived with Laplace transforms, the method of images, and separation of variables. The three most relevant to this study are the Green's functions of a semi-infinite body subject to a Dirichlet type boundary condition, denoted as g_{10}, a 1D slab subject to Dirichlet boundary conditions at both $x = 0$ and $x = L$, denoted as g_{11}, and a 1D slab subject to Dirichlet and Robin boundary conditions at $x = 0$ and $x = L$ respectively, denoted as g_{13}.

Throughout this study, there is no internal heat generation and the body is assumed to be initially isothermal at T_i. Defining a new temperature variable as $\vartheta(x,t) = T(x,t) - T_i$ and substituting into Eqn. 4.4 removes the initial condition term without changing the heat flux.

Referring back to the general solution in Eqn. 4.4 and making the necessary substitution for Dirichlet boundary conditions, the solution, $q(x,t)$, for all three cases are, respectively:

$$q_{10}(x,t) = -\alpha \left.\frac{\partial^2 g_{10}}{\partial x\, \partial x'}\right|_{x'=0} * T(0,t) \tag{4.5}$$

$$q_{11}(x,t) = -\alpha k \left.\frac{\partial^2 g_{11}}{\partial x\, \partial x'}\right|_{x'=0} * T(0,t) + \alpha k \left.\frac{\partial^2 g_{11}}{\partial x\, \partial x'}\right|_{x'=L} * T(L,t) \tag{4.6}$$

$$q_{13}(x,t) = -\alpha k \left.\frac{\partial^2 g_{13}}{\partial x\, \partial x'}\right|_{x'=0} * T(0,t) - \alpha \left.\frac{\partial g_{13}}{\partial x}\right|_{x'=L} * h_c T_{0,c}(t) \tag{4.7}$$

and the corresponding derivatives of Green's functions are:

$$\left.\frac{\partial^2 g_{10}}{\partial x\, \partial x'}\right|_{x'=0} = \frac{1}{\sqrt{4\pi}\alpha^{3/2}} e^{-\frac{x^2}{4\alpha(t-\tau)}} \left((t-\tau)^{-3/2} - \frac{x^2}{2\alpha}(t-\tau)^{-5/2} \right) \tag{4.8}$$

$$\left.\frac{\partial^2 g_{11}}{\partial x\, \partial x'}\right|_{x'=0} = \frac{2}{L} \sum_{m=1}^{\infty} \left(\lambda_m^2 e^{-\alpha\lambda_m^2(t-\tau)} \cos(\lambda_m x) \right) \tag{4.9}$$

$$\left.\frac{\partial^2 g_{11}}{\partial x\, \partial x'}\right|_{x'=L} = \frac{2}{L} \sum_{m=1}^{\infty} \left((-1)^m \lambda_m^2 e^{-\alpha\lambda_m^2(t-\tau)} \cos(\lambda_m x) \right) \tag{4.10}$$

$$\left.\frac{\partial^2 g_{13}}{\partial x\,\partial x'}\right|_{x'=0} = \frac{2}{L^3}\sum_{n=1}^{\infty}\left(e^{\frac{-\lambda_n^2}{L^2}\alpha(t-\tau)}\frac{\lambda_n^2\left(\lambda_n^2+B^2\right)}{\lambda_n^2+B^2+B}\cos\left(\frac{\lambda_n x}{L}\right)\right) \tag{4.11}$$

$$\left.\frac{\partial g_{13}}{\partial x}\right|_{x'=L} = \frac{2}{L^2}\sum_{n=1}^{\infty}\left(e^{\frac{-\lambda_n^2}{L^2}\alpha(t-\tau)}\frac{\lambda_n\left(\lambda_n^2+B^2\right)}{\lambda_n^2+B^2+B}\cos\left(\frac{\lambda_n x}{L}\right)\sin\left(\lambda_n\right)\right) \tag{4.12}$$

where $\lambda_m = {}^{m\pi}/_{L}$, λ_n satisfies the transcendental equation, $\lambda_n \cot(\lambda_n) + B = 0$, and $B = {}^{h_c L}/_{k}$.

The three sets of boundary conditions above were chosen because they best described the different experimental setups under study. Eqn. 4.5 describes heat conduction through an uncooled NGV that was 3D printed completely solid so that it can be assumed as being semi-infinite. This equation is used to post-process IR datasets from experiments on this vane. Eqn. 4.6 describes heat conduction through the polyimide/adhesive layers of the thin film gauge circuit. This equation is used to post-process thin film gauge datasets from experiments on a film-cooled vane. Eqn. 4.7 describes heat conduction through the outer wall of a film-cooled NGV, where the temperature boundary condition on the external surface is measured with the IR camera, and the convection boundary condition on the internal wall is unknown. This equation is used in a sensitivity analysis of h on $q(0,t)$ to determine the influence of the internal convection boundary condition on the net heat flux on the top surface. An expression for 'penetration time' similar to that proposed by Schultz and Jones [153] is derived.

Solution 4.5 is exact across the whole domain for all $t > 0$ in the sense that the integral is satisfied analytically. However the presence of a singularity at $t = 0$ and $x = 0$ in Eqn. 4.8 prevents direct substitution of $x = 0$. So it is not possible to say anything about Eqn. 4.8 in the limit of $t \to 0$ at $x = 0$. This makes numerical evaluation of the convolution integral intractable. In the case of solution 4.6, the solution is only valid on the half-open interval $0 < x \leq L$ because the summations in Eqn. 4.9 and Eqn. 4.10 are not uniformly convergent. Again, numerical evaluation of the convolution integral on the surface at $x = 0$ by direct application of the analytical form of the Green's function is not possible without some kind of approximation.

For the purposes of post-processing of real measured data, these analytical solutions cannot be used, so a numerical approach is sought.

4.4 Numerically Evaluating the Green's Function

While a number of methods are available for integrating across a singularity, this has not been pursued here. Consequently, of greater interest is the numerical evaluation of the Green's function as this allows some approximations to be introduced to alleviate this issue. The numerical approach also avoids the need for derivation of either the analytical Green's function or solutions to the conduction equation subject to different boundary conditions of different functional forms, e.g. sinusoidal, polynomial, etc. Finally the numerical approach offers a way of modelling heat conduction in geometries of arbitrary shapes in 2D and 3D without the use of FEA. This is described in greater detail in §4.7.

Referring back to the Green's function solution given by Eqn. 4.4, it can be seen that each boundary condition is decoupled from each other and contributes to the final solution via superposition. For two boundary conditions, two pairs of basis functions are required. A basis function pair consists of a function describing either temperature or heat flux on a boundary, and a function describing the body's response at some location x to that boundary. The type of quantity measured for the boundary or the body's response must be same as the equation it is being used in. These basis functions can be derived analytically or obtained numerically e.g. via FEA simulations.

The procedure is demonstrated on Eqn. 4.6, which we will call the *solution equation* for the purposes of this section. The basis function pairs required are $[q(x,t), T(0,t)]$ and $[q(x,t), T(L,t)]$. The latter can be derived by considering the following solution to a 1D slab with a Heavyside step temperature BC, T_w, at $x = 0$ and a Heavyside step convection BC, $h_c T_{0,c}$, at $x = L$. The temperature, $T(x,t)$, and

heat flux, $q\left(x,t\right)$, solutions are then given by:

$$T\left(x,t\right)=\frac{B}{L\left(1+B\right)}\left(T_{0,c}-T_{w}\right)x+T_{w}$$
$$+\sum_{n=1}^{\infty}\left(2T_{w}\frac{\lambda_{n}^{2}+B^{2}}{\lambda_{n}\left(\lambda_{n}^{2}+B^{2}+B\right)}+\frac{2Lh_{c}T_{0,c}}{k}\frac{\lambda_{n}^{2}+B^{2}}{\lambda_{n}^{2}\left(\lambda_{n}^{2}+B^{2}+B\right)}\sin\left(\lambda_{n}\right)\right)\sin\left(\frac{\lambda_{n}x}{L}\right)e^{-\alpha\frac{\lambda^{2}}{L^{2}}t}$$
$$q\left(x,t\right)=\frac{-kB}{L\left(1+B\right)}\left(T_{0,c}-T_{w}\right)$$
$$+k\sum_{n=1}^{\infty}\left(\frac{2T_{w}}{L}\frac{\lambda_{n}^{2}+B^{2}}{\lambda_{n}^{2}+B^{2}+B}+\frac{2h_{c}T_{0,c}}{k}\frac{\lambda_{n}^{2}+B^{2}}{\lambda_{n}\left(\lambda_{n}^{2}+B^{2}+B\right)}\sin\left(\lambda_{n}\right)\right)\cos\left(\frac{\lambda_{n}x}{L}\right)e^{-\alpha\frac{\lambda^{2}}{L^{2}}t}$$

where $\lambda_{n}\cot\left(\lambda_{\mathrm{n}}\right)+\mathrm{B}=0$, and $B={}^{h_{c}L}/_{k}$. These equations are called the *basis equations* for the purposes of this section. Setting $T_w = 0$ and evaluating $T(L,t)$ and $q(x,t)$ gives the first set of basis functions.

The remaining pair can be derived via two routes: (1) By considering the solution to a different set of boundary conditions, this time with a Heavyside step temperature BC, T_L, at $x = L$, and the BC at $x = 0$ can be of any type. This gives a new set of basis equations. Setting $T_L = 0$ and evaluating $T(0,t)$ and $q(x,t)$ gives the second set of basis functions. (2) By using the existing basis equations given above. Setting T_w to some arbitrary non-zero value and evaluating $T(L,t)$ and $q(x,t)$ gives a set of pseudo-basis functions $[q(x,t), T(L,t), T_w]$.

These could have been derived more simply using the solution to the original problem, i.e. Heavyside step temperature BCs at both ends, which immediately gives both pairs of basis functions. However, the basis equations above were chosen to demonstrate the point that, when deriving the basis functions analytically, it is necessary for at least one of the boundary conditions in the basis equations to be *of the same type* and *at the same boundary* as the boundary condition of the solution equation. This is to allow it to be set to zero. It also demonstrates the point that the non-zero boundary condition in the basis equations can be of any type, as long as the quantity measured matches the boundary condition type of the solution equation. This provides some flexibility in deriving basis functions.

Since they were derived with a zero boundary condition, substituting each pair

in turn into Eqn. 4.6 sets one of the boundary conditions to zero. With the pair, $[q(x,t), T(0,t)]$, this gives:

$$q_{11}(x,t) = -\alpha k \left.\frac{\partial^2 g_{11}}{\partial x\, \partial x'}\right|_{x'=0} * T(0,t) + \alpha k \left.\frac{\partial^2 g_{11}}{\partial x\, \partial x'}\right|_{x'=L} * \cancelto{0}{T(L,t)}$$

and with the pair, $[q(x,t), T(L,t)]$,

$$q_{11}(x,t) = -\alpha k \left.\frac{\partial^2 g_{11}}{\partial x\, \partial x'}\right|_{x'=0} * \cancelto{0}{T(0,t)} + \alpha k \left.\frac{\partial^2 g_{11}}{\partial x\, \partial x'}\right|_{x'=L} * T(L,t)$$

which makes the solution dependent on only one term. If the second pair was derived as a set a pseudo-basis functions, $[q(x,t), T(L,t), T_w]$, then rearranging gives:

$$q_{11}(x,t) + \alpha k \left.\frac{\partial^2 g_{11}}{\partial x\, \partial x'}\right|_{x'=0} * \cancelto{T_w}{T(0,t)} = \alpha k \left.\frac{\partial^2 g_{11}}{\partial x\, \partial x'}\right|_{x'=L} * T(L,t)$$

which requires $\partial_{xx'} g_{11}|_{x'=0}$ to be evaluated already.

So far, the basis functions have been obtained from analytical solutions to the problem. However, they can also be obtained from a numerical simulation of the same problem, by recording the relevant quantities. For example, a 1D slab with the same thermal properties is simulated with temperature BCs at both boundaries. The BC at $x = L$ is set to zero while the BC at $x = 0$ is non-zero, which gives $[q(x,t), T(0,t)]$. Reversing this so that the BC at $x = 0$ is set to zero while the BC at $x = L$ is non-zero gives $[q(x,t), T(L,t)]$. This provides an alternative to cases where an analytical solution is not known or where geometries are complex, such as multi-layered 1D slabs, or 2D and 3D geometries. This forms the basis of the application in §4.5 and the extension in §4.7.

The Green's functions and their derivatives can now be numerically evaluated using the basis functions obtained above. Recall that the analytical forms of 4.8 to 4.12 could not be evaluated at the surface, $x = 0$. Two numerical methods are now presented, which provide a way of approximating them such that they are amenable to numerical integration. The two methods are: the deconvolution filter as used in Oldfield [149], and a differentiation method.

4.4.1 Filter Deconvolution

The response of a linear time-invariant system subject to an input can be written in terms of the z-transform:

$$G(z) = \frac{Q(z)}{T(z)}$$

$$g_0 + z^{-1}g_1 + z^{-2}g_2 + \ldots = \frac{q_0 + z^{-1}q_1 + z^{-2}q_2 + \ldots}{T_0 + z^{-1}T_1 + z^{-2}T_2 + \ldots}$$

$$\Rightarrow g_0 = \frac{q_0}{T_0}, \qquad g_1 = \frac{q_1 - g_0 T_1}{T_0}, \qquad g_2 = \frac{q_2 - g_0 T_2 - g_1 T_1}{T_0}, \qquad \ldots \tag{4.13}$$

and noting that the RHS is a rational transfer function, filtering it with a delta function (whose z-transform is simply 1 with trailing zeroes) gives $G(z)$. This is done in MATLAB with the `filter` command.

However, this method is prone to instability in cases where T_i initially remains close to zero. The first term, g_0, is inversely proportional to T_0, and every subsequent term depends on every prior term.

4.4.2 Differentiation of Heavyside Step Input

Consider the general form of the solution:

$$q = \sum_{i}^{N} (g * T)$$

where N is the number of boundary conditions. The equation above is equally applicable to all dimensions; this is derived for 2D in §4.7. Since g is independent of the value of the boundary conditions and only depends on its type, all boundary conditions can be set to zero except one. In the case of a 1D semi-infinite domain, there is only one boundary condition. In the case of a 1D slab, there are two boundary conditions.

Setting one of these to zero leaves one non-zero condition. Now let this be the

Heavyside step, $H(t)$, and differentiate:

$$\begin{aligned}\frac{\partial q}{\partial t} &= \frac{\partial}{\partial t}(g * H) \\ &= g * \frac{\partial H}{\partial t} \\ &= g * \delta \\ &= g\end{aligned}$$

As described in §4.4.1, if g is initially zero, which is the case when $\mathbf{x}$ is an internal node, then the filter deconvolution method is unstable. In this case, differentiation is the preferred option.

4.5 Application of the Impulse Response Method to Multi-Layered Substrates

A multi-layered substrate is simply multiple 1D slabs whose boundary conditions that lie on an interface must satisfy additional constraints. The system is therefore linear and the solution is expected to be of the form in Eqn. 4.6. Consider two slabs in contact in which the top and bottom temperatures are known and the interface temperature is unknown. An equation can be written for each body that is of the form in Eqn. 4.6, which gives four unknowns. At the interface, there must be continuity of temperature and heat flux which provides two constitutive relations. Rearranging them gives the surface heat flux in terms of the two known temperatures.

The double-sided gauges used in this study are shown in §3.4.3. They consist of multiple layers of polyimide and adhesive, whose material properties and individual thickness are known. One option to solve for the heat flux is to use a numerical scheme such as finite differencing. However as will be shown later, the rate at which data can be post-processed in this manner is prohibitively slow. The alternative is to use the impulse response method.

The methods given in §4.4.1 and §4.4.2 allow the impulse response to be calculated

numerically, but some basis functions are still required. These can be analytical, semi-analytical [162], or completely numerical. Carr and Turner [162] provide an open source code for the semi-analytical solution which is readily available on GitHub. By setting one of the boundary conditions in Eqn. 4.6 to zero, the impulse response of the other can be found. Fig. 4.1 shows $\frac{\partial^2 g_{11}}{\partial x \partial x'}\Big|_{x'=0}$ and $\frac{\partial^2 g_{11}}{\partial x \partial x'}\Big|_{x'=L}$ derived using analytical, semi-analytical, and numerical basis functions. All three basis functions appear to give similar impulse responses.

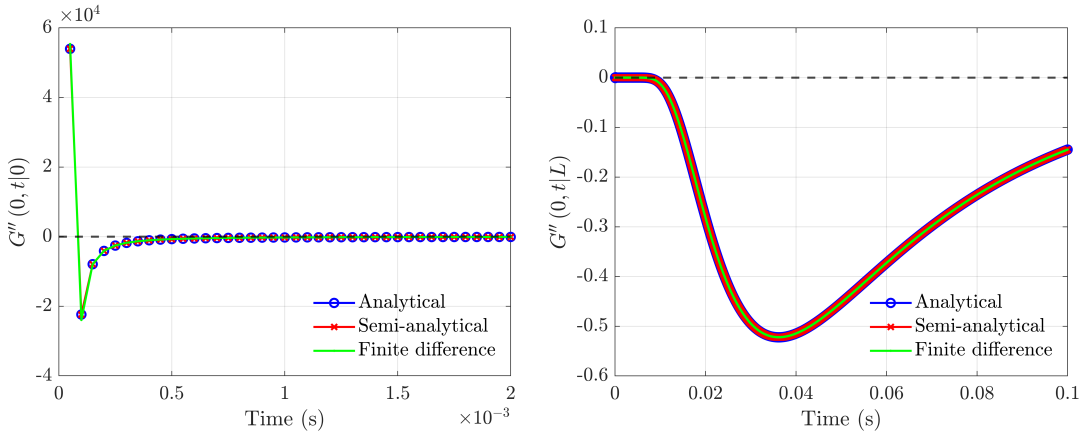


Figure 4.1: Impulse response of multi-layered substrate at $x = 0$ subject to temperature boundary conditions at $x' = 0$ (left) and $x' = L$ (right)

The impulse response method is tested against a Crank-Nicolson solver to measure the speed of both methods. Simulated data is generated for the top and bottom gauges and white noise is added to mimic actual experimental data. The sampling rate is 20 kHz, which matches the sampling rate of the experiment but the duration is only 2 s of data.

Fig. 4.2 shows that the numerical method is orders of magnitude slower than the impulse response method. Another drawback of the numerical method is that it is highly sensitive to noise when evaluated on the surface ($x = 0$). It is for this reason that heat flux was evaluated at $x = 12.7\,\mu$m for the numerical method. This inevitably introduces some attenuation of the signal and phase lag, which is why it appears to lag behind the impulse response solution.

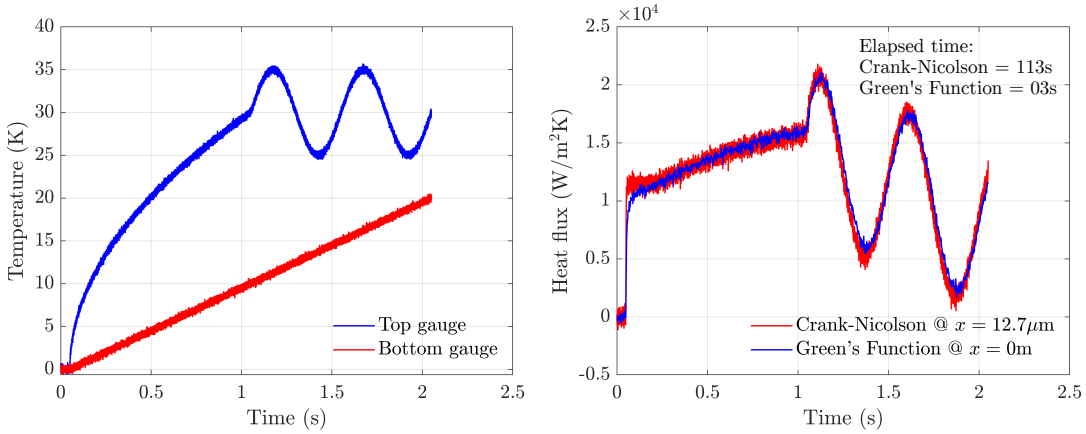


Figure 4.2: Comparison of the finite differencing and impulse response methods to post-process temperature to heat flux for double-sided thin film gauges. Simulated temperatures with white noise for top and bottom gauges (left). Heat flux post-processed with a finite differencing Crank-Nicolson solver and the impulse response method (right)

4.6 Application of the Impulse Response Method to Validating the Semi-Infinite Assumption

This section derives an expression for the penetration time for heat conduction through the thin wall of the film cooled NGV. A sensitivity analysis of surface heat flux, $q(0,t)$, to internal HTC, h_c, is performed for simulated Heavyside step temperature boundary conditions. Then the methodology presented in §4.4 is used to evaluate the impulse response of the wall, and the sensitivity analysis is repeated with real measured temperatures. It is demonstrated that for this experimental setup, surface heat flux is invariant to the internal HTC.

The thin wall is modelled as a 1D slab subject to temperature (Dirichlet) and convection (Robin) boundary conditions, so the heat flux on the external surface can be written as shown in Eqn. 4.7. The Robin boundary condition is the most appropriate here because the coolant fluid temperature is known whereas the heat flux and wall temperature on the inner wall are not. Specifying either would constrain the problem unrealistically since the inner wall temperature is expected to change over duration of a run. So the problem of validating the semi-infinite assumption and determining the influence of the inner wall temperature on the external heat flux reduces to a sensitivity analysis on h_c, the heat transfer coefficient on the inner wall.

Schultz and Jones [153] derived a 'penetration depth' for a semi-infinite body at zero initial temperature subject to a Heavyside step heat flux boundary condition. This is based on the depth at which the heat flux changes by 1% of the applied step heat flux. In the case of a 1D slab, this concept is less clear since heat is propagating from both boundaries at different rates. Instead, a 'penetration time' is derived and is defined as the time at which the contribution of the bottom BC (at $x = L$) on the net heat flux exceeds 1% of the top BC (at $x = 0$). This can be understood by examining Eqn. 4.7. The left hand side is the net heat flux at some depth, x. The first term on the right hand side, which we denote as $q\left(x, t|0\right)$, is the heat flux contribution of the top BC to the net heat flux at depth, x. The second term on the right hand side, which we denote as $q\left(x, t|L\right)$, is the heat flux contribution of the bottom BC to the net heat flux at depth, x. So the condition for the 'penetration time' is when the ratio, r, exceeds some threshold value if 1% and is written as:

$$r = \left| \frac{q\left(x, t|L\right)}{q\left(x, t|0\right)} \right| = 0.01 \tag{4.14}$$

The reasoning for this is if the bottom BC does not significantly contribute to the net heat flux, then it can be ignored so h_c does not need to be known. Alternatively, it gives the run duration for which h_c can be ignored.

It is assumed that the boundary conditions are scaled Heaviside step functions. Evidently, if the functional form of the BCs change, so does the expression (and therefore value) of the penetration time. Ideally, it should be calculated using real experimental data as shown in the sensitivity analysis later on. However, using simple BCs to derive the penetration time not only makes the integration analytically tractable, it is also useful as a rule-of-thumb guide when planning experiments. Substituting Eqn. 4.7 into Eqn. 4.14 gives:

$$\frac{h_c T_{0,c}}{k T_w} \cdot \frac{\left.\frac{\partial g_{13}}{\partial x}\right|_{x'=L} * H\left(t\right)}{\left.\frac{\partial^2 g_{13}}{\partial x \partial x'}\right|_{x'=0} * H\left(t\right)} = 0.01$$

where $H\left(t\right)$ is the Heaviside step function.

We note that the convolution of a function with the Heaviside step is simply the integral of the function over the range $[\infty, t]$. We also note that the function is causal and is only non-zero when $t \geq 0$, so the integration range is $[-\infty, t]$. Now substituting in Eqn. 4.11 and 4.12 gives:

$$\frac{h_c T_{0,c}}{kT_w} \cdot \frac{\displaystyle\int_0^t \frac{2}{L^2} \sum_{n=1}^{\infty} \left[e^{-\alpha \frac{\lambda_n^2}{L^2}(t-\tau)} \cdot \frac{\lambda_n\left(\lambda_n^2+B^2\right)}{\lambda_n^2+B^2+B} \cdot \cos\left(\frac{\lambda_n x}{L}\right) \cdot \sin\left(\lambda_n\right) \right] \mathrm{d}\tau}{\displaystyle\int_0^t \frac{2}{L^3} \sum_{n=1}^{\infty} \left[e^{-\alpha \frac{\lambda_n^2}{L^2}(t-\tau)} \cdot \frac{\lambda_n^2\left(\lambda_n^2+B^2\right)}{\lambda_n^2+B^2+B} \cdot \cos\left(\frac{\lambda_n x}{L}\right) \right] \mathrm{d}\tau} = 0.01$$

$$\frac{Lh_c T_{0,c}}{kT_w} \cdot \frac{\displaystyle\sum_{n=1}^{\infty} \left[\left(1 - e^{-\alpha \frac{\lambda_n^2}{L^2} t}\right) \cdot \frac{\lambda_n^2+B^2}{\lambda_n\left(\lambda_n^2+B^2+B\right)} \cdot \cos\left(\frac{\lambda_n x}{L}\right) \cdot \sin\left(\lambda_n\right) \right]}{\displaystyle\sum_{n=1}^{\infty} \left[\left(1 - e^{-\alpha \frac{\lambda_n^2}{L^2} t}\right) \cdot \frac{\lambda_n^2+B^2}{\lambda_n^2+B^2+B} \cdot \cos\left(\frac{\lambda_n x}{L}\right) \right]} = 0.01 \quad (4.15)$$

where λ_n satisfies the transcendental equation, $\lambda_n \cot\left(\lambda_n\right) + \mathrm{B} = 0$, and $B = {}^{h_c L}/_{k}$. Eqn. 4.15 gives the penetration time at depth, x, for fixed L, h_c, k, α, T_w, and $T_{0,c}$.

We are interested in the surface heat flux, $q\left(0, t\right)$, but as explained in §4.2, Eqn. 4.6 and 4.7 are only valid over the open interval, $(0, L)$. So Eqn. 4.15 cannot be evaluated at $x = 0$. Instead, it is evaluated very close to the surface and is expressed as a fraction of L, e.g. $x = 0.001L$. Fig. 4.3 shows that decreasing x tends towards an asymptotic curve. The curves for $x = 0.01$, $x = 0.001$ and $x = 0.0001$ lie so close together that they appear as a single curve in the plot, so $x = 0.0001$ gives a sufficiently good estimate of the penetration time.

A typical value for the step change in wall temperature is 20 °C. For the coolant, this is 1-5 °C. Note that we are working with a transformed temperature scale to eliminate the initial condition term to simplify the algebra. This means that T_w and $T_{0,c}$ represent *differences* from a zero initial condition, not the absolute value of temperature itself. Four values of h_c are shown, ranging from plausible values to very large values. The curves show that the dominant factor governing the penetration time is $T_{0,c}$, and to a lesser extent, h_c. Any further increase in h_c does not significantly

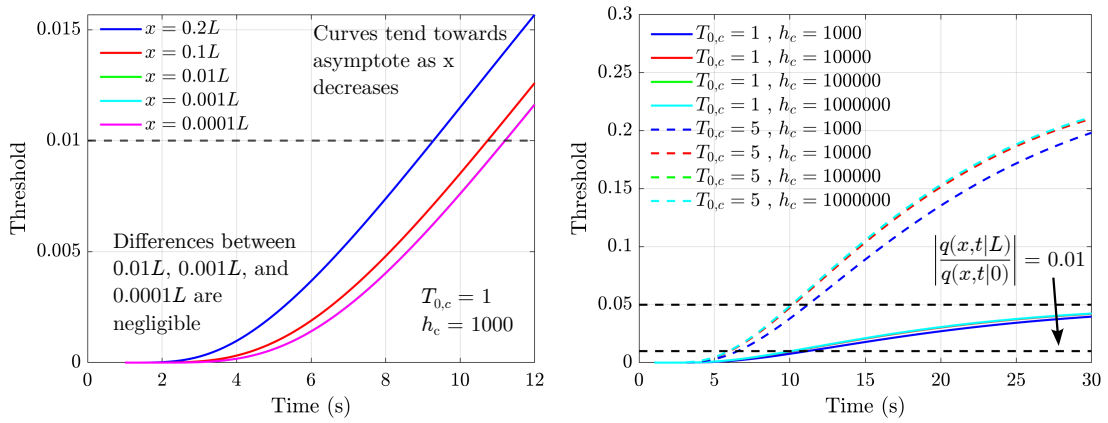


Figure 4.3: Sensitivity of penetration time to h_c and $T_{0,c}$ for Heaviside step boundary conditions. Left: Curves of penetration time for varying depth at which the ratio is calculated, and fixed $T_{0,c} = 1$ and $h_c = 1000$. Right: Curves of penetration time for varying $T_{0,c}$ and h_c and fixed $x = 0.0001L$

reduce the penetration time. For $T_{0,c} = 1$, the penetration time for a threshold value of 0.01 is on the order of 10 s. Relaxing the threshold to 0.05 gives a penetration time greater than 30 s. For $T_{0,c} = 5$, this threshold gives a penetration time of approx. 10 s. The typical post-processing duration of a run is 20 s, which is from when flow starts to when the heater mesh is switched off. While this suggests that the penetration time for large changes in $T_{0,c}$ is too short relative to the duration of the run, the estimates above are conservative because the actual change in coolant temperature is not a Heaviside step change. Instead it is more similar to a pulse function, as shown in Fig. 4.4. As stated previously, different functional forms of T_w and $T_{0,c}$ will change the penetration time.

Fig. 4.4 shows the freestream, coolant and vane external surface temperatures of a typical run. As part of standard operating procedure for the facility, runs are spaced 30 - 60 min apart to allow the vanes to cool down and reach isothermal conditions before another run is carried out. This also gives sufficient time for the coolant supply line to equilibrate as well; isenthalpic expansion across the regulators results in sub-zero temperatures immediately downstream of the regulator. This is evidenced by the initial temperatures shown being within 1 K of each other prior to the run starting. Furthermore, over the duration of one run, which lasts between 30 - 40 s, the coolant temperature only falls by 1 K

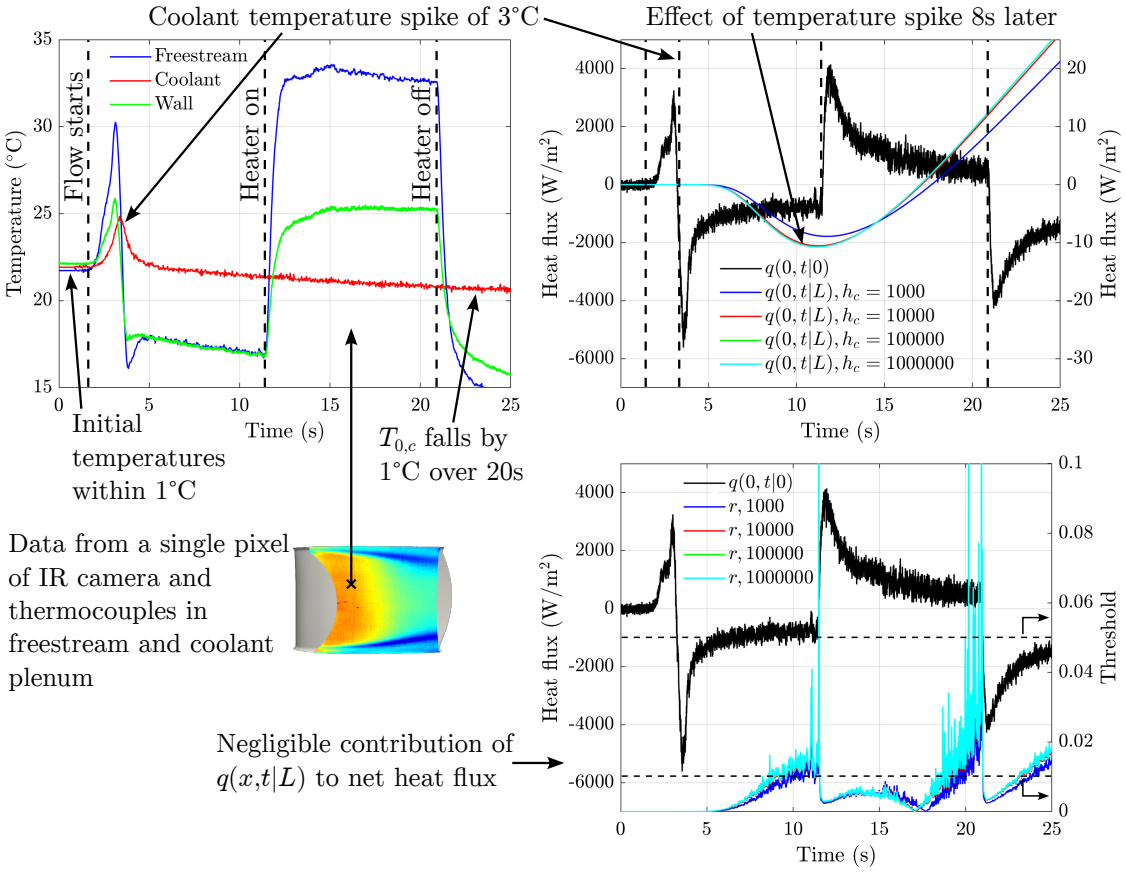


Figure 4.4: Sensitivity of penetration time to h_c and $T_{0,c}$ for real measured data. Top left: Freestream, coolant, and wall temperatures from a single run. Top right: Heat flux post-processed from measured temperatures. Contribution of bottom BC to net heat flux, $q(0,t|L)$, calculated for four different h_c. Bottom right: Ratio of heat flux from top BC to heat flux from bottom, r, calculated for four different h_c. Penetration time of bottom BC to top surface can be read from where r violates the chosen threshold values

Since the wall and coolant are initially in equilibrium, there is no heat transfer between them regardless of the size of h_c. During the run, the change in coolant temperature is still small such that the contribution of heat flux from the bottom BC is two orders of magnitude less than the contribution of heat flux from the top BC. The thermal diffusivity is also sufficiently low such that any changes to the coolant temperature propagate very slowly through the material, which is why the initial transient spike in coolant temperature due to adiabatic compression does not appear on the surface heat flux until approx. 8 s later. The magnitude of this spike is not sensitive to h_c, even with enormous values, as evidenced by the curves lying very close to each other. The dominant factor influencing its magnitude is the coolant temperature. Previously, the sensitivity analysis assumed this to be a Heaviside step

function. Now when the sensitivity analysis is carried out using real measured data for T_w and $T_{0,c}$, the magnitude of the heat flux from the bottom BC is small and the ratio $q(0,t|L)/q(0,t|0)$ remains below the 0.05 threshold value for most of the run duration. That is to say, the magnitude of the surface heat flux due to the bottom BC is negligible compared to the magnitude of the surface heat flux due to the top BC.

This can be propagated through to the evaluation of the external surface HTC, h_∞, using the two extremes of h_c investigated in this sensitivity analysis ($1000\,\mathrm{W/m^2}$ and $1\,000\,000\,\mathrm{W/m^2}$). For a value of $h_c = 1000$, then $h_\infty = 1148$. For a value of $h_c = 1000000$, then $h_\infty = 1146$. This is less than 0.2% change in external HTC for a change in internal HTC by three orders of magnitude. Hence the value of h_c does not need to be known and the vane can therefore be treated as a semi-infinite body.

4.7 Extensions to Arbitrary 2D and 3D Geometries

The impulse response characterises a linear time-invariant system's response to some input. Increasing the dimensionality of the heat conduction equation from 1D to 2D and 3D does not change the fact that the system still remains linear. A generalised form of the impulse response must therefore exist and its solution must still depend on the linear superposition of this response and input. We are therefore motivated to find this generalised solution and to apply it to arbitrary 2D and 3D geometries where analytical solutions may not necessarily exist.

This is where the interpretation of the impulse response as a Green's function is helpful, since the Green's function solution is the generalised form we are looking for.

The general solution in 2D is:

$$\begin{aligned} T\left(\mathbf{x},t\right) = & \int_{A'} G\left(\mathbf{x},t|\mathbf{x}',\tau\right)\Big|_{\tau=0} \cdot f\left(\mathbf{x}'\right) \mathrm{d}A' \\ & + \frac{\alpha}{k}\int_{\tau=0}^{t}\int_{A'} G\left(\mathbf{x},t|\mathbf{x}',\tau\right) \cdot h\left(\mathbf{x}',\tau\right) \mathrm{d}A'\mathrm{d}\tau \\ & + \frac{\alpha}{k}\sum_{i=1}^{N}\left[\int_{\tau=0}^{t}\int_{l_i'} G\left(\mathbf{x},t|\mathbf{x}',\tau\right)\Big|_{\mathbf{x}'=\mathbf{x}_i} \cdot \phi_i\left(\mathbf{x}',\tau\right) \mathrm{d}l_i'\mathrm{d}\tau\right] \end{aligned} \tag{4.16}$$

where A' is the area of the domain, $\mathrm{d}A'$ is the infinitesimal area of the domain, l_i' is the length of the i^{th} boundary, $\mathrm{d}l_i'$ is the infinitesimal length along the i^{th} boundary, and $i = 1, 2, \ldots, N$, where N is the total number of continuous boundary paths that outline region A.

The general solution in 3D is:

$$\begin{aligned} T\left(\mathbf{x},t\right) = & \int_{R'} G\left(\mathbf{x},t|\mathbf{x}',\tau\right)\Big|_{\tau=0} \cdot f\left(\mathbf{x}'\right) \mathrm{d}V' \\ & + \frac{\alpha}{k}\int_{\tau=0}^{t}\int_{R'} G\left(\mathbf{x},t|\mathbf{x}',\tau\right) \cdot h\left(\mathbf{x}',\tau\right) \mathrm{d}V'\mathrm{d}\tau \\ & + \frac{\alpha}{k}\sum_{i=1}^{N}\left[\int_{\tau=0}^{t}\int_{S_i'} G\left(\mathbf{x},t|\mathbf{x}',\tau\right)\Big|_{\mathbf{x}'=\mathbf{x}_i} \cdot \phi_i\left(\mathbf{x}',\tau\right) \mathrm{d}A_i'\mathrm{d}\tau\right] \end{aligned} \tag{4.17}$$

where R' is the volume of the domain, $\mathrm{d}V'$ is the infinitesimal volume of the domain, S_i' is the area of the i^{th} boundary surface, $\mathrm{d}A_i'$ is the infinitesimal area across the i^{th} boundary surface, and $i = 1, 2, \ldots, N$, where N is the total number of continuous boundary surfaces that enclose volume R'.

Eqn. 4.4, 4.16, and 4.17 are the Green's function solutions to the 1D, 2D, and 3D heat conduction equation respectively. In all three equations, $f\left(\mathbf{x}'\right)$ is the initial condition, $h\left(\mathbf{x}',\tau\right)$ is the heat generation source, and $\phi_i\left(\mathbf{x}',\tau\right)$ is the i^{th} boundary condition.

Eqn. 4.16 can be visualised in Fig. 4.5. The interpretation of Eqn. 4.16 is the temperature at some point, x, and time, t, when a boundary condition, ϕ_i, is applied along the path, l_i, for any i at some time, τ. Similarly the interpretation of Eqn. 4.17 is the temperature at some point, x, and time, t, when a boundary condition, ϕ_i, is applied onto the surface, S_i, for any i at some time, τ.

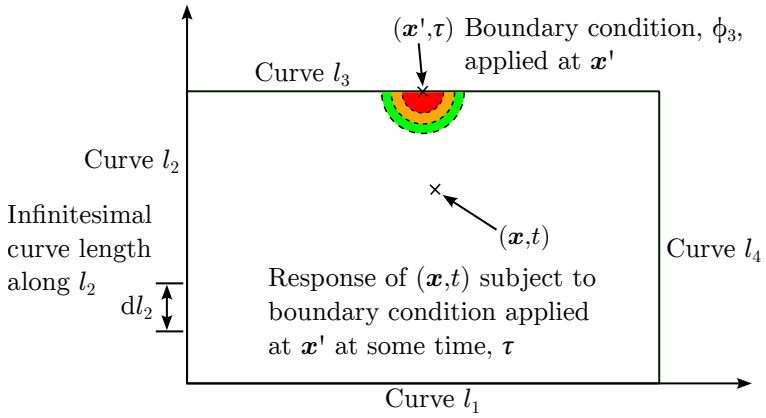


Figure 4.5: Physical representation of the 2D Green's function equation

We will now consider the 2D solution with zero initial condition and no heat generation and the boundary can be treated as a continuous closed curve, C. Eqn. 4.16 now simplifies to:

$$T\left(\mathbf{x},t\right)=\frac{\alpha}{k}\int_{\tau=0}^{t}\int_{C}G\left(\mathbf{x},t|\mathbf{x}',\tau\right)\Big|_{\mathbf{x}'=\mathbf{x}_i}\cdot\phi_i\left(\mathbf{x}',\tau\right)\mathrm{d}s\mathrm{d}\tau \tag{4.18}$$

where $\mathrm{d}s$ is the infinitesimal arc length along the curve C.

The impulse response is invariant to the numerical value of the boundary condition. So $G\left(\mathbf{x},t|\mathbf{x}',\tau\right)$ can be isolated at some arbitrary $\mathbf{x}'=\mathbf{x}_0$ by setting all other boundary conditions where $\mathbf{x}\neq\mathbf{x}_0$ to zero, i.e. $\phi_i\left(\mathbf{x}',\tau\right)=0\quad\forall\quad\mathbf{x}'\neq\mathbf{x}_0$. Now $\phi_i\left(\mathbf{x}',\tau\right)$ functions effectively like a delta function in space, and the integral of G with a delta function is just a sifting operation:

$$\int_{C}G\left(\mathbf{x},t|\mathbf{x}',\tau\right)\Big|_{\mathbf{x}'=\mathbf{x}_i}\cdot\phi_i\left(\mathbf{x}',\tau\right)\mathrm{d}s=G\left(\mathbf{x},t|\mathbf{x}_0,\tau\right)\cdot\phi\left(\mathbf{x}_0,\tau\right)$$

and now Eqn. 4.18 simplifies further to:

$$T\left(\mathbf{x},t\right)=\frac{\alpha}{k}\int_{\tau=0}^{t}G\left(\mathbf{x},t|\mathbf{x}_0,\tau\right)\cdot\phi\left(\mathbf{x}_0,\tau\right)\mathrm{d}\tau \tag{4.19}$$

$$=\frac{\alpha}{k}G\left(\mathbf{x},t|\mathbf{x}_0\right)*\phi\left(\mathbf{x}_0,t\right) \tag{4.20}$$

where either of the two methods listed in §4.4 can now be applied to numerically calculate the Green's function, G. For nodes very close to the surface, both methods are applicable. For nodes further away from the surface, when there is a phase lag

between the boundary condition being applied and the internal node experiencing a temperature rise, then the differentiation method should be used as the deconvolution method is prone to instability.

Eqn. 4.20 looks similar to the 1D case, however there are a few subtle differences. In the 1D case, there are only two boundary conditions. Its solution at any point is then the sum of the convolution of two Green's functions with the two boundary conditions, as shown by Eqn. 4.4. In the 2D case, every node on the curve, C, forms a boundary condition and the summation is replaced by an integral over the whole boundary, as shown by Eqn. 4.18. Thus each node in the mesh will have a family of curves that describe the node's temporal response to each boundary node. In 3D, the integral is performed over the whole surface, S.

Note that while the derivation here has used temperature as the solution, the method is equally applicable when using heat flux as the solution. Note also that the form of Eqn. 4.20 is the same when derived for a 3D domain.

4.7.1 General Procedure for Evaluating the Green's Functions in Discretised 2D & 3D Domains

The general procedure for calculating $G\left(\mathbf{x}, t|\mathbf{x}_0\right)$ is as follows. For a given mesh,

1. Pick any node on the boundary and apply a unit step temperature. All other boundary nodes are set to zero.

2. Solve the domain. This can be done with conventional solvers, e.g. FD, FEA, etc. The solution for the whole domain gives each node's temporal response to the chosen node.

3. Use the differentiation method to calculate $G\left(\mathbf{x}, t|\mathbf{x}_0\right)$ of each node.

4. Move to the next node on the boundary and repeat from step 1.

This procedure was implemented in MATLAB on a 20×20 square grid with arbitrary material properties.

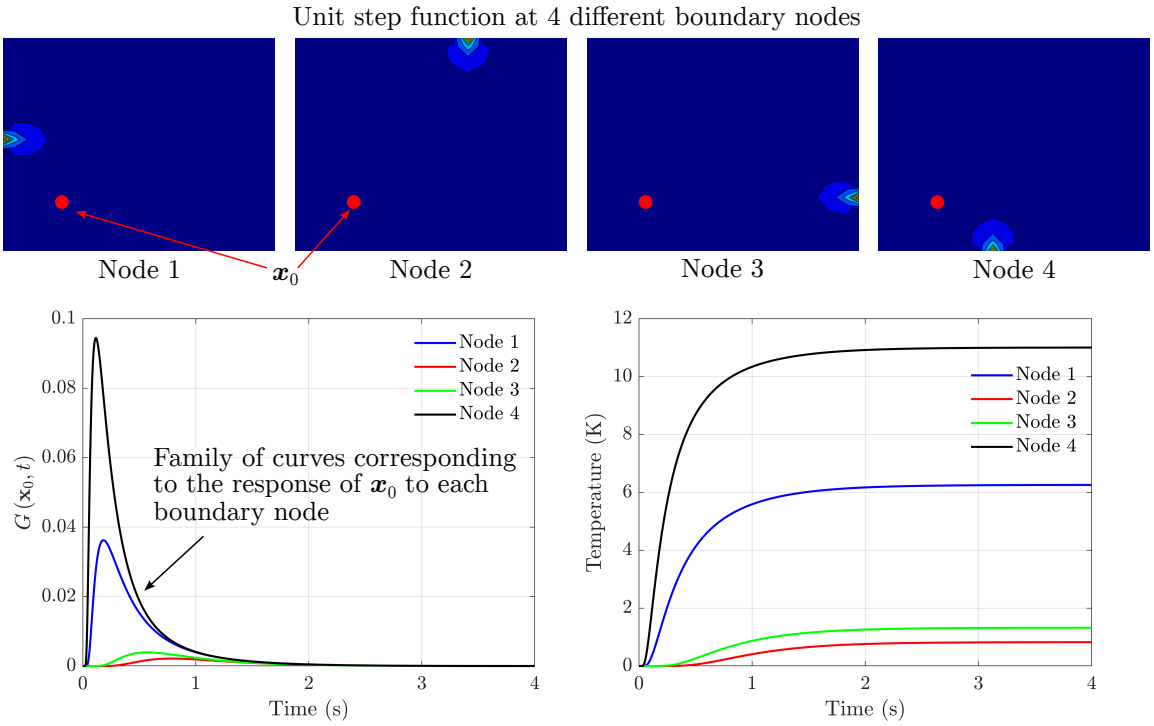


Figure 4.6: Methodology to evaluate the Green's function for a single node of an arbitrary geometry. Top: Solutions to four different sets of boundary conditions where the location of the step function is varied. Bottom left: Temperature history at location $\mathbf{x}_0$ for the four different sets of boundary conditions shown above. Bottom right: Green's function at location $\mathbf{x}_0$ when subject to an impulse at the four boundary nodes above

In Fig. 4.6, the δ function is applied at node 1 and the temperature field obtained via finite differencing. The temperature history at location $\mathbf{x}_0$ is shown as the blue line on the graph of temperature. Differentiating this gives the Green's function for $\mathbf{x}_0$ when subject to an input at node 1. This is shown as the blue line on the graph of Green's function. The location of the δ function is now moved to node 2 and the process is repeated.

Four nodes have been chosen to demonstrate this process and the corresponding Green's functions plotted. It can be seen that the further away the node is from $\mathbf{x}_0$, the shorter the peak in the Green's function and the later in time this peak occurs. This is because the $\mathbf{x}_0$ is less influenced by nodes which are further away from it and the distance over which heat applied at the node has to diffuse through to reach $\mathbf{x}_0$ is longer. When this process is carried out for all nodes, each node now carries an $[M \times N]$ family of curves, where M is the number of timesteps to solve for, and N is the number of boundary nodes, i.e. the number of boundary conditions.

The method is tested by applying arbitrary time and spatially-varying boundary conditions to all boundaries. Fig. 4.7 shows the expression of the boundary conditions applied and it can be seen that all four equations are functions of a spatial coordinate and time. The graph compares the solutions obtained from finite differencing and from numerical convolution with the Green's function at location $\mathbf{x}_0$.

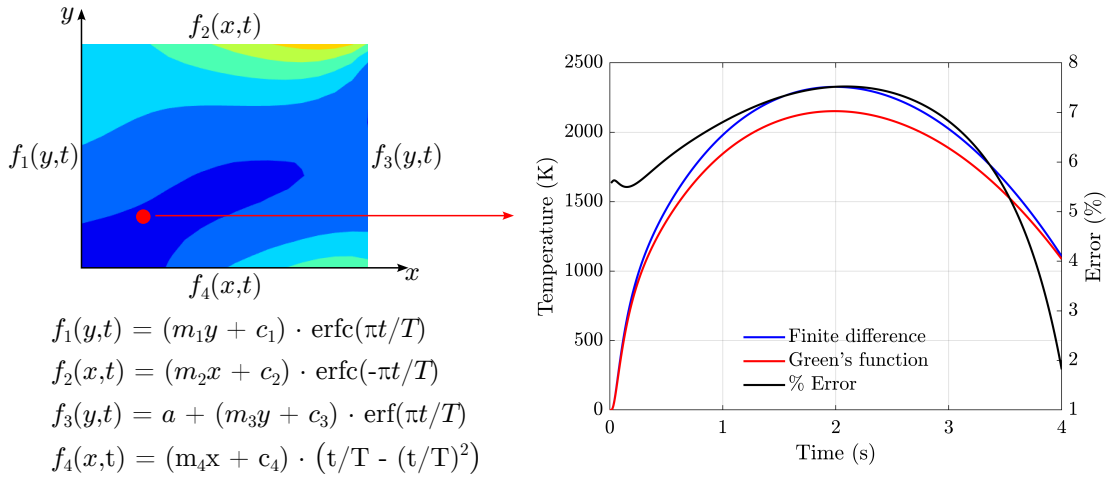


Figure 4.7: Comparison of temperature fields evaluated with finite differencing and impulse response methodologies with time and spatially varying boundary conditions. Left: Expressions for boundary conditions applied to all four edges. Right: Solutions at $\mathbf{x}_0$ obtained from finite differencing and convolution with the Green's function

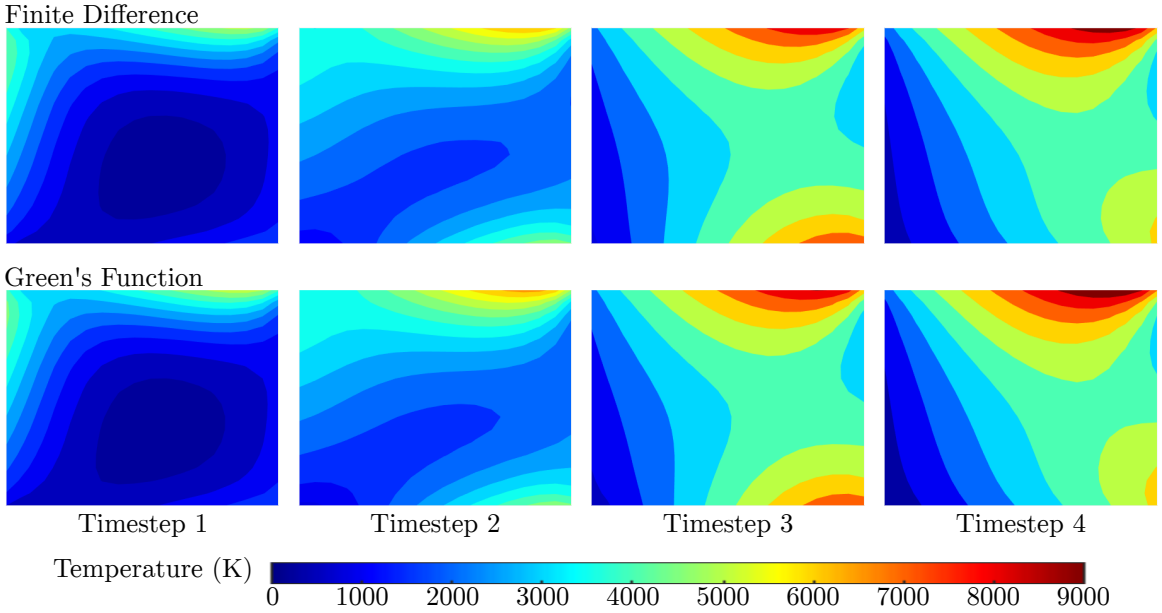


Figure 4.8: Temperature field at four different timesteps from finite differencing (top) and convolution with the Green's function (bottom)

Fig. 4.8 shows the solution field for four separate timesteps obtained from finite differencing and the impulse response approach. The impulse response method shows

good agreement with the numerical approach.

4.7.2 Potential Applications

The advantage of the impulse response method is the ability to front-load most of the computational load to the pre-processing stage. Once the Green's functions for each node has been calculated, this can be stored and reused at a later date for the same mesh, unlike conventional solvers which require a new simulation to be run every time. This method offers a reduction in processing time by orders of magnitude when compared to a typical Crank-Nicolson solver. This reduction in time is also expected when compared to FEA or BEM methods since the latter two involve iterative methods for solving a set of linear equations. The speed at which the impulse response method runs is limited by the machine's algorithm for performing convolution.

It can also be seen that every node is solved independently of every other node. This avoids the need to solve for whole domain if only a small region is of interest. For example, the Crank-Nicolson solver of §4.5 would have required the entire 1D substrate to be solved just when only the surface heat flux is of interest; not the internal temperature distribution. This also allows for mesh coarsening of internal nodes to reduce space requirements. This method is most suited to cases whereby many simulations need to be carried out on a fixed mesh with varying values for the applied boundary conditions.

4.7.3 Methods for Accelerating the Green's Function Procedure

While the actual processing stage does not involve conventional iterative methods such as those required for FEA and BEM, the pre-processing stage of finding the Green's function is reliant on these approaches. Obtaining the complete set of curves for every node in the domain requires N-many repeated simulations of the same geometry but with varying locations of the δ function, where N is the number of boundary nodes.

That is to say, the FD or FEA simulation must be repeated N times. As with BEM, the computational cost increases as the surface-to-volume ratio increases.

Although the workload is front-loaded to the pre-processing stage, it would still be beneficial to reduce the total time taken where possible. The most obvious solution is to coarsen the mesh to reduce the number of surface elements to solve for. However this may not always be possible if gradients must be accurately resolved on the surface.

Alternatively, it can be seen in Fig. 4.6 that the influence of boundary nodes far way from some point $\mathbf{x}_0$ is weaker than that of boundary nodes closer to it. The curves for Nodes 2 and 3 have smaller peaks compared to the curves for Nodes 1 and 4. If only a small portion of the domain is of interest, and if the diffusivity is sufficiently low, then a 'sphere of influence' can be drawn over each node in the region of interest that limits the number of boundary nodes that influence its solution. Hence only the boundary nodes within the union of all spheres need to be solved for.

The pre-processing and post-processing stages can also be parallelised very easily by noting that each node is solved independently of every other node. Thus each core only requires information about the nodes it is solving for, and the boundary conditions within the node's sphere of influence. No data transfer between cores is necessary, which speeds up execution time.

4.8 Summary

Existing methodologies for post-processing temperature into heat flux have been reviewed and the difficulties associated with applying them to the current experimental setup have been identified. These are: (1) The validity of the semi-infinite assumption for a film cooled vane with thin walls, for which only the external surface temperature is known. This is the case for the film cooling experiments carried out with the IR camera. (2) Accounting for the multi-layered construction of the double-sided thin film gauges with each layer having different thermal properties.

The impulse response method is expressed in terms of the Green's function solu-

tion, and finding the impulse response is equivalent to finding the Green's function or its derivatives. Their analytical forms cannot be evaluated at the boundaries $x = 0$ and $x = L$, which precludes their use in numerical integration when post-processing experimental data. Instead, a methodology is presented for finding basis functions to numerically evaluate the impulse responses such that they are amenable to numerical integration.

This methodology is applied to efficiently post-process thin film gauge data. The execution time for this convolution operation is compared against a finite differencing Crank-Nicolson solver, in post-processing the same sample temperature data to get heat flux. It is shown that the former is orders of magnitude faster than the latter.

Another application of the methodology is in the sensitivity analysis of the surface heat flux to the internal heat transfer coefficient, h_c, using experimentally measured data. Different basis functions are obtained for varying h_c, which are used to evaluate the impulse responses. Applying these to the measured data showed that the surface heat flux is not significantly affected by h_c, and that the vane can be assumed to be semi-infinite. An expression for the 'penetration time' for a thin-walled slab was derived, that is analogous the concept of penetration depth used for semi-infinite bodies. This provides a useful rule-of-thumb when estimating the contribution of the bottom BC to the top BC and therefore gives the duration for which this contribution is less than some threshold value.

Finally, the methodology is extended to arbitrary 2D and 3D domains, to demonstrate its use as a faster alternative to simulating heat conduction in fixed meshes. The procedure front-loads most of the work into a pre-processing stage, so that the post-processing stage only performs a very fast convolution. Its potential uses and methods for acceleration are discussed.

Chapter 5
Flow Interactions at the Combustor-Turbine Interface for Single & Multicore Swirlers (LES)

High-fidelity LES was carried out on the entire combustor-turbine interface with two different swirler geometries: the single-core swirler and the 8-core swirler, shown in Fig. 5.1. The incoming flow to the NGV is characterised and the dominant flow structures are identified. Their interactions with the potential field and secondary flows around the unshielded NGV are also described and the impact on the aerothermal performance of the vane is quantified. Both swirler geometries used in this LES study were chosen as they are representative of combustor swirlers in use today. The single-core swirler is common in many combustor-related studies, as well as integrated combustor-turbine interface studies [137, 81, 87]. The MHI 8-core swirler was included as it is representative of an advanced radially-staged LPM combustor in use by MHI.

The full domain consists of an inlet section, the swirler, the transition duct, and the NGV blade row with two full passages for periodicity. By modelling the CTI as a single domain, the unsteadiness of the large scale coherent structures in combustor flows and their instantaneous effects on the NGV is captured. Furthermore, as highlighted in §2.3.7, the presence of the NGV has been shown to have a two-way coupling with the combustor, by altering the potential field and acoustic modes of the combustor.

The single-core swirler has one pilot swirler surrounded by a bypass and the multi-core swirler has one pilot swirler surrounded by 8 main swirlers. The main swirlers impart swirl in the same direction and are counter-rotating to the pilot swirler. The

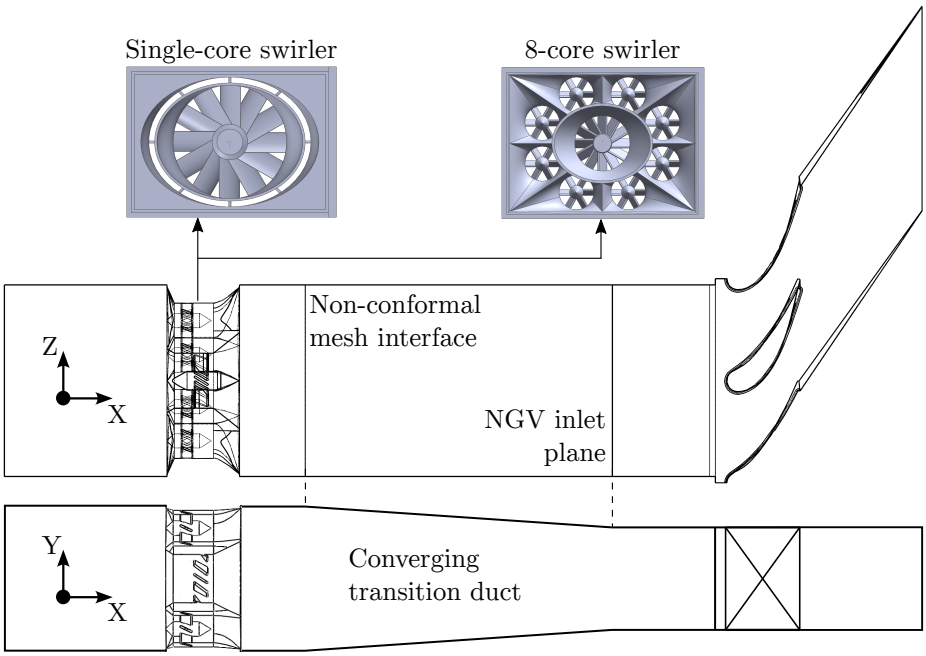


Figure 5.1: LES flow domain for the single and 8-core swirler cases. Pilot swirlers for both geometries have the same sense of rotation. The main swirlers for the 8-core swirler have the opposite sense of rotation to the pilot swirler, i.e. they counter-rotate against the pilot swirler

transition duct forms the walls of the can combustor and is a converging section leading to the NGVs. In the gas turbine being studied there are two vanes to every can combustor, so two passages are included here. The boundary conditions for each simulation was obtained from experiments carried out on the corresponding geometries.

5.1 Flow Field Downstream of the 8-Core Swirler

Fig. 5.2 shows time-averaged LES results of a cross-sectional plane of the 8-core swirler. The recirculating zone can be clearly seen as the region of low total pressure. The boundary of this zone is outlined by the isoline of zero axial velocity (black) since this is where streamlines (white) reverse in direction. The region of highest fluctuations in total pressure occurs on the boundary of the recirculation zone and is likely due to the precessing vortex core [139]. Both the pilot and main swirlers undergo vortex breakdown and have individual recirculating zones that precess about their respective geometric centres.

Strong shear layers develop at the boundary of the CTRZ and are responsible for

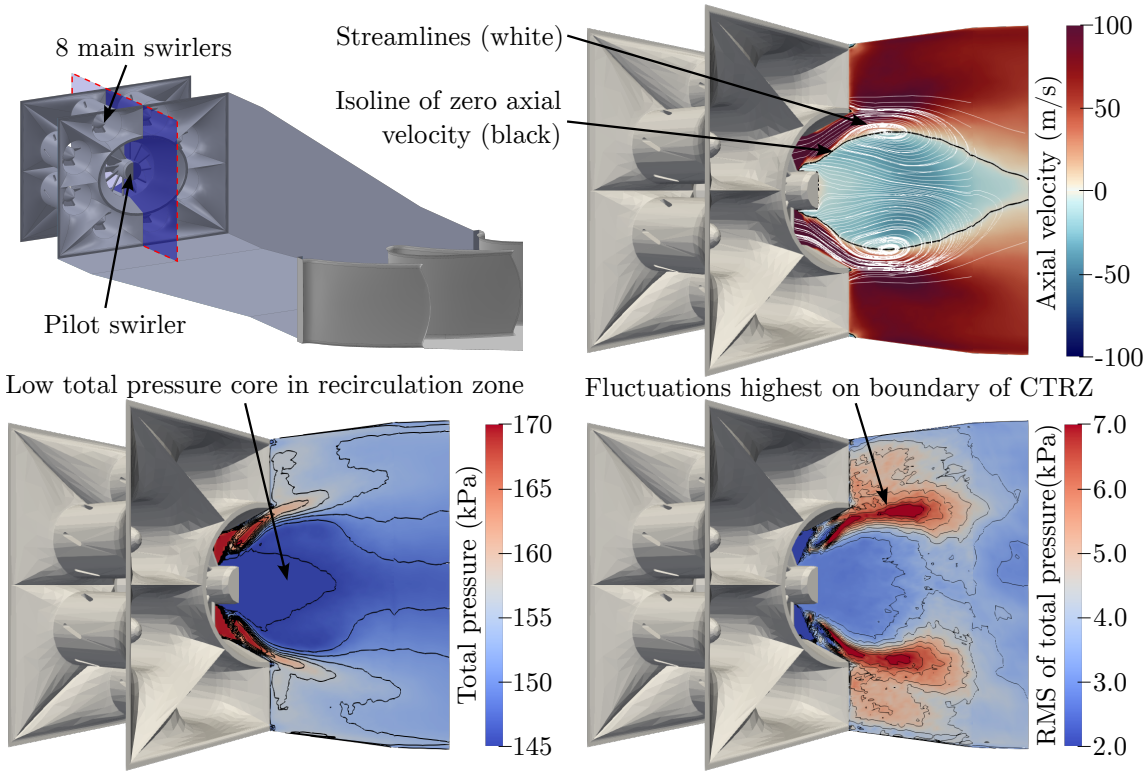


Figure 5.2: Cross-sectional views of the 8-core swirler showing time-averaged contour plots of axial velocity (top right), total pressure (bottom left), and RMS fluctuations of total pressure (bottom right). The zero axial velocity contour (black) demarcates the recirculating zone where streamlines (white) reverse

the formation and shedding of large scale coherent structures [91]. In non-swirling and weakly swirling jet flows, axial shear dominates and Kelvin-Helmholtz instability in the axial shear layer produces vortex rings. In strongly swirling flows, where the azimuthal velocity is comparable to the axial velocity, centrifugal instabilities dominate and the vortex has a radial pressure gradient due to the centripetal acceleration term, ω^2/r. A sudden expansion at the swirler exit now causes an adverse pressure gradient in the axial direction which reverses flow and results in vortex breakdown and formation of the central toroidal recirculation zone (CTRZ).

The formation of the CTRZ is accompanied by a precessing vortex core (PVC), which has been well documented, [15, 85, 91, 136]. The PVC is a three-dimensional unsteady flow structure in which the low pressure vortex core of the recirculation zone is initially axially aligned, but then begins to precess around the axis of the swirler further downstream. This is visualised in Fig. 5.3. The precession for a single-core swirler has been shown to persist far downstream into the vane inlet resulting in a

swirl core that is highly unsteady in space and time [120]. This instability has also been observed for the 8-core swirler.

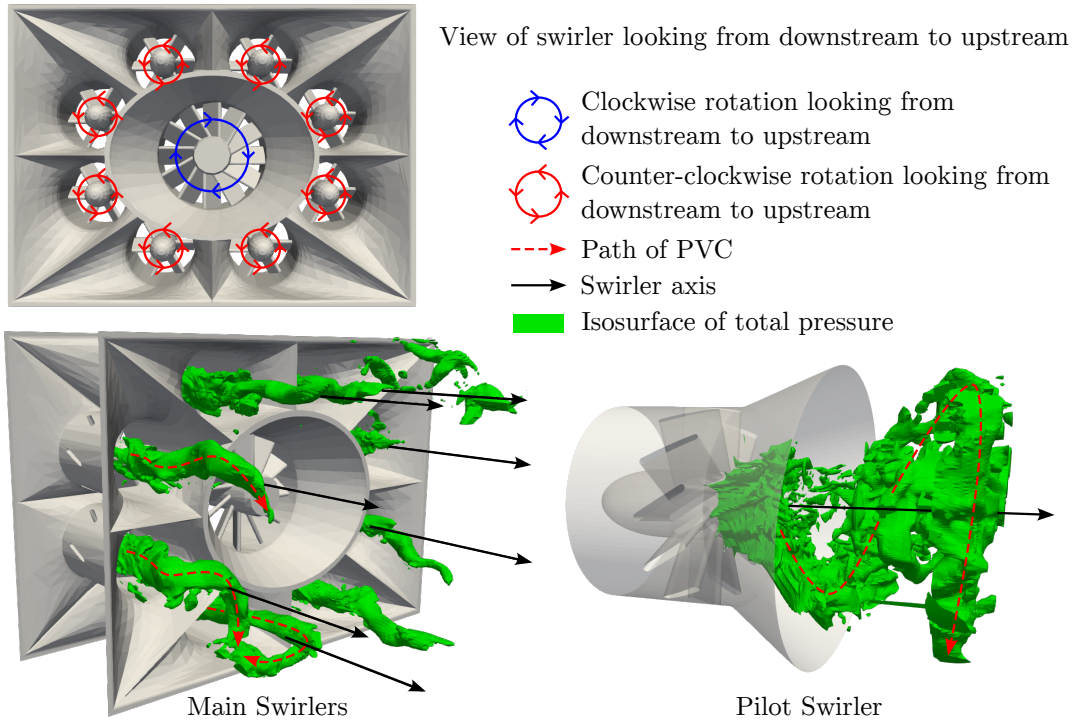


Figure 5.3: Precession of the vortex cores for the main swirlers (bottom left) and pilot swirler (bottom right) for the 8-core swirler. Visualised as isosurfaces of total pressure (green)

Fig. 5.3 is a single instantaneous snapshot of isosurfaces of total pressure (green), and shows the precession of the vortex cores for each main swirler and the pilot swirler. The vortex cores are initially aligned in the axial direction. Further downstream, they are driven away from the centreline and precess about it, forming helical structures. As the PVC rotates, large structures are peeled off periodically and convected downstream by the local flow [91]. The sense of rotation of the precession is in the opposite sense of rotation to the swirl, which is consistent with existing studies [139, 136]. In this case, the swirl direction of the pilot swirler is clockwise (CW) looking from downstream to upstream, and the vortex core precesses in a counter-clockwise (CCW) sense. The PVC is located near the boundary of the recirculation zone, leading to very high fluctuations in total pressure, as shown in Fig. 5.2. This is consistent with the observations of Lilley [84] and Syred [85].

The total pressure at $4D$ downstream of the pilot swirler was sampled to measure

the frequency of precession. Fig. 5.4 shows the power spectral density (PSD) of the total pressure at this location, and a well-defined peak at 178 Hz. It is thought that this peak corresponds to the frequency of precession as this roughly corresponds to the time lapse sequence of images showing precession. However, further investigation is required to validate this as it is difficult to isolate the PVC to obtain clear images of precession in all frames. There is also significant power in other peaks although their cause is not known. This demonstrates that low frequency oscillations up to 1 kHz are present just downstream of the combustor.

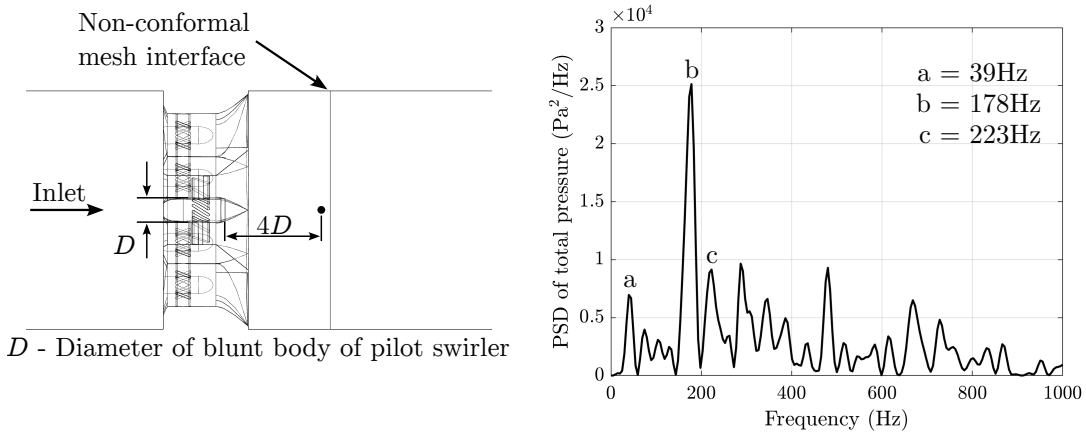


Figure 5.4: PSD of total pressure just downstream of the pilot swirler of the 8-core swirler

The residuals of these swirl cores, their precession, and large structures generated and shed from the shear layers of the recirculating zone give rise to large scale coherent structures in the transition duct that fluctuate in space and time. Data was sampled at various planes in the transition duct to identify structures and quantify their turbulence intensities, rate of decay, and the amount of residual swirl in the transition duct. Combustor studies typically quantify the amount of swirl using the definition provided by Gupta et al. [15]:

$$S = \frac{\int_0^R \rho u_x u_\theta r^2 dr}{R \int_0^R \rho u_x^2 dr}$$

which is the ratio of the axial flux of angular momentum to the axial flux of axial momentum. For ease of comparison with existing literature, this definition is used with some slight modifications. In the case of a rectangular cross-section, the assumption

of axisymmetry does not apply so the integral is performed over the whole area and R is defined as the hydraulic radius. Angular momentum is a vector quantity and can be negative or positive depending on the direction of swirl. In the case of multi-core swirlers with counter-rotating swirl directions, preserving the sign can understate the actual level of swirl in the plane. To avoid this, the absolute value of u_θ is used instead.

In the case of the single-core swirler, the downstream flow is characterised by a single large precessing vortex core with very high turbulence intensity. For the multi-core swirler, this is comprised of multiple smaller swirl cores. Fig. 5.5 shows this in terms of x-vorticity at two cross-sections in the transition duct for both swirlers.

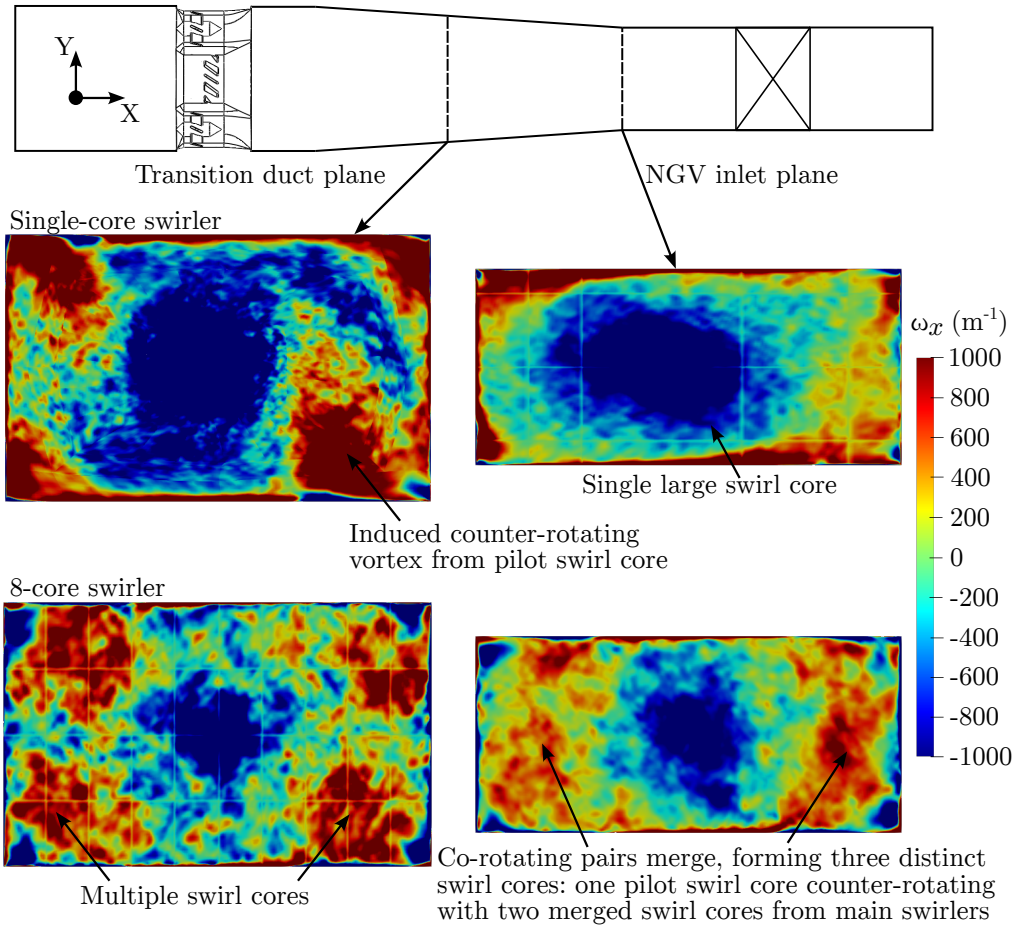


Figure 5.5: Cross-section views of time-averaged axial vorticity in the transition duct (left) and at the NGV inlet plane (right). Gradients were calculated after time-averaging the flow field

The large positive x-vorticity component in the transition duct for the single-core swirler is simply induced counter-rotation by the central swirl core. This does not

indicate the presence of an additional swirl core as it decays by the time it has reached the NGV inlet plane. In the case of the 8-core swirler, the multiple swirl cores can be seen to persist into the NGV inlet plane. The co-rotating swirl core pairs from the main swirlers merge such that the inlet plane to the NGV now consists of three distinct swirl cores of smaller size and lower vorticity than the single-core swirler.

However, it is not immediately obvious which geometry results in a more rapidly decaying turbulence field and swirl number, due to competing factors. The persistence of free vortices has been shown to be due to the dispersion of perturbations for highly swirling flows, i.e. flows with high angular momentum relative to its axial momentum. Such flows are inherently stable due to the 'stratification' of shear flow by rotation, which prevents turbulent transport of angular momentum into or out of the vortex core [163, 164]. Yao et al. [165] showed that wall shear stress is the dominant mode of swirl decay. Kreith and Sonju [166] showed that swirl decay in a fixed pipe is largely dependent on the Reynolds number and not the inlet swirl intensity. For fixed Reynolds number, increasing swirl intensity also results in a higher rate of decay due to increasing wall shear stress [167]. However this rate of decay reduces further downstream [168]. The 8-core swirler also contains co-rotating main swirlers which are likely to merge into a single larger vortex, which may hinder its dissipation [169].

The decay of these structures through the transition duct is tracked by sampling various planes in the transition duct up to the vane leading edge. The mass-weighted plane average turbulent kinetic energy and swirl number across each plane for both cases are shown in Fig. 5.6. The turbulent kinetic energy, k, and swirl number, S, for the 8-core swirler is significantly lower compared to the single-core swirler; up to 43% lower k and 55% lower S at the NGV inlet plane. The decay rate of k for the single-core swirler is higher than the 8-core and the gradients of both decrease with increasing axial distance. The rates of decay for both swirlers appear to converge to the same value.

Based on arguments by Choi et al. [167] and Yao et al. [165], the higher initial

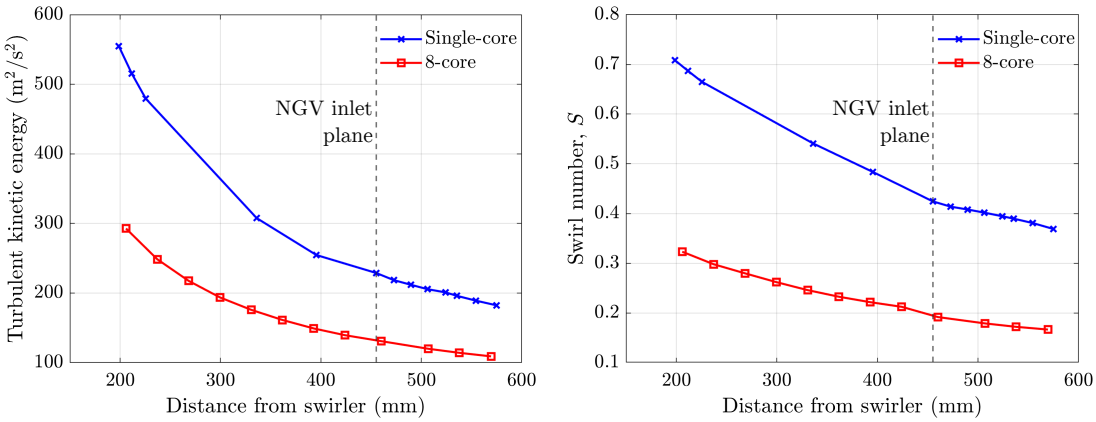


Figure 5.6: Mass-weighted plane average turbulent kinetic energy (left) and swirl number (right) for both single and 8-core swirlers at various axial locations downstream of the swirler. The NGV inlet plane is shown as the dashed line

rate of decay of k for the single-core swirler can be partially attributed to higher swirl number. A decrease in swirl number reduces the wall shear stress acting to dissipate the angular momentum, therefore leading to a reduced rate of decay of k. However, this is not the only mechanism responsible for the decay of k since the rates of decay of both swirlers appear to be similar near the vane LE, despite the 8-core swirler having a lower swirl number everywhere. Comparisons of the mechanisms of turbulence decay between these two swirlers are difficult because of the more complex interactions between multiple co-rotating and counter-rotating swirl cores in the case of the 8-core swirler. Identification of all the mechanisms governing the decay of k in such a complex flowfield will require further study.

5.2 Time-Averaged Freestream Flow Deviation at the Inlet to the NGV

It was shown above that flows at the inlet plane of the NGV consist of a single large swirl core for the single-core swirler and three smaller swirl cores for the 8-core swirler. While the swirl and turbulent kinetic energy for the latter case is comparatively lower than the single-core swirler, the overall levels remain sufficiently high to result in deviations in total pressure and yaw angle distribution. Fig. 5.7 and 5.8 show the contours of total pressure, yaw, and pitch measured at the inlet plane to the NGV

for both the single-core swirler and 8-core swirler, obtained from time-averaged LES and experiments. Experimental measurements were made by Jacobi et al. [120] and Shaikh [132].

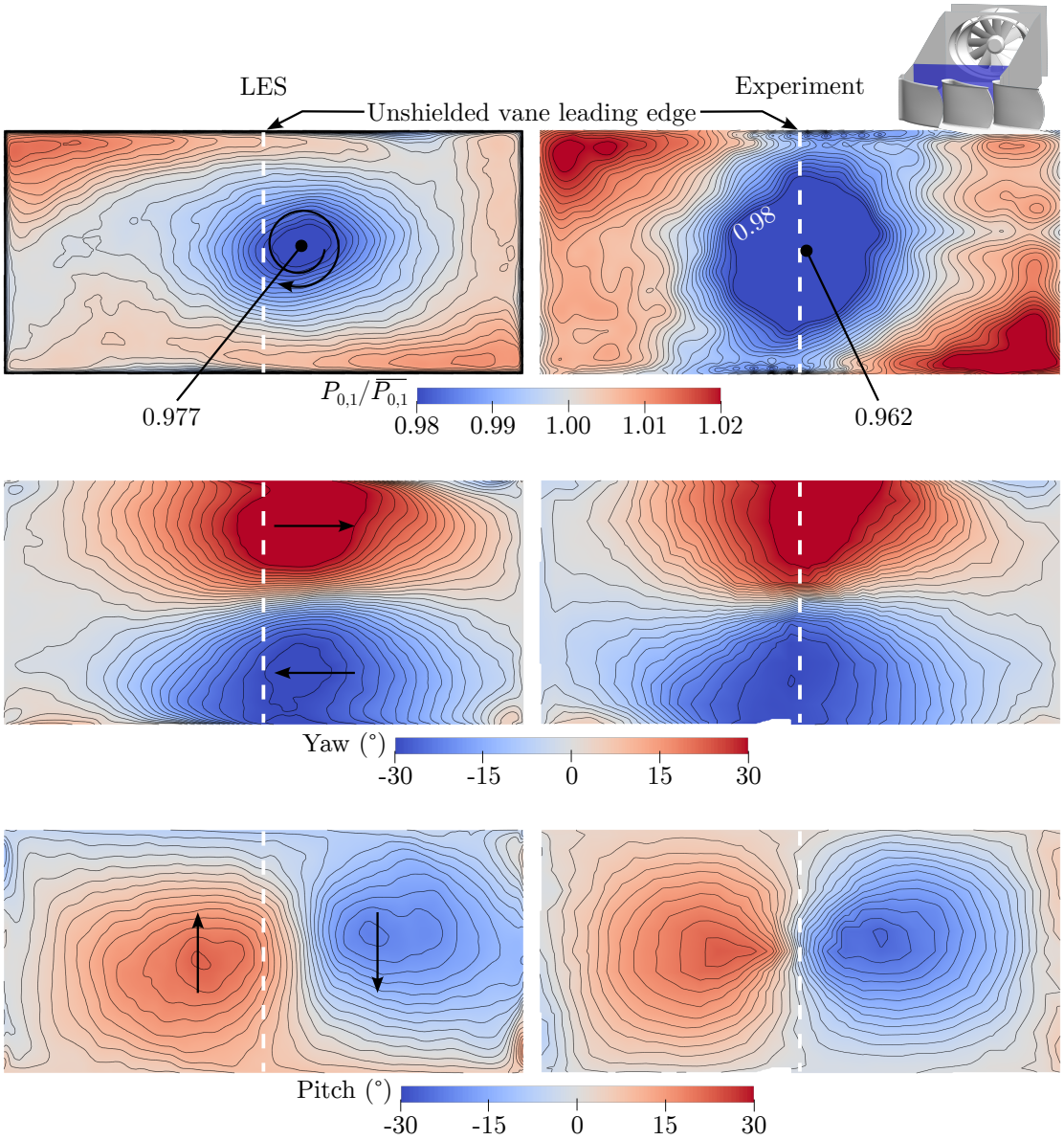


Figure 5.7: Contours of total pressure, yaw angle, and pitch angle at the NGV inlet plane for the single-core swirler obtained from time-averaged LES (left) and experiments (right)

A pronounced low pressure core is evident in the case of the single-core swirler. Regions of high total pressure are located in the top left and bottom right corners where flow stagnates. The loss core of the single-swirler is also more intense than that in the 8-core swirler. The higher swirl number also results in greater yaw and pitch angle deviation. As highlighted previously, three loss cores are also present in the case

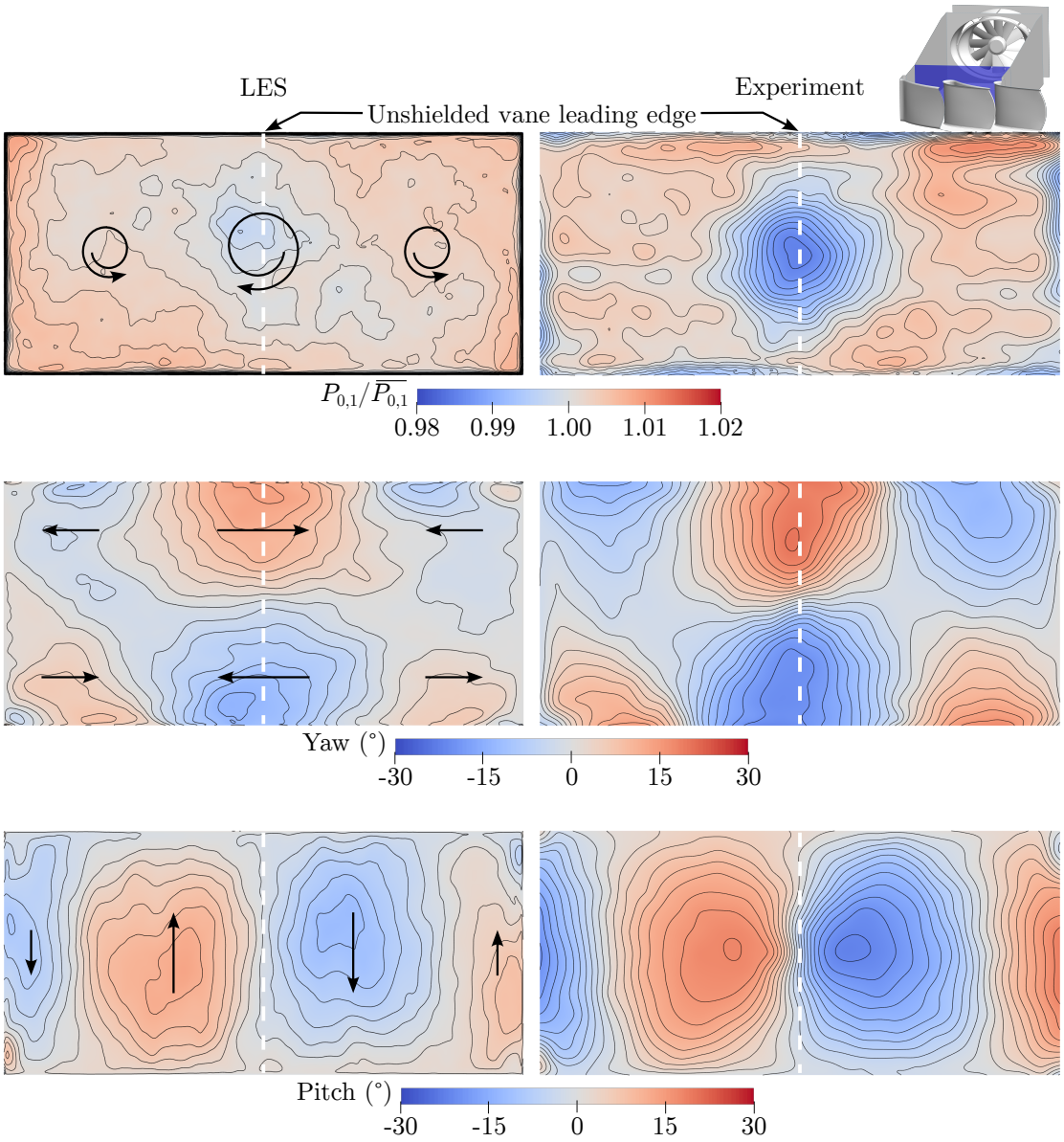


Figure 5.8: Contours of total pressure, yaw angle, and pitch angle at the NGV inlet plane for the 8-core swirler obtained from time-averaged LES (left) and experiments (right)

of the 8-core swirler. The central core is due to the pilot swirler as its yaw angle is consistent with the swirler's sense of rotation, i.e. clockwise looking from downstream to upstream, leading to negative yaw near the hub and positive yaw near the casing. The two cores along the combustor walls are merged residual swirl cores from the main swirlers. These rotate in a counter-clockwise sense (looking from downstream to upstream), resulting positive yaw angle deviation near the hub and negative yaw angle deviation near the casing.

The time-averaged LES and experimental results show good qualitative and quan-

titative agreement. The size and pressure minima of the loss core is slightly under-predicted in LES compared to experiments. For both swirler cases, experimental results consistently show a lower total pressure loss core than LES results. This may be due to the use of a 5-hole probe (5HP) to measure total pressure, which can result in an underestimation of total pressure due to fluctuating flow angles [170]. An instantaneous change in flow angle from zero incidence will result in a measurement at the central hole that is lower than the true total pressure. This response is symmetric to positive and negative incidence angles, thus consistently resulting in instantaneously lower total pressure readings whenever the flow angle changes. Consequently, when time-averaged the total pressure measured will be lower than the true value or that measured by a Kiel-shrouded probe - which is largely insensitive to flow angles. In this study, this difference between LES and experimental results is small; less than 5% for the single-core swirler and less than 2% for the 8-core swirler, however Coull et al. [170] report an overestimation of total pressure loss with a 5HP of up to 44% compared to a Kiel probe.

In the case of the single-core swirler, another source of error is the slight tangential shift in the LES result of the location of the loss core towards the pressure side of the unshielded vane. The center of the experimentally measured total pressure loss core is located along the leading edge of the unshielded vane. It should be noted that the experiment was carried out without the linear cascade and NGVs present as access was required to the transition duct where the measurement was made. It was previously not possible to access the upstream plane of the NGV with the cascade present. This slight tangential shift is likely due to the potential field of the NGV being felt upstream by the swirl core. A slotted flange has been designed by the author to interface between the transition duct and the linear cascade that will allow 2D traverse measurements to be made at the inlet plane to the NGV. This will be used in a future study to investigate the coupling between the potential fields of the combustor and NGV; see §8.3.

5.3 Effects of Inlet Flow Conditions on the Aerodynamics of the NGV

5.3.1 At the Leading Edge

The residual swirl core interacts with the potential field of the NGV, resulting in the formation of a new structure and flow deviation around the vane. The former is shown in Fig.5.9. Incoming flow to the NGV's leading edge has a total pressure gradient

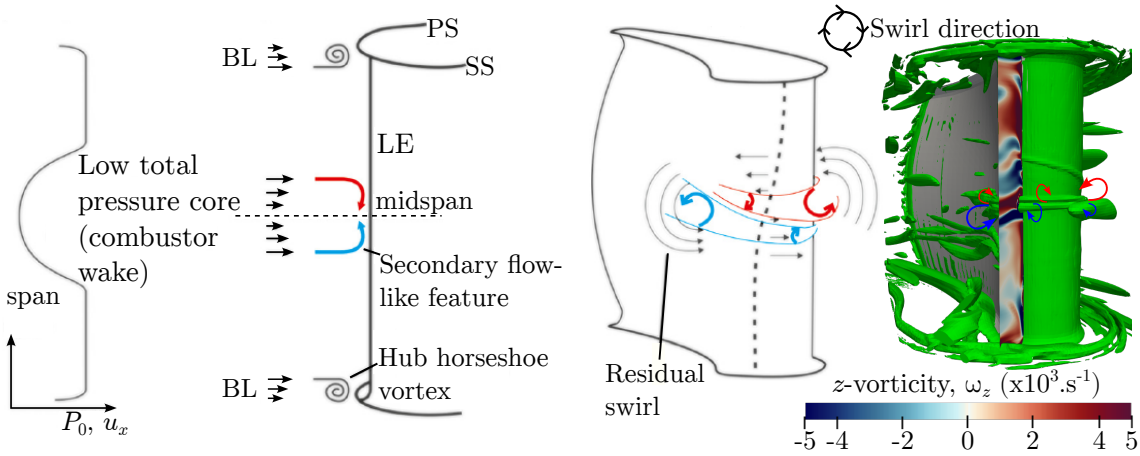


Figure 5.9: Schematic showing the interaction of the incoming combustor wake with the vane's potential field (left) and the formation of a new secondary flow-like counter-rotating midspan vortex pair (right). Adapted from Jacobi et al. [120]

towards the center due to the low total pressure core arising from the residual swirl from the combustor. The potential field exerted by the vane causes low momentum fluid in the centre of the core to be turned quicker than high momentum fluid away from the core. This leads to tangentially-aligned (z-direction) vorticity forming on the vane leading edge near the midspan, causing fluid to 'roll-up' into two counter-rotating vortices. This can also be explained by considering the ring of vortex filaments at the inlet, which wrap around the LE. This is an inviscid phenomena and can occur in the absence of swirl, as long as a total pressure gradient is present - analogous to the formation of the horseshoe vortex (HV). The vortex pair initially has the same magnitude of vorticity on the leading edge. On the suction side, the red vortex has the same sense of rotation as the residual swirl in the suction side passage and is

therefore strengthened. Conversely on the pressure side, the blue vortex has the same sense of rotation as the residual swirl in the pressure side passage and is therefore strengthened.

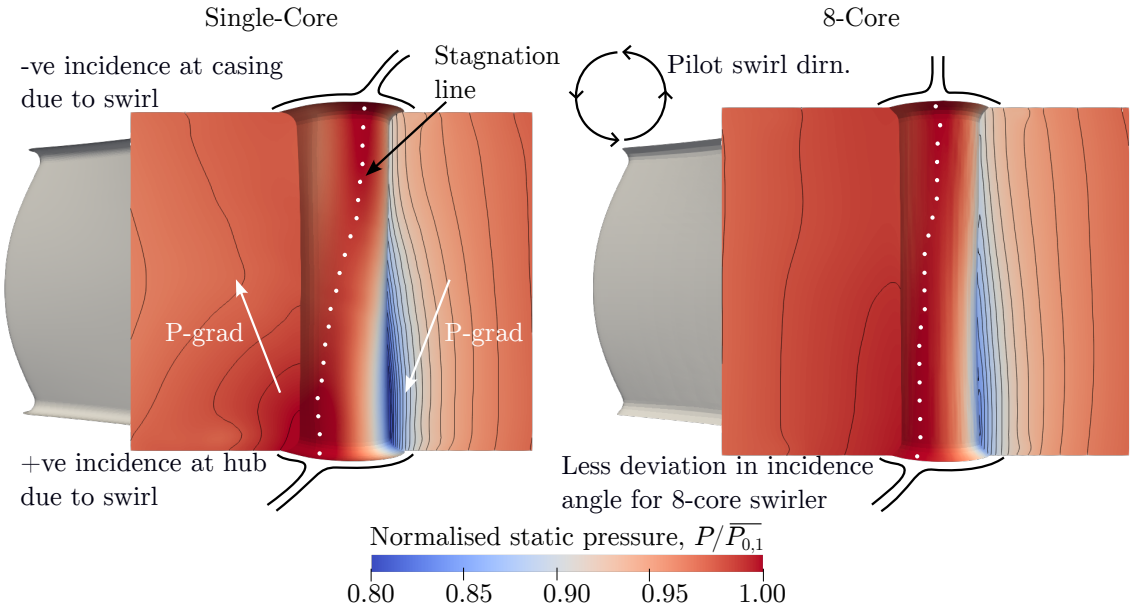


Figure 5.10: Normalised static pressure distribution in the passage and on the unshielded vane leading edge for the single-core swirler (left) and 8-core swirler (right). Stagnation point evaluated at multiple spanwise locations shown as white dots

The inlet flow deviations also alter the potential field of the unshielded NGV. In a non-swirling inflow case, uniform flow impinges on the leading edge at a radially-constant incidence angle, giving a vertical stagnation line. In the presence of swirl, flow enters with non-zero yaw angle distributions as shown in Fig. 5.7 and 5.8 above. This results in positive incidence near the hub, shifting the stagnation line towards the pressure side. This leads a higher pressure towards the hub pressure side and greater flow acceleration over suction side, resulting in a lower static pressure (compared to flow at zero incidence). Conversely, near the casing, the positive yaw angle results in a negative incidence angle, which shifts the stagnation line towards the suction side. There is a higher static pressure near the casing suction side, while greater flow acceleration over the casing pressure side results in a lower static pressure on the pressure side. Fig. 5.10 shows this skewing of the stagnation line and the static pressure distribution near the leading edge of the unshielded NGV for both swirlers. The static pressures for both cases have been normalised by the upstream mass-

averaged total pressure to allow direct comparisons between both plots. This creates a radial static pressure gradient near the unshielded vane surfaces. Towards the middle of the passage, this radial gradient is less pronounced. The gradient is also greater in the case of the single-core swirler compared to the 8-core swirler, although a slight shift in stagnation line and the radial pressure gradient are still evident in the latter, due to the non-zero yaw angle deviation.

5.3.2 In the Vane Passages

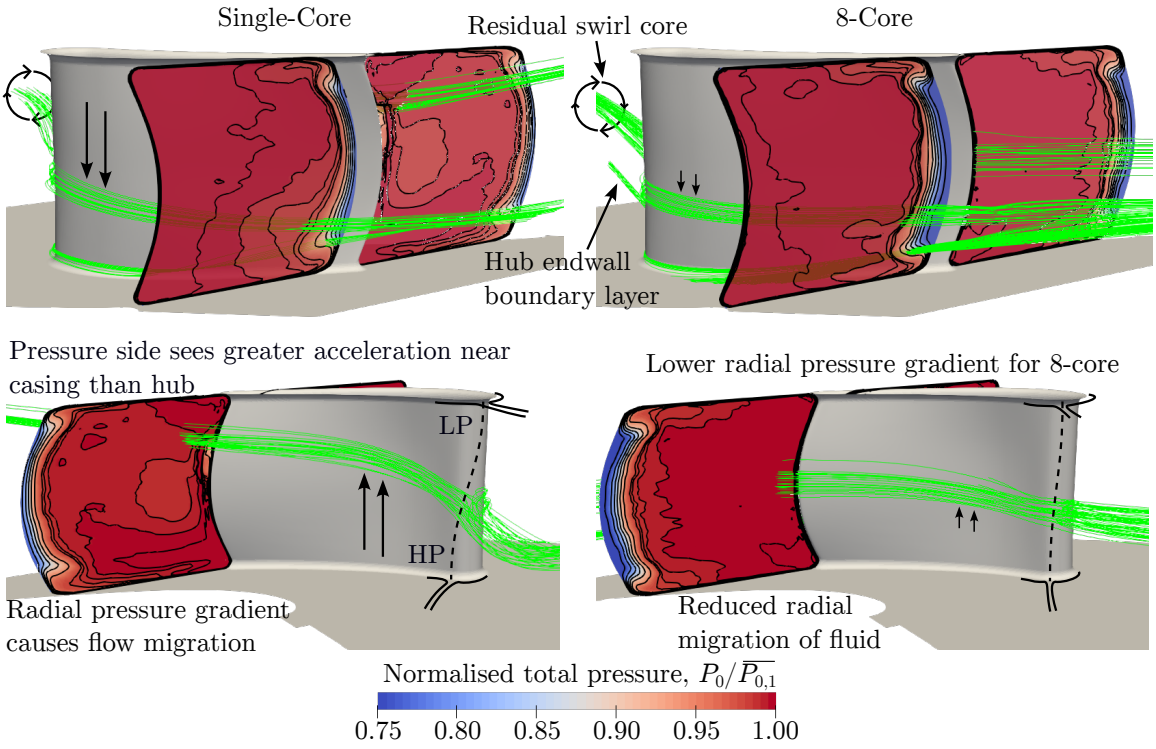


Figure 5.11: Normalised total pressure distribution in the passage near the unshielded vane trailing edge for the single-core swirler (left) and 8-core swirler (right). Flow migration of streamlines in the freestream and in the hub endwall boundary layer shown in green

The radial pressure gradient results in the migration of fluid near the vane surfaces. On the suction side, flow migrates from the casing to the hub, while on the pressure side, flow migrates from the hub to the casing, as evidenced by the streamlines (shown in green) in Fig. 5.11. This effect is less pronounced in the case of the 8-core swirler.

The migration of the midspan vortex can also be seen in contour plots of normalised total pressure and streamwise vorticity in Fig. 5.12. The low total pressure cores of the midspan vortex (A) are clearly seen in the single-core swirler case, with

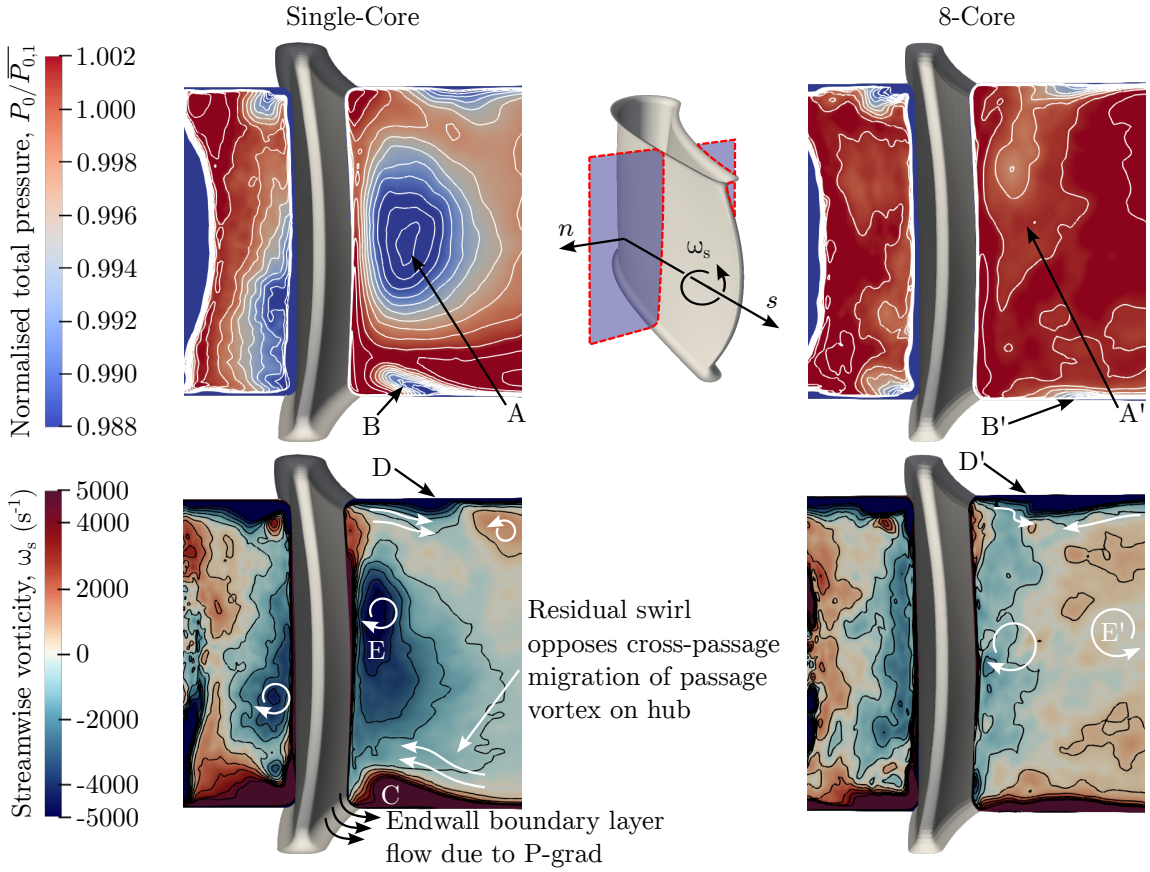


Figure 5.12: Contours of normalised total pressure (top) and streamwise vorticity (bottom) at axial distance $x/C_{ax} = 0.739$

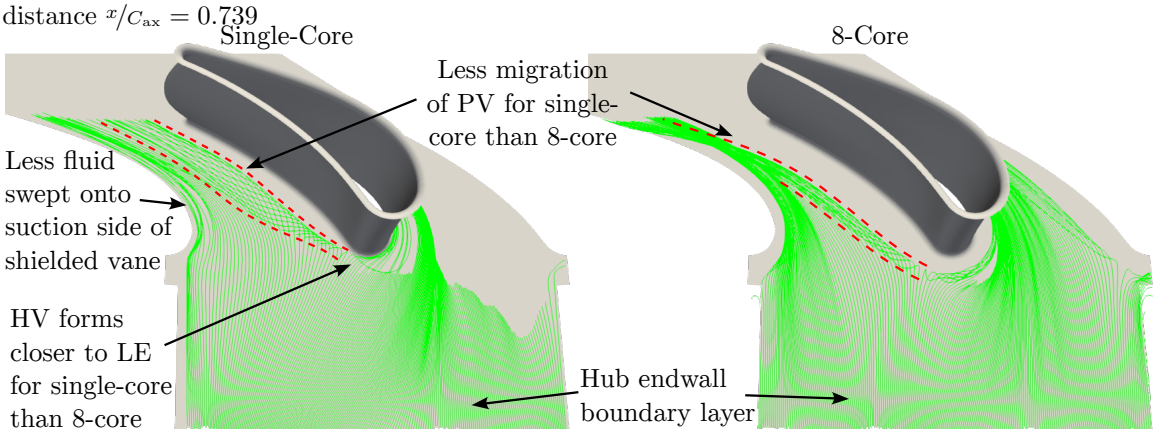


Figure 5.13: Streamlines along the hub endwall boundary layer showing the migration of the passage vortex for the single-core swirler (left) and 8-core swirler (right)

the pressure side leg located closer to the casing, while the suction side leg is located closer to the hub. These vortex cores still remain coherent within the vane passages and have significant vorticity.

On the hub endwall, this residual swirl opposes the cross-passage secondary flow and passage vortex migration (B) from the pressure side of the unshielded vane to the suction side of the shielded vane. The mean location of the passage vortex for

the single-core swirler (B) is therefore closer to the pressure side of the unshielded vane compared to the 8-core swirler case (B'). This effect is seen by the thickening of positive streamwise vorticity towards the vane pressure side (C). This can also be seen in the boundary layer streamlines in Fig. 5.13. On the casing endwall, the residual swirl is aligned with the cross-passage secondary flow and the casing passage vortex for the single swirler (D) migrates further across the passage than the 8-core swirler (D'). This is partially due to the higher clockwise residual swirl in the former (E). However, the latter case also has freestream residual swirl in the counter-clockwise direction due to the main swirlers; see Fig. 5.5 and 5.8. This merged residual swirl core is located towards the suction side of the shielded vane (E') and opposes the migration of the casing passage vortex.

In the suction side passage, the suction side leg of the hub and casing horseshoe vortices can be seen as small concentrated vortices with the opposite sense of rotation as the passage vortices. In the case of the single-core swirler, the hub SS leg and passage vortex have migrated further up the suction surface compared to the 8-core swirler. This earlier migration of the hub secondary flows is due to the increased cross-passage static pressure gradient along the hub endwall. This is a result of the skewed stagnation line seen in Fig. 5.10. Since the degree of skew scales with swirl intensity, the hub secondary flows in the case of the 8-core swirler experience a lower pressure gradient and therefore migrate later compared to the single-core swirler case. This shifting of suction side secondary flows that scale with swirl intensity have also been observed in experiments; see Fig. 6.5.

5.3.3 At the Trailing Edge Exit Plane

The effects of the swirl cores can be seen to persist far into the passage and even downstream of the NGV. Fig. 5.14 shows the experimental validation of the time-averaged LES results for the single-core swirler. Experimental measurements were carried out by Jacobi et al. [120]. The sampling plane is 17% of the axial chord length downstream from the trailing edge. There is very good agreement between

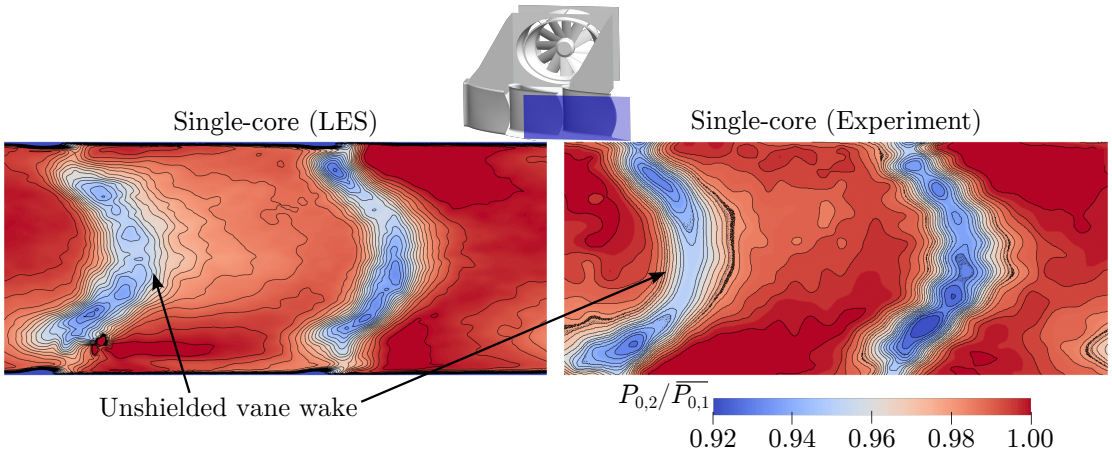


Figure 5.14: Experimental validation of LES simulation for the the single-core swirler case. Contours of normalised total pressure at the exit plane obtained from time-averaged LES (left) and experiments (right). Local total pressure is normalised by the upstream total pressure

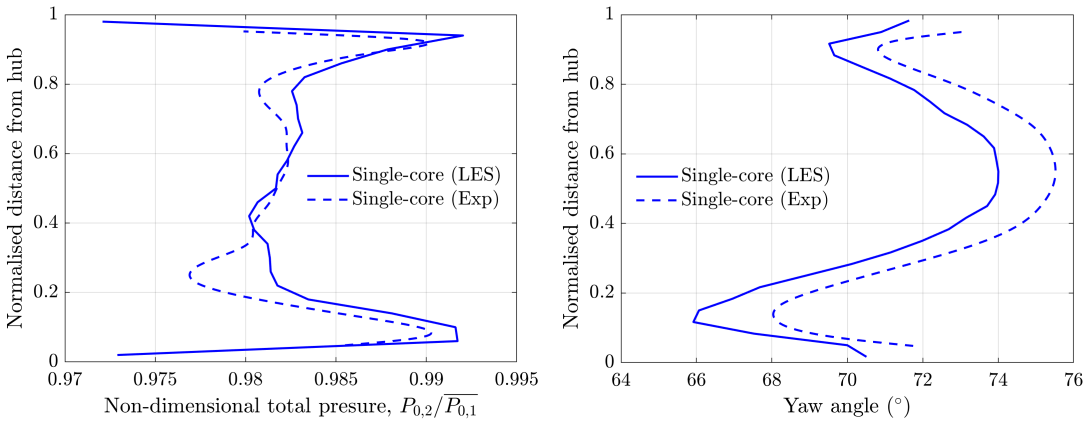


Figure 5.15: Mass-weighted pitchwise average profiles of total pressure normalised by the upstream total pressure (left) and yaw angle (right) measured at the exit plane for the single-core swirler case

the experimental validation results and the time-averaged LES results. The wake of the shielded vane has a higher loss compared to the unshielded vane. This is due to the presence of the combustor wall upstream of the shielded vane, which undergoes vortex shedding. These shed vortices impinge on the shielded vane and are convected over its surfaces and end up in its wake.

Near the hub, the wake of the unshielded vane also appears shifted tangentially and the hub has a higher loss core compared to the casing. The former is due to the residual swirl opposing the migration of the hub endwall boundary layer fluid and passage vortex, resulting in underturning of the hub loss core; see the underturned yaw angle profile in Fig. 5.15. The latter is due to the additional contribution of the midspan vortex, which migrates towards the hub on the suction side due to the radial

pressure gradient. This can be seen following the streamlines in Fig. 5.11, which originate from the swirl core and the hub endwall boundary layer. These streamlines impinge on the leading edge, accelerate over the suction side while migrating radially, and eventually meet at the trailing edge.

In the pressure side passage, the freestream shows significant loss distribution. This is due to the residual swirl core, which remains as a large coherent structure even after acceleration through the passage. This swirl core is highly unsteady and precesses across the passage freestream, as will be shown in Fig. 5.22 of §5.4, where instantaneous snapshots track its location. When time-averaged, the loss arising from this swirl core is 'smeared' across its precession path.

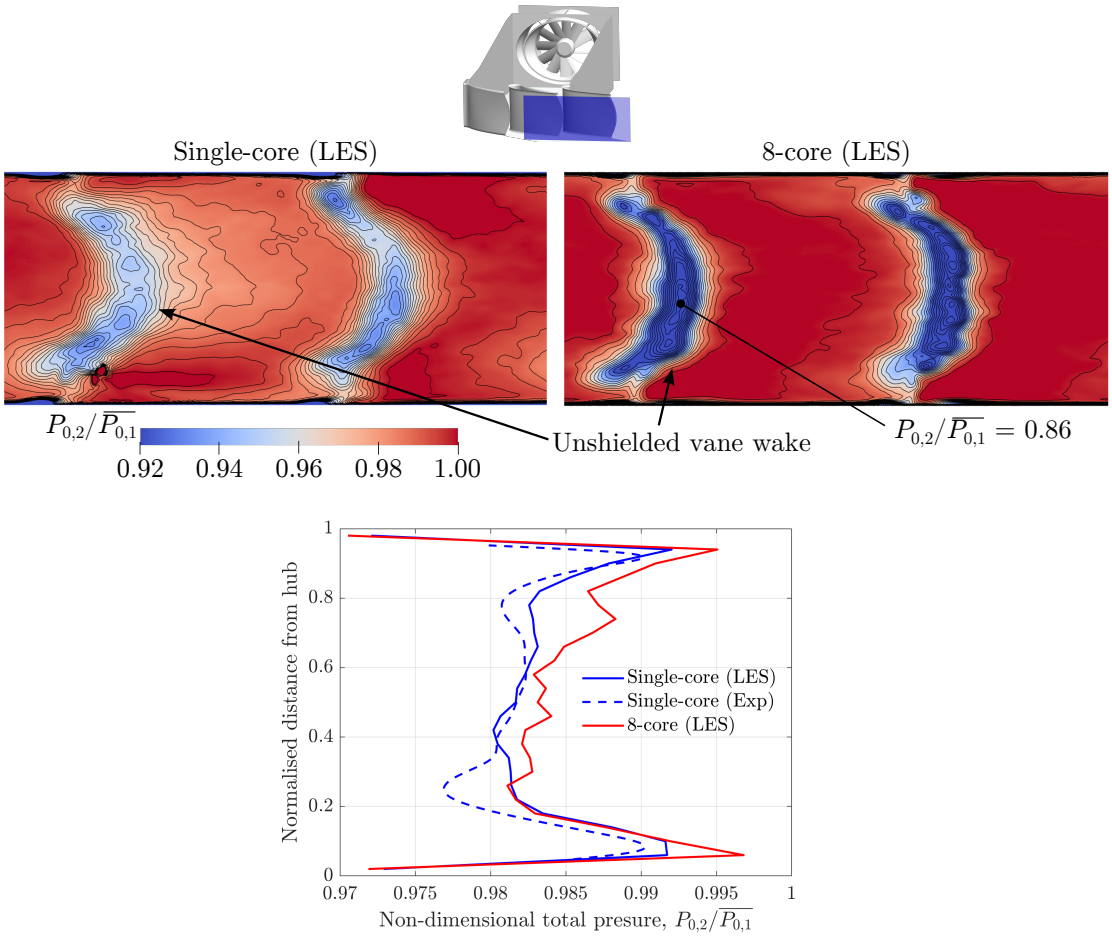


Figure 5.16: Top: Contours of normalised total pressure at the exit plane obtained from time-averaged LES for the single-core swirler (top left) and 8-core swirler (top right). Bottom: Mass-weighted pitchwise average profiles of total pressure at the exit plane. Total pressure is normalised by the upstream total pressure

In the case of the 8-core swirler, the freestream loss is lower, the distribution is

more uniform, and the wake of the unshielded vane is sharper and has a higher loss. The mass-weighted pitchwise average profiles of total pressure show that the overall loss across whole exit plane is lower compared to the single-core swirler.

5.4 Unsteadiness of the Freestream and Secondary Flows Around the NGV

5.4.1 Unsteadiness at the Inlet Plane to the NGV

The previous section studied the time-averaged flow field and its effects on the NGV. In reality, the incoming flow is highly unsteady, with significant pressure fluctuations

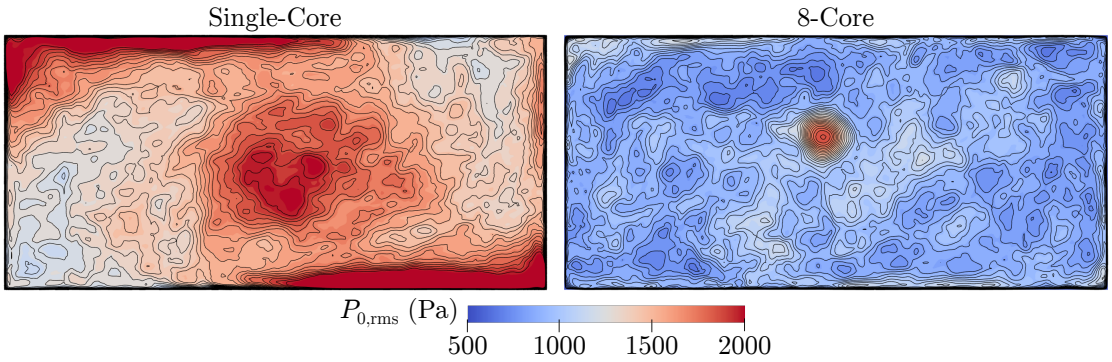


Figure 5.17: Contours of RMS of total pressure at the NGV inlet plane obtained from time-averaged LES for the single-core swirler (left) and 8-core swirler (right)

as shown in Fig. 5.17. The RMS fluctuations in total pressure at the inlet are significantly higher in the single-core swirler case compared to the 8-core swirler case, and are concentrated around the residual swirl core.

The nature of these fluctuations can be seen in Fig. 5.18, which are instantaneous snapshots of normalised total pressure at the inlet plane. The snapshots of normalised total pressure for the single-core swirler are remarkably similar to its equivalent time-averaged contour. The residual swirl core is present in every frame and is consistently the region with lowest total pressure. Its position is tracked as a minima in total pressure and the pathlines are shown in white. Its precession is confined to slightly off-centre of the plane, towards the unshielded vane pressure side.

The 8-core swirler however does not show such consistency. While its time-

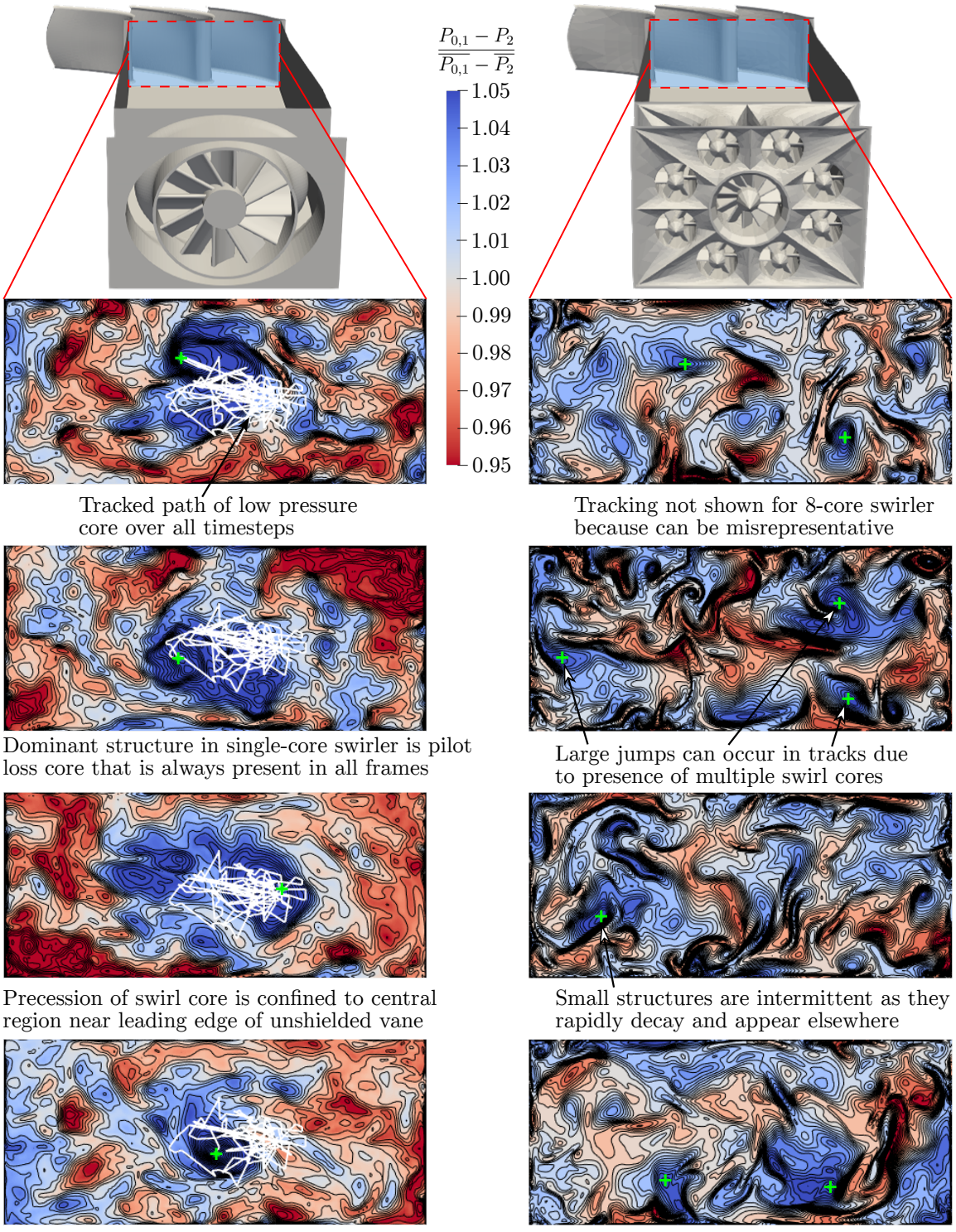


Figure 5.18: Instantaneous snapshots of normalised total pressure at the inlet plane to the NGV looking from upstream to downstream. Tracks of the swirl core migration for the single-core swirler are shown in white and approximate swirl core centres are shown as green crosses

averaged contours suggests the presence of three residual swirl cores, these cannot be seen in the instantaneous snapshots. Multiple swirl cores can be seen in some frames, however these are intermittent and rapidly decay, making the number of cores

present at any one time variable. The RMS fluctuations in the single-core swirler in the time-averaged plots are therefore dominated by the pilot loss core. Fluctuations in the 8-core swirler are due to multiple smaller loss cores that are distributed across the entire plane. These loss cores are residuals from complex interactions and merging between co-rotating and counter-rotating swirl cores.

5.4.2 Unsteadiness of Secondary Flows

The swirl core also alters the flow field along its entire length by imparting angular momentum to the surrounding boundary layers. On the downwash side of the vortex, the boundary layer has a higher velocity and is thinner compared to the upwash side of the vortex. The magnitude and location of these effects vary with the position of the swirl core, resulting in secondary flows which are highly unsteady.

5.4.2.1 Oscillations in the Position of the Horseshoe Vortex

The oscillatory nature of horseshoe vortex was studied by Baker for laminar [41] and turbulent flows [171] and it was found that the horseshoe vortex *system* consisted of a varying number of vortices that depended on the Reynolds number. He also studied the oscillation frequencies for varying Reynolds number and boundary layer thickness and measured a Strouhal number (non-dimensional frequency) of $\mathrm{Sr} = 0.53$ for Reynolds number of $\mathrm{Re} = 1.4\mathrm{E}4$, with slight a increase in Sr for increasing Re. This is consistent with Lin et al. [42] who investigated Re up to 5000 with $\mathrm{Sr} = 0.35$. They identify four different flow regimes as a function of Reynolds number, Re, based on the freestream velocity and the width of the vertical junction. These are the steady vortex system for $\mathrm{Re} < 1300$, the periodic oscillation system with small displacement for $1300 \leq \mathrm{Re} < 1700$, the periodic breakaway system for $1700 \leq \mathrm{Re} < 5000$, and the turbulent system for $\mathrm{Re} \geq 5000$.

The Reynolds number for the single-core swirler was measured to be $\mathrm{Re} = 1.6\mathrm{E}5$, which places this in the turbulent regime of the studies above. This value of Re was estimated from the mean axial velocity, density, and dynamic viscosity at the inlet

plane, and the vane leading edge diameter. However the presence of the swirl core results in local changes in the fluid velocity and boundary layer thickness close to the horseshoe vortex, which have been identified as the governing parameters influencing the location of the saddle point in the horseshoe vortex system; see §2.2.1. These local changes also fluctuate with the swirl core's precession, thus making it difficult to predict the 'true' values for evaluating the Reynolds number. Nevertheless, the value estimated for these cases is an order of magnitude larger than that of Baker [41], so the velocity would have to decrease by more than a factor of 10 to change flow regime.

Based on the values from literature and the monotonic increasing relationship between Sr and Re, it can be inferred that $\mathrm{Sr} > 0.53$ for this LES study. This gives a vortex oscillating frequency greater than 1040 kHz. Indeed, this was measured by Shaikh [132] to be in the range 1.1 - 2.0 kHz, giving a Strouhal number of 0.55 - 1.0. §5.4.3 carries out spectral analysis on the frequency of oscillation of the horseshoe vortex system and it is shown that the dominant frequencies are in the sub-1 kHz range, with decreasing power content at higher frequencies. This lends confidence that the observed fluctuations in the position of the horseshoe vortex are predominantly due external factors, such as the swirl core precession and not its self-excited instability.

That is not to say that this self-excitation does not exist. However, its identification is difficult since the frequency range over which it occurs gives a period of 5 to 10 frames (export frequency of domain is 10 kHz). The flow domain is populated with coherent structures, some of which originate from the boundary layer due to separation and roll-up, while others are convected from the freestream. During this period, multiple structures from upstream will have interacted with the horseshoe vortex, impinging and merging with it.

This is visualised in Fig. 5.19 as a sequence of images taken 200 µs apart ($T_s = 100$ µs). The sequence is taken from the single-core swirler case, however similar observations can be made for the 8-core swirler case, so it is not repeated. Initially,

the primary HV (A), secondary HV (B), and corner vortex (C) are visible. The primary HV moves away from the LE while the secondary vortex moves towards the LE. These two vortices then amalgamate at time $4T_s$. This is the new primary vortex (A). At the same time, an upstream structure impinges on the vane LE (D). This is convected downwards onto the hub endwall at time $6T_s$, where it wraps around the LE, temporarily forming a new horseshoe vortex ahead of the primary vortex. At time $8T_s$, the new HV (D) migrates upstream away from the LE, while primary HV (A) migrates downstream towards the LE. At time $10T_s$, they merge together and to form the new primary HV (A) and it moves towards the LE. At time $12T_s$ another upstream structure (E) is seen and is very quickly convected onto the hub endwall and merges with the primary HV (A) at time $14T_s$. This process of an external flow structure forming a new horseshoe vortex ahead of the primary vortex, their migration, and eventual merging appears to be at least partly responsible for the oscillation of the horseshoe vortex.

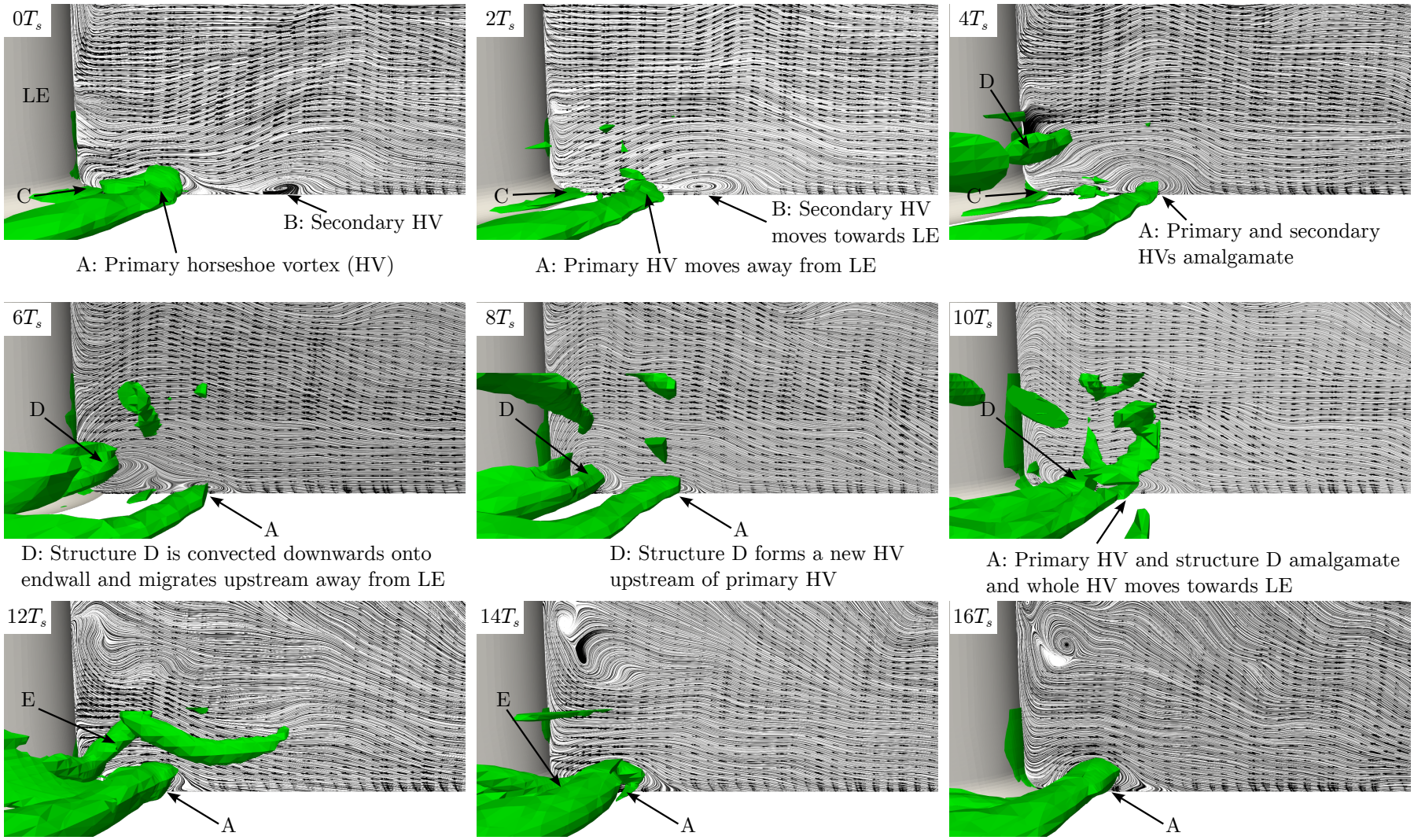


Figure 5.19: Sequence of images for the single-core swirler case at the the vane leading edge near the hub, showing the migration of the horseshoe vortex (green). Spanwise cross-section shows streamlines of flow. Export timestep, $T_s = 100\,\mu s$

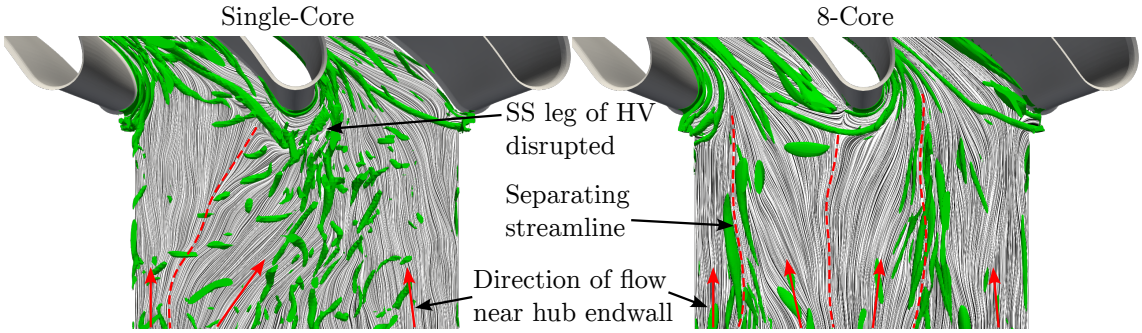


Figure 5.20: Migration of coherent structures along hub endwall for the single-core swirler (left) and 8-core swirler (right). Separation streamlines along hub endwall are shown in red

Fig. 5.20 shows a single instance in time of the streamlines near the hub endwall and identifies coherent structures at a threshold value of Q-criterion. Separating streamlines are shown in red. The single-core swirler has much higher swirl intensity and greater yaw angle deviation. This leads to a skewing of the separation line near the hub endwall, causing most of the smaller structures near the boundary layer to be convected towards the suction side. These structures impinge on the vane leading edge and the horseshoe vortex, disrupting it, and in this case the suction side leg of the horseshoe vortex is no longer visible at the threshold value of Q-criterion.

In the case of the 8-core swirler, this separating streamline is less skewed. The pilot swirl core counter-rotates against the two residual main swirl cores, resulting in two additional separating streamlines, one in each passage. At this threshold value of Q-criterion, most of the structures appear to form in the boundary layer along these two streamlines and are axially aligned. These structures then travel along the two streamlines into either passage and interact with the suction side and pressure side legs of the horseshoe vortex.

Another possible influence on the oscillation of the horseshoe vortex is the precession of the swirl core. Observations of the migration pattern of the horseshoe vortex show that it migrates closer to the leading edge when the swirl core impinges on the unshielded vane's leading edge. Conversely, the horseshoe vortex migrates further away when the swirl core precesses away from the leading edge. This is shown in Fig. 5.21 with two timesteps for the single-core swirler case. The swirl core is identified using the pressure-minimum criterion (shown in red) and secondary flows are iden-

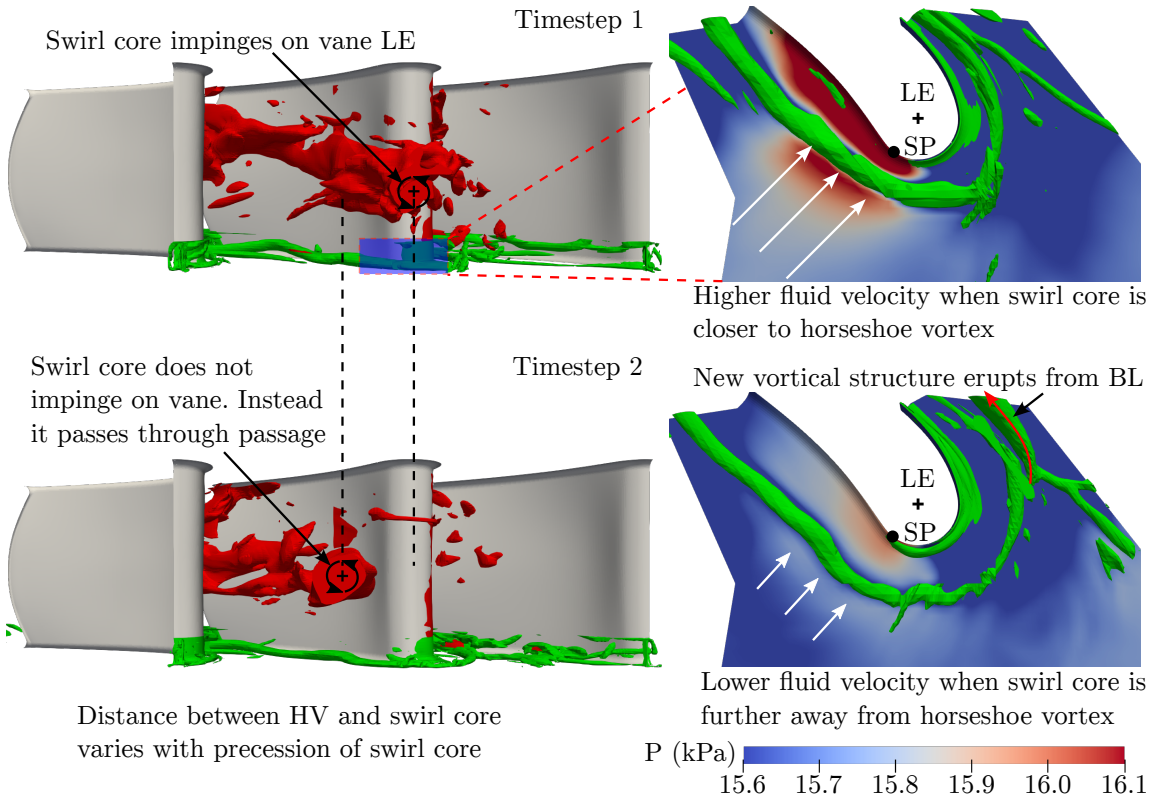


Figure 5.21: Pitchwise precession of the total pressure loss core (red) and corresponding migration of the horseshoe vortex (green) at two timesteps, obtained from the single-swirler case. Horseshoe vortex identified by Q-criterion. Static pressure distribution on the hub endwall shown (right). Stagnation point (SP) shown as a black dot

tified using the Q-criterion (shown in green). This could be due to a local change in fluid velocity and boundary layer thickness, however the exact mechanism for this migration and the coupling between the swirl core and the horseshoe vortex is not fully understood. Spectral analysis is performed in §5.4.3 to identify similar peaks with the precession of the swirl core.

The suction side leg of horseshoe vortex is consistently smaller in size and streamwise vorticity magnitude than the pressure side leg across all frames. Its size and location is also more variable and frequently breaks down such that it is not detectable in some frames. This is due in part to acceleration around leading edge which causes vortex stretching and a reduction its size. The positive incidence on the hub due to swirl increases the distance over which the suction side leg must accelerate compared to zero incidence. Furthermore, Fig. 5.20 showed that small structures are convected towards the suction side leg of the horseshoe vortex. Irregular bursts of

these small structures can be seen when they impinge on and interact with the SS leg, causing it to breakdown and resulting in an irregular shape. The increased mixing and turbulence also causes it to dissipate and become more diffuse, consistent with observations by other workers [29].

In the case of the 8-core swirler, the suction side leg of the horseshoe vortex appears more stable (not shown), i.e. it does not appear to breakdown as frequently as in the single-core swirler case. This is likely due to the modified separation lines on the hub endwall as shown in Fig. 5.20 in which structures are no longer convected to impinge directly onto the HV, as is the case in the single-core swirler, but instead are are convected into the passage. However in movies of the HV, its position has still been observed to oscillate, although it is difficult to correlate this with any external event since there is no persistent swirl core to track.

5.4.2.2 Oscillations in the Position of the Passage Vortex

The passage vortex is also highly unsteady, migrating across the entire pitch under the action of the precessing swirl core. The timesteps shown in Fig. 5.22 are for the single-core swirler and are at the same instance in time as those shown in Fig. 5.21. The coherence of the swirl core even after accelerating through the passage can be seen. The sense of rotation of the swirl core opposes the migration of the passage vortex. The magnitude of swirl is dependent on the proximity of the swirl core to the passage vortex.

In timestep 1, the swirl core does not impinge on the vane leading edge, instead flowing completely into the passage and precesses towards the hub. This is sufficiently close to the passage vortex such that the swirl velocity prevents it from migrating towards the shielded vane's suction side. In fact, the contour of static pressure shows that there is actually a local pressure gradient towards the pressure side of the unshielded vane. The passage vortex therefore remains attached to the pressure side and eventually interacts with the trailing edge wake of the unshielded vane. In timestep 2, the swirl core impinges on the leading edge of the vane, forming a midspan vortex

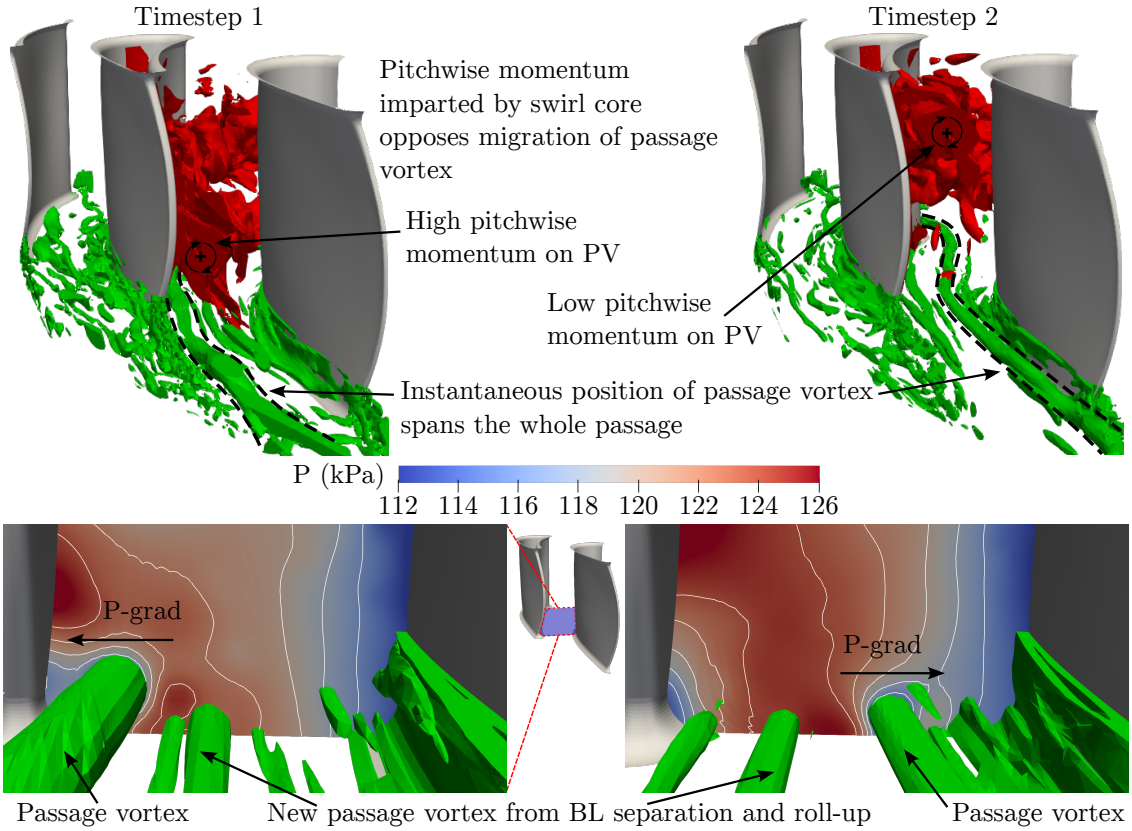


Figure 5.22: Radial precession of the total pressure loss core (red) and corresponding migration of the passage vortex (green) at two timesteps, obtained from the single-swirler case. Passage vortex identified by Q-criterion. Static pressure distribution near the hub trailing edge shown (bottom). Secondary flow structures on the casing are not shown as the focus here is on the hub flow

that migrates towards the casing, reducing the swirl velocity opposing the passage vortex. The pressure gradient now acts towards the suction side of the shielded vane.

5.4.3 Spectral Analysis of Unsteady Features

The previous sections identified sources of unsteadiness around the NGV. Significant total pressure fluctuations were measured just downstream of the pilot swirler and at the NGV inlet plane due to the precessing swirl core. The position of the horseshoe vortex has been observed to fluctuate in time and this is thought to be due to a number of factors, e.g. interactions with upstream structures, swirl core precession, and self-excited instability. This section studies the spectra measured at different locations around the flow domain to identify similar peaks and correlate events. It is important to determine the frequency content of these fluctuations, especially if there is significant content at low frequencies. From a heat transfer perspective, these

low frequency fluctuations can result in significant temperature change. Finally, comparisons between numerically and experimentally measured spectra serve to identify frequency content that is not due to facility-related resonance; see §7.5.

§5.4.2.1 showed that the position of secondary flow features such as the horseshoe vortex and passage vortex is be correlated with the position of the swirl core. This can be measured by comparing the power spectral densities (PSDs) of the radial distance of the horseshoe vortex from the leading edge with the pitchwise precession of the swirl core. The latter is obtained from the tracks shown in Fig. 5.18.

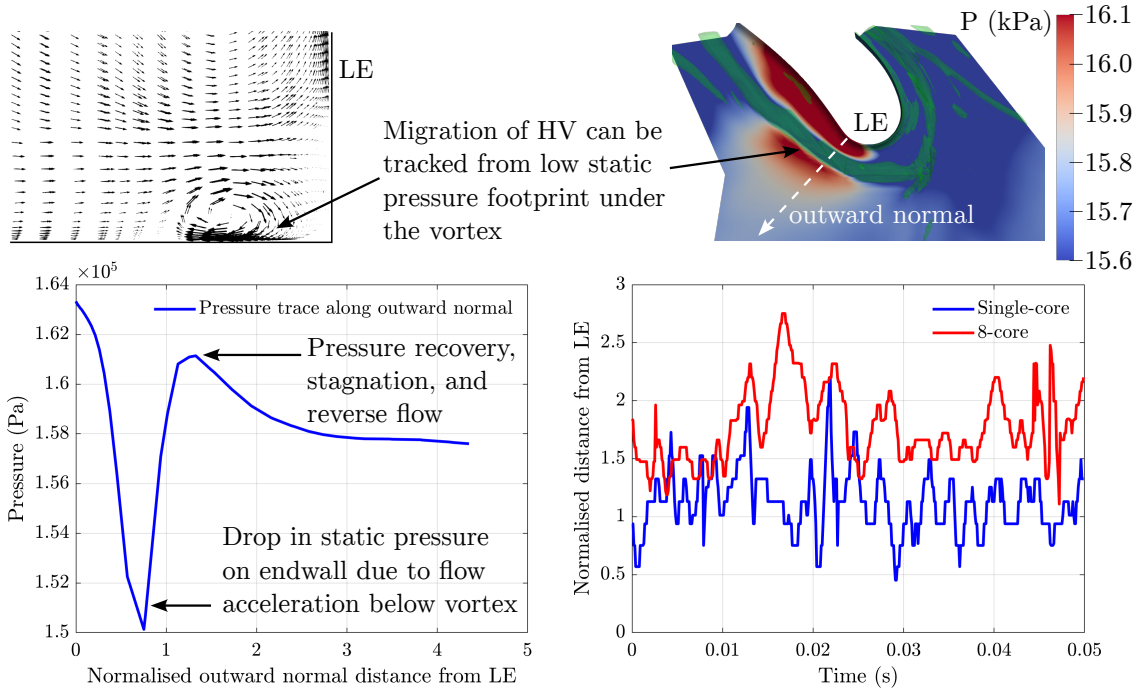


Figure 5.23: Time history of the position of the horseshoe vortex for both swirler cases. Position tracked by its instantaneous endwall static pressure distribution as a function of increasing outward normal distance measured from the blade surface around the vane leading edge (left)

The former is tracked by searching for the minima in static pressure along the outward normal of the vane leading edge, as shown in Fig. 5.23. This minima is due to acceleration of the boundary layer fluid under the vortex. The time history of the fluctuating position of the horsehoe vortex is shown for both swirler cases. It should be noted that tracking the precessing swirl core is only possible for the single-swirler geometry, where the loss core is well-defined.

Following the analysis of Lin et al. [42], who studied horsehoe vortex formation

at a vertical plate-base plate junction, the streamwise velocity at the time-averaged horsehoe vortex core was also measured for spectral analysis. The coordinates of the mean HV core was obtained from time-averaged LES isosurfaces of Q-criterion. Fig. 5.24 shows the time history of the streamwise velocity at this point for both swirler cases. This quantity was included because it is a more sensitive measure of oscillations in the horseshoe vortex system than the tracking of static pressure minima. Also

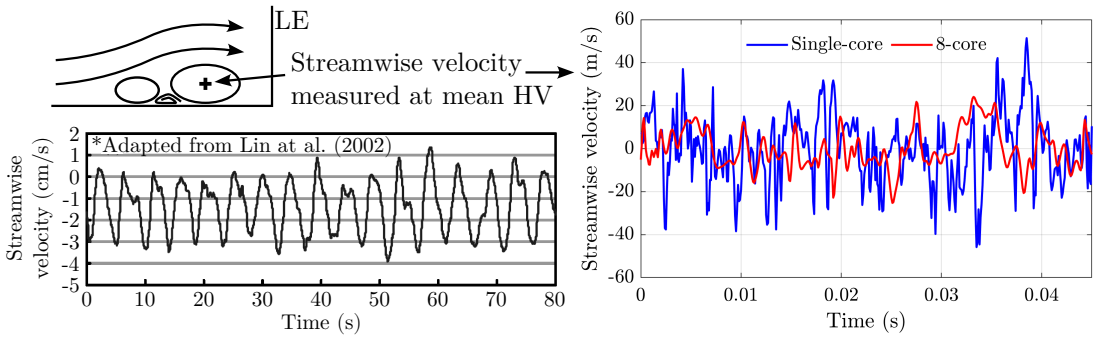


Figure 5.24: Time history of streamwise velocity in the periodic breakaway region, from Lin et al. [42] (left). Time history of the streamwise velocity measured at the centre of the mean horseshoe vortex location for both swirler geometries (right)

shown is a sample time history measurement of streamwise velocity taken from Lin et al. [42], for flow in the periodic breakaway regime. The latter shows a very clean signal with a well-defined frequency at 0.2 Hz as the inlet flow was uniform and well-conditioned with defined flow velocities and boundary layer thickness. Conversely, the signal measured from LES is much noisier due to the random interactions of the horseshoe vortex with large structures from upstream.

Fig. 5.25 shows the spectra of total pressure measured at Point 2 (see Fig. 3.20), the radial distance of the HV from the vane LE, the streamwise velocity at the HV core and the pitchwise precession of the swirl core. The spectra of total pressure measured at $4D$ downstream of the pilot swirler is repeated here; see Fig. 5.4. The spectra for both swirler cases are shown except the pitchwise precession of loss core for the the 8-core swirler, since there is no distinct pressure-minima criterion to track, and data was also not available just downstream of the single-core swirler.

The time history data for HV position, streamwise velocity at mean HV position, and PVC pitchwise position were obtained from exports of the flow domain, since

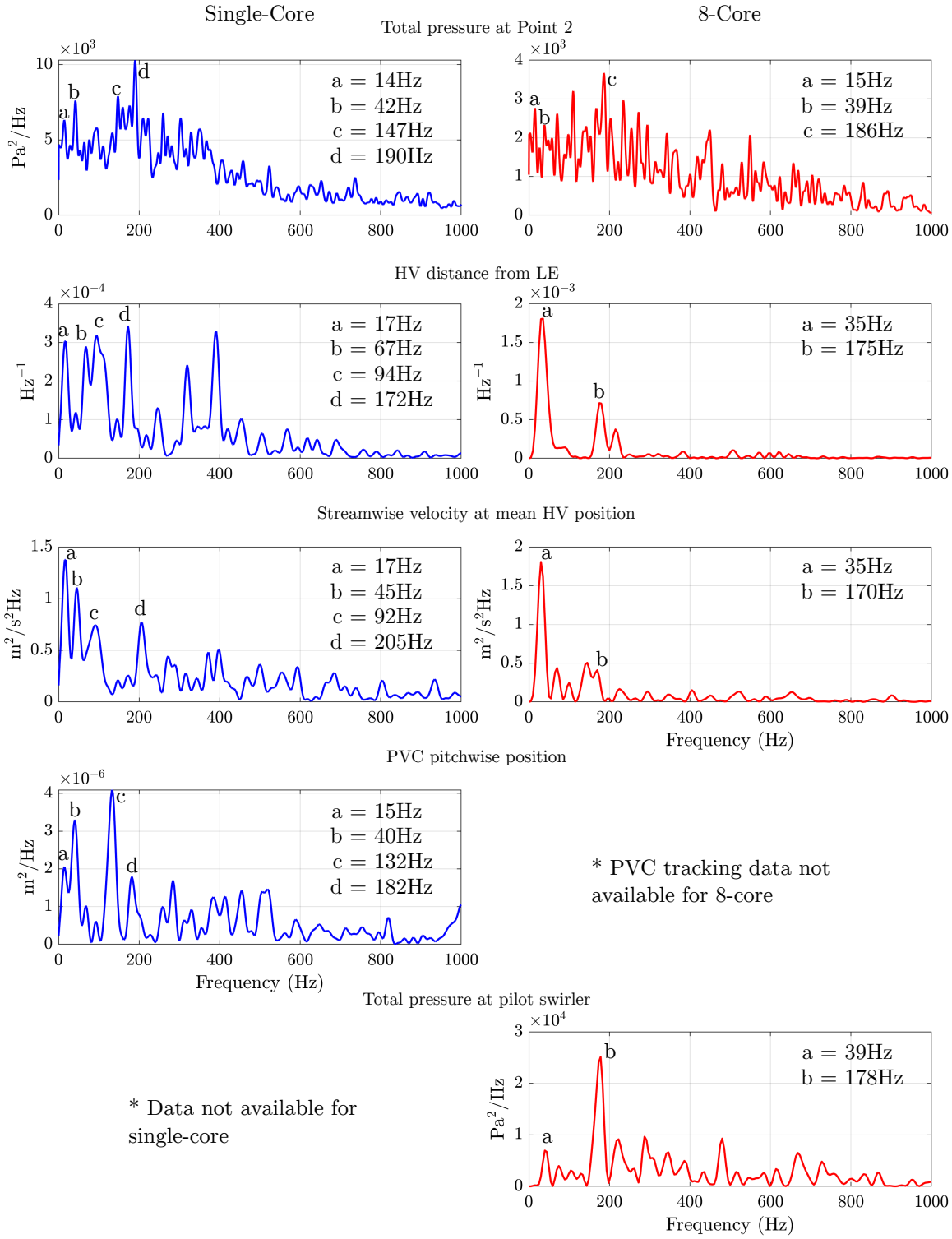


Figure 5.25: Power spectral densities (PSDs) of the total pressure measured at Point 2 (see Fig. 3.20, the horseshoe vortex distance from the leading edge, the pitchwise position of the swirl core at the NGV inlet plane, and the total pressure measured at $4D$ downstream of the pilot swirler (D is the diameter of the central blunt body of the pilot). PVC tracking data for the 8-core swirler and total pressure data near the single-core swirler are not available

these require some data manipulation to obtain the relevant quantities. The export frequency is 10 kHz and is limited to 1000 timesteps for the single-core swirler and 500 timesteps for the 8-core swirler case due to practical considerations on file size and file handling. This corresponds to a total sample duration of 0.1 s and 0.05 s respectively. The simulations themselves have a solution timestep of 4 µs (250 kHz) and the total solution durations were approx. 1 s for the single-core swirler and 0.45 s for the 8-core swirler. So the flow domain export constitutes a small window (0.1 s and 0.05 s) of the total solution duration.

The time history data for total pressure at Point 2 was sampled at a single point for each time step (250 kHz), across the whole solution duration. This means that for the single-core swirler, Point 2 has approx. 250 times more samples than the quantities obtained from flow domain exports, thus giving a higher frequency resolution. For the 8-core swirler, Point 2 has approx. 225 times more samples than flow domain exports. The frequency resolution, Δf, is the smallest frequency that can be resolved in the spectra. It is given as $\Delta f = {}^{f_s}/_{N}$, where f_s is the sampling frequency and N is the number of samples. This is why the spectra for total pressure at Point 2 has more peaks and the peaks appear sharper. Conversely, the frequency resolution of the spectra generated from the flow domain exports is lower and the spectra are more sensitive to uncorrelated events, e.g. a random breakdown in the HV that is uncorrelated with any other external event. The spectra of total pressure at Point 2 provides a baseline for comparison with other spectra as it has a higher frequency resolution and is less susceptible to these random events.

The spectra for both cases show significant frequency content in the sub-500 Hz region, with decreasing power at higher frequencies. Many of these peaks are concentrated in the sub-200 region. Some of these peaks are highlighted where they are shared across different measurement locations. In the case of the single-core swirler, all locations show a low frequency peak between 14-17 Hz. This is not simply non-stationarity in the flow domain export since the same peak can be seen in the spectra

of total pressure at Point 2. The spectra share other peaks over a broad band at 40-67 Hz and 172-205 Hz. It should be noted that the frequency resolution of the spectra generated from flow domain exports is approx. 10 Hz. This means that two peaks less than 10 Hz apart will simply appear as a single merged peak. A larger peak may also dominate over a smaller one, making it impossible to isolate them. The cause for these fluctuations is not known and further study is required to determine the coupling between these fluctuations.

In the case of the 8-core swirler, a similar low frequency peak is seen at 15 Hz in the spectra of total pressure at Point 2. However, the frequency resolution of the quantities derived from flow domain exports is 20 Hz. This results in a single merged peak that is seen across all spectra in the range 35-39 Hz. So it is not possible to say whether this peak at 15 Hz is present in these derived quantities due to the low resolution. There is another shared peak in the range 170-186 Hz, which was previously attributed to the frequency of precession of the vortex core of the pilot swirler. This is the dominant peak in both spectra of total pressure. While it also registers in the spectra of the HV's position and its streamwise velocity, it does not appear to be dominant. Thus it can be see that the horseshoe vortex oscillations are dominated by a peak at 35-39 Hz and, to a lesser degree, the precession of the vortex core. More sample points are required to obtain a higher frequency resolution for determining whether the low frequency peak at 15 Hz is registered at the horseshoe vortex and just downstream of the swirler.

It is also interesting to note that the magnitude of the fluctuations of the horseshoe vortex for the 8-core swirler is comparable to the single-core swirler but these are predominantly low frequency oscillations, whereas in the single-core swirler, there are peaks above 200 Hz of similar magnitude to the lower frequency peaks.

5.5 Summary

A numerical study using LES of the full combustor-turbine interface was carried out for two different swirler geometries: the single-core swirler and the 8-core swirler. The flow field downstream of the 8-core swirler was analysed and salient features such as the central toroidal recirculation zone (CTRZ) and precessing vortex core (PVC) were identified, with a precession frequency of 178 Hz. The flow field in this region experiences very high fluctuations in total pressure, predominantly confined to the boundary of the CTRZ, where the PVC is located. The single-core swirler results in a much higher turbulent kinetic energy, k, and swirl intensity, S, and rates of decay than the 8-core swirler at the same axial location downstream of the swirler. Some of this decay can be explained by the higher swirl intensity of the single-core swirler, leading to higher wall shear stress that dissipates angular momentum. However this does not fully explain the loss mechanism since the 8-core swirler can have a higher rate of decay of k despite consistently having a lower swirl intensity.

Time-averaged LES results were then studied and it was found that the single-core swirler resulted in a single large residual loss core at the NGV inlet plane. The swirl intensity is still very high, resulting in significant yaw and pitch angle deviations. Conversely, the 8-core swirler resulted in a weaker loss core (in terms of total pressure loss) and less flow angle deviation, however the inlet now has three swirl cores. The central core is due to the pilot swirler, while the two cores to either side are merged residual cores from the main swirler. The low pressure loss core impinges on the unshielded NGV's leading edge, forming a pair of counter-rotating vortical structures, called the midspan vortex. The yaw angle deviation alters the incidence angle from hub to casing, creating a radial pressure gradient near the vane surface, resulting in flow migration of the midspan vortex towards the hub and casing. In the case of the single-core swirler, the swirl core retains its coherence while in the passage and its precession results in significant loss distribution in the freestream at the exit plane. The 8-core swirler has much sharper wakes and a lower and more uniform loss

distribution in the freestream.

Analysis of the instantaneous results showed that flow around the NGV is inherently unsteady. The single-core swirler consistently showed a precessing low total pressure core, whereas the 8-core swirler showed a variable number of cores across different timesteps. The horseshoe and passage vortices were also observed to fluctuate in their positions and is thought to be correlated with the precession of the vortex core. To investigate this correlation, spectral analysis was carried out on the time histories of the total pressure at the inlet plane, the HV location, the streamwise velocity at the mean HV location, the precession of the swirl core (single-core swirler), and the total pressure near the pilot swirler (8-core swirler). It was found that there is significant frequency content in the sub-200 Hz band and many of these peaks are shared between the HV oscillation and the precessing vortex core for both swirler cases, particularly at 14-17 Hz (single-core swirler) and 35-39 Hz (8-core swirler).

Literature reviewed in §2.2.3 has shown that locations of peak heat transfer around the NGV are dominated by vortical motion. It is therefore plausible that these fluctuations in secondary flows are of sufficiently low frequency such that the surface temperature can change appreciably during a single period of oscillation, which can lead to unforeseen high cycle fatigue in these regions. Hence the need for studies of unsteady heat transfer in turbine blades is warranted.

Chapter 6
Time-Averaged Effects of Combustor Geometry on Uncooled and Film-Cooled NGVs

Previous studies by Jacobi and Rosic [147] and Shaikh [132] have shown that changing swirler geometries can result in significant changes in the levels and distribution of HTC. These studies were only carried out on uncooled vanes and with fewer swirler geometries than considered here. Shaikh [132] carried out experiments with the single-core and 8-core swirlers and found that the latter reduced the overall levels of HTC across the pressure and suction sides and the hub endwall. This was postulated to be due to the reduction in the size of coherent structures shed from the swirler and the overall levels of turbulent intensity, however this was not pursued further. The LES simulations carried out in this study for both geometries confirmed that the single-core swirler produced a single large residual swirl core, whereas the 8-core swirler produced three smaller vortex cores at the inlet to the NGV, with weaker flow distortions due to swirl and lower overall turbulent kinetic energy compared to the single-core swirler; see Fig. 5.6, 5.7 and 5.8. This experimental study investigates a wider range of swirler geometries for both the uncooled and film-cooled NGVs. Time-averaged experimental results for six different inlet conditions (clean inflow, turbulence grid, and four swirler geometries) are presented in §6.1 and §6.2 for the uncooled and film-cooled NGVs respectively. §6.3 discusses the main factors contributing to the distortion of the coolant film on the vane suction surface.

This study focuses on heat transfer on the suction side of the unshielded NGV. Ultimately, the quantities of interest must be scalable from low-temperature experiments

to engine conditions and provide designers with sufficient information to calculate the heat flux and wall temperature of the vane. Heat flux depends on the local HTC and driving temperature, given by Newton's Law of Cooling as:

$$q(t) = h(t)\left(T_{\text{ad}}(t) - T_w(t)\right)$$

where T_{ad} is the adiabatic wall temperature and h is the HTC, which is typically fixed by the aerodynamics. In the case of an uncooled vane, T_{ad} depends on $T_{0,\infty}$ and the recovery factor.

In the case of film cooling, T_{ad} now depends on mixing between the freestream total temperature, $T_{0,\infty}$, and the coolant total temperature $T_{0,c}$. It is reported as a non-dimensional figure of merit measuring the effectiveness of coolant coverage over a surface, η. The HTC is typically higher than an uncooled vane since discrete cooling holes can have locally very high HTC due to turbulent mixing around the counter-rotating vortex pair (CVP) exiting the cooling hole. Experiments without film cooling are carried out to draw comparisons between the uncooled and cooled vane since the effects of flow phenomena on the vane are easier to decouple and understand without the added complications of film cooling. This shows how the coolant film is influenced by flow phenomena, and by extension the combustor geometry.

Infra-red thermography and a transient method were used to resolve h and η across the vane suction side. Time-averaged results provide the overall levels and distribution of the heat load experienced by the vane. This is a heuristic approach to determining whether there are any (if at all) downstream effects as a result of changing swirler geometry, and if so, which swirler geometries are the most detrimental. It is necessary to answer these questions prior to investigating high-speed instantaneous results. This is indicative of regions of high heat transfer and low cooling effectiveness and needs to be accounted for in the design of NGV.

6.1 Heat Transfer on an Uncooled Vane

6.1.1 Clean Inflow and Uniform Turbulence

For the clean inflow case, which does not have a turbulence grid or swirlers, there are clear regions of very low HTC with sudden transitions to high HTC. This demarcates where the laminar boundary layer transitions to a turbulent one, although this is highly dependent on the local surface roughness and imperfections on the vane surface that may act as sudden trips, which generate wedges of turbulent flow that merge to form a turbulent boundary layer, e.g. spray paint splats. In the presence of film cooling and in the turbulence grid case (as well as all swirling inflow cases) this is not seen as the boundary layer is already turbulent.

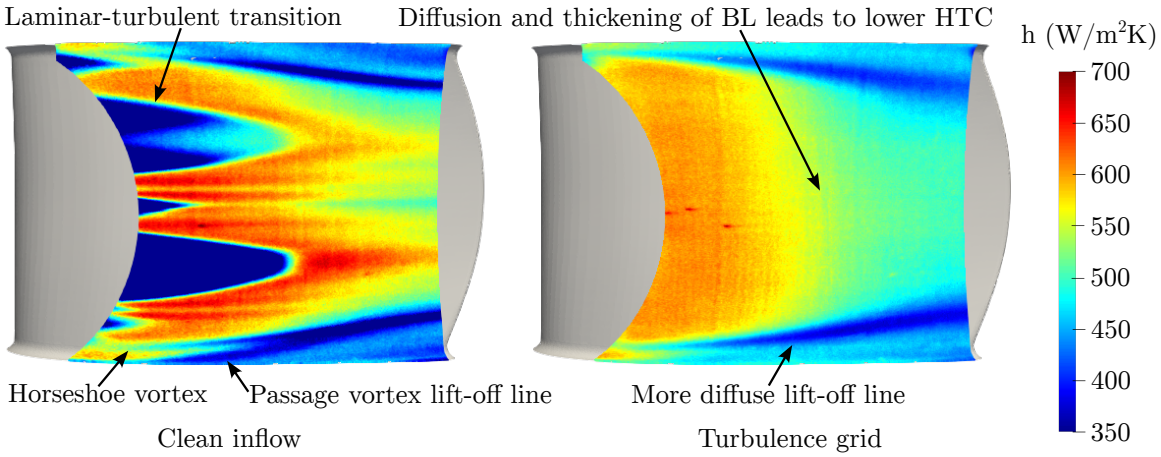


Figure 6.1: Contours of HTC on the unshielded vane's suction side for clean inflow (left) and turbulence grid (right)

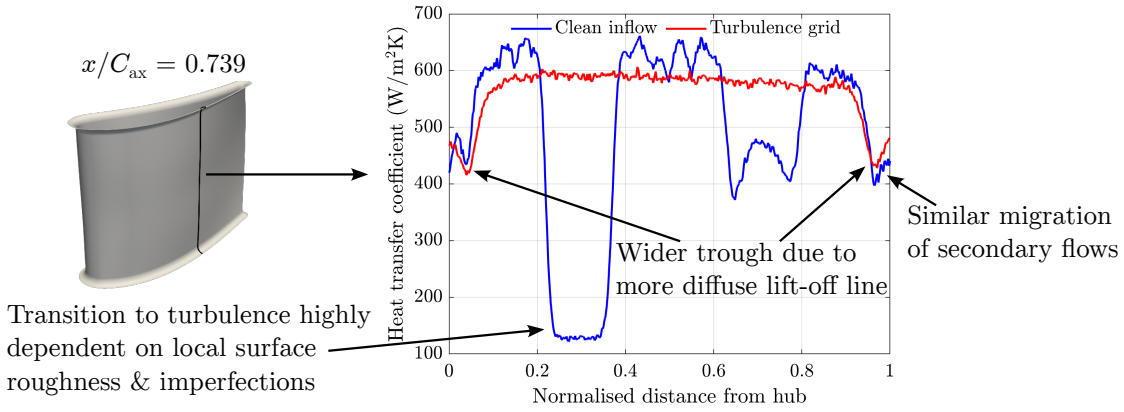


Figure 6.2: Spanwise distribution of HTC at axial distance, $x/C_{ax} = 0.739$, for clean inflow (blue) and turbulence grid (red)

In Fig. 6.1, two streaks of low HTC originating from the leading edge (LE) and from the endwall can be clearly seen in the clean case. These streaks intersect and merge on the suction side (SS), resulting in a single streak of even lower HTC. These are respectively the trajectories of the horseshoe vortex (HV) as it forms on the leading edge and wraps around the suction side and merges with the passage vortex (PV) forming a vortex system.

Fig. 6.2 shows multiple troughs near the hub endwall in the clean inflow case where the HV and PV still remain distinct from each other. The influence of secondary flows on heat transfer is much clearer in the clean inflow case, whereas the trajectories in turbulence grid case appear more diffuse and spread over a larger footprint on the vane suction side. This is seen as the widening of the troughs in h near the hub and casing which arises due to increased turbulence mixing out of the secondary flows. There is no augmentation to heat transfer around the secondary flows from increasing turbulence intensity which suggests that heat transfer in this region is dominated by vortical motion and not freestream turbulence. This is consistent with the findings of Thole et al. [102], Radomsky and Thole [43], Li et al. [93].

The case of uniform turbulence intensity represents the idealised test case, as used in a conventional design process of an NGV. This results in a uniform heat load across the vane and a symmetric distribution of passage vortex lift-off lines.

6.1.2 Single-Core Swirler and Reverse Single-Core Swirler

§5.2 showed that significant amount of residual swirl still present at inlet to the NGV cascade. The introduction of swirl into a flow necessitates a low pressure centre and increasing pressure with increasing radius to maintain rotational motion. When this low total pressure core impinges on the leading edge of the unshielded vane, a pair of counter-rotating vortices is formed, which wraps around the leading edge and then becomes aligned in the streamwise direction, hence forming the midspan vortex; see §5.3.1 and Fig. 5.9 for a detailed description of the formation of the midspan vortex. The deviation in yaw angle at the inlet also results in the positive incidence on the

hub and negative incidence on the casing. This shifts the stagnation point towards the pressure side on the hub and towards the suction side on the casing. Flow over the suction side is accelerated more on the hub than it is near the casing. Consequently for any axial location on the vane suction side, a radial pressure gradient exists from casing to hub, which causes flow to migrate in this direction, including the suction side leg of the midspan vortex.

In the case of the single-core swirler, this midspan vortex appears to be the largest structure present within the passage; even larger than the passage vortex, which makes sense given that it originated from the swirler whose diameter set the integral length scale. On the other hand, the passage vortex arises from boundary layer separation and roll up of the endwall boundary layer as it migrates across the passage. We might expect heat transfer on the vane surface to be dominated by these vortices and not freestream turbulence (although turbulence intensity at the inlet plane is very high). High uniform turbulence intensity simply leads to increased heat transfer everywhere on a flat plate. In contrast, the midspan vortex behaves like a secondary flow structure, and therefore shows a local increase in heat transfer on the downwash side and a local decrease on the upwash side of the vortex.

To demonstrate the effects of the midspan vortex and flow migration on heat transfer, results for the single-core swirler are compared against the reverse single-core swirler. The opposite direction of swirl still results in the formation of the midspan vortex, but flow on the suction side now migrates from hub to casing. The approximate location of peak h is traced by the dashed line; see Fig. 6.3. The regions of high heat transfer due to downwash are evident and the opposite directions of migration of the midspan vortex for each swirler can be seen clearly. Additionally, the footprint of the passage vortex lift-off appears more diffuse on the side where the residual swirl core migrates to, i.e. in the case of the single-core swirler, this is the hub passage vortex, and in the case of the reverse single-core swirler, this is the casing passage vortex. This may be due to several factors: (1) Increased turbulence which

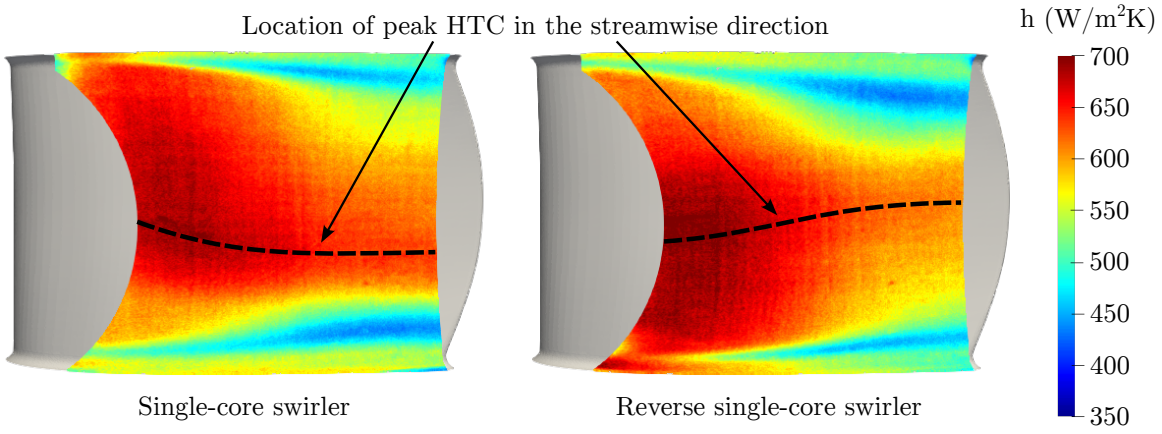


Figure 6.3: Contours of HTC on the unshielded vane's suction side for the single-core swirler (left) and the reverse single-core swirler (right)

results in more mixing between the PV and the surrounding fluid, thus being more diffuse in these cases. (2) The passage vortex remains distinct, but fluctuates in its position. When time-averaged, either of these phenomena will result in a footprint that is spread over the passage. (3) The midspan vortex counter-rotates against the passage vortex, which induces lift-off from the vane surface. (4) A thicker boundary layer on the upwash side of the passage vortex, resulting lower HTC. These results show that heat transfer on the suction side is dominated by the migration of the midspan vortex and secondary flows.

6.1.3 8-Core Swirler and 12-Core Swirler

LES results in §5.2 have shown that the the single-core swirler produces a single total pressure loss core that is persistent across all timesteps and when time-averaged. Residual levels of turbulence and swirl remain high throughout the passage, resulting in significant flow distortion around the vane. The footprint of the midspan vortex due to this loss core can be seen in Fig. 6.3 above. In contrast, the 8-core swirler produces multiple smaller structures with little coherence and which are intermittent any one timestep. When time-averaged, three small residual swirl cores are observed at the inlet plane to the NGV with a low level of swirling motion in the bulk fluid and little flow distortion around the NGV. This suggests there are potential gains to be made in the reduction of the heat load on the NGV by redesigning the combustor

swirler.

The aim therefore is to reduce the size of structures on the vane surface by reducing the size of turbulent structures present in the freestream. This was achieved by reducing the size of the pilot swirler and adding eight main swirlers. The 12-core swirler is fabricated by reducing the size of the main swirlers in order to fit an additional four swirlers. Table 6.1 lists the characteristic length scales of the swirlers and turbulence grid.

Geometry	**Pilot Diameter (m)**	**Main Diameter (m)**
Single-core	140	-
8-core	68	42.5
12-core	68	36
Turbulence grid	45	-

Table 6.1: Diameters of the pilot and main swirlers for the single-core, 8-core, and 12-core swirlers, and diameter of the aperture of the turbulence grid

Fig. 6.4 compares the idealised case of uniform turbulence intensity with the single-core, 8-core, and 12-core swirlers. These geometries have pilot swirlers with the same sense of rotation (anti-clockwise when looking from upstream down towards the vane leading edge) which result in a pressure gradient from casing to hub on the suction side. The single-core swirler has a bypass around the pilot swirler. The 8-core and 12-core swirlers have main swirlers that counter-rotate against the pilot swirler. The 8-core swirler shows a reduction in h by approx. 10% of the spanwise average at the streamwise location, $^{x}/_{C_{\mathrm{ax}}} = 0.739$, compared to the single-core swirler. The passage vortex lift-off lines are also more distinct with a lower minima. The hub lift-off line also appears more diffuse than the casing lift-off line The 12-core swirler shows the greatest reduction in heat transfer across the whole surface. The footprint of the midspan vortex is only slightly visible and it does not appear to migrate radially, instead flowing down the midspan. This implies a weaker radial pressure gradient and less flow distortion at the inlet plane. It therefore has the most uniform distribution of h of all the swirlers and is most similar to the ideal turbulence grid case. It is interesting to note that for all swirler cases, the direction of flow migration on the

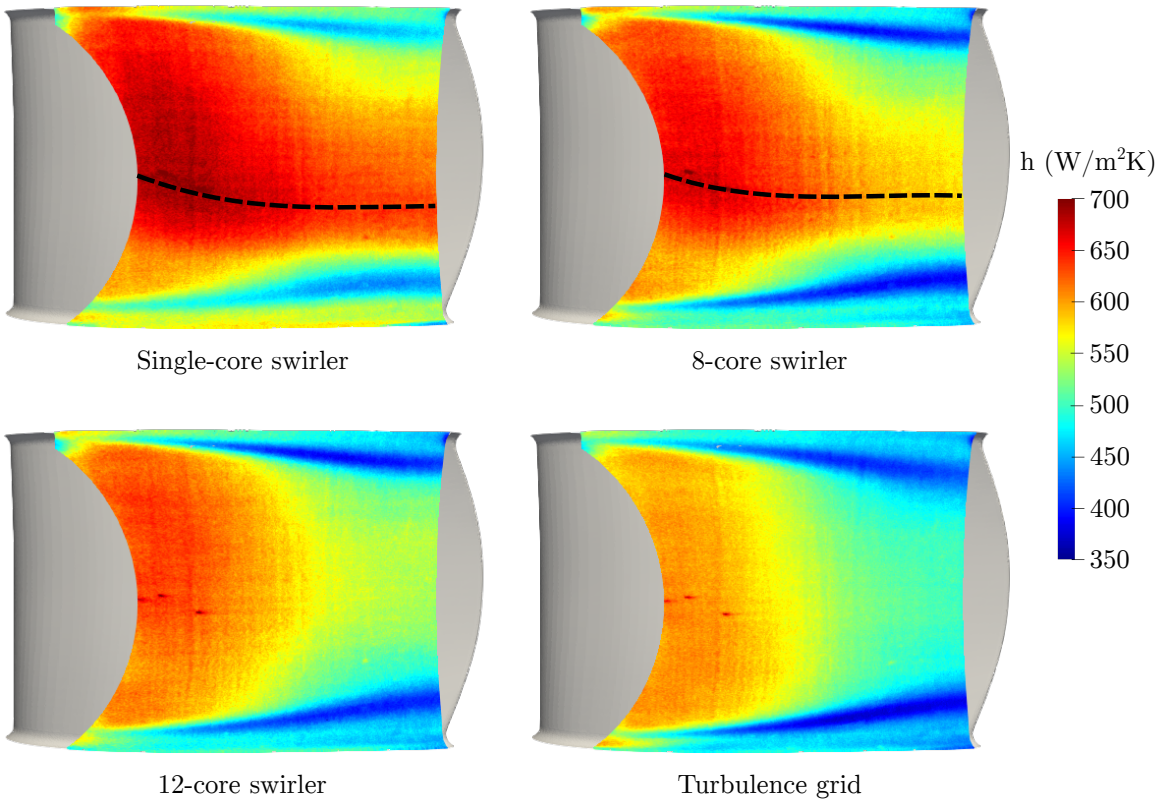


Figure 6.4: Contours of HTC on the unshielded vane's suction side for the single-core swirler (top left), 8-core swirler (top right), 12-core swirler (bottom left), and turbulence grid (bottom right)

suction side follow the sense of rotation of the pilot swirler, not the main swirlers.

Fig. 6.5 extracts the spanwise distribution of h at the streamwise location, $x/C_{ax} = 0.739$ for all the swirlers and the turbulence grid. Looking from the casing to the hub,

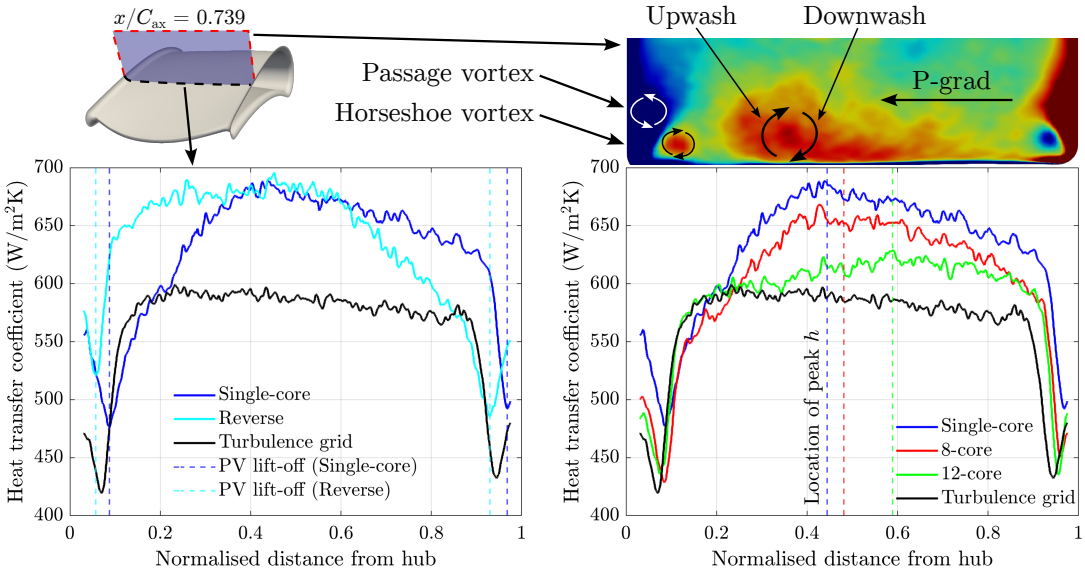


Figure 6.5: Spanwise distribution of HTC at axial distance, $x/C_{ax} = 0.739$. Left: Comparisons between the single-core swirler, the reverse single-core swirler, and the turbulence grid. Right: Comparisons between the single-core swirler, the 8-core swirler, the 12-core swirler, and the turbulence grid. Location of peak h demarcated by dashed lines

past the casing passage vortex lift off, there is a gradual rise in h up to a maxima at certain spanwise locations. The rate of increase in h is highest for the the single-core and 8-core swirlers, followed by the 12-core swirler. This spanwise location of peak h for each swirler is denoted by the dashed lines. Beyond this point, in the case of the single-core swirler, h drops rapidly until the minima of the passage vortex lift-off line is reached. In the case of the 8-core swirler, there is an initial rapid drop in h, but this remains distinct from the drop due to the passage vortex lift-off line. The 12-core swirler shows a very shallow drop in h across the rest of the span until the sharp drop near the lift-off line. The turbulence grid case shows the lowest rate of increase h and it continues to rise until the hub passage lift-off line is reached. The observations for the single-core swirler are mirrored in the case of the reverse single-core swirler.

These results are compared against a contour of time-averaged streamwise vorticity obtained from LES for the single-core swirler at the same streamwise location. The contour plot clearly shows salient features such as the passage vortices, horseshoe vortices, and the midspan vortex, and their sense of rotation are denoted by the arrows. The downwash of the midspan vortex results in a thin boundary layer and corresponds to the location of peak h for the single-core swirler. Conversely, the boundary layer in the upwash region is thickened, resulting in a rapid drop in h. In the case of the 12-core swirler, the footprint of the midspan vortex in Fig. 6.5 is much weaker and also does not show any spanwise migration, so the effects of downwash and upwash are less pronounced, leading to a shallower rise and drop in h on their respective sides of the vortex

The mean position of secondary flows is also affected by swirl. The spanwise distribution of h in Fig. 6.5 shows a shift in the location of the passage lift-off lines towards the casing for all swirler geometries. This is correlated with the intensity and sense of rotation of the residual swirl core since the single-core swirler shows the greatest shift, followed by the 8-core swirler, then the 12-core swirler. In the latter case, the location of the lift-off line is almost the same as the turbulence grid case.

The reverse single-core swirler was designed to give the same swirl intensity as the single-core swirler, but with the opposite sense of rotation. The resulting lift-off lines are now shifted towards the hub and by roughly the same distance as the single-core swirler, i.e. the hub and casing lift-off lines of the turbulence grid case is centred between the respective lift-off lines of the single-core and reverse single-core swirlers. Hence the residual swirl in the freestream is shown to be responsible for the migration of secondary flows.

Thus, the residual swirl core is shown to persist far downstream of the combustor to the inlet to the NGV cascade, and results in an overall increase in HTC levels as well as a non-uniform distribution across the vane suction side. By reducing the size of the swirlers, the overall HTC levels is reduced and a more uniform distribution is obtained. This trend can be seen in Fig. 6.4 and Fig. 6.5 when going from the single-core swirler to the 8-core swirler and finally to the 12-core swirler. This is attributed to the reduction in the size of coherent structures and turbulent kinetic energy as shown in §5.1.

If unaccounted for in the placement of cooling holes, this will result in non-uniform heating of the vane as the swirl core will not only increase the heat transfer in certain regions, but will also redistribute the coolant flow, potentially exposing parts of the vane to the freestream. Similar distributions of adiabatic effectiveness can be expected in the case of the film-cooled vane

6.2 Heat Transfer on a Film-Cooled Vane

This section presents time-averaged results of the effects of swirl on a film-cooled vane. Fig. 6.6 presents these results on the suction side for all swirler geometries tested. The same operating conditions were used in all cases and only the swirl generator was changed between the tests. The contour of $\eta = 0.5$ is outlined in black as this is typically used by designers as a gauge of film cooling performance. Similar trends are observed here as with the uncooled vane. The single-core swirler

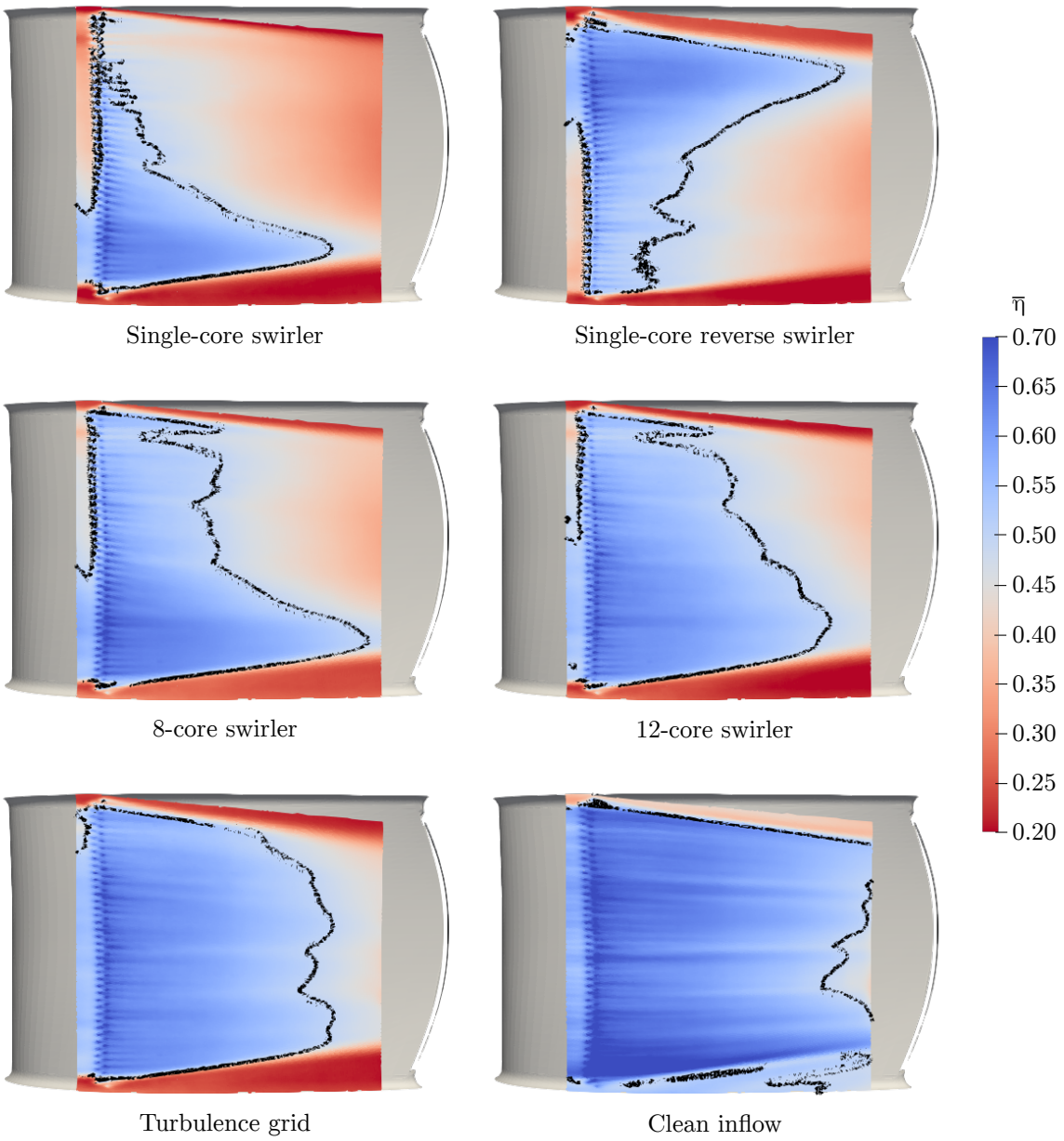


Figure 6.6: Contours of adiabatic cooling effectiveness on the unshielded vane's suction side for all inflow conditions. Contour of $\overline{\eta} = 0.5$ shown

has the lowest overall effectiveness and the most spatially non-uniform, followed by the 8-core swirler and the 12-core swirler. The turbulence grid case has the most uniform distribution and a comparison with the clean inflow case confirms that higher freestream turbulence results in lower effectiveness due to increased mixing. In the clean inflow case, individual streaks of high effectiveness can be seen exiting the coolant holes, whereas this appears more diffuse in the turbulence grid case. Coolant distribution near the hub and casing is confined by secondary flows, which explains the sudden drop in η and the narrowing spread along the axial length. A large

triangle region of very high effectiveness is clearly seen for single-core and reverse swirler towards the hub and casing side respectively.

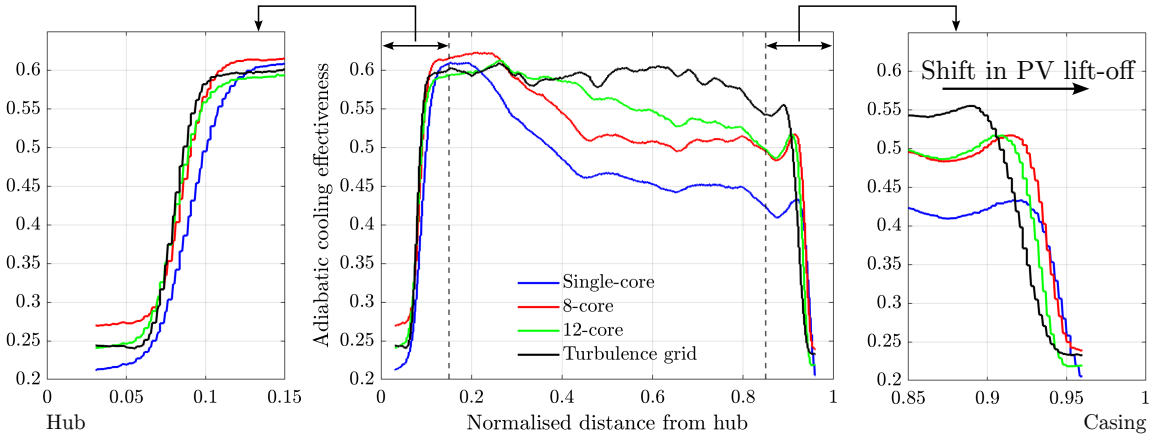


Figure 6.7: Spanwise distribution of adiabatic cooling effectiveness at axial distance, $x/C_{ax} = 0.739$, for the single-core swirler (top left), the 8-core swirler (top right), the 12-core swirler (bottom left), and the turbulence grid (bottom right). Regions near the hub and casing are enlarged to show shift in passage vortex lift-off lines

The previous section showed that the residual swirl resulted in a shift in the passage vortex lift-off lines for an uncooled vane, with increasing swirl intensity causing larger shifts. In the case of a cooled vane, this results in a spanwise shift in coolant distribution, since coolant flow near the hub and casing are confined by the lift-off lines. Fig. 6.7 plots $\overline{\eta}$ for the single, 8, and 12-core swirlers and the turbulence grid case. Similar observations can be made whereby the single-core swirler produces the largest shift in coolant coverage, followed by the 8-core, and then the 12-core. In reality, these secondary flows are highly unsteady and the positions of the lift-off lines can fluctuate significantly, temporarily resulting in large uncooled regions near the hub; see Fig. 7.4. This shows the effect of swirl on secondary flows and highlights the need for swirl to be accurately modelled or otherwise measured and applied as a boundary condition to account for this mean shift.

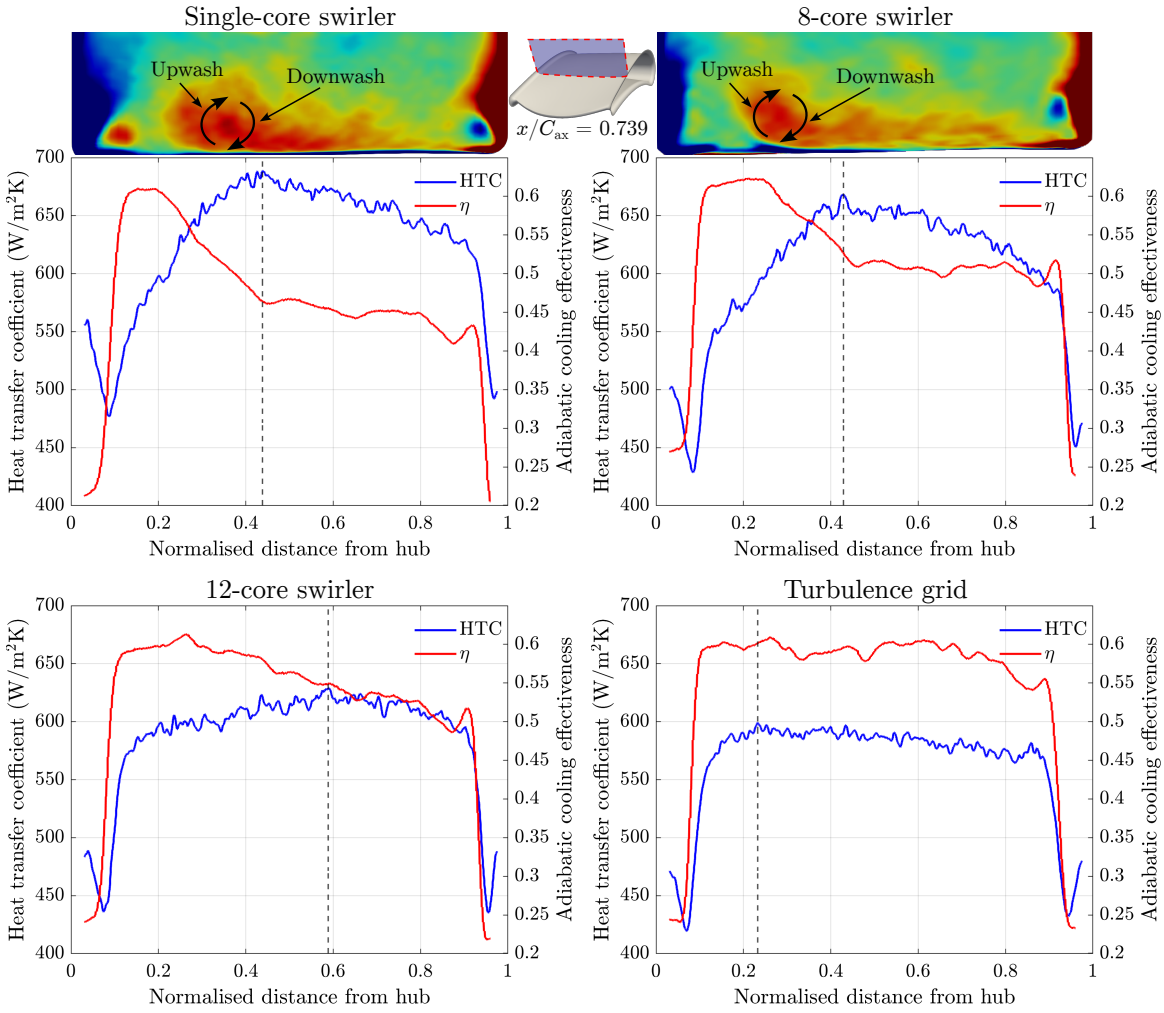


Figure 6.8: Spanwise distribution of HTC and adiabatic cooling effectiveness at axial distance, $x/C_{ax} = 0.739$, for the single-core swirler (top left), the 8-core swirler (top right), the 12-core swirler (bottom left), and the turbulence grid (bottom right). Location of peak HTC demarcated by black dashed line

6.3 Influence of Combustor Flows on Film Cooling Distribution

There are multiple factors in which combustor flows can influence the non-uniformity of coolant distribution. The mass flow rate through each hole is governed by the pressure ratio across it, since they are unchoked. The static pressure on suction side is higher near the casing and lower near the hub, as shown in Fig. 5.9 in §5.3.1 (for clockwise swirl when looking from downstream to upstream). This leads to increased coolant flow near the hub compared to casing. Downstream of the holes, low momentum fluid migrates under the action of the spanwise pressure gradient. This may also

lead to increased coolant coverage near the hub compared to the casing, but it will be shown later that this effect is not significant. Additionally, downwash from the midspan vortex increases local adiabatic wall temperature, which reduces adiabatic effectiveness. The magnitude of downwash increases from the casing side towards the swirl core centre. Conversely, upwash will increase the adiabatic effectiveness. The midspan vortex also redistributes the coolant flow either by changing the potential field around the jet when the vortex stagnates on it or by viscous shearing of the coolant film.

The combined effects of downwash, upwash, and coolant redistribution due to the midspan vortex is most clearly seen in Fig. 6.8 which compares h with $\overline{\eta}$. Cross-section planes of time-averaged streamwise vorticity at $x/C_{\text{ax}} = 0.739$ obtained from LES are shown for the single-core and 8-core swirlers. Across all swirler cases, the location of peak h corresponds to the location of the swirl core where downwash from the vortex is greatest. This is marked by the black dashed line. In the upwash region, HTC rapidly drops and this correlates with a sharp rise in $\overline{\eta}$. Cooling effectiveness in the presence of a swirl core appears to be dominated by the vortical motion of the midspan vortex.

Fig. 6.9 compares the exit trajectories of coolant jets at different spanwise locations. This data is taken from the same dataset as Fig. 6.6 by zooming into the cooling holes. A colour bar is not provided in this figure because scales have been chosen for maximum contrast, which differs across each case. The purpose here is to compare jet angles, not to compare magnitude in $\overline{\eta}$. The cooling holes at this location are axially aligned.

The coolant jet is seen to be deflected only along the midspan and not at the hub or casing. This implies that near the hole exit and up to 8 hole diameters downstream, the radial pressure gradient does not affect the migration of the coolant film. This is likely due to the high momentum flux of the jet near the hole exit. Instead, this localised turning of the the jets near the midspan is caused by the midspan vortex.

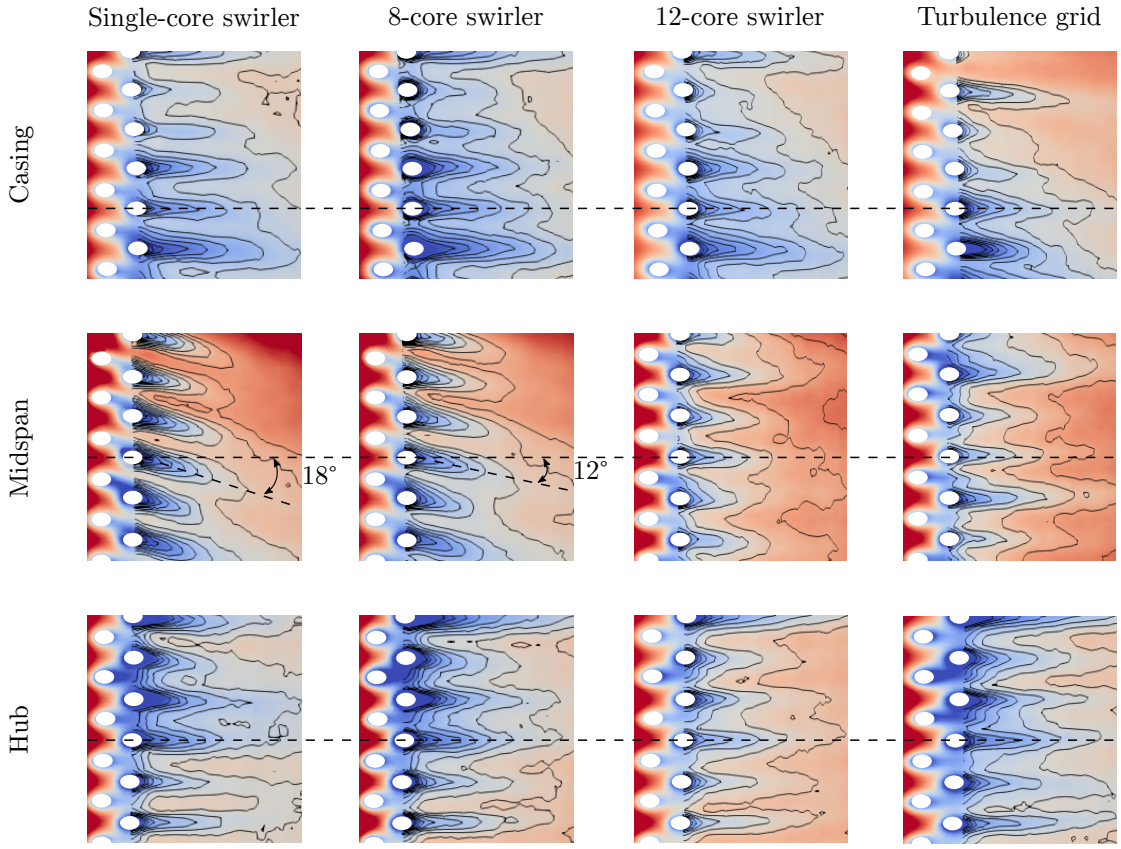


Figure 6.9: Adiabatic cooling effectiveness near cooling holes located around the hub, midspan, and casing. All holes are axially aligned

In the case of the 12-core swirler, no turning is observed and the midspan vortex does not migrate radially, thus giving a more uniform distribution. Some radial variation is still expected due to the varying pressure ratio across the span, which varies the mass flow rate through each hole.

The relative contributions of the midspan vortex and the pressure ratio effect to the overall distribution of η can be assessed from Fig. 6.8 for the single-swirler case. The turbulence grid case shows a flat distribution of η across most of the span, so there is no spanwise pressure gradient. All swirler cases will have a spanwise pressure gradient, though with varying strengths that depend on the swirl intensity. This leads to a lower coolant mass flow towards the casing and a higher mass flow towards the hub, which can be seen from the gradual increase in η from the casing to the location of peak h (black dashed line). Beyond this point there is a sudden sharp increase of η, which coincides with the location of the midspan vortex core. This discontinuity

is unlikely to be due to the pressure ratio effect alone. Assuming that the spanwise distribution of mass flow rate is continuous and that the trend in η towards the casing can be extrapolated towards the hub, then this suggests that the pressure ratio effect on film cooling distribution is of secondary importance to the effect of the midspan vortex.

6.4 Summary

Time-averaged heat transfer coefficients and adiabatic effectiveness were measured on the suction side of the uncooled and film-cooled vane respectively, for six different inlet flow conditions. These are the clean inflow, turbulence grid, single-core swirler, reverse single-core swirler, the 8-core swirler, and the 12-core swirler. Large variations in HTC and coolant coverage are observed across different flow conditions, which demonstrates the need for considering the combustor geometry and modelling the full combustor-turbine interface in aerothermal studies of the NGV. Clear bands of low h are seen at the passage vortex lift-off line. Regions of very high h near the midspan show the footprint of the midspan vortex as it migrates across the vane. Heat transfer on the vane surface is therefore dominated by vortical motion, and significant reduction in the overall levels of h can be obtained simply by changing the swirler geometry.

In the case of swirling flow, this reduction is due in part to the smaller size and weaker residual swirl core which leads to a smaller midspan vortex. This was shown in §5.2 for the single-core and 8-core swirlers, where the single large precessing residual swirl core in the former was replaced by three smaller swirl cores with lower total pressure loss and swirl. The levels of turbulent kinetic energy are also lower, which leads to lower overall levels of heat transfer across the whole vane surface. The same arguments can be applied to the 12-core swirler, which has the lowest h of all four swirler geometries tested. The influence of swirl on secondary flows has also been observed, which causes a shift in the passage vortex lift-off lines towards the hub or

casing depending on the swirl direction. This also causes the coolant distribution to shift accordingly as the lift-off lines form bounds on the coolant flow path. Hence residual swirl in the passages should be accounted for during the design of NGVs.

In film-cooled flows, the distribution of adiabatic effectiveness is also largely determined by the midspan vortex, with the 12-core swirler yielding the most uniform distribution and highest levels of η, followed by the 8-core swirler, and then the single-core swirler. The factors affecting this distribution are: (1) A lower pressure ratio across cooling holes near the casing compared to holes near the hub, which leads to lower coolant mass flow out of holes near the casing. (2) Radial migration of the coolant flows from casing to hub due to the radial static pressure gradient. (3) Deflection of the coolant flow by the midspan vortex, either by altering the potential field around the coolant jet, or by viscous shearing. (4) An increase in the adiabatic wall temperature, T_{ad}, near the downwash side of the midspan vortex and a decrease in T_{ad} on the upwash side. The large triangular region of high η in Fig. 6.6 is predominantly due to the latter two factors. It would therefore be beneficial to design combustors that do not result in large total pressure gradients across the bulk fluid.

Chapter 7
Unsteady Effects of Combustor Geometry on a Film-Cooled NGV

This study into the unsteadiness of the aerothermal field around the NGV is motivated by the LES results previously presented in §5.4 as well as past studies by Jacobi et al. [120] and Shaikh and Rosic [172] who carried out experiments on the same facility. §7.1 presents experimentally measured spectra of temperature and pressure fluctuations at different locations in the flow domain. §7.2 then shows the instantaneous effects of these fluctuations on the film cooling effectiveness. The levels of these fluctuations is then quantified in §7.3. §7.4 scales these fluctuations up to engine conditions to estimate the peak-to-peak difference in wall temperature in a real engine. §7.5 identifies sources of these oscillations as being due to the acoustics and hydrodynamics of the flow alone, as well as some facility-related resonance.

7.1 Spectra of Temperature and Pressure Fluctuations

Combustor flows entering the turbine section have been shown to contain coherent structures of varying scales that interact with the NGV, resulting in fluctuations in the aerodynamic field of the unshielded NGV. The spectra measured from LES also showed that most of the frequency content of these oscillations is contained in the sub-1 kHz band. These have also been measured experimentally using various instruments such as a high-speed infra-red camera, double-sided thin film gauges, and high-speed pressure transducers. It will later be shown in §7.5 that the experimentally measured spectra for pressures is similar to that from LES. In this section, the spectra is limited to the sub-100 Hz band and is presented in Fig. 7.1.

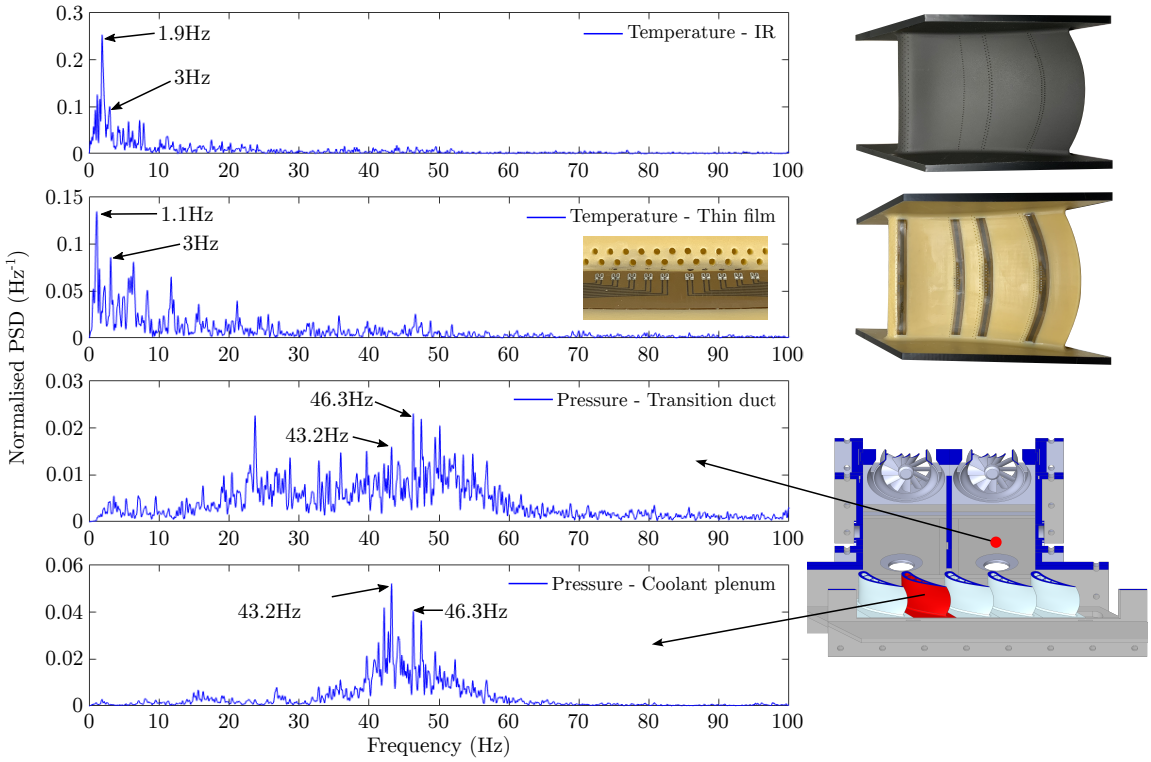


Figure 7.1: Normalised power spectral densities for the single-core swirler obtained from experiments with IR, thin-film gauges, and high-speed pressure transducers located in the transition duct (red dot) and the film-cooled vane plenum (red vane)

The spectra shows that there is significant frequency content in the sub-100 Hz range. This forms the frequency range of interest for this study since high frequency fluctuations are unlikely to result in significant surface temperature fluctuations. This is justified in §7.4.

The spectrum for the IR camera is generated from a the time history of a single pixel taken near a cooling hole on the midspan. This point was chosen to correspond to the same location as one of the thin film gauges on the vane suction side, so that the spectrum for this gauge can be compared to the IR result. The pressure transducer in the transition duct is mounted in the streamwise direction, opposing the flow, so that it measures fluctuations in total pressure, while the transducer in the coolant plenum is wall-mounted on the plenum wall.

The spectra of temperature from IR and thin-film gauges have peaks at frequencies less than 10 Hz, whereas the spectra of pressure in the transition duct shows a broadband peak in the range 20 - 60 Hz. The vane coolant plenum shows very similar

peaks to the spectra from the transition duct over the range 40 - 60 Hz. No other peaks are present in the coolant plenum spectra and it is unlikely that these peaks are fluctuations in the coolant line propagating into the transition duct due to the combustor wall dividing the two flow streams and the significantly smaller mass flow rate of the coolant relative to the freestream. This suggests that the converse must be true, i.e. pressure fluctuations in the transition duct are propagating into the coolant plenum. The origins of these fluctuations are addressed later in this chapter. Suffice to say for now that these fluctuations exist and are of sufficiently large magnitude and low frequency to impact film cooling performance.

7.2 Effect of Fluctuations on the Instantaneous Distribution of Cooling Effectiveness

Fig. 7.1 only shows the spectra of fluctuations for a single point. Now the effect of these fluctuations can be visualised across the entire vane surface by plotting the instantaneous distributions of temperature or adiabatic effectiveness. This is shown in Fig. 7.2 where the instantaneous adiabatic effectiveness, η, has been lowpass filtered to 100 Hz to visualise only the low frequency fluctuations.

Fig. 7.2 presents instantaneous contours of $\eta = 0.5$ evaluated at two different timesteps, demarcated by the green and yellow lines. The contours are overlaid onto the time-averaged surface map of $\overline{\eta}$ and the time-averaged contour of $\overline{\eta} = 0.5$ is shown in black. The timesteps were chosen to qualitatively outline the minimum and maximum bounds on the fluctuations of η. The green contour represents the minimum bound, i.e. where cooling distribution is reduced across the whole suction surface. The yellow contour represents the maximum bound, i.e. where cooling distribution appears enhanced across the whole suction surface. These fluctuations take place about the time-averaged contour of $\overline{\eta} = 0.5$ (black).

The timesteps for these contours were chosen to qualitatively demonstrate the *global* extremes. These are not necessarily the maximum and minimum at every loca-

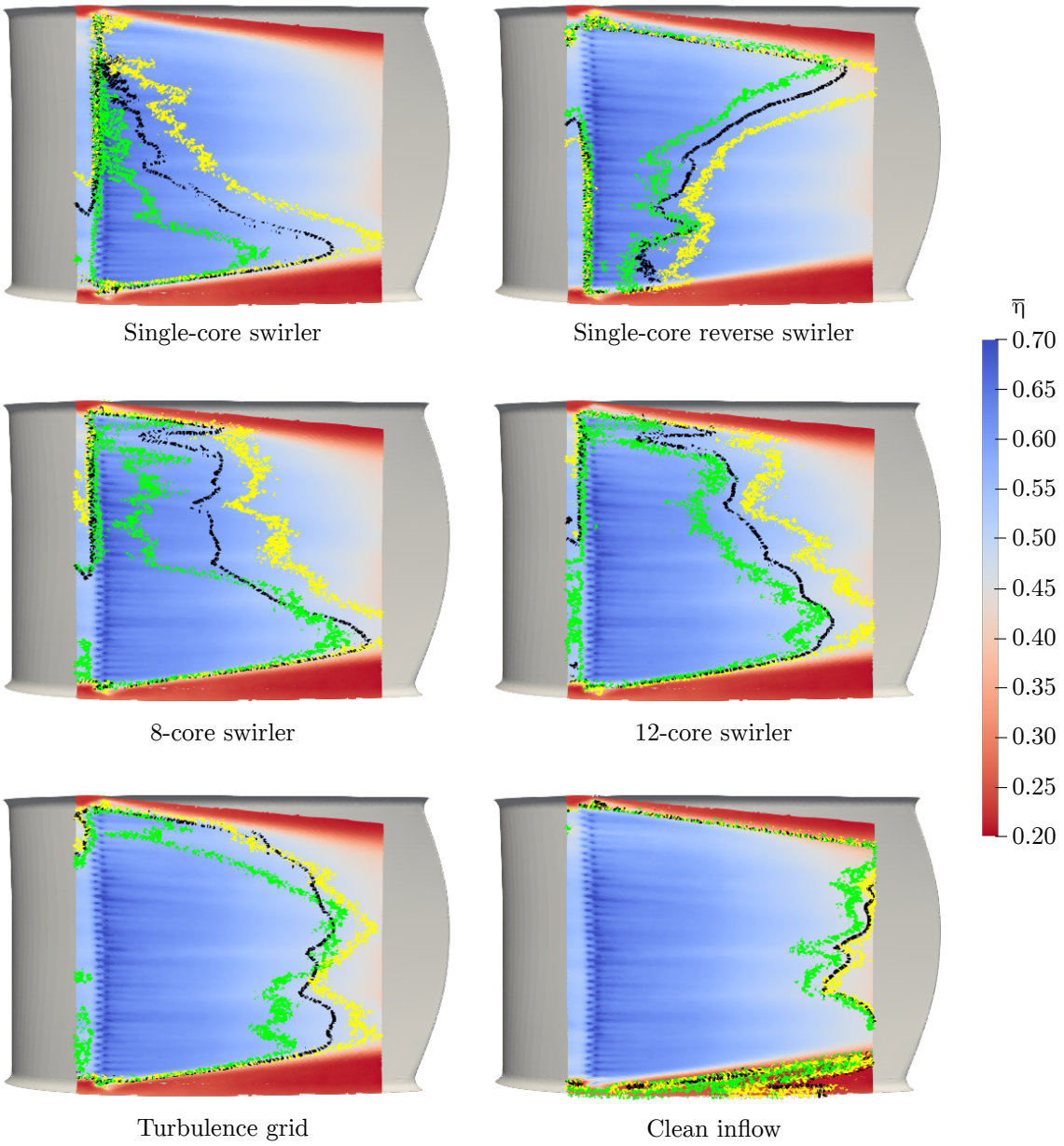


Figure 7.2: Contours of instantaneous adiabatic cooling effectiveness on the unshielded vane's suction side for all inflow conditions. Contour of time-averaged effectiveness, $\overline{\eta} = 0.5$ shown in black. Green and yellow contours are of instantaneous $\eta = 0.5$ showing qualitative minimum and maximum bounds of fluctuations, respectively

tion, since these instantaneous fluctuations involve complex interactions of the coolant flow with different flow structures. The flow field is highly chaotic and these interactions are to some extent random as larger structures in the freestream breakdown into smaller ones, forming random perturbations that can instantaneously enhance or reduce cooling locally. In some cases the average appears outside the bounds of the the indicative minimum and maximum examples.

The fluctuations appear to be axial pulsations, with little change to the overall

shape of the distribution. This can be due to either the precession of the swirl core from one passage to another, thereby instantaneously increasing or decreasing effectiveness in one passage, or longitudinal waves travelling through the flow domain. The clean inflow case also displays these axial pulsations but to a much lesser extent, i.e. the contours of instantaneous $\eta = 0.5$ lie very close to the mean contour, $\overline{\eta} = 0.5$. Since there is no swirl core to precess for the clean inflow and turbulence grid cases, these fluctuations are likely due to a travelling longitudinal wave. §7.5 visualises this travelling wave for the clean inflow case, and estimates the fundamental frequency of a pipe resonator and cavity resonator with different length scales. This models a case with clean inflow and a case where there is a blockage due to the presence of a turbulence grid or swirler. These estimates are then compared with the power spectrum of static pressure that was measured experimentally using a high-speed pressure transducer on the vane surface.

The contours of instantaneous $\eta = 0.5$ show significant deviation from the mean distribution, $\overline{\eta} = 0.5$. Since the fluctuations have been lowpass filtered, this means that large regions of the vane suction side experience relatively long periods of undercooling before being overcooled. This period may be sufficiently long to result in significant fluctuations to the surface temperature. This will later be shown in §7.4 to result in peak-to-peak temperature fluctuations as high as 65 °C when scaled to engine conditions.

7.3 Quantifying Levels of Fluctuations of Cooling Effectiveness

The previous section showed qualitatively the extent of fluctuations in coolant coverage. Now the levels of these fluctuations are calculated across the whole surface to identify the locations of highest deviations from the mean. It is assumed here that the instantaneous effectiveness, η, can be separated into its mean and fluctuating components, $\eta = \overline{\eta} + \eta'$. A low-pass filter with a passband frequency of 100 Hz is

applied since we are only interested in low frequency fluctuations. The magnitude of these fluctuations is quantified in terms of its RMS. The raw values of RMS do not convey much meaning since regions of high fluctuations and high mean are still well protected. They must also be compared to the baseline case, which is the turbulence grid case, to mitigate fluctuations arising from other sources, i.e. facility-related resonance. This gives rise to two methods of normalising the RMS of η':

$$\eta'_{\text{norm}} = \frac{\eta'_{\text{RMS}}}{\overline{\eta}} \times 100\%$$
$$\eta'_{\text{rel}} = \frac{\eta'_{\text{RMS,i}} - \eta'_{\text{RMS,turb}}}{\eta'_{\text{RMS,turb}}} \times 100\%$$

where the subscript i refers to the inflow condition that is not the turbulence grid; attempting to evaluate η'_{rel} for the turbulence grid case will simply give a value of 0 everywhere.

Normalising by its local mean quantifies how well protected a location is at any instant in time. Normalising by the local RMS of the turbulence grid case highlights flow structures since fluctuations in the turbulence grid case are due to uniform freestream turbulence. The latter normalisation method is also important for the following reason. The working section may experience fluctuations arising from sources outside the domain, such as pipe resonance from the supply line, Helmholtz resonance in the pressure vessel, etc. This biases raw RMS data for all cases by introducing additional fluctuations that are unrelated to the working section. We therefore make two assumptions: 1) The facility-related resonance is independent of the swirler used. 2) Pressure waves due to facility-related resonance do not interact with existing fluctuations in the working section, i.e. that both modes of oscillations are not coupled and are purely superposed. The former is a reasonable assumption since these fluctuations are determined by geometry of the entire facility, and the flow velocities are relatively constant across all cases since mass flow is fixed by a choked orifice. The latter is more difficult to validate without extensive work on the facility itself. The assumptions allow the bias to be subtracted out by normalising with some baseline case.

Hence normalising by the turbulence grid case provides a more useful quantification of RMS fluctuations.

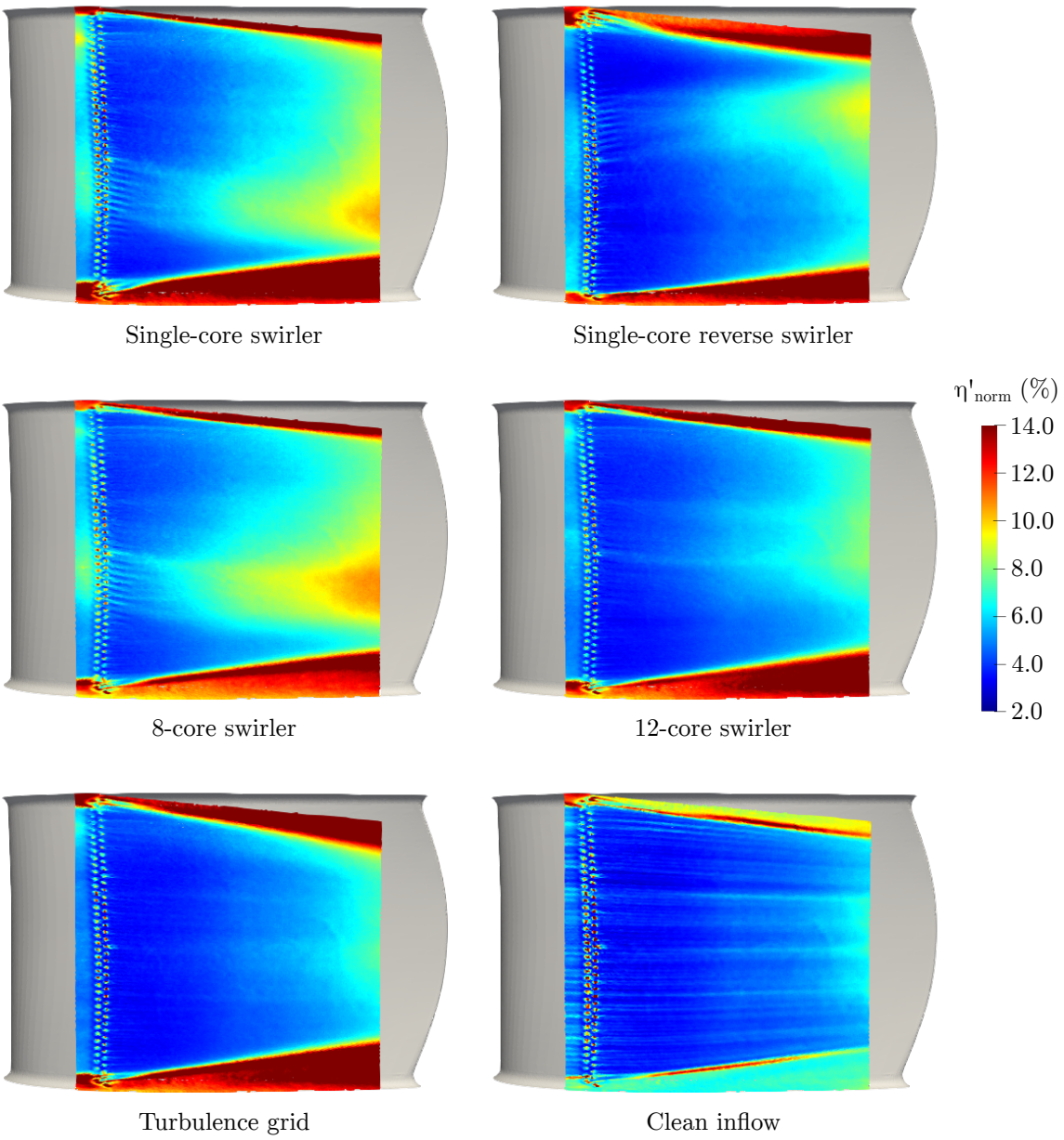


Figure 7.3: Contours of normalised RMS of adiabatic cooling effectiveness on the unshielded vane's suction side for all inflow conditions. The RMS of η' for each inflow condition is normalised by its local mean adiabatic effectiveness, $\overline{\eta}$

Fig. 7.3 and 7.4 present suction side maps of η'_{norm} and η'_{rel} respectively. The same overall trends can be seen observed, with decreasing fluctuations going from the single-core swirler to the 8-core swirler and the 12-core swirler. The migrating midspan vortex drives the largest fluctuations on the suction side. The lack of migration in the 12-core swirler case can also be seen as the streaks of high η'_{norm} and η'_{rel} travel

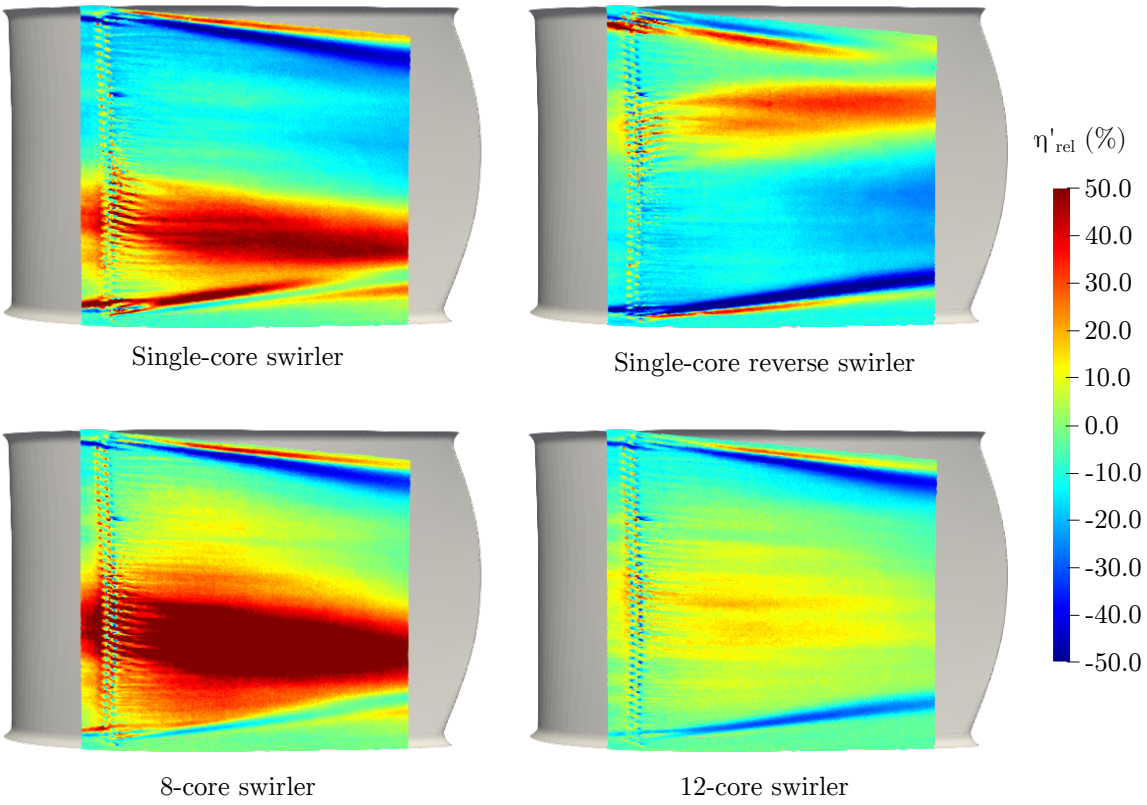


Figure 7.4: Contours of relative RMS of adiabatic cooling effectiveness on the unshielded vane's suction side for all inflow conditions. The RMS of η' for each inflow condition is normalised by the local RMS of η' from the turbulence grid case

axially with little to no radial component, similar to the turbulence grid and clean inflow cases.

An interesting result is that the fluctuations with the 8-core swirler are higher than the single-core swirler, despite having a lower turbulence intensity, swirl number, and total pressure loss core at the inlet plane to the NGV and the midspan vortex being weaker. In Fig. 7.4, the single-core, 8-core, and 12-core swirlers show two adjacent narrow bands of high and low η'_{rel} near the casing. In the case of the revere single-core swirler, these two streaks are mirrored onto the hub. This is due to the shift in the passage vortex lift-off lines caused by the residual swirl. For swirl in the CW direction (as seen looking from downstream to upstream), the lift-off lines move towards the casing; see Fig. 6.7 in §6.2. In the turbulence grid case, this region is occupied by the PV lift-off line and therefore had very little cooling. The vortex position also fluctuates significantly, resulting in high η'_{RMS}. In cases of swirl, this region is now well protected by coolant and is more quiescent as the PV lift-off line has migrated

further up towards the casing. This produces the band of low η'_{rel}. The PV now fluctuates in its new position nearer the casing, resulting in the band of high η'_{rel} that sits above the band of low η'_{rel}. A higher swirl intensity causes the lift-off lines to migrate further towards the casing. Consequently, these two bands are widest for the single-core swirler and narrowest for the 12-core swirler.

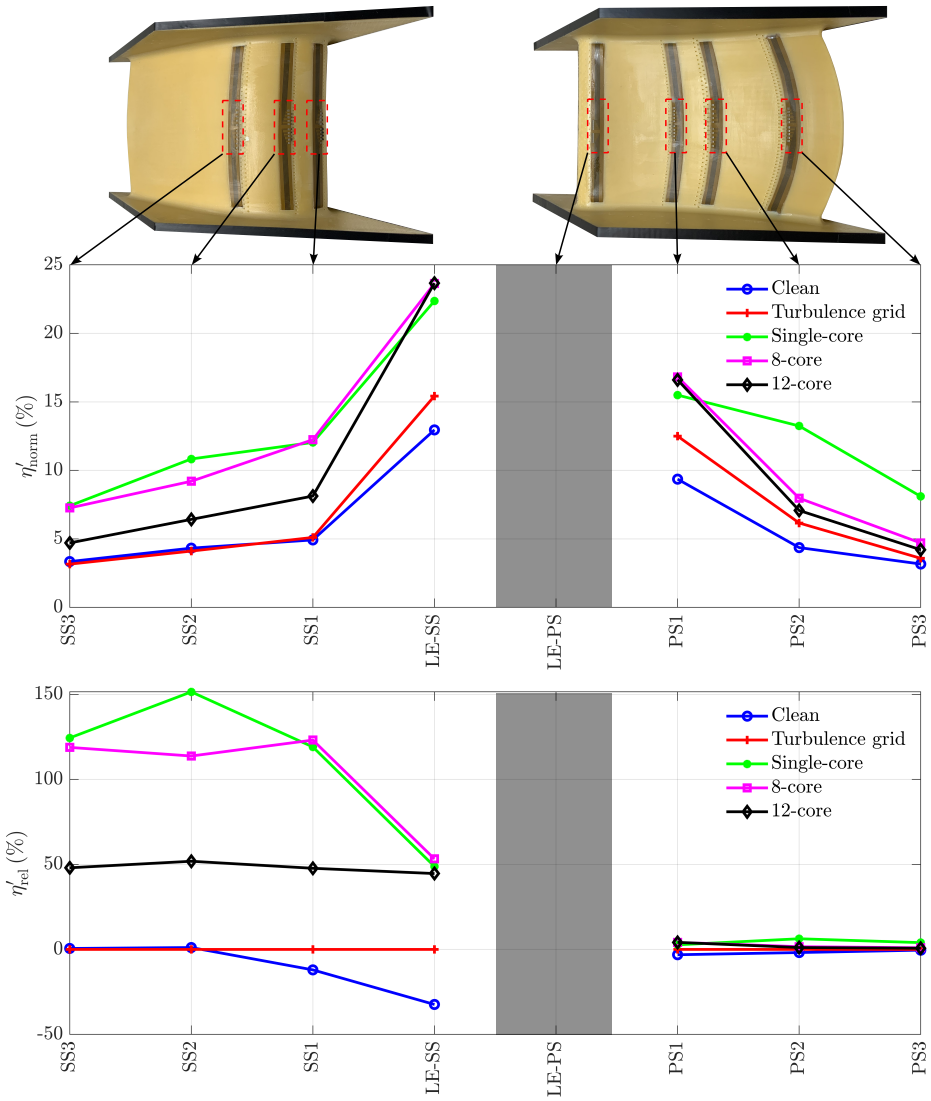


Figure 7.5: Laterally-averaged normalised RMS of adiabatic cooling effectiveness for all inflow conditions obtained from thin-film gauges

So far the results of unsteadiness presented have been of the vane suction side obtained using a high-speed IR camera. The size of the IR camera only allowed for this view as other views of the vane such as the leading edge and pressure side were inaccessible. Double-sided thin film gauges were therefore used to measure fluctuations at the midspan of each set of cooling hole rows. Fig. 7.5 presents the

laterally-averaged fluctuations at each set of rows. The row of cooling holes visible to the IR camera corresponds to set SS3 of the thin-film gauges.

The trends are broadly consistent with the IR results above, with the 12-core swirler having the lowest fluctuations of the three swirlers and the clean inflow case being the lowest of all geometries tested. Fluctuations are highest near the leading edge and decrease along the axial length due to acceleration of flow. The thin film gauges give higher overall fluctuations compared to IR measurements. This is thought to be due to the protrusion of the Kapton substrate into the flow, leading to local impingement and recirculation of the coolant jet as it exits the hole.

The row, LE_PS, corresponds to the gauges downstream of the showerhead on the pressure side. This has been removed from the dataset due to erroneous readings. The high curvature near the shower head resulted in large strains on the gauges, increasing its resistance, which biases the Wheatstone bridge element. The resulting gauge resistance exceeded the maximum input signal of the NI data acquisition equipment, causing the output to saturate.

7.4 Effect of Fluctuations on Surface Temperature at Engine Conditions

Fig. 7.3 has shown that cooling effectiveness can vary by more than 10% of its time-averaged value, and Fig. 7.1 has shown that the spectrum of the surface temperature near a cooling hole contains peaks in the sub-10 Hz. This suggests that the fluctuations of the cooling film are of sufficiently low frequency such that the surface temperature will change appreciably. This is potentially detrimental in a real engine due to high-cycle fatigue that has not been accounted for. These fluctuations occur at much higher frequencies than those typically considered in fatigue studies of thermal barrier coatings [173, 174]. These studies are typically concerned with low cycle fatigue due to starting up and stopping the gas turbine. Time scales are typically measured in hours and the number of cycles to failure are on the order a

few thousand.

This section scales the results presented by the two figures referenced to engine conditions to assess the impact of this unsteadiness on the thermal response of the vane. This is quantified in terms of the peak-to-peak amplitude of the surface temperature. Splitting η into its mean and fluctuating components gives: $\eta = \overline{\eta} + \eta'$, where $\overline{\eta}$ is the D.C. offset and η' can be modelled as a sine wave with an amplitude that satisfies $\eta'_{\text{norm}} = \eta'_{\text{RMS}}/\overline{\eta}$ for some desired value of η'_{norm}. Since the RMS of a sine wave with an amplitude of one is $1/\sqrt{2}$, then η' can be written as:

$$\begin{aligned} \eta' &= \sqrt{2} \cdot \overline{\eta}\eta'_{\text{norm}} \cdot \sin(\omega t) \\ \Rightarrow \eta &= \overline{\eta} + \sqrt{2} \cdot \overline{\eta}\eta'_{\text{norm}} \cdot \sin(\omega t) \\ \Rightarrow T_{\text{ad}} &= T_{0,\infty} - \left(T_{0,\infty} - T_{0,c}\right) \overline{\eta} \left(1 + \sqrt{2} \cdot \eta'_{\text{norm}} \cdot \sin(\omega t)\right) \end{aligned}$$

The surface temperature can be found by assuming the body is 1D semi-infinite subject to a Robin boundary condition on the surface. The methodology described in §4.4 can be used to obtain the impulse response of this system, evaluated at the surface, $g(0,t)$. The solution, $T(0,t)$, is then given by:

$$T(0,t) = g(0,t) * h \cdot T_{\text{ad}}(t)$$

where the initial condition corresponding to the D.C. offset of T_{ad} has been ignored since we are only interested in the peak-to-peak amplitude.

Shaikh [132] performed a similar study but assumed a fluctuating HTC field, h', and constant driving temperature field. However, the basis functions used to derive the impulse response assume a constant HTC. The analysis carried out in §3.3.3.3 showed that the contributions to the fluctuations in heat flux, q', is dominated by fluctuations in the adiabatic wall temperature, T'_{ad}, followed by fluctuations in the aerodynamic field h'. Hence the use of the constant HTC assumption in this analysis is justified.

Table 7.1 lists some typical material properties for thermal barrier coatings (TBCs)

and vanes in use today. The freestream and coolant temperatures are $T_{0,\infty} = 1691\,\mathrm{K}$ and $T_{0,c} = 687\,\mathrm{K}$ respectively. The heat transfer coefficient, h, has been scaled using a simple Nusselt number correlation for turbulent flow over an isothermal flat plate as follows:

$$\frac{\mathrm{Nu}_{\mathrm{eng}}}{\mathrm{Nu}_{\mathrm{exp}}} = \left(\frac{hL}{k}\right)_{\mathrm{eng}} \cdot \left(\frac{k}{hL}\right)_{\mathrm{exp}} = \frac{0.037\mathrm{Re}_{\mathrm{eng}}{}^{0.8}\mathrm{Pr}_{\mathrm{eng}}{}^{1/3}}{0.037\mathrm{Re}_{\mathrm{exp}}{}^{0.8}\mathrm{Pr}_{\mathrm{exp}}{}^{1/3}} \cdot \left(\frac{T_f}{T_w}\right)^{0.12}$$

$$\frac{h_{\mathrm{eng}}}{h_{\mathrm{exp}}} = 1.76 \cdot \frac{k_{\mathrm{eng}}}{k_{\mathrm{exp}}} \cdot \frac{L_{\mathrm{exp}}}{L_{\mathrm{eng}}} \cdot 2^{0.12}$$

$$= 4.5$$

where the subscripts 'eng' and 'exp' refer to engine and experimental quantities respectively, T_f is the fluid temperature and T_w is the wall temperature. It is assumed that the Prandtl number, Pr, does not change significantly between experimental and engine conditions. Many correlations for Nu exist that depend on the geometry and boundary condition of the wall, however the aim here is only to obtain an estimate of the temperature fluctuations in a real engine, so this simple correlation is used.

Material	k	$\alpha \times 10^{-6}$	h_{eng}	$\overline{\eta}$	η'_{norm}	f(Hz)	ΔT_{pp}(K)
YSZ porous	0.8	0.32	4500	0.5	0.05	10	21.7
					0.1	10	43.4
					0.05	50	11.3
					0.1	50	22.5
YSZ non-porous	2.3	0.6	4500	0.5	0.05	10	11.9
					0.1	10	23.8
					0.05	50	5.7
					0.1	50	11.4
Inconel 625	25	7.3	4500	0.5	0.05	10	4.2
					0.1	10	8.3
					0.05	50	1.9
					0.1	50	3.8

Table 7.1: Material properties of typical NGV components and the associated peak-to-peak amplitude for a range of forcing frequencies and η'_{norm}

The results in Table 7.1 can be generalised by analysing the impulse response

function for this system (a semi-infinite body subject to a Robin BC):

$$g\left(0,t\right)=H\sqrt{\frac{\alpha}{\pi t}}-H^{2}\alpha e^{H^{2}\alpha t}\cdot\operatorname{erfc}\left(H\sqrt{\alpha t}\right)$$

and taking its Laplace transform gives the transfer function of the system:

$$g\left(0,t\right)\Leftrightarrow G\left(0,s\right)$$
$$G\left(0,s\right)=\frac{1}{1+\frac{\sqrt{s}}{H\sqrt{\alpha}}}$$

which can be easily converted to the frequency domain by substituting $s=j\omega$. It can then be seen that the surface temperature scales with $1/\sqrt{\omega}$ and $1/\sqrt{\rho c_p k}$, i.e. the RMS of surface temperature fluctuations decreases with increasing frequency and increasing thermal effusivity.

This analysis can be extended further to incorporate experimentally measured values for h, $\overline{\eta}$, and η'_{norm}. Fig. 7.6 shows the engine-scale peak-to-peak amplitude of surface temperature on the suction side. Data from the single-core swirler case is used in this analysis.

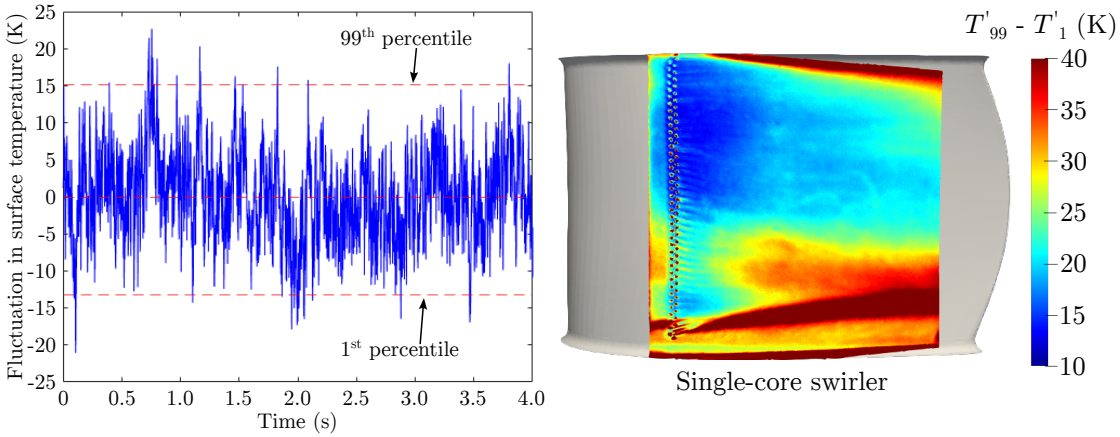


Figure 7.6: Peak-to-peak temperature fluctuations at engine conditions evaluated for a single pixel (left) and across the suction surface (right). Analysis based on data from the single-core swirler case

The peaks are taken as the 1st and 99th percentile. In regions away from vortex dominated flows, e.g. secondary flows and midspan vortex, surface temperature fluctuates by 20 °C. Near the midspan vortex, this rises to 35 °C. The highest amplitude fluctuation is seen along the passage vortex lift-off line on the hub side at approx.

65 °C. To put this into context, Bogard and Thole [64] asserts that the reduction in the mean wall temperature by only 25 °C can increase blade life by a factor of 2.

So far it has been taken for granted that the frequency range of interest is 0 - 100 Hz. Applying the equation above to the material used in this study - a UV-curable plastic resin - an appropriate cutoff frequency can be estimated. The cutoff frequency will determine the minimum sampling rate to avoid aliasing since the material acts as a lowpass filter. Evidently the D.C. component is not attenuated, when $\omega = 0$, $\left|G\left(0, j\omega\right)\right| = 1$. A cutoff frequency of 100 Hz corresponds to an attenuation of -32 dB - a factor of 2.5% of the forcing amplitude. That is to say, for an adiabatic temperature fluctuation of 10 °C (an excessively large estimate), the surface temperature registers a peak-to-peak amplitude of 0.25 °C, which is just within the precision of the instruments used in this study.

7.5 Identifying Sources of Fluctuations

For the purposes of this study, the sources of oscillations that drive combustion instabilities via a feedback loop can be broadly categorised into non-reacting and reacting flow modes. In the case of non-reacting flows, these modes are purely acoustic and hydrodynamic, with no heat input into the system. There is no coupling between the acoustic and thermal field and thus no mechanism for driving further instabilities. In the case of reacting flows, in addition to the modes above, there are injection oscillations, flame surface variations, and atomisation oscillations[91].

This study includes the whole combustor-turbine interface to investigate the effects of these non-reacting oscillations on heat transfer to an NGV from an acoustic and hydrodynamic perspective. By modelling the entire interface, these oscillations are fully captured. Acoustic modes include pipe (longitudinal) resonance in the transition duct, transverse and radial modes, vortex shedding off the swirler, vortex shedding off the combustor wall, and precession of the vortex core. Convective-acoustic fluctuations occur when coherent structures convect downstream and encounter a blockage

such as the leading edge of a vane. A pressure wave is produced and is reflected upstream, resulting in an axial pulsations. This interacts with and modulates the shedding process that produced the coherent structures. The vortex breakdown process is also responsible for convective instabilities and hydrodynamic and acoustic fluctuations. In the case of film cooled vanes, flow over the vane with a coolant plenum also results in Helmholtz resonance.

We might argue that any observed fluctuations are therefore due entirely to these modes. However, this may not be the case. Flow conditions in the facility are typically assumed to be quasi-steady when measurements are made. Ideally, any fluctuations observed on the vane surface can then be attributed to acoustic oscillations in the combustor-turbine interface alone. However, the facility itself functions as a resonator. Air flow through the inlet run to the pressure vessel results in pipe resonance. Flow out of the linear cascade into the pressure vessel results in Helmholtz resonance. This is further complicated by the presence of 'blockages' such as the swirler and vanes. Note that this means that even with a clean inflow, oscillations can still be present.

The observed fluctuations in P, h, and η on the vane surface are therefore the result of coupled interactions between different modes of oscillations, e.g. facility-related resonance, resonance within the transition duct, and impingement and precession of the vortex core and smaller coherent structures. It is therefore necessary to identify some of these fluctuations to attribute them to either geometrical and flow characteristics within the working section or facility-related resonance.

To render such problems tractable by simple analytical solutions, the geometry is simplified into that of a simple straight pipe resonator open at both ends and a cavity resonator. While such simplifications may not be entirely accurate, this provides an order-of-magnitude estimate of resonant frequencies to expect and whether they overlap with the frequency range of interest for heat transfer (0-100 Hz). The complexity of the facility geometry - which includes expansions, contractions, and blockages - makes it difficult to identify an obvious length scale to use. Fig. 7.7 shows the various

length and volume scales that can be associated with the resonators. Table 7.2 lists the different combinations and the resulting fundamental tone.

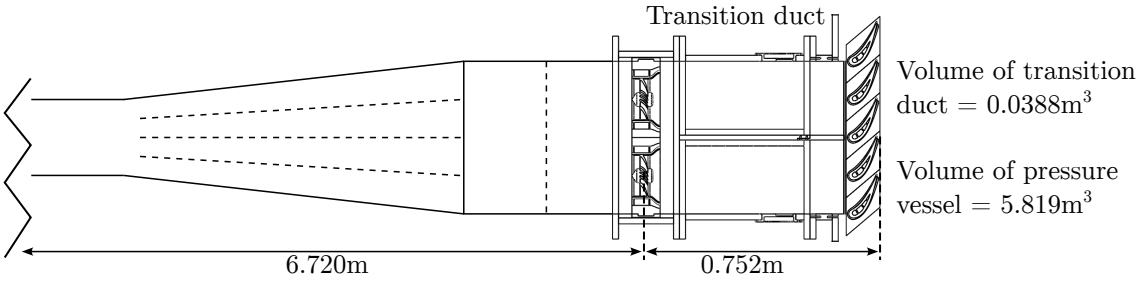


Figure 7.7: Relevant length and volume scales of the facility and working section that may contribute resonance

Resonator	**Resonant frequency**	**Scale**	**Fundamental Tone**
Pipe resonator	$\frac{nc}{2L}$	0.752 m 7.472 m	226 Hz 23 Hz
Cavity resonator	$\frac{c}{2\pi}\sqrt{\frac{A}{VL}}$	0.0388 m^3 5.819 m^3	133 Hz 2 Hz

Table 7.2: Fundamental tones of from various length and volume scales

For cavity resonance, A is the area of the exit and L is the length of the neck. In the case of the transition duct, A is taken to be the throat area of all four passages (approx. 0.0208 m^2), and L is taken to be the axial chord length ($C_{\text{ax}} = 89$ mm). In the case of the pressure vessel, A is the area of the exhaust line (approx. 0.0707 m^2), and L its length (approx. 10 m). Although the values used above are slightly arbitrary and can change the frequency of the fundamental tone, all estimates give resonant frequencies in the sub-1 kHz range. In particular, there are also resonant frequencies in the sub-100 Hz range, which is the frequency range of interest.

The estimates above can be compared with the spectra of static pressure on the vane leading edge obtained from LES of the single-core swirler. The LES result provides a baseline since it is independent of facility-related resonance. However the relatively short simulation time does not allow for high frequency resolution due to the uncertainty principle, $\Delta T \cdot \text{BW} \geq 1$, where ΔT is the total sampling duration and BW is the bandwidth. This is compared against experiments using a vane instrumented with high-speed pressure transducers. The experimentally measured result provides

much higher frequency resolution but is affected by facility-related resonance.

The single-core swirler and clean inflow cases are chosen for this analysis. The former will validate LES results. The latter will identify peaks related to facility-related resonance and show their effects on the NGV, since with clean inflow there are no fluctuations arising from the working section. The sensors are numbered as shown in Fig. 7.8.

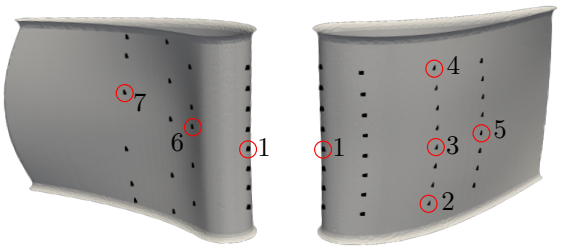


Figure 7.8: Unsteady pressure vane instrumented with high-speed pressure transducers. The transducer locations are shown as black dots. The transducers referenced by this study are numbered from 1 to 7

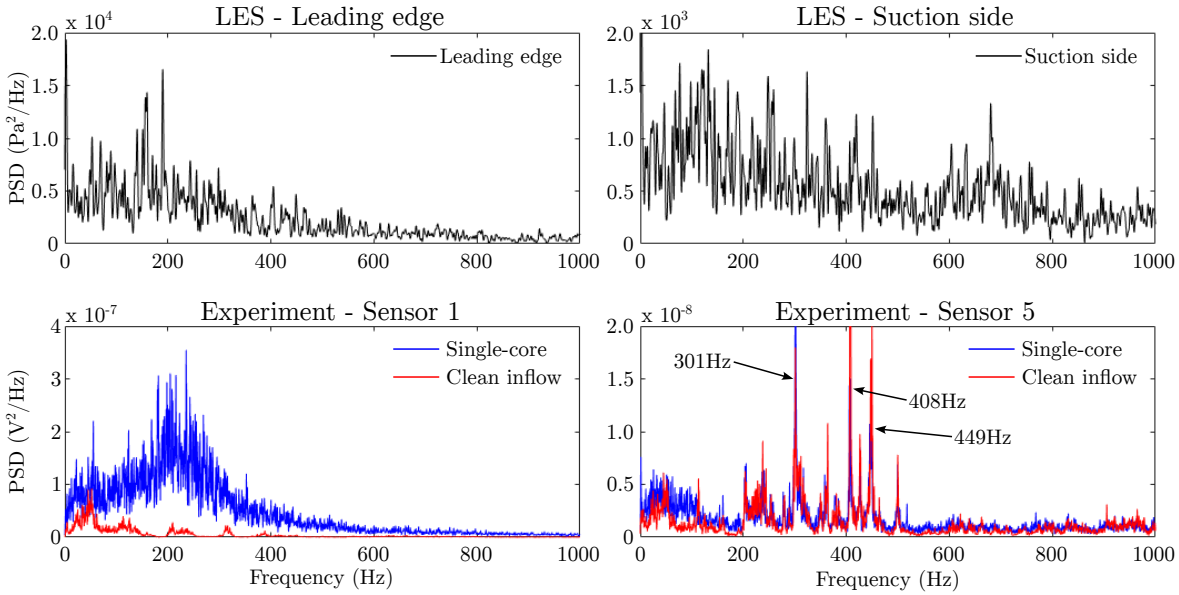


Figure 7.9: Top: PSD of total pressures obtained from LES of the single-core swirler case. Bottom: PSD of raw voltage from pressure transducers. Sensor 1 corresponds to the leading edge of the vane. Sensor 5 corresponds to the suction side of the vane

Fig. 7.9 compares the PSDs of the single-core and clean inflow cases for sensors 1 and 5 against the PSD obtained from LES at roughly the same location on the vane. The PSDs in this figure are not normalised so that the magnitudes of peaks can be compared across experiments. Note however that the magnitude of the LES spectra cannot be compared with the magnitude of the experiments' spectra due to

the different scales used; Pascal for LES and microvolts for experiments.

The LES spectra shows significant broadband frequency content over the range 0-400 Hz centred on 200 Hz. This agrees with the PSD of sensor 1 for the single-core swirler case, which lends confidence that some contribution to the experimentally measured fluctuations arises from the working section. The clean inflow also has broadband peak in the sub-100 Hz range, but is much smaller in magnitude. The total signal power integrated from 0-100 Hz for the single-core swirler is 3.3 times that of clean inflow. This shows that fluctuations arising from the working section dominate over facility-related resonance in the frequency range of interest.

Towards the late suction side corresponding to sensor 5, the PSDs for both LES and experiments are lower amplitude compared to the leading edge. Additional peaks appear in the experiment between 200 Hz and 500 Hz that are very sharp and dominate over the lower frequency peak. This is seen for both the single-core swirler and clean inflow cases. The LES spectrum has many peaks in this region however none of them dominate like those seen in the experiments. This suggests that these high frequency peaks are due to facility-related resonance and not due to swirler geometry.

The low frequency peak for both experimental cases occur at approx. 50 Hz and the total signal power integrated from 0-100 Hz for the single-core swirler is 1.9 times that of clean inflow. However, even if they share a similar low frequency peak, this does not imply these fluctuations are due to the same source. Analysis of their phases suggests that the nature of these fluctuations differ.

Fig. 7.10 presents the phase difference between sensors 3 and 5, $\phi_{3,5}$, for both the single-core swirler and clean inflow cases. The phase is calculated as the argument of the complex-valued cross-power spectral density of sensors 3 and 5. Calculation of the phase presumes some linearity in the system that governs the 'input' (sensor 3) and 'output' (sensor 5), i.e. a fluctuation in sensor 3 will be felt at sensor 5 some constant time later; the system being the acoustic wave equation. In the case of clean inflow, fluctuations around the vane are expected to be correlated since there

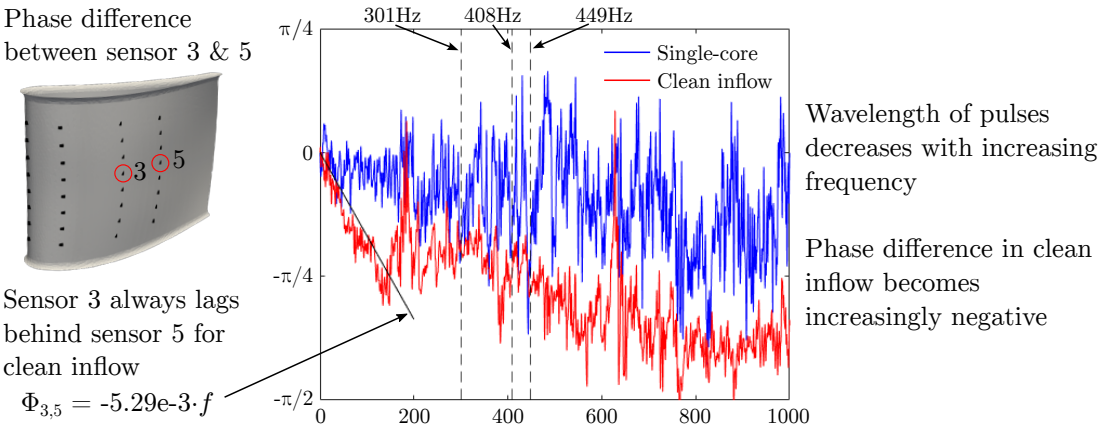


Figure 7.10: Phase difference between sensors 3 and 5 for the single-core swirler (blue) and clean inflow (red)

are no unsteady flow features that contribute to local fluctuations, unlike the single-core swirler case. In the latter case, correlation between signals will only hold in regions that are spatially close and only over smaller frequency ranges. Local changes that occur over sensor 3 may not register on sensor 5, hence introducing some non-linearities into the system. The variance of the phase of the single-core swirler is therefore much larger. In regions of low correlation, the phase can be discontinuous and oscillate between $-\pi$ and π.

Sensors 3 and 5 are sufficiently close such that the system is still linear in the frequency range of interest. For a sound wave propagating from sensor 3 to 5, the solution to the 1D wave equation is:

$$P = P_0 \cdot \sin\left(\omega t \mp kx\right)$$

where $k = {}^{\omega}/_{c}$ is the wavenumber. For a fixed distance, Δx, between them, the solution for sensor 3 is:

$$\begin{aligned} P_3 &= P_{0,3} \cdot \sin\left(\omega t \mp k\left(x + \Delta x\right)\right) \\ \Rightarrow -\phi_{3,5} &= \frac{2\pi\Delta x}{c} f \\ &= 5.29\text{E}{-3} f \end{aligned} \tag{7.1}$$

which is shown as a black line in Fig. 7.10. This gives a good fit to the distribution

of phase lag over the frequency range 0-150 Hz for the clean inflow case. Eqn. 7.1 shows that sensor 3 lags behind sensor 5 and that the phase is proportional to the frequency of the travelling wave, f. As the frequency of this wave increases, its wavelength decreases, resulting in increasing phase lag between the sensors. These results suggest that the in the case of clean inflow, the broadband peak around 50 Hz is due a travelling wave that propagates from downstream towards the upstream direction, passing first over sensor 5, and then sensor 3.

This process is visualised in Fig. 7.11 as a sequence of images of static pressure fluctuations on the vane surface over a duration of 29 ms. Experimentally measured data from each transducer has been interpolated onto a CAD model of the vane surface, with the transducers shown as white dots corresponding to their real space locations on the actual NGV test article. The data presented is for the clean inflow case and has been subtracted by its local mean, i.e. $P - \overline{P}$, to clearly visualise the fluctuations in static pressure over the whole vane surface.. The data was also lowpass filtered at 100 Hz to isolate the fluctuations to the frequency range of interest.

A pressure wave first propagates from the trailing edge and over the suction side. Its initial propagation speed is very low because it must pass through the region where flow velocity in the opposite direction is highest. Sensors 3 and 5 therefore register a phase lag. Past this point, the flow velocity in the downstream direction decreases rapidly, allowing the wave to propagate more quickly over the leading edge and to the pressure side. Hence the phase difference between sensors 1 and 7 is much smaller, such that it is within the noise band. While not shown here, the phase difference between sensors 1 and 7 for the clean inflow case appears to be zero across the same frequency range, i.e. they are in phase.

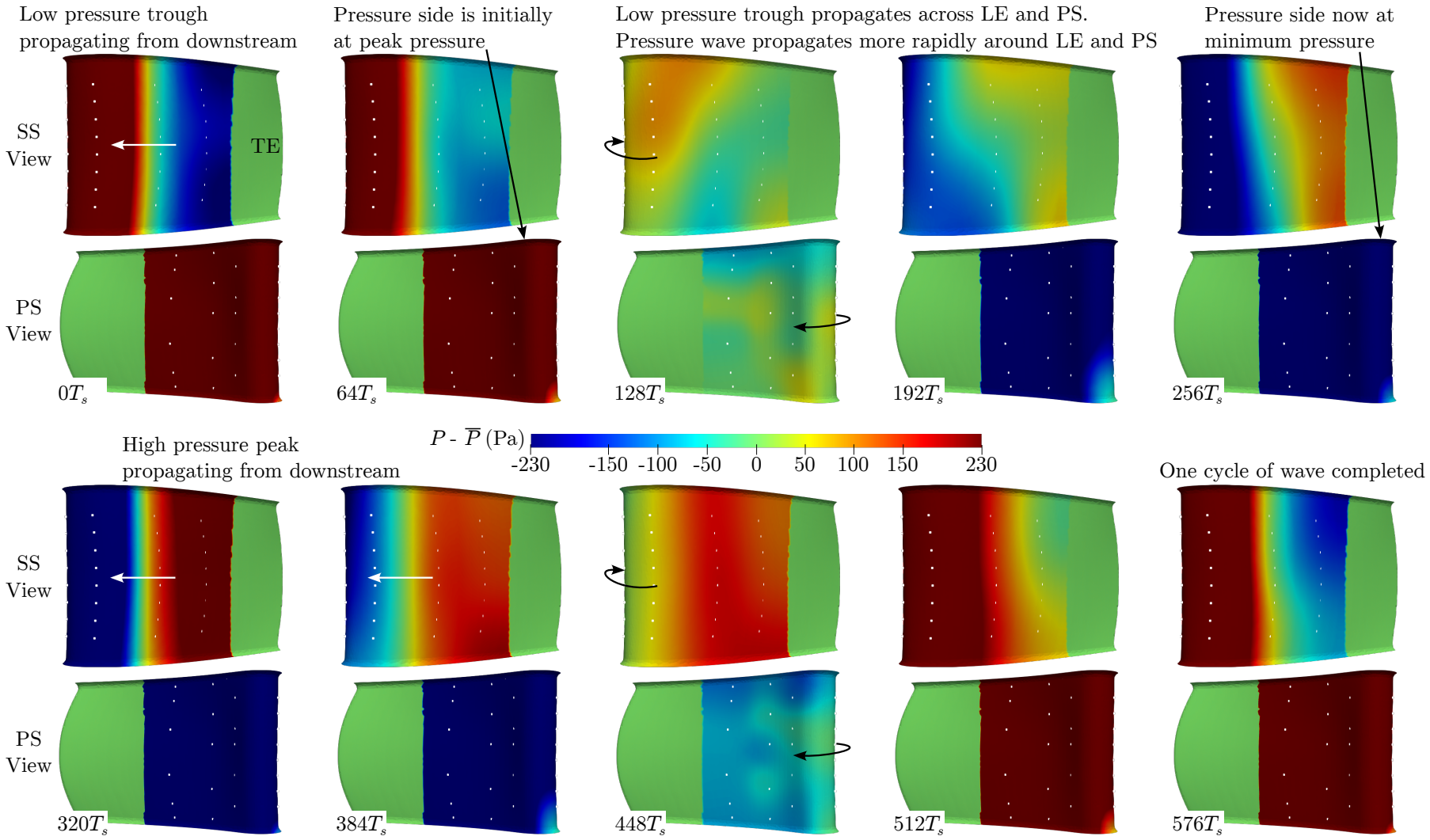


Figure 7.11: Sequence of images of experimentally measured static pressure fluctuation (about zero mean) for the clean inflow case, showing the propagation of a pressure wave from downstream at the trailing edge, over the suction side, then over the leading edge and pressure side. Sampling period, $T_s = 50\,\mu s$

In the single-core swirler case, the phase difference of sensors 3 and 5 is constant at approx. -0.1 rad across the frequency range 0-100 Hz. When observing movies of these fluctuations that have been lowpass filtered to this frequency band, no travelling wave was observed. Instead, fluctuations appear as local streaks of high or low pressure on the vane surface. These localised effects suggest that unsteadiness in the single-core swirler case is due primarily to upstream structures and not facility-related resonance.

The overlapping of peaks in the frequency range of interest means that the influence of the swirler cannot be decoupled from other acoustic modes by filtering. Therefore it is only possible to evaluate the effects of a swirler geometry relative to a baseline case without swirlers. This baseline case is taken to be the turbulence grid and results of RMS unsteadiness are reported as relative to turbulence grid case, which justifies the use of η_{rel} in §7.3.

7.6 Summary

High-speed data acquisition instruments were used to carry out an unsteady analysis of the pressure and temperature field around the unshielded NGV. The experimentally measured spectra of pressures in the flow domain and temperatures of the vane surface have shown significant content in the sub-100 Hz band. When film cooling is present, the distribution of adiabatic effectiveness has been observed to fluctuate significantly, leaving some parts undercooled and others overcooled. The regions of highest fluctuations are at the passage vortex lift-off lines and below the midspan vortex. This demonstrates the inherent unsteadiness of secondary flows and the midspan vortex in the presence of real combustor flows. Measurements made with thin-film gauges around the midspan of the vane show that the highest fluctuations are located at the leading edge of the vane and decrease very rapidly over the early suction side due to the high acceleration of flow. The 12-core swirler was the lowest levels of fluctuations across all swirler cases, but is still higher than the turbulence grid case.

In the case of the single-core swirler, the magnitude of fluctuations of the instan-

taneous adiabatic effectiveness can be higher than 10% of the local mean. The period of these fluctuations in coolant coverage is sufficiently long such that the vane surface temperature changes appreciably due to exposure to the hot freestream. When scaled to engine conditions, this can result in a peak-to-peak temperature oscillation of 65 °C near the hub passage vortex. In comparison, a reduction in the mean wall temperature by 25 °C can lead to an increase in blade life by a factor of two [64]. While fluctuations do not result in a change in mean wall temperature (assuming they are symmetric about the mean), part life is non-linear with temperature. A part subjected to these fluctuations in wall temperature will experience high-cycle thermo-mechanical fatigue, resulting in a shorter life than a part with that only experiences a steady temperature at the same mean value. This effect can be seen qualitatively from Basquin's Law of fatigue, which describes a power-law dependence between component life and the stress amplitude it is subjected to.

These fluctuations are shown to arise from two different sources. The first is from the hydrodynamic and acoustic modes caused by flow through the swirler and over the NGV. The second is from resonance within the pressure vessel itself that propagates as a travelling wave from downstream near the trailing edge in the upstream direction. These oscillations lie in the frequency range of interest and are broadband. While they therefore cannot be decoupled by filtering, the total integrated power of the spectra show that fluctuations arising from the former dominate over the latter. This lends confidence that the observed fluctuations are due primarily to combustor flows.

Chapter 8
Conclusions

The demand for gas turbines with higher efficiencies, lower emissions, and increasing flexibility have driven research into more novel combustor designs as well as higher loading turbine blades. The next generation of gas turbines will feature novel combustor geometries that allow for greater flexibility in fuel type and part-load operation, as well as higher efficiency turbine blades with increased maximum TET and lower cooling requirements. Thus, the combustor and nozzle guide vane will face increasingly extreme operating conditions. A greater understanding of the effects of real combustor flows on the nozzle guide vane is therefore required.

Traditionally, these systems have been studied and designed in isolation, where only bulk flow properties were targeted or applied as boundary conditions. Hence, this thesis had set out to address this gap in knowledge by studying the combustor-turbine interface, which integrates both domains and thus accurately captures the complex interactions between the two systems.

This final chapter reviews the main objectives of this thesis and how they have been met, presents a summary of the main findings of each investigation, and proposes potential avenues for further research. These findings have wider implications on academia as well as the gas turbine industry, in particular the modelling and design of NGVs.

8.1 Summary of Key Objectives

The thesis experimentally and numerically investigated the steady and unsteady effects of different combustor swirler geometries on the aerodynamics and heat transfer on an uncooled and film-cooled NGV. To that end, a film cooling system was designed, built, and commissioned to provide a controlled mass flow of foreign gas to the working section for film cooling. The gas used in this study was CO_2 to better

match the density ratio of a real engine.

Experiments were carried out in the MHI High Speed Linear Cascade facility for four different swirler geometries, a turbulence grid, and a clean inflow, to simulate six different inlet flow conditions to the NGV. Measurements of wall temperature, wall heat flux, and static and total pressure fluctuations were made using a high-speed infra-red camera, double-sided thin film gauges, and high-speed pressure transducers respectively. These instruments were also able to resolve the full spectrum of fluctuations in the working section and on the vane surface, thus allowing unsteady analysis of the measured quantities listed above. The steady effects of these different inlet flow conditions were quantified in terms of heat transfer on the unshielded NGV for an uncooled and film-cooled NGV. The unsteadiness of the film-cooling was also quantified and locations of highest fluctuations were identified.

LES simulations of the full combustor-turbine interface were carried out for two of the four swirler geometries that were investigated experimentally. These were the single-core swirler and the 8-core swirler. The simulations were able to resolve the dominant flow structures within the swirler, such as the recirculating zone and precessing vortex core, as well as structures entering the NGV. The steady state profiles of total pressure, pitch, and yaw were quantified and agreed very well with experimentally measured values obtained by Jacobi et al. [120] and Shaikh [132]. The steady and unsteady effects of these combustor flows were assessed and the physical mechanism for each effect was explored.

8.2 Summary of Main Findings

8.2.1 Generalisation and Application of the Impulse Response Method

Typical applications of the impulse response method to calculate heat flux have relied on the semi-infinite assumption or otherwise measured it directly with double sided gauges assuming a single layer between the gauges of known material properties.

However, the experimental setup in this study called these assumptions into question, e.g. the thin walls of the film-cooled vane and the multi-layered construction of the double-sided gauges.

To address this, the impulse response method was generalised using the Green's function solution equation for arbitrary 1D, 1D multi-layered, 2D, and 3D bodies. A general methodology was proposed to numerically evaluate the impulse responses of these bodies. This was applied in a sensitivity analysis of the surface heat flux to the internal heat transfer coefficient, which was unknown. It was shown that regardless of its value, the surface heat flux did not change appreciably and thus the body could be treated as semi-infinite for this experimental setup.

A research outcome that will aid similar studies using thin-walled bodies is the derivation of a 'penetration time', which quantifies the contribution of one boundary condition to the overall solution. This provides a useful guide when planning experiments by providing an estimate of time before which this threshold value will be exceeded.

Another application of this methodology is in the very efficient post-processing of temperature measurements made with double-sided thin film gauges into heat flux, as was done in this study. Comparisons with a finite differencing Crank-Nicolson solver on the same sample dataset showed that this methodology performed orders of magnitude faster. The methodology also allows for any number of layers between the two gauges without sacrificing execution time as it only involves a simple convolution operation, instead of solving a system of equations.

8.2.2 Effect of Combustor Geometry on Downstream Flow

The LES study of the single-core swirler has revealed the highly turbulent and unsteady nature of combustor flows at the inlet to the NGV. This flow field is dominated by the presence of a single large coherent residual swirl core that precesses about the centreline of the transition duct. The persistence of the vortex is seen in every instance of time across the whole transition duct and even in the NGV pas-

sages, allowing its precession to be easily tracked. The swirl core introduces a total pressure gradient and significant pitch and yaw angle deviation at the leading edge of the unshielded vane, while its precession results in fluctuations in the potential field around the vane. Further downstream the exit plane of the NGV, the swirl core is still present as a coherent structure that now precesses within the passage freestream. When time-averaged, this results in a high loss distribution in the freestream.

In comparison, the 8-core swirler produces lower overall levels of turbulent kinetic energy and swirl intensity throughout the entire domain. Time-averaged measurements at the inlet plane to the NGV reveal that the single swirl core has now been replaced by three smaller swirl cores with lower total pressure loss. The central swirl core is due to the pilot swirler and is consistent with its sense of rotation, while the two cores on either side of the central core are residual swirl cores from the main swirlers that have merged. Instantaneous snapshots in time of the total pressure field do not consistently show these swirl cores. Instead, the flow field appears to contain a variable number of cores that appear and rapidly disappear, making tracking of these cores difficult. The weaker swirl cores introduce a lower total pressure gradient and less pitch and yaw angle deviation to the unshielded vane's leading edge. The exit plane shows a more uniform distribution and lower levels of loss in the freestream and sharper and more distinct wakes. The mass-weighted pitchwise average of this loss is lower in the case of the 8-core swirler compared to the single-core swirler.

Thus the geometry of the combustor has been shown to significantly affect the instantaneous and time-averaged flow field in the transition duct and at NGV inlet and outlet planes. These findings provide a heuristic design rule whereby a combustor with smaller and more numerous swirl cores result in smaller coherent structures and lower levels of turbulence and swirl intensity compared to a design with a single large swirl core. This presents opportunities for further research into optimising the number of swirl cores, swirl orientation, etc. More generally this opens up fundamental questions about the interactions, evolution, and decay of multiple co and counter-

rotating vortices in confined flows.

8.2.3 Effect of Swirl and a Total Pressure Gradient on the Potential Field

Flow approaching the leading edge of the unshielded vane has a low total pressure core and a high degree of swirl. The potential field exerted by the vane causes low momentum fluid toward the centre of the core to turn more quickly compared to high momentum fluid towards the edge of the core. The leads to pitchwise vorticity forming on the leading edge of the vane and causing fluid to roll-up into a pair of counter-rotating vortices. The vortex lines wrap around the leading edge onto the suction and pressure sides and become aligned in the streamwise direction. This vortex pair that forms on the midspan is termed the midspan vortex.

A swirling flow alters the potential field of the vane by changing the angle of incidence on the hub and casing. For counter-clockwise swirl, looking from upstream to downstream, this results in positive incidence on the hub and negative incidence on the casing. This skews the stagnation line resulting in a radial pressure gradient from casing to hub on the suction side and from hub to casing on the pressure side. Fluid close to the vane suction surface, including the suction side leg of the midspan vortex, now migrates radially towards the hub, while its pressure side leg migrates towards the casing.

In the pressure side passage, the CCW swirl core opposes the migration of the hub passage vortex while enhancing the migration of the casing passage vortex. This migration is reduced in the 8-core swirler case due to the weaker pilot swirl as well as the presence of the residual main swirl which counter-rotates against the pilot swirl. In the suction side passage, swirl still opposes the migration of secondary flows but the cross-passage pressure gradient is enhanced on the hub and reduced on the casing due to the skewed stagnation line. This results in earlier migration of the hub passage vortex compared to the casing passage vortex. Consequently, the PV lift-off lines on

the suction side of the unshielded vane feature a spanwise shift upwards from the hub towards the casing.

The amount of migration of secondary flows and the midspan vortex scales with swirl intensity. Consequently these migration patterns are not as pronounced in the case of the 8-core swirler. These patterns have also been observed experimentally for a wider range of inlet flow conditions. The baseline case is the turbulence grid, which features PV lift-off lines that are nearly symmetric about the midspan. The 12-core swirler, features minimal shift in the lift-off lines and there is little to no migration of the midspan vortex. This is followed by the 8-core swirler and then the single-core swirler. The latter features the largest shift in the lift-off lines and migration of the midspan vortex. This is consistent with the increasing swirl intensity of their respective inflow conditions.

It is therefore crucial for the design of NGVs to account for swirl in combustor flows as this alters the potential field around the vane, which in turn determines the aerodynamics of the blade.

8.2.4 Effect of Unsteadiness on Secondary Flows

The incoming flow to the NGV has been shown to be highly unsteady, resulting in fluctuations in the position and size of the horseshoe vortex and passage vortex. Possible causes for the oscillating HV position are: (1) merging of the primary HV with secondary HVs formed from the convection of upstream structures onto the endwall. (2) The impingement of these upstream structures onto the HV, causing it to breakdown. (3) Precession of the swirl core towards the unshielded vane LE, which increases the local fluid velocity stagnating on the HV itself, thus forcing the HV closer to the LE.

The passage vortex has also been observed to fluctuate significantly. In some frames, it appears to have migrated across the passage towards the suction side of the shielded vane. In other frames, it appears attached to the pressure side of the unshielded vane. This correlates with the precession of the residual swirl core, whereby

a closer proximity results in the passage vortex not migrating and remaining close to the pressure side. This is due to the swirl velocity stagnating on one side of the PV, thus establishing a local static pressure gradient that prevents its migration.

Spectral analysis of the oscillations of the HV and the precession of the residual swirl core has shown that they share some peaks. The frequency of these oscillations are broadband, but significant power is contained in the sub-100 Hz. This combined with the fact that vortical motion is responsible for regions of high heat loads, suggests that surface temperatures may change appreciably and therefore warrants further investigation.

8.2.5 Effect of Combustor Flows on Heat Transfer and Film Cooling on the NGV

The time-averaged and unsteady surface maps of HTC and cooling effectiveness for the unshielded vane's suction side were obtained using a high-speed IR camera. The findings here support the heuristic design rule of reducing the size of swirler cores to achieve lower swirl and turbulence intensities, with the 12-core swirler offering the lowest overall levels of HTC, highest levels of cooling effectiveness, the most uniform distribution of heat load, and the lowest levels of fluctuations out of all the swirler geometries studied.

Combustor flows were found to result in a highly non-uniform distibution of coolant on the NGV. In particular a large triangular region of overcooling near the hub is seen for the single-core swirler, and near the casing for the reverse single-core swirler, indicating that this distribution is due to swirl. This overcooling leaves large regions of the vane undercooled, which is deleterious to blade life if unaccounted for.

Four factors influencing this non-uniform distribution were explored, two of which were governed by the potential field of the NGV, and the other two were governed directly by the motion of the midspan vortex. It is likely that the latter two are the dominant factors.

Unsteady analysis of the fluctuations in adiabatic effectiveness showed that the highest oscillations were due primarily to fluctuations in vortical motion. These include the hub and casing passage vortices and the midspan vortex. This supports the LES findings concerning the unsteadiness of the secondary flow system.

While it was found that some of these oscillations arose from facility-related resonance, it was also shown that fluctuations due to combustor flows dominated and that the observed unsteadiness was therefore realistic.

The measured fluctuations in adiabatic effectiveness for the single-core swirler was used to calculate the peak-to-peak surface temperature fluctuation in a real gas turbine. This was found to be as high as approx. 65 °C near the hub passage vortex lift-off line. This finding emphasises the need to consider the unsteady thermal field around the NGV.

8.2.6 Integration of Numerical and Experimental Studies in the CTI

The combination of experiments and high-fidelity LES carried out in this study have provided a more holistic understanding of the nature of combustor flows and their effects on the aerothermal field of the NGV. The inherent unsteadiness of such flows and the resulting fluctuations within the turbine section mean that, if accurate simulation of unsteady flows in the NGV with time-resolved combustor flows is desired, then the whole CTI must be modelled with LES so that these turbulent structures are resolved.

However, this is a computationally expensive and time intensive undertaking, due to the size of the flow domain involved and the complexity of the flow path. In particular, large volumes of the domain, such as the transition duct, require a suitably fine mesh so that the inertial subrange is captured. Such a method is impractical if the goal is to explore novel combustors and quantify its effects on the NGV.

However, this study has shown that the time-averaged LES results and the time-

averaged experimental results of HTC and adiabatic effectiveness distributions are governed by the potential field and vortical structures around the NGV. This means that, if only the mean flow field around the NGV is desired, this can be achieved with RANS simulations of the turbine section alone using accurate time-averaged inlet boundary conditions of total pressure and flow angles. These in turn can be obtained from 2D traverse measurements of the full CTI. This provides a compromise between accurate but resource-intensive LES of the full CTI, and a quick turnaround time for design optimisation purposes of novel combustor geometries.

8.3 Future Work

Combustor flows are inherently unsteady, with highly coupled interactions in a complex flow field. More fundamental studies are required to decouple each aspect so that they can be studied in isolation. These include studies on swirl flows in a confined space and the interaction of co/counter-rotating vortices with different configurations and swirl orientations. Of interest is the interaction, evolution, and mechanism for decay of these structures, as seen in LES results of the 8-core swirler. This can also inform the design of future novel combustors such that the requirements of flame stability, homogeneous mixing, etc. are satisfied while also producing a more uniform flow at the inlet to the NGV.

The study of secondary flows was complicated by the presence of the unsteady swirl core, making it difficult to decouple the sources of oscillations and attribute the cause of HV migration to any one source. This also makes comparisons across different swirlers difficult. A future study should include the turbulence grid geometry to provide a baseline case with isotropic turbulence. In that way, oscillations due to precession are removed and flow enters axially with no swirl. The Reynolds number remains the same as the studies here and the boundary layer thickness is more easily defined.

Work is also already underway to investigate the two-way coupling between the

combustor and turbine sections. The traverse measurements used in this study were obtained without the linear cascade installed due to access requirements. This resulted in a small discrepancy between the inlet profile of total pressure obtained from LES simulations and that obtained from experiments. This was postulated to be due to the coupling between the NGV's potential field and the swirl core.

Finally, a caveat to this study is the use of non-reacting flows. Existing literature has shown that hydrodynamic modes are damped in the presence of combustion, while acoustic modes are now coupled with the temperature field and can result in resonance. It would therefore be interesting to repeat this investigation into the unsteadiness around the NGV with reacting flows and noting the differences in findings.

8.4 Final Remarks

The integration of experimental and high-fidelity numerical simulations has provided a more holistic view of the complex flow phenomena in combustor flows. This study has highlighted a few key findings regarding the effects of combustor flows on the aerothermal field around the NGV. There are doubtless still many more features to be found.

Bibliography

[1] BP. Statistical Review of World Energy 2021. Technical report, 2021.

[2] International Energy Agency and Group of Eight (Organization) Summit. *Energy Technology Perspectives 2012: Pathway to Clean Energy System*. OECD/IEA, Paris, France, 2012. ISBN 978-92-64-17488-7.

[3] Allied Market Research. Gas Turbine Market Growth Analysis - 2030. Technical report, 2021.

[4] McKinsey. Global Energy Perspective 2022: Executive Summary. Technical report, 2022.

[5] Mitsubishi Heavy Industries. Combined Cycle Gas Turbine Power Plant Catalogue, 2022.

[6] HM Government. Net Zero Strategy: Build Back Greener. Technical report, 2021.

[7] Konstantinos G. Kyprianidis. Future Aero Engine Designs: An Evolving Vision. In Ernesto Benini, editor, *Advances in Gas Turbine Technology*. InTech, November 2011.

[8] Bill Gunston, editor. *Jane's Aero-Engines*. Jane's Information Group, Coulsdon, 11th edition, 2001.

[9] Mitsubishi Heavy Industries. Steam Power Plant Catalogue, 2021.

[10] Koval Svetlana. Application and Improvement of Gas Turbine Blades Film Cooling. In *Proceedings of International Conference on Aerospace System Science and Engineering 2018*, 2019.

[11] Ronald S. Bunker. Evolution of Turbine Cooling. In *Proceedings of ASME Turbo Expo 2017*, Charlotte, North Carolina, USA, June 2017.

[12] Robert A Miller. History of Thermal Barrier Coatings for Gas Turbine Engines. Technical Memorandum NASA/TM-2009-215459, NASA Glenn Research Center, March 2009.

[13] U.S. Department of Energy-National Energy Technology Laboratory (NETL), Lance Smith, Hasan Karim, Shahrokh Etemad, and William Pfefferle. *The Gas Turbine Handbook*. 2006.

[14] Arthur H. Lefebvre and Dilip R. Ballal. *Gas Turbine Combustion: Alternative Fuels and Emissions*. Taylor & Francis, Boca Raton, 3rd edition, 2010.

[15] A. K. Gupta, D. G. Lilley, and N. Syred. *Swirl Flows*. Abacus Press, Tunbridge Wells, Kent, 1984.

[16] Ioanna Aslanidou, Budimir Rosic, Vasudevan Kanjirakkad, and Sumiu Uchida. Leading Edge Shielding Concept in Gas Turbines with Can Combustors. *Journal of Turbomachinery*, March 2013.

[17] R. J. Goldstein, K. Y. Lau, and C. C. Leung. Velocity and turbulence measurements in combustion systems. *Experiments in Fluids*, June 1983.

[18] S. G. Goebel, N. Abuaf, J. A. Lovett, and C.-P. Lee. Measurements of Combustor Velocity and Turbulence Profiles. In *Proceedings of ASME Turbo Expo 2017*, Cincinnati, Ohio, USA, May 1993.

[19] Michael Schroll, Ulrich Doll, Guido Stockhausen, Ulrich Meier, Chris Willert, Christoph Hassa, and Imon Bagchi. Flow Field Characterization at the Outlet of a Lean Burn Single-Sector Combustor by Laser-Optical Methods. *Journal of Engineering for Gas Turbines and Power*, January 2017.

[20] Mark D. Turrell, Philip J. Stopford, Khawar J. Syed, and Eoghan Buchanan. CFD Simulation of the Flow Within and Downstream of a High-Swirl Lean Premixed Gas Turbine Combustor. In *Proceedings of ASME Turbo Expo 2004*, Vienna, Austria, January 2004.

[21] Christian Vandervort, David Leach, David Walker, and Jerry Sasser. Commercialization and Fleet Experience of the 7/9HA Gas Turbine Combined Cycle. In *Proceedings of ASME Turbo Expo 2019*, Phoenix, Arizona, USA, June 2019.

[22] Jeffrey Goldmeer. Gas Turbines: Hydrogen Capability and Experience - A presentation to the DOE Hydrogen and Fuel Cell Technology Advisory Committee, 2020.

[23] Jeongseog Oh, Minki Kim, and Youngbin Yoon. The tuning methodology of a GE 7FA + e DLN-2.6 gas turbine combustor. *Applied Thermal Engineering*, April 2012.

[24] David Noble, David Wu, Benjamin Emerson, Scott Sheppard, Tim Lieuwen, and Leonard Angello. Assessment of Current Capabilities and Near-Term Availability of Hydrogen-Fired Gas Turbines Considering a Low-Carbon Future. *Journal of Engineering for Gas Turbines and Power*, February 2021.

[25] Tomohiro Asai, Keisuke Miura, Yoshinori Matsubara, Yasuhiro Akiyama, Mitsuhiro Karishuku, Satoschi Dodo, Teruyuki Okazaki, and Satoshi Tanimura. Development of Gas Turbine Combustors for Fuel Flexibility. In *Proceedings of the 8th International Gas Turbine Conference*, Brussels, Belgium, October 2016.

[26] Taesong Lee and Kyu Tae Kim. Combustion dynamics of lean fully-premixed hydrogen-air flames in a mesoscale multinozzle array. *Combustion and Flame*, 218, August 2020.

[27] W. R. Hawthorne. Rotational Flow Through Cascades Part 1. The Components of Vorticity. *The Quarterly Journal of Mechanics and Applied Mathematics*, January 1955.

[28] B. Lakshminarayana. *Fluid Dynamics and Heat Transfer of Turbomachinery*. John Wiley & Sons, Inc., Hoboken, NJ, USA, 1995.

[29] Kristina S. Hermanson and Karen A. Thole. Effect of Inlet Conditions on Endwall Secondary Flows. *Journal of Propulsion and Power*, March 2000.

[30] O. P. Sharma and T. L. Butler. Predictions of Endwall Losses and Secondary Flows in Axial Flow Turbine Cascades. In *Proceedings of ASME Turbo Expo 1986*, Dusseldorf, West Germany, June 1986.

[31] L. S. Langston, M. L. Nice, and R. M. Hooper. Three-Dimensional Flow Within a Turbine Cascade Passage. *Journal of Engineering for Power*, January 1977.

[32] LS Langston. Secondary Flows in Axial Turbines - A Review. *Annals of the New York Academy of Sciences*, May 2001.

[33] LS Langston. Crossflows in a Turbine Cascade. *Journal of Engineering for Gas Turbines and Power*, October 1980.

[34] R. J. Goldstein and R. A. Spores. Turbulent Transport on the Endwall in the Region Between Adjacent Turbine Blades. *Journal of Heat Transfer*, November 1988.

[35] Hai-Ping Wang, Steven J. Olson, Richard J. Goldstein, and Ernst RG Eckert. Flow Visualization in a Linear Turbine Cascade of High Performance Turbine Blades. In *Proceedings of ASME Turbo Expo 1995*, Houston, Texas, USA, June 1995.

[36] R. J. Goldstein, H. P. Wang, and M. Y. Jabbari. The Influence of Secondary Flows Near the Endwall and Boundary Layer Disturbance on Convective Transport From a Turbine Blade. In *Proceedings of ASME Turbo Expo 1994*, The Hague, Netherlands, June 1994.

[37] M. Y. Jabbari, R. J. Goldstein, K. C. Marston, and E. R. G. Eckert. Three Dimensional Flow at the Junction between a Turbine Blade and Endwall. *Wärme- und Stoffübertragung*, January 1992.

[38] P. H. Chen and R. J. Goldstein. Convective Transport Phenomena on the Suction Surface of a Turbine Blade Including the Influence of Secondary Flows Near the Endwall. *Journal of Turbomachinery*, October 1992.

[39] G. I. Mahmood and S. Acharya. Experimental Investigation of Secondary Flow Structure in a Blade Passage With and Without Leading Edge Fillets. *Journal of Fluids Engineering*, March 2007.

[40] G. A. Zess and K. A. Thole. Computational Design and Experimental Evaluation of Using a Leading Edge Fillet on a Gas Turbine Vane. *Journal of Turbomachinery*, April 2002.

[41] C. J. Baker. The laminar horseshoe vortex. *Journal of Fluid Mechanics*, November 1979.

[42] Chang Lin, Peng-Hao Chiu, and Shyh-Jiunn Shieh. Characteristics of horseshoe vortex system near a vertical plate–base plate juncture. *Experimental Thermal and Fluid Science*, December 2002.

[43] R. W. Radomsky and K. A. Thole. High Free-Steam Turbulence Effects on Endwall Heat Transfer for a Gas Turbine Stator Vane. *Journal of Turbomachinery*, October 2000.

[44] J. D. Denton. Loss Mechanisms in Turbomachines. In *Proceedings of ASME Turbo Expo 1993*, Cincinnati, Ohio, USA, May 1993.

[45] John Coull, Christopher Clark, and Raul Vazquez. The Sensitivity of Turbine Cascade Endwall Loss to Inlet Boundary Layer Thickness. *Journal of the Global Power and Propulsion Society*, March 2019.

[46] John Denton and Graham Pullan. A Numerical Investigation Into the Sources of Endwall Loss in Axial Flow Turbines. In *Proceedings of ASME Turbo Expo 2012*, Copenhagen, Denmark, June 2012.

[47] S Harrison. Secondary Loss Generation in a Linear Cascade of High-Turning Turbine Blades. In *Proceedings of ASME Turbo Expo 1989*, Toronto, Canada, June 1989.

[48] A Perdichizzi and V Dossena. Incidence Angle and Pitch-Chord Effects on Secondary Flows Downstream of a Turbine Cascade. In *Proceedings of ASME Turbo Expo 1992*, Cologne, Germany, June 1992.

[49] H J Gladden and J N B Livingood. Procedure for scaling of experimental turbine vane airfoil temperatures from low to high gas temperatures. NASA Technical Note NASA TN D-6510, NASA Lewis Research Center, September 1971.

[50] L. D. Hylton, V. Nirmalan, B. K. Sultanian, and R. M. Kaufman. The effects of leading edge and downstream film cooling on turbine vane heat transfer. NASA Contractor Report NASA-CR-182133, General Motors Corp., November 1988.

[51] Nathan J. Greiner, Marc D. Polanka, James L. Rutledge, and Andrew T. Shewhart. Effect of Variable Properties and Radiation on Convective Heat Transfer Measurements at Engine Conditions. *Journal of Heat Transfer*, June 2016.

[52] J. Kestin and P.D. Richardson. Heat Transfer Across Turbulent, Incompressible Boundary Layers. *International Journal of Heat and Mass Transfer*, February 1963.

[53] W. Kays, M. Crawford, and B. Weigand. *Convective Heat & Mass Transfer*. McGraw-Hill Companies Inc., 4th edition, 2005.

[54] Simon Jacobi and Budimir Rosic. Thermal Investigation of Integrated Combustor Vane Concept Under Engine-Realistic Conditions. *Journal of Turbomachinery*, February 2017.

[55] N. W. Harvey, M. G. Rose, J. Coupland, and T. V. Jones. Measurement and

Calculation of Nozzle Guide Vane End Wall Heat Transfer. *Journal of Turbomachinery*, 121, April 1999.

[56] N. W. Harvey and T. V. Jones. Measurement and Calculation of End Wall Heat Transfer & Aerodynamics on a Nozzle Guide Vane in Annular Cascade. In *Proceedings of ASME Turbo Expo 1990*, Brussels, Belgium, June 1990.

[57] Michael G. Dunn. Convective Heat Transfer and Aerodynamics in Axial Flow Turbines. *Journal of Turbomachinery*, 2001.

[58] T. W. Simon and J. D. Piggush. Turbine Endwall Aerodynamics and Heat Transfer. *Journal of Propulsion and Power*, March 2006.

[59] Je-Chin Han, Sandip Dutta, and Srinath Ekkad. *Gas Turbine Heat Transfer and Cooling Technology*. CRC Press, 2012.

[60] Ronald S. Bunker. A Review of Shaped Hole Turbine Film-Cooling Technology. *Journal of Heat and Mass Transfer*, April 2005.

[61] Lucas Giller and Heinz-Peter Schiffer. Interactions Between the Combustor Swirl and the High Pressure Stator of a Turbine. In *Proceedings of ASME Turbo Expo 2012*, Copenhagen, Denmark, June 2012.

[62] Francesco Ornano and Thomas Povey. Theory of Non-Dimensional Groups in Film Effectiveness Studies. *Journal of Turbomachinery*, April 2020.

[63] Richard J. Goldstein. Film Cooling. In Thomas F. Irvine and James P. Hartnett, editors, *Advances in Heat Transfer*. Elsevier, January 1971.

[64] D. G. Bogard and K. A. Thole. Gas Turbine Film Cooling. *Journal of Propulsion and Power*, March 2006.

[65] J. H. Horlock, D. T. Watson, and T. V. Jones. Limitations on Gas Turbine Performance Imposed by Large Turbine Cooling Flows. *Journal of Engineering for Gas Turbines and Power*, July 2001.

[66] T. F. Fric and A. Roshko. Vortical structure in the wake of a transverse jet. *Journal of Fluid Mechanics*, November 1994.

[67] R. J. Goldstein, P. Jin, and R. L. Olson. Film Cooling Effectiveness and Mass/Heat Transfer Coefficient Downstream of One Row of Discrete Holes. *Journal of Turbomachinery*, April 1999.

[68] Dibbon K. Walters and James H. Leylek. A Detailed Analysis of Film–Cooling Physics: Part I—Streamwise Injection with Cylindrical Holes. In *Proceedings of ASME Turbo Expo 1997*, Orlando, Florida, USA, June 1997.

[69] R. J. Goldstein, E. R. G. Eckert, and F. Burggraf. Effects of Hole Geometry and Density on Three-Dimensional Film Cooling. *International Journal of Heat and Mass Transfer*, May 1974.

[70] C. J. P. Forth and T. V. Jones. Scaling Parameters in Film Cooling. In *Proceedings of the Eighth International Heat Transfer Conference*, San Francisco, USA, 1986.

[71] S. V. Ekkad, J. C. Han, and H. Du. Detailed Film Cooling Measurements on a Cylindrical Leading Edge Model: Effect of Free-Stream Turbulence and Coolant Density. *Journal of Turbomachinery*, October 1998.

[72] James L. Rutledge and Marc D. Polanka. Computational Fluid Dynamics Evaluations of Unconventional Film Cooling Scaling Parameters on a Simulated Turbine Blade Leading Edge. *Journal of Turbomachinery*, July 2014.

[73] James L. Rutledge, Marc D. Polanka, and Nathan J. Greiner. Computational Fluid Dynamics Evaluations of Film Cooling Flow Scaling Between Engine and Experimental Conditions. *Journal of Turbomachinery*, September 2016.

[74] Ronald S. Bunker, Jeremy C. Bailey, and Ali A. Ameri. Heat Transfer and Flow on the First Stage Blade Tip of a Power Generation Gas Turbine: Part 1 -

Experimental Results. In *Proceedings of ASME Turbo Expo 1999*, Indianapolis, Indiana, USA, June 1999.

[75] F. E. Ames and M. W. Plesniak. The Influence of Large-Scale, High-Intensity Turbulence on Vane Aerodynamic Losses, Wake Growth, and the Exit Turbulence Parameters. *Journal of Turbomachinery*, April 1997.

[76] B. Lakshminarayana. Effects of Inlet Temperature Gradients on Turbomachinery Performance. *Journal of Engineering for Power*, January 1975.

[77] Thomas Povey and Imran Qureshi. Developments in Hot-Streak Simulators for Turbine Testing. *Journal of Turbomachinery*, July 2009.

[78] Holger Werschnik, Jonathan Hilgert, Manuel Wilhelm, Martin Bruschewski, and Heinz-Peter Schiffer. Influence of Combustor Swirl on Endwall Heat Transfer and Film Cooling Effectiveness at the Large Scale Turbine Rig. *Journal of Turbomachinery*, August 2017.

[79] M. D. Barringer, K. A. Thole, and M. D. Polanka. Developing a Combustor Simulator for Investigating High Pressure Turbine Aerodynamics and Heat Transfer. In *Proceedings of ASME Turbo Expo 2004*, Vienna, Austria, June 2004.

[80] Tommaso Bacci, Riccardo Becchi, Alessio Picchi, and Bruno Facchini. Adiabatic Effectiveness on High-Pressure Turbine Nozzle Guide Vanes Under Realistic Swirling Conditions. *Journal of Turbomachinery*, November 2018.

[81] I Qureshi and T Povey. A Combustor-Representative Swirl Simulator for a Transonic Turbine Research Facility. *Proceedings of the Institution of Mechanical Engineers, Part G: Journal of Aerospace Engineering*, July 2011.

[82] Benjamin Kirollos, Roderick Lubbock, Paul Beard, Frédéric Goenaga, Anton Rawlinson, Erik Janke, and Thomas Povey. ECAT: An Engine Component

Aerothermal Facility at the University of Oxford. In *Proceedings of ASME Turbo Expo 2017*, Charlotte, North Carolina, USA, June 2017.

[83] S. Luque, V. Kanjirakkad, I. Aslanidou, R. Lubbock, B. Rosic, and S. Uchida. A New Experimental Facility to Investigate Combustor–Turbine Interactions in Gas Turbines With Multiple Can Combustors. *Journal of Engineering for Gas Turbines and Power*, May 2015.

[84] David G. Lilley. Swirl Flows in Combustion: A Review. *AIAA Journal*, August 1977.

[85] Nicholas Syred. A review of oscillation mechanisms and the role of the precessing vortex core (PVC) in swirl combustion systems. *Progress in Energy and Combustion Science*, January 2006.

[86] Tommaso Bacci, Gianluca Caciolli, Bruno Facchini, Lorenzo Tarchi, Charlie Koupper, and Jean-Louis Champion. Flowfield and Temperature Profiles Measurements on a Combustor Simulator Dedicated to Hot Streaks Generation. In *Proceedings of ASME Turbo Expo 2015*, Montreal, Quebec, Canada, June 2015.

[87] Tommaso Bacci, Bruno Facchini, Alessio Picchi, Lorenzo Tarchi, Charlie Koupper, and Jean-Louis Champion. Turbulence Field Measurements at the Exit of a Combustor Simulator Dedicated to Hot Streaks Generation. In *Proceedings of ASME Turbo Expo 2015*, Montreal, Quebec, Canada, June 2015.

[88] Chong M. Cha, Peter T. Ireland, Paul A. Denman, and Vivek Savarianandam. Turbulence Levels are High at the Combustor-Turbine Interface. In *Proceedings of ASME Turbo Expo 2012*, Copenhagen, Denmark, June 2012.

[89] Sébastien M. Candel. Combustion instabilities coupled by pressure waves and their active control. In *Proceedings of the Combustion Institute*, Sydney, Australia, July 1992.

[90] Sebastien Ducruix, Thierry Schuller, Daniel Durox, and Sebastien Candel. Combustion Dynamics and Instabilities: Elementary Coupling and Driving Mechanisms. *Journal of Propulsion and Power*, September 2003.

[91] Ying Huang and Vigor Yang. Dynamics and stability of lean-premixed swirl-stabilized combustion. *Progress in Energy and Combustion Science*, August 2009.

[92] M. D. Barringer, K. A. Thole, M. D. Polanka, J. P. Clark, and P. J. Koch. Migration of Combustor Exit Profiles Through High Pressure Turbine Vanes. *Journal of Turbomachinery*, April 2009.

[93] Zhigang Li, Bo Bai, Luxuan Liu, Jun Li, Shuo Mao, Wing Ng, Hongzhou Xu, and Michael Fox. Effects of Freestream Turbulence Intensity, Turbulence Length Scale, and Exit Reynolds Number on Vane Endwall Secondary Flow and Heat Transfer in a Transonic Turbine Cascade. In *Proceedings of ASME Turbo Expo 2020*, September 2020.

[94] Jens H. M. Fransson and Shahab Shahinfar. On the effect of free-stream turbulence on boundary-layer transition. *Journal of Fluid Mechanics*, September 2020.

[95] Sean Jenkins, Krishnakumar Varadarajan, and David G. Bogard. The Effects of High Mainstream Turbulence and Turbine Vane Film Cooling on the Dispersion of a Simulated Hot Streak. *Journal of Turbomachinery*, January 2004.

[96] Sean C. Jenkins and David G. Bogard. The Effects of the Vane and Mainstream Turbulence Level on Hot Streak Attenuation. *Journal of Turbomachinery*, January 2005.

[97] K. A. Thole and D. G. Bogard. Enhanced Heat Transfer and Shear Stress due to High Freestream Turbulence. In *Proceedings of ASME Turbo Expo 1994*, The Hague, Netherlands, June 1994.

[98] Forrest E Ames. The Influence of Large Scale High Intensity Turbulence on Vane Heat Transfer. In *Proceedings of ASME Turbo Expo 1995*, Houston, Texas, USA, June 1995.

[99] P. E. Hancock and P. Bradshaw. The Effect of Free-Stream Turbulence on Turbulent Boundary Layers. *Journal of Fluids Engineering*, September 1983.

[100] Michael J. Barrett and D. Keith Hollingsworth. Heat Transfer in Turbulent Boundary Layers Subjected to Free-Stream Turbulence—Part I: Experimental Results. *Journal of Turbomachinery*, April 2003.

[101] Michael J. Barrett and D. Keith Hollingsworth. Heat Transfer In Turbulent Boundary Layers Subjected to Free-Stream Turbulence—Part II: Analysis and Correlation. *Journal of Turbomachinery*, April 2003.

[102] K.A. Thole, R.W. Radomsky, M.B. Kang, and A. Kohli. Elevated Freestream Turbulence Effects on Heat Transfer for a Gas Turbine Vane. *International Journal of Heat and Fluid Flow*, April 2002.

[103] D. G. Gregory-Smith and J. G. E. Cleak. Secondary Flow Measurements in a Turbine Cascade With High Inlet Turbulence. In *Proceedings of ASME Turbo Expo 1990*, Brussels, Belgium, June 1990.

[104] Forrest E. Ames, Pierre A. Barbot, and Chao Wang. Effects of Aeroderivative Combustor Turbulence on Endwall Heat Transfer Distributions Acquired in a Linear Vane Cascade. *Journal of Turbomachinery*, April 2003.

[105] Donald L. Schmidt and David G. Bogard. Effects of Free-Stream Turbulence and Surface Roughness on Film Cooling. In *Proceedings of ASME Turbo Expo 1996*, Birmingham, UK, June 1996.

[106] Michael W. Cruse, Ushio M. Yuki, and David G. Bogard. Investigation of Various Parametric Influences on Leading Edge Film Cooling. In *Proceedings of ASME Turbo Expo 1997*, Orlando, Florida, USA, June 1997.

[107] Forrest E Ames. Aspects of Vane Film Cooling With High Turbulence: Part I - Heat Transfer. In *Proceedings of ASME Turbo Expo 1997*, Florida, USA, June 1997.

[108] Forrest E Ames. Aspects of Vane Film Cooling With High Turbulence: Part II - Adiabatic Effectiveness. In *Proceedings of ASME Turbo Expo 1997*, Florida, USA, June 1997.

[109] Daniel J. Dorney, Karen L. Gundy-Burlet, and Douglas L. Sondak. A Survey Of Hot Streak Experiments And Simulations. *International Journal of Turbo and Jet Engines*, January 1999.

[110] Charlie Koupper. *Unsteady multi-component simulations dedicated to the impact of the combustion chamber on the turbine of aeronautical gas turbines.* PhD Thesis, University of Toulouse, France, May 2015.

[111] T. L. Butler, O. P. Sharma, H. D. Joslyn, and R. P. Dring. Redistribution of an inlet temperature distortion in an axial flow turbine stage. *Journal of Propulsion and Power*, January 1989.

[112] M. Munk and R. Prim. On the Multiplicity of Steady Gas Flows Having the Same Streamline Pattern. *Proceedings of the National Academy of Sciences*, May 1947.

[113] Zakaria Mansouri. Numerical Prediction of Heat Transfer Characteristics on a Turbine Nozzle Guide Vane Under Various Combustor Exit Hot-Streaks. *Heat Transfer*, September 2021.

[114] Daniel J. Dorney, Roger L. Davis, David E. Edwards, and Nateri K. Madavan. Unsteady analysis of hot streak migration in a turbine stage. *Journal of Propulsion and Power*, March 1992.

[115] Jonathan Ong and Robert J. Miller. Hot Streak and Vane Coolant Migration in a Downstream Rotor. *Journal of Turbomachinery*, September 2012.

[116] Imran Qureshi, Arrigo Beretta, and Thomas Povey. Effect of Simulated Combustor Temperature Nonuniformity on HP Vane and End Wall Heat Transfer: An Experimental and Computational Investigation. *Journal of Engineering for Gas Turbines and Power*, March 2011.

[117] Imran Qureshi, Andy D. Smith, and Thomas Povey. HP Vane Aerodynamics and Heat Transfer in the Presence of Aggressive Inlet Swirl. *Journal of Turbomachinery*, March 2013.

[118] Stavros Pyliouras, Heinz-Peter Schiffer, Erik Janke, and Lars Willer. Effects of Non-Uniform Combustor Exit Flow on Turbine Aerodynamics. In *Proceedings of ASME Turbo Expo 2012*, Copenhagen, Denmark, June 2012.

[119] Gregor Schmid, Alexander Krichbaum, Holger Werschnik, and Heinz-Peter Schiffer. The Impact of Realistic Inlet Swirl in a 1 $\frac{1}{2}$ Stage Axial Turbine. In *Proceedings of ASME Turbo Expo 2014*, Düsseldorf, Germany, June 2014.

[120] Simon Jacobi, Cosimo Mazzoni, Budimir Rosic, and Krishan Chana. Investigation of Unsteady Flow Phenomena in First Vane Caused by Combustor Flow With Swirl. *Journal of Turbomachinery*, April 2017.

[121] Zakaria Mansouri and Riyadh Belamadi. The Influence of Inlet Swirl Intensity and Hot-Streak on Aerodynamics and Thermal Characteristics of a High Pressure Turbine Vane. *Chinese Journal of Aeronautics*, November 2021.

[122] F. Duchaine, J. Dombard, L. Y. M. Gicquel, and C. Koupper. On the importance of inlet boundary conditions for aerothermal predictions of turbine stages with large eddy simulation. *Computers & Fluids*, September 2017.

[123] S. Cubeda, L. Mazzei, T. Bacci, and A. Andreini. Impact of Predicted Combustor Outlet Conditions on the Aerothermal Performance of Film-Cooled High Pressure Turbine Vanes. *Journal of Engineering for Gas Turbines and Power*, May 2019.

[124] B. Khanal, L. He, J. Northall, and P. Adami. Analysis of Radial Migration of Hot-Streak in Swirling Flow Through High-Pressure Turbine Stage. *Journal of Turbomachinery*, July 2013.

[125] Cosimo Maria Mazzoni, Christian Klostermeier, and Budimir Rosic. Influence of Large Wake Disturbances Shed From the Combustor Wall on the Leading Edge Film Cooling. *Journal of Engineering for Gas Turbines and Power*, August 2014.

[126] C. M. Mazzoni, B. Rosic, and C. Klostermeier. Combustor Wall Axial Location Effects on First Vane Leading-Edge Cooling. *Journal of Propulsion and Power*, July 2015.

[127] P. M. Ligrani, R. Gong, J. M. Cuthrell, and J. S. Lee. Bulk Flow Pulsations and Film Cooling l - Injectant behavior. *International Journal of Heat and Mass Transfer*, July 1996.

[128] P. M. Ligrani, R. Gong, J. M. Cuthrell, and J. S. Lee. Bulk Flow Pulsations and Film Cooling II - Flow Structure and Film Effectiveness. *International Journal of Heat and Mass Transfer*, July 1996.

[129] P. M. Ligrani, R. Gong, J. M. Cuthrell, and J. S. Lee. Effects of Bulk Flow Pulsations on Film-Cooled Boundary Layer Structure. *Journal of Fluids Engineering*, March 1997.

[130] C M Bell, P M Ligrani, W A Hull, and C M Norton. Film cooling subject to bulk flow pulsations: effects of blowing ratio, freestream velocity, and pulsation frequency. *International Journal of Heat and Mass Transfer*, December 1999.

[131] P. M. Ligrani and C. M. Bell. Film Cooling Subject to Bulk Flow Pulsations: Effects of Density Ratio, Hole Length-to-Diameter Ratio, and Pulsation Frequency. *International Journal of Heat and Mass Transfer*, May 2001.

[132] Faisal Shaikh. *Unsteady Phenomena and Realistic Geometry Effects at the Combustor-Turbine Interface of a Large Gas Turbine*. PhD thesis, University of Oxford, 2020.

[133] M. D. Barringer, K. A. Thole, and M. D. Polanka. Experimental Evaluation of an Inlet Profile Generator for High-Pressure Turbine Tests. *Journal of Turbomachinery*, July 2006.

[134] Baoyu Guo, Tim A. G. Langrish, and David F. Fletcher. Simulation of Turbulent Swirl Flow in an Axisymmetric Sudden Expansion. *AIAA Journal*, January 2001.

[135] P. Wang, X. S. Bai, M. Wessman, and J. Klingmann. Large eddy simulation and experimental studies of a confined turbulent swirling flow. *Physics of Fluids*, September 2004.

[136] Shanwu Wang, Vigor Yang, George Hsiao, Shih-Yang Hsieh, and Hukam C. Mongia. Large-eddy simulations of gas-turbine swirl injector flow dynamics. *Journal of Fluid Mechanics*, July 2007.

[137] C. D. Cameron, J. Brouwer, C. P. Wood, and G. S. Samuelsen. A Detailed Characterization of the Velocity and Thermal Fields in a Model Can Combustor With Wall Jet Injection. *Journal of Engineering for Gas Turbines and Power*, January 1989.

[138] S. Roux, G. Lartigue, T. Poinsot, U. Meier, and C. Bérat. Studies of mean and unsteady flow in a swirled combustor using experiments, acoustic analysis, and large eddy simulations. *Combustion and Flame*, April 2005.

[139] L Selle. Compressible large eddy simulation of turbulent combustion in complex geometry on unstructured meshes. *Combustion and Flame*, 137, June 2004.

[140] Simone Salvadori, Giovanni Riccio, Massimiliano Insinna, and Francesco Martelli. Analysis of Combustor/Vane Interaction With Decoupled and Loosely

Coupled Approaches. In *Proceedings of ASME Turbo Expo 2012*, Copenhagen, Denmark, June 2012.

[141] Massimiliano Insinna, Simone Salvadori, and Francesco Martelli. Simulation of Combustor/NGV Interaction Using Coupled RANS Solvers: Validation and Application to a Realistic Test Case. In *Proceedings of ASME Turbo Expo 2014*, Düsseldorf, Germany, June 2014.

[142] S. Roux, M. Cazalens, and T. Poinsot. Outlet-Boundary-Condition Influence for Large Eddy Simulation of Combustion Instabilities in Gas Turbines. *Journal of Propulsion and Power*, May 2008.

[143] M. P. Escudier, A. K. Nickson, and R. J. Poole. Influence of outlet geometry on strongly swirling turbulent flow through a circular tube. *Physics of Fluids*, December 2006.

[144] Ioanna Aslanidou and Budimir Rosic. Effect of the Combustor Wall on the Aerothermal Field of a Nozzle Guide Vane. *Journal of Turbomachinery*, April 2018.

[145] Ioanna Aslanidou. *Combustor and turbine aerothermal interactions in gas turbines with can combustors*. PhD Thesis, University of Oxford, 2016.

[146] P. E. Roach. The generation of nearly isotropic turbulence by means of grids. *International Journal of Heat and Fluid Flow*, 1987.

[147] Simon Jacobi and Budimir Rosic. Influence of Combustor Flow With Swirl on Integrated Combustor Vane Concept Full-Stage Performance. *Journal of Turbomachinery*, January 2018.

[148] T. V. Jones. Theory for the use of foreign gas in simulating film cooling. *International Journal of Heat and Fluid Flow*, 1999.

[149] M. L. G. Oldfield. Impulse Response Processing of Transient Heat Transfer Gauge Signals. *Journal of Turbomachinery*, 2008.

[150] FLIR Systems. FLIR X6900sc Datasheet, 2018.

[151] Benjamin Kirollos and Thomas Povey. Laboratory Infrared Thermal Assessment of Laser-Sintered High-Pressure Nozzle Guide Vanes to Derisk Engine Design Programs. *Journal of Turbomachinery*, April 2017.

[152] Devin Owen O'Dowd. *Aero-Thermal Performance of Transonic High-Pressure Turbine Blade Tips*. PhD thesis, University of Oxford, 2010.

[153] D. L. Schultz and T. V. Jones. Heat-Transfer Measurements in Short-Duration Hypersonic Facilities. AGARDograph AGARD-AG-165, Advisory Group for Aerospace Research and Development, France, February 1973.

[154] J. E. Doorly and M. L. G. Oldfield. The theory of advanced multi-layer thin film heat transfer gauges. *International Journal of Heat and Mass Transfer*, June 1987.

[155] E. Piccini, S. M. Guo, and T V Jones. The development of a new direct-heat-flux gauge for heat-transfer facilities. *Measurement Science and Technology*, April 2000.

[156] Stephen B. Pope. *Turbulent Flows*. Cambridge University Press, Cambridge, UK, August 2000.

[157] Cosimo Maria Mazzoni, Salvador Luque, and Budimir Rosic. Capabilities of Thermal Wall Functions to Predict Heat Transfer on the NGVs of a Gas Turbine With Multiple Can Combustors. In *Proceedings of ASME Turbo Expo 2015*, Montreal, Quebec, Canada, June 2015.

[158] Christian Klostermeier. *Investigation into the capability of large eddy simula-*

tion for turbomachinery design. PhD Thesis, University of Cambridge, United Kingdom, October 2008.

[159] H. S. Carslaw and J. C. Jaeger. *Conduction of Heat in Solids*. Clarendon Press, Oxford, UK, 2nd edition, 1959.

[160] K. D. Cole, A. Haji-Sheikh, J. V. Beck, and Bahman Litkouhi. *Heat Conduction using Green's functions*. CRC Press, Boca Raton, 2nd edition, 2011.

[161] David W. Hahn and M. Necati Özişik. *Heat Conduction*. John Wiley & Sons, Inc., Hoboken, NJ, USA, 3rd edition, August 2012.

[162] E.J. Carr and I.W. Turner. A semi-analytical solution for multilayer diffusion in a composite medium consisting of a large number of layers. *Applied Mathematical Modelling*, August 2016.

[163] Laurent Jacquin and Carlos Pantano. On the persistence of trailing vortices. *Journal of Fluid Mechanics*, November 2002.

[164] Aline J. Cotel and Robert E. Breidenthal. Turbulence inside a vortex. *Physics of Fluids*, October 1999.

[165] Jiaxu Yao, Jin Xu, Ke Zhang, Jiang Lei, and Lesley M. Wright. Effect of Density Ratio on Film-Cooling Effectiveness Distribution and its Uniformity for Several Hole Geometries on a Flat Plate. In *Proceedings of ASME Turbo Expo 2017*, Charlotte, North Carolina, USA, June 2017.

[166] Frank Kreith and O. K. Sonju. The decay of a turbulent swirl in a pipe. *Journal of Fluid Mechanics*, June 1965.

[167] Jaehoon Choi, Eunbeom Jung, Seongwon Kang, and Hyungrok Do. Modeling Swirl Decay Rate of Turbulent Flows in Annular Swirl Injectors. *AIAA Journal*, December 2018.

[168] A .F. Najafi, S. M. Mousavian, and K. Amini. Numerical investigations on swirl intensity decay rate for turbulent swirling flow in a fixed pipe. *International Journal of Mechanical Sciences*, October 2011.

[169] C. Cerretelli and C. H. K. Williamson. The physical mechanism for vortex merging. *Journal of Fluid Mechanics*, January 2003.

[170] John D. Coull, Henry C.-H. Ng, Tony Dickens, José Serna, and Kenan Cengiz. Pneumatic-Probe Measurement Errors Caused by Fluctuating Flow Angles. *AIAA Journal*, May 2023.

[171] C. J. Baker. The turbulent horseshoe vortex. *Journal of Wind Engineering and Industrial Aerodynamics*, July 1980.

[172] Faisal Shaikh and Budimir Rosic. Unsteady Phenomena at the Combustor-Turbine Interface. In *Proceedings of Global Power & Propulsion Society*, Online Conference, September 2020.

[173] Philippe Robin, François Gitzhofer, Pierre Fauchais, and Maher Boulos. Remaining Fatigue Life Assessment of Plasma Sprayed Thermal Barrier Coatings. *Journal of Thermal Spray Technology*, September 2010.

[174] Krishna Praveen Jonnalagadda, Robert Eriksson, Xin-Hai Li, and Ru Lin Peng. Fatigue life prediction of thermal barrier coatings using a simplified crack growth model. *Journal of the European Ceramic Society*, May 2019.